In-situ X-ray scattering studies of growth at liquid metal-electrolyte interfaces

Dissertation

in fulfilment of the requirements for the degree of
Doctor of Natural Sciences (Dr. rer. nat.)
of the Faculty of Mathematics and Natural Sciences
at Kiel University

submitted by
Andrea SARTORI

Kiel, 2022

First examiner:	Prof. Dr. Olaf M. Magnussen
Second examiner:	Prof. Dr. Martin Müller
Date of the oral examination:	07.06.2022

Abstract

In-situ X-ray scattering studies of growth at liquid metal-electrolyte interfaces

Electrochemical growth at liquid-metal electrolyte interfaces was investigated with *in-situ* X-ray scattering techniques.

Here, it is presented why liquid-liquid interfaces are intriguing for nanomaterial synthesis and how interfacial processes such as absorption, condensation, and diffusion are essential aspects of crystal growth. Due to powerful *in-situ* X-ray techniques, understanding these mechanisms was possible, allowing access to the buried interfaces. Three studies of different combinations of liquid metal working electrodes and electrolytes are presented.

In the first, a liquid mercury electrode immersed in a solution of NaX + PbX_2 (X= Br, Cl, F) was probed by X-ray reflectivity and grazing incidence X-ray diffraction as a function of applied potential. Phenomenon previously observed at liquid metal-electrolyte interface in the system NaBr + NaF + $PbBr_2$ were confirmed, namely first ad-layer formation followed by crystal growth. In this study, $PbBr_2$ and $PbCl_2$ containing solutions showed a defined layer formation at a potential close to the deamalgamation region of Pb from Hg. For more positive potential, the systems exhibited quasi-epitaxial growth of bulk crystals of Pb(OH)Y (Y=Br, Cl) oriented with the c-axis of the precursor layer along the surface normal direction. On the contrary, growth in the F-containing solution resulted in a more disordered deposit, with random crystal orientations on the Hg surface. This study reveals how the ad-layer can act as a template and determine the orientation of the bulk crystals.

The interface between Hg-$Na_2B_4O_7$ and Hg-$Na_2B_4O_7$ + GeO_2 was also investigated in situ with X-ray reflectivity studies. The Hg surface in $Na_2B_4O_7$ solution displayed a similar structure to that previously observed for Hg-NaF. Once GeO_2 was introduced in the system, the data suggested an enriched H_2GeO_3 and/or $HGeO_3^-$ at the working electrode's surface. At positive potentials, an incomplete ultrathin film was observed at the Hg-electrolyte interface, likely formed by condensation reaction driven by the concentration of $HGeO^{3-}$ at the liquid Hg/electrolyte interface.

In order to study alternative electrodes, the deposition of crystalline Ge on different working electrode compositions $Hg_{1-x}In_x$ (for x= 0, 0.3, 0.5, 0.7, 1) was investigated. The focus of the thesis was on the interface of Hg-$Na_2B_4O_7$ and $Hg_{0.3}In_0.7$–$Na_2B_4O_7$. Changes were observed in the Ge crystals' shape, both as a function of potential and composition. X-ray reflectivity indicates that the very first layer of the liquid electrode is Hg. Thus, nucleation and growth must occur underneath the surface of the substrate. The crystalline grain morphology is mainly affected by In as a liquid metal component due to the strong affinity between In and Ge.

Kurzfassung

In-situ Wachstumsuntersuchung an Flüssigmetall-Elektrolyt-Grenzflächen mittels Röntgenstreuung

Elektrochemisches Wachstum an Flüssig-Metall-Elektrolyt-Grenzflächen wurde mittels Röntgenstreutechniken untersucht.
Im Folgenden wird dargelegt weshalb Flüssigkeits-Flüssigkeits-Grenzflächen für die Nanomaterialsynthese von Interesse sind und Grenzflächenprozesse wie Absorption, Kondensation und Diffusion wesentliche Aspekte des Kristallwachstums darstellen. Dank leistungsfähiger Röntgentechniken war es möglich, diese Mechanismen zu verstehen und Zugang zu den vergrabenen Grenzflächen zu erhalten. Es werden drei Studien mit verschiedenen Kombinationen von Flüssigmetall-Arbeitselektroden und Elektrolyten vorgestellt.
In der ersten Studie wurde eine flüssige Quecksilberelektrode, die in eine Lösung von NaX + PbX_2 (X= Br, Cl, F) eingetaucht war, mittels Röntgenreflexion und Röntgenbeugung unter streifenden Einfall als Funktion des angelegten Potentials untersucht. Die zuvor an der NaBr+ NaF + $PbBr_2$ Flüssigmetall-Elektrolyt-Grenzfläche beobachteten Phänomene wurden bestätigt, zunächst die Bildung von Ad-Schichten, gefolgt von Kristallwachstum. In der hier präsentieren Studie zeigten $PbBr_2$- und $PbCl_2$-haltige Lösungen eine definierte Schichtbildung bei einem Potential nahe dem Deamalgamierungsbereich von Pb aus Hg. Bei positiverem Potential zeigten die Systeme ein quasi-epitaktisches Wachstum von Kristallen bestehend aus Pb(OH)Y (Y=Br, Cl), die mit ihrer c-Achse entlang der Oberflächennormalen ausgerichtet sind. Im Gegensatz dazu führte das Wachstum in der Fluor haltigen Lösung zu einer eher ungeordneten Ablagerung mit zufälligen Kristallorientierungen auf der Hg-Oberfläche. Diese Studie zeigt, wie Ad-Schichten als Schablone fungieren und die Orientierung der Kristalle bestimmen.
Die Grenzfläche zwischen Hg-$Na_2B_4O_7$ und Hg-$Na_2B_4O_7$ + GeO_2 wurde ebenfalls in situ mit Röntgenreflexionsstudien untersucht. Die Hg-Oberfläche in $Na_2B_4O_7$ - Lösung zeigte eine ähnliche Struktur wie die, die zuvor für Hg-NaF beobachtet wurde. Sobald GeO_2 in das System eingebracht wurde, deuten die Daten auf angereichertes H_2GeO_3 und/oder $HGeO_3^-$ an der Oberfläche der Arbeitselektrode hin. Bei positiven Potentialen wurde ein unvollständiger ultradünner Film an der Hg-Elektrolyt-Grenzfläche beobachtet, der wahrscheinlich von einer Kondensationsreaktion herrührt, die durch die Konzentration von $HGeO^{3-}$ an der flüssigen Hg/Elektrolyt-Grenzfläche angetrieben wurde. Um im Weiteren alternative Elektroden zu untersuchen, wurde die Abscheidung von kristallinem Ge auf verschiedenen Zusammensetzungen der Arbeitselektrode $Hg_{1-x}In_x$ (für x= 0, 0,3, 0,5, 0,7, 1) untersucht. Der Schwerpunkt der Untersuchung lag dabei auf der Grenzfläche von Hg-$Na_2B_4O_7$ und $Hg_{0.3}In_0.7$–$Na_2B_4O_7$. Es wurden Veränderungen in der Form der Ge-Kristalle

beobachtet, sowohl als Funktion des Potentials als auch der Zusammensetzung. Untersuchungen mittels Röntgenreflexions zeigen, dass die erste Schicht der flüssigen Elektrode aus Hg besteht. Keimbildung und Wachstum müssen also unterhalb der Oberfläche des Substrats stattfinden. Die Morphologie der Kristallite wird aufgrund der starken Affinität zwischen In und Ge hauptsächlich durch In als Flüssigmetallkomponente beeinflusst.

Contents

1 Introduction

Liquid surfaces and liquid-liquid interfaces play an important role in many modern scientific fields, such as bioscience, biochemistry, polymerizations, catalysis, electrochemistry, material synthesis [1–6]. In recent years there has been a growing interest in liquid interfaces, especially as a basis for the controlled production of crystalline nanostructures, such as nanoparticles [7], nanocubes [8] two-dimensional films [9, 10], needles [11], nanowires [12], plates [13, 14], asymmetric particles [15].

Significant advantages of liquids over solid substrates for growth processes, are the lack of strain and stress, steps, lattice mismatch that strongly affect the crystal growth process. Liquid substrates have smooth flat interfaces over a large length scale providing a template for high-quality crystals. Furthermore, a liquid substrate can act as a solvent for precursors of the synthesis, and later the deposit can be easily separated from the substrate.

Standard synthesis techniques for crystalline materials such semiconductors include molecular beam epitaxy, chemical vapor deposition, sputtering deposition. While these techniques yield high purity and high-quality inorganic semiconductor materials, these methods are usually resource-intensive as they require high temperature, low pressures, and expensive instrumentation [16–18].

Similar results can be obtained from liquids with lower temperatures at a liquid-liquid interface [19], where the deposit is mainly influenced by controllable parameters such as precursor concentration in solution and temperature.

In an electrochemical system, it is also possible to control the reaction by adjusting the applied potential over the interface, which affects the properties of the products, for example, the form and size of crystals [20, 21]. Despite extensive investigations of electrochemically controlled processes for the production of crystalline nanostructures, to date, there are only a few in situ studies of growth at the liquid-liquid interface [22–27].

Most studies to characterize crystalline structure formation at the liquid interface are limited to ex-situ imaging such as transmission electron microscopy and scanning electron microscopy [28–30], requiring the materials to be removed from the system in which they were grown. Therefore, a modification of the system cannot be ruled out. Moreover, the kinetics cannot be investigated.

A detailed understanding of the effects that influence the growth at the interface between two liquids is a prerequisite for the future use of such systems for upscale production of low-defect crystalline nanostructures.

Although it is of significant interest to resolve the structure of surfaces and interfaces on the atomic scale, the characterization of an interface buried in two liquids is not accessible for many methods, and it is highly challenging. X-ray scattering, the focus of this thesis, allows in-situ studies of structural changes on the atomic-scale at liquid-liquid interfaces [31]. X-ray beams with high photon energy and flux can penetrate the liquid phase and be employed to investigate the interface, giving information about the structure of a crystalline phase that is formed and the structure of the interface itself. Usually, the prerequisites for these experiments are not achievable in a typical lab source. Hence synchrotron radiation is required. Another requirement is to direct the beam onto the liquid surface as the liquid sample can not be tilted. Therefore a diffractometer capable of deflecting a synchrotron beam is essential. Such as Liquid Interfaces Scattering Apparatus (LISA) at P08 (PETRA III, DESY) [32]. It employs a double crystal monochromator in Bragg condition to tilt the beam. In this way, performing an X-ray reflectivity is possible without moving the sample, advantageous for experiments where *in-situ* sub nanolayer are investigated and where a mechanical perturbation might influence the nucleation and growth.

The focus of this work was to investigate growth at liquid metal-electrolyte interface in an electrochemical environment. Here, X-ray scattering techniques such as X-ray reflectivity (XRR) and Grazing incidence diffractions (GID) are combined with electrochemical methods including cyclic voltamogramm (CV) and potentiostatic. In order to examine the stages of nucleation and growth and understand the influence of different solutions or liquid metal composition on the final deposit and the interface. For such studies, a dedicated sample cell was designed and commissioned, as described in 3.4.
Three different studies will be presented in this thesis:

In Chapter 4, mercury substrate as working electrode was investigated in electrolytes containing lead-halides species. The goal was to understand the process of a possible ad-layer formation and crystal growth on the Hg surface. In addition, to examine similarities to previous studies, where it is reported a formation of a PbFBr unit cell thick ad-layer accompanied by 3D crystal formation on liquid Hg in a solution containing NaF + NaBr + $PbBr_2$. Here the influence of the halide species was studied by deposition from aqueous electrolytes of composition NaX + PbX2 with X = Br, Cl, F. Namely electrolytes containing only one halide anion at the time. A systematic study of potential-dependent behavior was investigated by a combination of electrochemistry techniques such as cyclic voltammetry and potentiostatic in combination with X-ray scattering techniques like X-ray reflectivity time-resolved X-ray reflectivity and grazing incidence X-ray diffraction.

Using the same methods discussed in Chapter 4,a mercury electrode in a buffer solution containing germanium dioxide was studied. This solution is generally used to deposit crystalline germanium on liquid metals [12, 24, 33, 34]. However, it was never investigated *in-situ*. Here the study focus on seeing whenever the surface of

the working electrode was affected by the precursor prior deposition. First, characterization of Hg in only buffer solution was performed as the benchmark and only after the GeO_2 was inserted. Then, we present a complete characterization of the interface as a function of potential. The details and the complete discussion can be found in Chapter 5.

In a third experiment (Chapter 6), a Hg-In alloy was chosen as electrode. In collaboration with the University of Michigan, we studied electrodeposition of Ge using different compositions of HgIn alloys at different potentials. The deposit was characterized ex-situ and showed significant differences. To understand them *in-situ* X-ray reflectivity investigations of the pristine substrates were performed.

The experimental techniques and basic theory are presented in Chapter 2. Methods and the instrument used are presented in Chapter 3.

2 Liquid interfaces and characterization

This chapter will explain the basic properties and structure of liquid interfaces, with a particular focus on liquid metal and liquid metal electrolyte interface. It will also outline experimental methods used in this thesis, such as x-ray scattering techniques and electrochemical methods.

2.1 Structural properties of liquid interfaces

The state of a matter (solid, liquid or gas) depends on the balance between the kinetic energy of the individual particles (molecules or atoms) and the intermolecular forces. The intermolecular forces are attractive forces due to electrostatic phenomena that try to draw the particles together, causing the ordering range of different states of matter. Long-range order for solid and short for liquid and gas. The kinetic energy provides the energy required to overcome the attractive forces and increase the distance between particles. In a solid the intermolecular forces allow the particle only to vibrate and not freely move. As a result a solid has closely packed particles and a stable and define volume. On the opposite in a gas the molecules has enough kinetic energy such that the intermolecular forces are small (zero for an ideal gas). Therefore a gas has no define shape or volume. The typical distance between neighbouring molecules is much greater than the molecular size. A liquid instead the particles are loosely packed and they are able to flow, contrary to solid. Liquids have not define shape but a constant volume.
The properties of a liquid are determined mainly by forces that act between the particles; i.e. "cohesion" describes the interaction between particles of the same phase to group them with an attractive force. This interaction includes hydrogen bond in water and interaction with electron gas with the atomic cores in liquid metals. Interaction with different phases is called "adhesion". Different cohesion and adhesion forces influence the structure and interfaces.
If we consider a molecule within the bulk liquid phase, it is subject to an isotropic cohesion force with their neighbors, due to symmetry, resultant force is zero. Instead, both cohesive and adhesive forces are present on a molecule directly at the interface with a gas phase or second liquid.

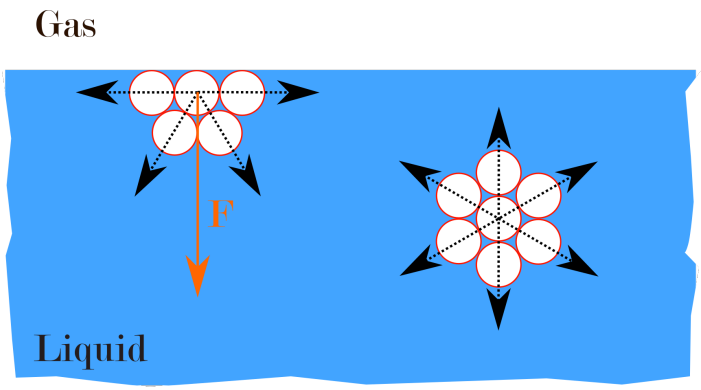

Figure 2.1: Schematic representation of the formation of the surface tension due to imbalance of the attractive forces on the molecules at the interface.

2.1.1 Surface tension

A molecule located on the surface of a liquid lacks some neighbouring molecules and thus, experiences an imbalance of cohesive force. Attractive forces of a molecule to its remaining neighbors are stronger on the surface of the liquid. As a result, a force (F) develops directed at the interior of the medium (Figure 2.1). The missing (negative) binding energy can be viewed as positive energy added to the surface itself. This cause a liquid to contract to the smallest possible surface area. Mathematically, increasing the area of an interface with energy density γ by an amount dA requires a work dW equal to the surface energy contained in the extra piece of the interface [35]:

$$dW = \gamma \cdot dA \tag{2.1}$$

The energy density γ is also called surface tension.
The positivity of the surface tension guarantees that such interfaces seek towards the minimal area consistent with the other forces at play, such as gravity. As the cohesion and adhesion material properties like γ, depend strongly on the composition of the two phases.

The shape of the interface is determined by the pressure difference Δp between the two liquids. In equilibrium condition the work necessary to increase the interface area A by dA must be equal to the work that is required to change the volume of the two liquids against the pressure difference follows the Young-Laplace equation [36]:

$$\Delta P = \gamma \left(\frac{1}{R_1} + \frac{1}{R_2} \right) \tag{2.2}$$

where R_1 and R_2 are the local radii of curvature of the interface. Using 2.2, the shape of each liquid interface can be described theoretically in equilibrium. When the local curvature of the interface is the same, namely $R_1 = R_2$, the formula can be simplified to $\Delta P = 2\gamma \frac{1}{R}$

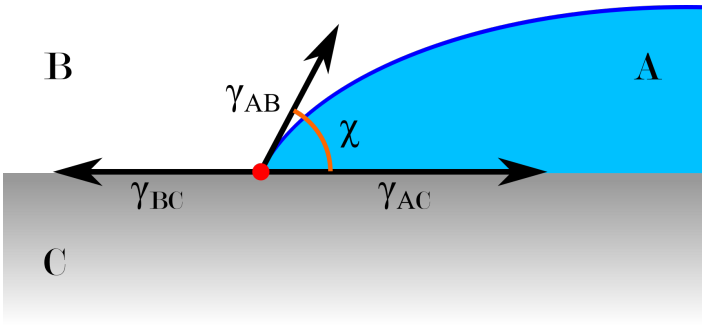

Figure 2.2: Scheme describing the contact angle. The arrows indicate the surface tensions.

Contact angle

For the typical case of a three-phase contact between phase A, phase B and a solid phase C the contact angle χ is defined as the angle between the solid and the interface (inside the phase A), see Figure 2.2. The three interfaces will create three different surface tensions. Let γ_{BC} be the surface tension between phase B and the solid C, γ_{AC} the surface tension between phase A and C and γ_{AB} the surface tension between A and B. Considering the material adhesion can maintain a tension normal to the solid phase, the tangential tension has to cancel out at the contact line; otherwise, it will start to move. Therefore an equilibrium relation can be drawn:

$$\gamma_{BC} = \gamma_{AC} + \gamma_{AB} \cos\chi \tag{2.3}$$

Given the three surface tensions, the critical angle can be calculated as:

$$\cos\chi = \frac{\gamma_{BC} - \gamma_{AC}}{\gamma_{AB}} \tag{2.4}$$

An example would be water and air against clean glass meeting in a small contact angle $\chi \approx 0°$, whereas mercury and air meet glass at an obtuse contact angle of $\chi \approx 140°$ [35]. Due to its small contact angle, water is very efficient in wetting many surfaces, whereas mercury tends to contract into pearls. It should be emphasized that the contact angle is extremely sensitive to surface properties, fluid composition, and additives.

2.1.2 Liquid metals

Metals in their solid state are part of everyday life, however liquid metals have many useful applications, in biology, engineering, and chemical. Typical uses include thermometers, thermostats, switches, barometers. In order to exploit them, the basic concepts and fundamentals have to be understood.
Liquid metals consist of atomic cores surrounded by delocalized electrons. However, since the vapor phase of the metal consists of neutral atoms, the forces acting

on electrons and atomic cores are strongly anisotropic in the transition region at the interface [37–39]. Therefore, there is a substantial reduction in the density of delocalized electrons in the metal within a transition region of a few atomic diameters. That is accompanied by a decrease in the effective interaction potential. However, for dielectric liquids, the interaction between atoms depends mainly on the distribution of electrons within the atoms and only slightly on the density of the atoms at the interface. Therefore, these differences in the atomic interactions should lead to different surface and volume structures between dielectric liquid and a liquid metal[38, 40]. The appearance of different surface structures in liquid metals and dielectric liquids was first theoretically confirmed in the early 1980s based on Monte Carlo simulations by Rice et al. [40]. While for dielectric liquids at temperatures close to the freezing point, the density along the surface normal drops monotonically over a range of about two atomic diameters [41–43], stratification over three to four atomic layers has been observed for liquid metals [44–48]. Layering on liquid was also observed in a non-metallic liquid such as tetrakis(2-ethylhexoxy)silane [49] and ionic liquids [50]. Since the layering along the normal direction of the surface influences its optical properties, methods with spatial resolution along the perpendicular direction are suitable for the characterization and investigation of the interface. X-ray reflectivity is one of the method which can probe the structure region with atomic resolution. Liquid metals have a high atomic number and surface tension, which results in low surface roughness; an advantage for X-ray studies since it reduces the scattering. However, they are usually relatively non-noble, so the characteristic reflectivity features of the atomic layering can be covered by the formation of an oxide layer. Oxide formation at the interface between a metal and a gas can be prevented by excluding oxygen from the atmosphere, e.g., inert gas. Alternatively, in an electrochemical environment, a suitable electrolyte and potential can be chosen to reduce or dissolve a possible oxide layer.
The atomic layering at the surface has already been demonstrated for numerous metals, including K [51], Cs [52], Ga [53, 54], In [55], Hg [56–60] and alloys [21, 61–68] employing X-ray reflectivity measurements.

2.1.3 Capillary waves

At liquid interfaces in addition to intrinsic roughness, an effective roughness can be observed, due to thermally induce wave motion of the liquid particles. Two different types of transverse waves occur at the interface between two fluid phases, distinguished based on the active force. For gravity waves, this force is gravity; for capillary waves, it is the surface tension. In contrast to gravity waves, the amplitude of capillary waves is generally smaller than their wavelength λ_w [69]. From the dispersion relation of the transverse waves, the wave velocity is [70]:

$$c(\lambda_w) = \sqrt{\left(\frac{g\lambda_w}{2\pi} + \frac{2\pi\gamma}{\rho_m\lambda_w}\right)} \tag{2.5}$$

where λ_w is the wavelength g is the gravitational constant, γ the surface tension ρ_m the bulk density of the liquid. It follows that at large wavelength where the effect of gravity is dominant , the waves are called gravity waves. At small length scales where surface tension dominates, the waves are called capillary waves. The threshold wavelength where the capillary waves turn into gravity waves is:

$$\lambda_{w,max} = 2\pi\sqrt{\frac{\gamma}{\rho_m \lambda_w}} \tag{2.6}$$

The dispersion relation below λ_{max} is abnormal, i.e., the speed of the capillary waves increases with decreasing wavelength. For the description of the roughness on microscopic length scales, only the capillary waves are relevant. Since capillary waves can be excited by the thermal movement of the liquid particles, they also occur without external excitation [69, 71, 72].

2.2 X ray scattering

Wilhelm Conrad Röntgen discovered X-ray radiation in 1895 [73], and it is electromagnetic radiation with photons having wavelength from 100 to 0.1 ångstrom. The application of the theoretical basis was then applied to structural analysis of matter. That has been used since Laue, Knipping and Bragg [74–76] exploit it to produce diffraction patterns, for the first time.
Nowadays the theoretical foundation is well known. So only the basics concepts of the methods used, are briefly explained in the following sections. For more detailed information and deeper discussion refer to the literature [71, 77–80].

The X-rays are scattered by electrons of the atomic shells. Therefore, the expected scattering behavior of an electromagnetic wave in matter can be determined if the electron density distribution is known. Assume to be in the far-field approximation [77], with an electromagnetic wave with wavelength λ so with a wave-vector $k = 2\pi/\lambda$. In the elastic case, with the same wavelength, we can define k' the wave-vector scattered from a charge distribution (Figure 2.3). So that:

$$q = k' - k \tag{2.7}$$

q is called scattering vector. And from the scattering triangle
$|q| = 2|k| \sin\theta = (4\pi/\lambda)\sin\theta$.

If we consider scattering from a single atom with Z electrons, with electron distribution $\rho(r)$, with r a space coordinate, we can define the *atomic form factor* [77]:

$$f^0(q) = \int \rho(r) e^{iq\cdot r} dr \tag{2.8}$$

Where in the limit $q \to 0$, $f^0(q = 0) = Z$. Instead $f^0(q \to \infty) = 0$. The scattering intensity $I \propto |\ f(q)\ |^2$, this is the intensity measured in the experiments. Hence the

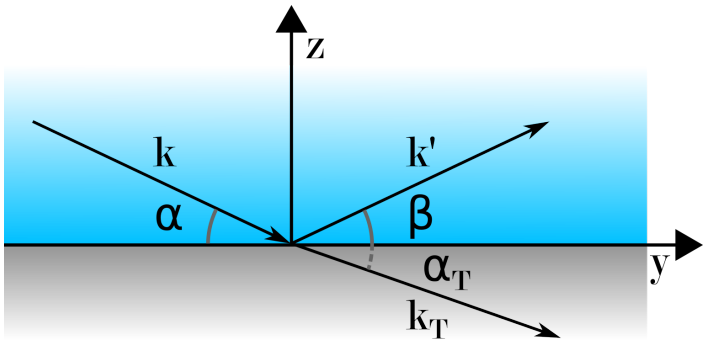

Figure 2.3: Scattering geometry of X-ray refraction in the elastic case.

scattering intensity is proportional to the square of Fourier transform of the distribution of electrons on the sample. Whereby it is easy to understand that the phase information is lost.

Let us consider now a crystal. The crystal structure can be represent by repeating unit cells described as the most basic and least volume consuming repeating structure [80]. The position of the nth unit cell is define by the vector $R_n = n_1a + n_2b + n_3c$ with n_1, n_2, $n_3 \in \mathbb{Z}$ and the position of the mth atom in a unit cell as $r_m = m_1a + m_2b + m_3c$ with m_1, m_2, $m_3 \in \mathbb{Z}$. So that the position of any atom in the crystal is given by $R_n + r_m$. Thus the scattering amplitude $F^{crystal}$ can be describe as the sum of the contribution of each single atom:

$$F^{crystal}(q) = \sum_{l}^{all\ atoms} f_l(q)e^{iq\cdot r_l} \tag{2.9}$$

where $f_l(q)$ is the atomic form factor of the atom in the position r_l . The scattering amplitude can be decomposed into two contributions, from the lattice and from the unit cell as:

$$F^{crystal}(q) = \sum_{l,m} f_l(q)e^{iq\cdot R_n + r_j} = \sum_{l} f_l(q)e^{iq\cdot r_j} \sum_{m} e^{iq\cdot R_m} \tag{2.10}$$

Where the fist sum of the right hand side of the equation is the sum of the scattering of the atoms in the unit cell called *unit cell structure factor* and the second the sum over the lattice sites. The latter sum is of the order unity unless the scattering vector fulfil the condition :

$$q \times R_m = 2\pi w \tag{2.11}$$

w is an integer.

The periodicity of the lattice makes possible the mathematical description of the Fourier transform of the lattice, the so-called reciprocal lattice. The translation vector R becomes then the reciprocal lattice vector $G_{hkl} = ha^* + kb^* + lc^*$, where h, k l, $\in \mathbb{Z}$

and

$$a^* = 2\pi \frac{b \times c}{a \cdot (b \times c)} \qquad b^* = 2\pi \frac{c \times a}{a \cdot (b \times c)} \qquad c^* = 2\pi \frac{a \times b}{a \cdot (b \times c)} \tag{2.12}$$

a^*, b^* and c^* are reciprocal basis vectors.
A solution of 2.11 can be found when:

$$q = G_{hkl} \tag{2.13}$$

This is the Laue condition [79]. The scattered signal from a crystal is measurable when the scattering vector is equal to a reciprocal lattice vector of the crystal structure. This condition defines a sphere in reciprocal space, which is called *Ewald sphere*. Every point of the reciprocal lattice that lies on this sphere contributes to the scattered signal.
If a scattering vector is observed under the condition $q = G_{hkl}$, this signal comes from a group of planes that meet the scattering condition and is denoted by (hkl). The distances between these lattice levels are given by $d_{hkl} = 2\pi / \mid G_{hkl} \mid$. The scattering condition is thus directly equivalent to the Bragg condition [77]:

$$2d_{hkl} \sin(2\theta/2) = \lambda \tag{2.14}$$

where 2θ is the angle between k' and k.

2.2.1 X-ray diffraction

To understand the observable Bragg peaks on a detector a Ewald sphere concept needs to be further discussed. As introduced before, the Ewald sphere, or sphere of reflection, is a sphere (in reciprocal-space) of radius $1/\lambda$ passing through the origin of the reciprocal lattice of the sample.
A peak observed on the detector indicates that a reciprocal-space peak is intersecting with the Ewald sphere.
The crystallites where the Bragg peaks are generated from, could have different structures. Let us consider three of them: single crystal, 2D powder crystallites oriented along one axis and powder. The three structures will arise to different shape peaks on the detector. The first one will show well defined spot, ideally a point, because the Ewald sphere cut the reciprocal space in a single point. Whenever the sample is rotated, this means exploring q_x and q_y wave-vector, the signal will change because the detector will intersect different points in the reciprocal space of the crystal (Bragg condition). An example of the geometry is reported in Figure 2.4 left. Let us suppose well oriented crystals along the vertical direction, but randomly oriented in the other two directions. The reciprocal space will look different. In particular, instead of having points describing the reciprocal space of the crystals, we have rings "piled up" along the q_z direction with radius $q_{//} = \sqrt{q_x^2 + q_y^2}$ because the crystals

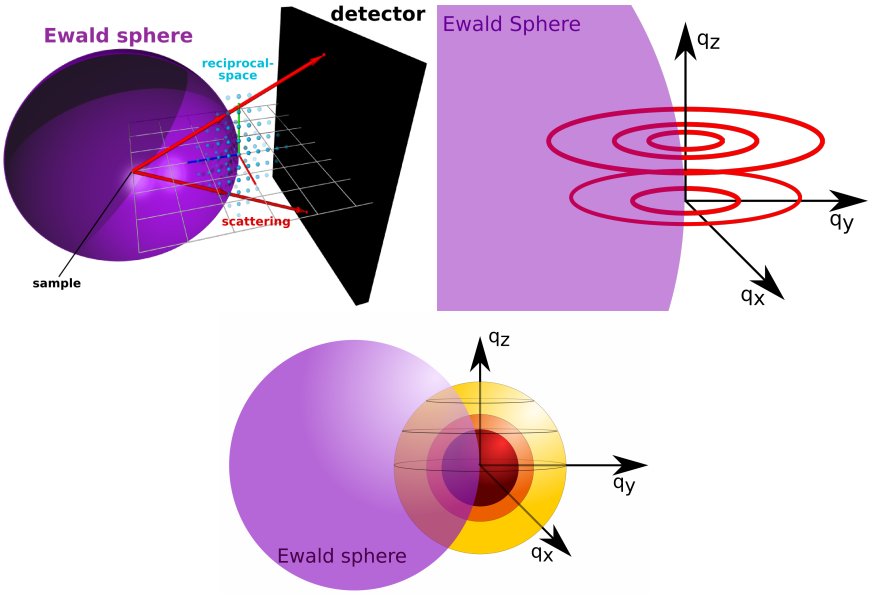

Figure 2.4: Example of different representation of reciprocal space diffraction geometry depending on the crystals structure. Left: single crystal, the reciprocal space is represented as ordered points [81], middle: 2D powder, oriented in the vertical direction, therefore in q-space we obtain rings piled up along z, right: powder, in this case we have nested spheres. Intersections of the different shapes arrangement of the Bragg reflections with the Ewald sphere manifest as different shape diffraction peaks on the two-dimensional X-ray detector

are oriented along z but randomly oriented along x and y. Due to the anisotropy of the $q_{//}$ rotating, the sample will give the same signal on a two dimensional x-ray detector, namely, ideally a point. The geometry reported in Figure 2.4 middle.
In the third scenario, the reciprocal the Bragg reflections will be represented by concentric spheres. Where the radius is given by the total $q = \sqrt{q_x^2 + q_y^2 + q_z^2}$. In this case, the crystals are oriented randomly along with all direction and can be rotated arbitrarily about an axis parallel to the incident beam, so the intensity scattered in a cone [82]. The signal on a two-dimensional detector will be rings since since it is the shape obtained by intercepting two spheres. These rings are called "Debye-Scherrer rings".
The energy of the X-ray beam determines the radius of the Ewald sphere. Therefore, for example, a higher energy will have a bigger Ewald sphere, therefore a more "flat" surface intersecting the reciprocal lattice of the crystals. More information is reported in the literature, as example [83].

2.2.2 Grazing Incidence X-Ray Diffraction (GID)

When examining a crystal interface in Bragg geometry, the incident and scattered wave vectors lie in a plane perpendicular to the interface. When the incident and exit angles are varied, an intensity maximum can then be observed if the Bragg condition 2.14 is satisfied. However, this method does not provide information about

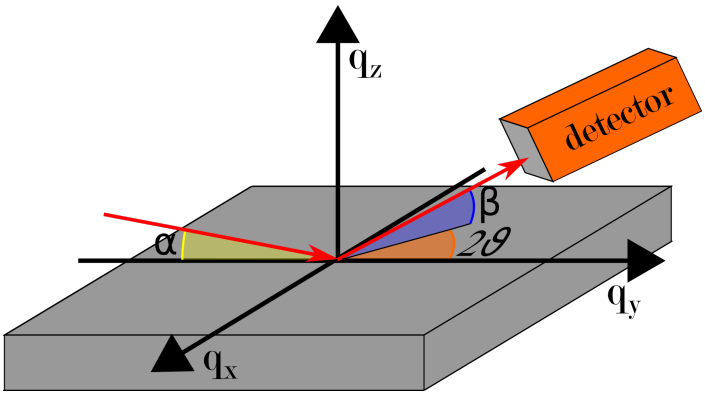

Figure 2.5: Grazing incidence diffraction geometry. The incident angle is usually on the order of the critical angle of the interface under investigation. The detector collects the intensity at different angles either in plane θ or out of plane β.

the planes perpendicular to the interface. However, by choosing a very shallow angle of incidence and rotating the sample about the vertical axis, the Bragg geometry can also be applied to these planes. Because of the slight incidence angle, this method is called grazing incidence X-ray diffraction (GIXD or simply GID).
The geometry of the experiment is shown in Figure 2.5.

When the incidence angle is smaller than the critical angle ($\alpha < \alpha_c$ (see 2.2.4)) a total reflection occurs. However, this is only correct under the assumption that the entire intensity is directly at the interface $z = 0$ is reflected. Part of the incident wave propagates perpendicular to the surface by a few Å to nm, depending on the critical angle, the penetration depth Γ_c can be approximated $\Lambda_c \approx \frac{1}{2q_c}$ [84]. This portion of the wave is called evanescent wave. The amplitude of the evanescent wave decays exponentially into the material [85–87]. The penetration depth for angles is $\alpha > \alpha_c$ in the micrometer range [77]. The dependence of the penetration depth on the angle of incidence can therefore be used to adjust the surface sensitivity of a scattering experiment [88, 89]. In this way, it is possible to obtain information about the structure of a layer adsorbed on the liquid surface and to keep the contribution of the undesired scattering by the liquid volume below.
In the case of scattering under grazing incidence, the detector is allowed to move along θ and β (Figure 2.5). In this way, components of the scattering vector q in the x–y plane parallel to the sample surface are obtained. Complementary to the reflectivity measurement, information about the lateral structure of the surface can be captured, and films grown on substrates can be investigated for lattice constants, crystallite size, and deformations [90].

2.2.3 Liquid structure factor

In contrast to the crystalline solids, liquids do not have a long–range order. On short length scales, however, there is a local order that is caused by the interaction of the liquid particles with one another. Even in a simple model in which the particles are

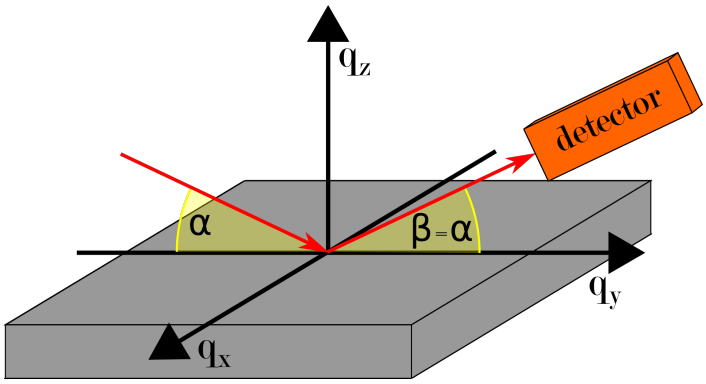

Figure 2.6: X-ray reflectivity geometry. The incident angle α is equal to the exit angle β where the intensity of the specular beam is collected by the detector.

hard spheres with a radius r and the simplistic repulsive interaction potential is zero when the distance is greater than r and infinity when the particles are closer then its radius (hard sphere). Each particle has a shell of the particle around itself, and therefore the distance between them is $2r$ [91]. Therefore, the radial distribution function $G(r)$ of the particles has maxima at approximate multiples of $2r$, localizing them with r decreases. Analogous to the crystalline structure factor, a liquid structure factor is defined as a Fourier transform of $G(r)$. When a liquid scatters an X-ray beam, the liquid structure factor produces broad, ring-shaped diffraction maxima. The structure factor of water can also be simplified to this model [92, 93]. Let's take the radius of the water molecule $r \sim 1.4$Å, the expected maximum of the structure factor in q-space is $q_{Sf(H_2O)} = \frac{2\pi}{2r} \sim 2.2\text{Å}^{-1}$. So an increase in scattering is expected in this region. In all X-ray diffraction and X-ray reflectivity measurements on liquids, the maximum caused by the liquid structure factor can be observed as the background intensity, which must be subtracted from the raw data.

2.2.4 X-ray reflectivity (XRR)

From X-Ray Reflectivity, information on the electron density profile of the surface normal can be drawn, therefore details of a layer thickness when present, density and roughness of the interface. The experiment is performed by recording the specular reflected beam intensity as a function on the angle of incidence α equal to the exit angle β. The geometry is shown in Figure 2.6.
The reflectivity is define as the specular intensity normalized by the incidence beam intensity (primary beam), $R(\alpha) = I(\alpha)/I_0$. From the relation introduced in 2.7 one can define:

$$q_z = \frac{4\pi}{\lambda} = \sin\left(\frac{\alpha+\beta}{2}\right) = \frac{4\pi}{\lambda}\sin(\alpha)$$

and therefore define a R independent of the wavelength, namely $R(q_z)$. Naturally, the reflectivity strongly depends on the refraction index of the two media at the interface.

Index of Refraction

When an electromagnetic plane wave hits an interface, a portion of the intensity is refracted into the medium, and a part is reflected (Figure 2.3).

The changes can be accounted by considering the refractive index $n(r)$, that for x-rays is [69]:

$$n(r) = 1 - \delta(r) + i\beta(r) \tag{2.15}$$

Where δ being the dispersion, β the absorption and r describe a point in space. It should be emphasized that for X-rays, $\delta(r)$ is always positive and therefore $n < 1$. Now if we consider j atoms per unit volume of a material [69]:

$$\delta(r) = \frac{\lambda^2}{2\pi} r_e \rho(r) \sum_{j=1}^{N} \frac{f_j^0 + f_j'}{Z} \tag{2.16}$$

and

$$\beta(r) = \frac{\lambda^2}{2\pi} r_e \rho(r) \sum_{j=1}^{N} \frac{f_j''}{Z} = \frac{\lambda}{4\pi} \mu(r) \tag{2.17}$$

with $r_e = e^2/(4\pi\epsilon_0 mc^2) = 2.814 \times 10^{-5}$ Å, the total number of electrons $Z = \Sigma_j Z_j$, the electron density ρ, the linear absorption coefficient $\mu(r)$. f^0 is the form factor and f' and f'' are the dispersion correction of it. Those quantities are q-dependent and it has to be considered whenever measurements over a large q region are analyzed. However, in the region where glancing incident and exit angles is small (small q), $f_j^0 \approx Z_j$. In the case of a homogeneous medium and far away from absorption edges, one may simplify the expression for the refractive index to:

$$n(r) = 1 - \frac{\lambda^2}{2\pi} r_e \rho(r) + i \frac{\lambda^2}{4\pi} \mu(r) \tag{2.18}$$

From the equation 2.18, it can be seen that n is proportional to the scattering length density (SLD) of the material , $SLD = r_e \rho$. That is valid for the region away from the absorption edge. There the index of refraction changes abruptly.

Critical angle

Let us consider a single vacuum/medium interface, a electromagnetic plane wave propagating in vacuum falling onto a perfectly flat surface of a material with index n, with incident angle α_i and exit angle α_t. The refraction law gives:

$$cos\,\alpha_i = n_0 cos\,\alpha_t \tag{2.19}$$

When $\alpha_t = 0$, $\alpha_i = \alpha_c$ is called critical angle. If $\alpha_i < \alpha_c$ then the intensity is fully reflected: total external reflection. Therefore the formula 2.19 becomes:

$$cos\,\alpha_c = n_0 \tag{2.20}$$

In the case of small angle and neglecting the absorption, by using the Taylor expansion for cosine and by the formula 2.16 and 2.18, we obtain:

$$1 - \frac{\alpha_c^2}{2} \approx n_0 \Rightarrow \alpha_c \approx \sqrt{2\delta_0} \tag{2.21}$$

For the interface between two different media A and B, the critical angle results from:

$$\alpha_c \approx \sqrt{2(\delta_A - \delta_B)} \tag{2.22}$$

When $\delta_A > \delta_B$.

2.2.5 Reflectivity of ideal Interfaces

The X-ray reflectivity of an ideal perfectly flat interface between two semi-infinite media is described by the Fresnel equation.

In reciprocal coordinates, the Fresnel reflectivity is given by [94]:

$$R_F(q_z) = \left| \frac{q_z - \sqrt{q_z^2 - q_c^2 - \frac{32i\pi^2\beta}{\lambda^2}}}{q_z + \sqrt{q_z^2 - q_c^2 - \frac{32i\pi^2\beta}{\lambda^2}}} \right| \tag{2.23}$$

where $q_c = \frac{4\pi}{\lambda} \sin \alpha_c$

The absorption factor is most important at a shallow angle as it can be seen in Figure 2.7).
Unfortunately Fresnel reflectivity fails to describe an actual interface.

2.2.6 Reflectivity of real Interfaces

A real interface is not abruptly flat. Instead, it has an intrinsic roughness and the distribution of electrons around the atoms, which are described by the atomic form factor [95]. Both cause a weakening of the specular reflectivity. The roughness contribution σ can easily taken into account by considering a "Debye-Waller-like factor" [94] $\exp\left[-\frac{q_z^2\sigma}{2}\right]$. So that the reflectivity of the simple slab model can be described as [96]:

$$R(q_z) = R_F(q_z) \exp\left[-\frac{q_z^2\sigma}{2}\right] \tag{2.24}$$

Some example of how roughness absorption affect the reflectivity is reported in Figure 2.7. Where the absorption coefficient β was changed from 0 to 1e-7 and the roughness σ was changed from 0 to 1 Å. Taking into account this small considerations, the model 2.24 works for simple interfaces, for example water-vapour as shown in Figure 2.8), where the absorption at 18 keV is on the order of 5e-10 and the roughness for the given resolution is about $\sigma = 2.57$Å.

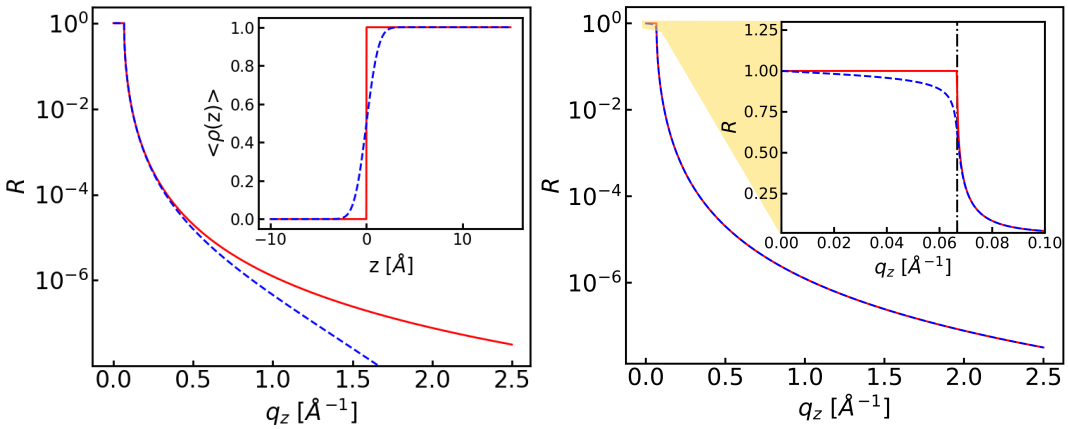

Figure 2.7: Left: Effect of the roughness on the reflectivity. Solid red curve show the reflectivity profile of a perfectly flat surface, dashed blue with a roughness of 1 Å. Inset: electron density profile of the interface with the same color code for comparison. Right: the effect of absorption. Red with no absorption ($\beta = 0$, dashed blue line with $\beta = 1e-7$). Inset zoom view of the low angle region to display clearly the effect, dashed-dotted line indicate the critical angle position.

In the previous section 2.2.5 the reflectivity of an ideal surface has been discussed. In this part we want to find a model able to describe any interfaces, an in particular liquid metal-electrolyte interfaces.

A reflectivity from a not ideal surface, with multiple layer for example, can be described using a recursive Parrat method [97]. This method takes into account refractions and multiple scattering processes. The main idea of this method is to slice the substrate in m layers, each with a refractive index n_m. This method gives exact results down to the region of the critical angle. The problem is that it can be very computational heavy depending on the chosen widths of the layers. Moreover using this approach define a model and justify the different parameters are often complex. In the region of $q_z \gg q_c$ where the scattering cross-section is small, refraction and multiple reflection can be neglected, and the reflection coefficient at each interface is proportional to the difference of electron density, the reflectivity can be described in the kinematic approximation. Taking into account the position dependency of the electron distribution at the interface, which leads to a phase shift of the reflected radiation, and neglecting the diffuse scattering. The approximation results in the following description of the reflectivity, called Master formula [77]:

$$\frac{R(q_z)}{R_F(q_z)} = |\Phi(q_z)|^2 = \left| \frac{1}{\Delta\rho_\infty} \int \frac{d\,\langle\rho(z)\rangle}{dz} e^{iq_z z}\, dz \right|^2 \tag{2.25}$$

Where $\rho(z)$ describes the averaged density profile normal to the interface, $\Delta\rho_\infty$ is the difference in electron densities of the two phases at infinity, $\Phi(q_z)$ is the structure factor. Note that $R(q_z)$ depends on the square of the absolute value. Meaning that all phase information is lost in an X-ray reflectivity measurement. A unique solution of

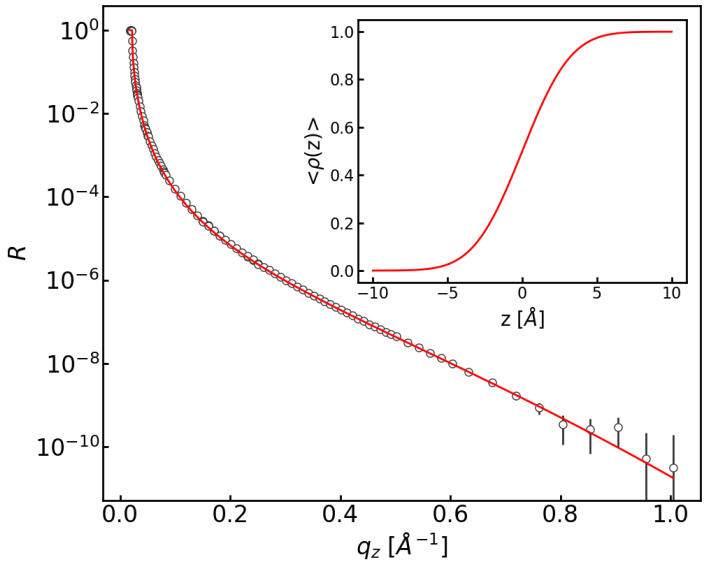

Figure 2.8: X-ray reflectivity of water-vapour interface. Data recorded at 18 keV with LISA diffractometer at DESY (beamline P08). Red line show a fit with roughness 2.57 Å. Inlet the electron density profile generate from the fit.

the formula 2.25, does not exist [98]. Here lies one of the difficulties in interpreting X-ray scattering data. Based on physical assumptions, a model for $\langle\rho(z)\rangle$ has to be found. From there by calculating $|\Phi(q_z)|^2$ the XRR data can be fitted. In the construction of the electron density profiles, it has been neglected that only the position of the atomic cores is described by the models given. However, the scattering of the X-rays takes place at their electron shell, so the distribution of the electrons around the atomic cores must be taken into account. That can be considered by convolution of the model with the Fourier transform of the atomic form factor introduced before. That describes the distribution of electrons within the atom. The actual electron density distribution of a phase is then given by:

$$\rho(z,\lambda) = F(z,\lambda) \otimes \rho'(z) \tag{2.26}$$

Now by using the Master formula 2.25 and keeping in mind the derivative of a convolution is the multiplication of the derivative:

$$\begin{aligned}
\Phi(q_z) &= \int_{-\infty}^{\infty} \frac{\delta\rho'}{\delta z}\, e^{iq_z z}\, dz \\
&= \int_{-\infty}^{\infty} \left(\frac{\delta}{\delta z}(F(z,\lambda) \otimes \rho(z)) \right) e^{iq_z z}\, dz \\
&= \int_{-\infty}^{\infty} F(z,\lambda) \otimes \frac{\delta\rho}{\delta z}\, e^{iq_z z}\, dz \\
&= g(q_z,\lambda) \int_{-\infty}^{\infty} \frac{\delta\rho}{\delta z} e^{iq_z z}\, dz.
\end{aligned} \tag{2.27}$$

The function $g(q_z,\lambda)$ is the atomic form factor corrected by the dispersion term $f' + if''$ [77], such that $g(q_z,\lambda) = f^0(q_z) + f'(\lambda) + if''(\lambda)$. Value for analytical

approximations of $f^0(q_z)$, $f'(\lambda)$ and $f''(\lambda)$ can be found in database such as [99] or online databases [100, 101]. So for each element we want to describe the reflection $R(q_z)$ with the its electron density profile $\rho(z)$, we need to consider different $g(q_z, \lambda)$ functions.

X-ray reflectivity on liquids

Capillary waves has been already introduced in section 2.1.3. Those waves are always present on a liquid surface/interface. Capillary waves cause fluctuations and therefore a change of height of the surface or interface and its potential energy.
This leads to a further contribution in the roughness of the system, it can be demonstrated that the contribution of the capillary wave roughness is described by [78]:

$$\sigma_{CW}^2 = \left(\frac{K_b T}{2\pi\gamma}\right) \ln\left(\frac{q_{max}}{q_{min}}\right) \tag{2.28}$$

Where K_b is the Boltzmann constant, T the temperature of the system, γ the surface tension, q_{max} the highest wave vector achievable, and it has given by $q_{max} = 2\pi\,/a$ (with an atomic or molecular diameter) and q_{min} is dictated by the instrumental resolution. Thus, the overall roughness is then [78]:

$$\sigma_i^2 = \sigma_0^2 + \sigma_{CW}^2 \tag{2.29}$$

In this thesis, only σ_i will be considered. Where it describes the overall contribution of intrinsic and capillary wave roughness.

Distorted Crystal Model

From equation 2.25 and 2.27 is clear we need to find a model to describe $\rho(z)$ in order to explain the experimental behaviour of $R(q_z)$.
For metals, the electron density profile essentially coincides with the density profile of the ion cores, since most of the electrons are localized in these.
In order to describe the mercury-vapor interface and liquid metal in general, the distorted crystal model (DCM) was introduced [56]. The DCM describes the stratification of the atomic layer near the surface. As the sum of layers broadens as goes to the bulk, the distance from the interface increases. In general those layer are described by a sum of Gaussians, with the width og the nth layer being:

$$\sigma_n = \sqrt{\sigma_i^2 + n\,\sigma_b^2} \tag{2.30}$$

From equation 2.30 we see two terms: σ_i, common to all the layers and a growing part $\sqrt{n}\,\sigma_b$ to model the decay and broadening of the Gaussians. The amplitude of the the layer, as a function of n is $d\,\frac{\rho_{lm}}{\sigma_n\sqrt{2\pi}}$, where the appendix lm refers to *"liquid metal"*. The distance between each layer is d, typical of the liquid metal. $n = 0$

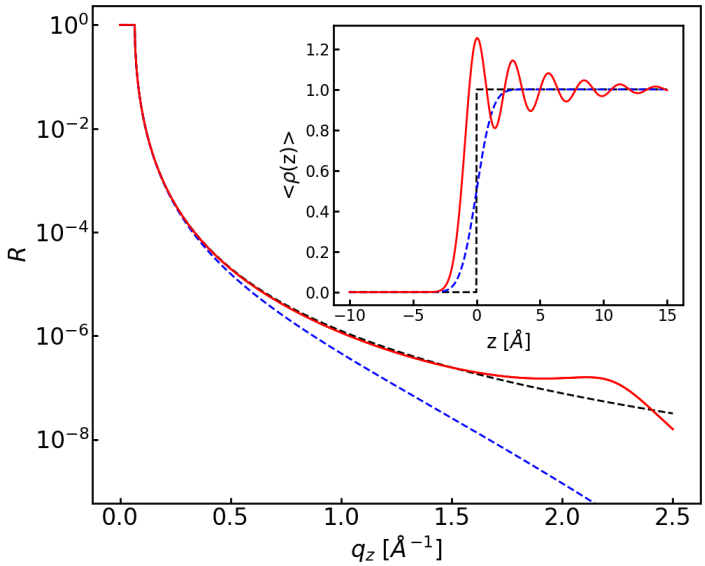

Figure 2.9: Simulation of different reflectivity profiles. Red: unmodified distorted crystal model, it shows a "quasi Bragg-peak" around $q_z \sim 2.15$ Å due to the atomic layer stratification of liquid metals. dashed lines: black slab model with no roughness, blue with a roughness of 1 Å. Inset: electron density profiles describing the reflectivity curves

describe the interface, the top most layer of the liquid metal.
The electron density profile of a liquid metal could mathematically be described as:

$$\rho_{DCM}(z) = F_{lm} \otimes \sum_{n=0}^{\infty} \frac{\rho_{lm}}{\sigma_n \sqrt{2\pi}} \exp\left[-\frac{(z - n\,d - z_0)^2}{2\sigma_n^2}\right] \tag{2.31}$$

Where F_{lm} is the Fourier transform of the atomic form factor of the liquid metal, and for simplicity, z_0 is set to 0. It means that the interface of the liquid metal, or first layer, is set to 0 along the z axes.
The density preservation is achieved by multiplying the Gaussian functions with the layer spacing d. Such that at infinity, the density is equal to the bulk density of the liquid metal. Moreover, this model can reproduce the liquid metals' x-ray reflexivity peculiarity, namely the so-called "quasi-Bragg peak". Maximum positioned at $q_{z,peak} = \frac{2\pi}{\sqrt{3}r}$ with r the atomic radius of the liquid metal, constructive interference from the atomic laying.
A plot of a comparison between the DCM model and a error function is shown in Figure 2.9. Equation 2.31 is a simplification of the model used in this thesis.
Liquid metal like mercury does not follow the unmodified DCM, in particular in the q_z region smaller than 1.5 Å^{-1} [56, 58–60, 102], where the intensity is lower as would the model prediction.
So it has been modelled by including a Gaussian layer with a width σ_{ad} at position z_{ad} over the first layer of the DCM with a significantly lower electron density ρ_{ad} than the other layers. The additional layer's origin is generally attributed to an impoverished or incomplete mercury layer [58]. In this thesis the nature of the additional

ad-layer was attributed to Hg, therefore convoluted with its Fourier transform of the atomic form factor (F_{Hg}).
In this work liquid metal immersed in an electrolyte was studied. To account for the second phase, an error function with density ρ_{H_2O}, position z_{H_2O} and roughness σ_{H_2O}, convoluted with the Fourier transform of the form factor of water (F_{H_2O}) has been employed. Due to the low concentration of electrolytes used, the assumption of considering only water is justified.
Thus a modification of the DCM called "*ad-layer model*", results to be :

$$\langle \rho(z) \rangle = \rho_{DCM}(z) + \rho_{ad,Hg}(z) + \rho_{electrolyte}(z) \tag{2.32}$$

In the specific:

$$\begin{aligned} \langle \rho(z) \rangle = F_{Hg} \otimes \Bigg\{ \sum_{n=0}^{\infty} d \, \frac{\rho_{Hg}}{\sigma_n \sqrt{2\,\pi}} \exp\left[-\frac{(z-nd)^2}{2\sigma_n^2} \right] \\ + \frac{\rho_{ad}}{\sigma_{ad}\sqrt{2\pi}} \exp\left[-\frac{(z-z_{ad})^2}{2\sigma_{ad}^2} \right] \Bigg\} \\ + F_{H_2O} \otimes \left\{ \frac{\rho_{H_2O}}{2} \left(1 - \mathrm{erf}\left[\frac{z - z_{H_2O}}{\sigma_{H_2O}\sqrt{2}} \right] \right) \right\} \end{aligned} \tag{2.33}$$

By inserting eq 2.33 in eq 2.25, one obtain the surface structure factor:

$$\begin{aligned} \phi(q_z) = \frac{1}{\rho_{Hg} - \rho_{H_2O}} \Bigg\{ \frac{f^0_{Hg}(q_z) + f'_{Hg}}{Z_{Hg} + f'_{Hg}} \Bigg[i\, q_z\, d\, \rho_{Hg} \frac{\exp\left(-\frac{q_z^2 \sigma_i^2}{2} \right)}{\left(1 - \exp\left(i\, q_z\, d - \frac{q_z^2 \sigma_b^2}{2} \right) \right)} \\ + i\, q_z\, \rho_{ad} \exp\left(-i\, q_z\, z_{ad} - \frac{q_z^2\, \sigma_{ad}^2}{2} \right) \Bigg] \\ + \frac{f^0_{H_2O}(q_z) + f'_{H_2O}}{Z_{Hg} + f'_{H_2O}} \left[-\rho_{H_2O} \exp\left(i\, q_z\, z_{H_2O} - \frac{q_z^2\, \sigma_{H_2O}}{2} \right) \right] \Bigg\} \end{aligned} \tag{2.34}$$

Where f^0 is the atomic form factor, f' the anomalous dispersion factor [103] and Z_{Hg} is the atomic number of Hg. It is possible to obtain similar results by modifying the very first layer of the stacked described in the DCM. In particular, the amplitude (ρ_f) and move the DCM into the bulk liquid by a distance (d_f). This idea is also based on some theoretical works [47, 104]. This model is described in [78] and it is similar to the model developed by Runge et al. [60], and it is named "*one-bump model*" or more commonly "*first layer model*". The general electron density is:

$$\langle \rho(z) \rangle = \rho_{DCM_m}(z - d_f) + \rho_{f,Hg}(z) + \rho_{electrolyte}(z) \tag{2.35}$$

The electron density profile in details is described as:

$$\begin{aligned}\langle\rho(z)\rangle = F_{Hg}\otimes\Bigg\{ \sum_{m=0}^{\infty} d\,\frac{\rho_{Hg}}{\sigma_m\sqrt{2\,\pi}}\exp\left[-\frac{(z-d_f+nd)^2}{2\sigma_m^2}\right]\Bigg\} \\ +\frac{d_f\,\rho_f}{\sigma_i\sqrt{2\pi}}\exp\left[-\frac{z^2}{2\sigma_i^2}\right] \\ +F_{H_2O}\otimes\left\{\frac{\rho_{H_2O}}{2}\left(1-\mathrm{erf}\left[\frac{z-z_{H_2O}}{\sigma_{H_2O}\sqrt{2}}\right]\right)\right\}\end{aligned} \tag{2.36}$$

Here the interface ($z = 0$) is centred at the first modified layer. This first layer has amplitude $d_f \cdot \rho_f$ and it is shifted from the other stack by d_f and the width is fixed to be σ_i. In this model the σ of the mth layer σ_m differs from σ_n (eq 2.30). Here $\sigma_m = \sqrt{\sigma_i^2 + (m+1)\,\sigma_b^2}$. But as the other models the σ at the interface ($z = 0$) is described by σ_i, in the second layer ($m = 0$) $\sigma = \sqrt{\sigma_i^2 + \sigma_b^2}$ and son on.The surface structure factor for the "*first layer model*" is:

$$\begin{aligned}\phi(q_z) = \frac{1}{\rho_{Hg}-\rho_{H_2O}}\Bigg\{\frac{f^0_{Hg}(q_z)+f'_{Hg}}{Z_{Hg}+f'_{Hg}}\Bigg[i\,q_z\,d\,\rho_{Hg}\frac{\exp\left(-\frac{q_z^2\,(\sigma_i^2+\sigma_b^2)}{2}\right)}{\left(1-\exp\left(i\,q_z\,d-\frac{q_z^2\,\sigma_b^2}{2}\right)\right)}\exp\left(iq_z\,d_f\right) \\ +i\,q_z\,\rho_f\,d_f\exp\left(-\frac{q_z^2\,\sigma_i^2}{2}\right)\Bigg] \\ +\frac{f^0_{H_2O}(q_z)+f'_{H_2O}}{Z_{Hg}+f'_{H_2O}}\left[-\rho_{H_2O}\exp\left(i\,q_z\,z_{H_2O}-\frac{q_z^2\,\sigma_{H_2O}}{2}\right)\right]\Bigg\}\end{aligned} \tag{2.37}$$

Using this model to fit experimental data gives almost identical results of the ad-layer model.

An example is reported in Figure 2.10. Where the same result can be obtained by changing the ad-layer parameters (ρ_{ad} and z_{ad}) and the first layer (ρ_f and d_f). Namely, a decrease of the very first layer is equivalent to a small accumulation of density at the interface. The other parameters common to both models, differ in less than 2%. In this thesis the ad-layer model was used to describe the interface of mercury immersed in different solutions, where the main focus of study was the formation of ad-layer/crystal on the liquid metal surface. Instead to model Hg-alloy the first-layer model was used, since the primary effect observed was on the first layer of the liquid metal.

The surface structure in of the ad-layer model (eq 2.34) and first-layer model (eq 2.37) were then used to fit the experimental XRR data. Considering that, there is an analytical solution of the master formula, it is convenient to use it, instead of calculating the numerical solution of the Fourier transform for each fit.

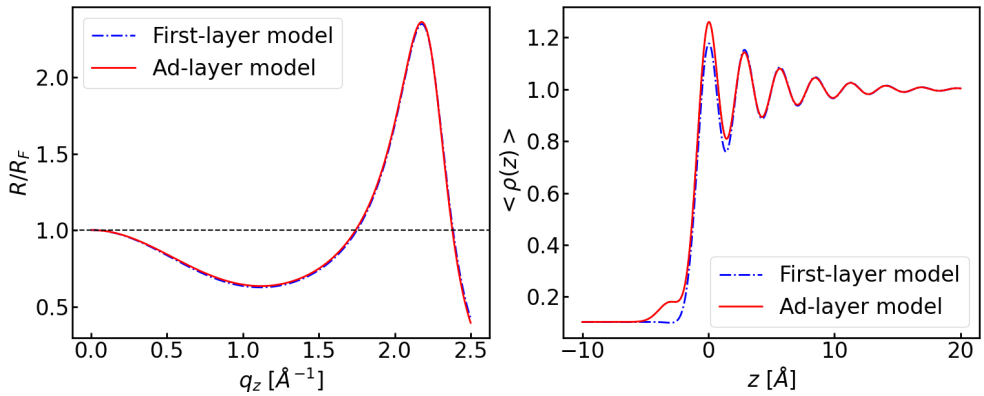

Figure 2.10: Comparison of two different variations of the distorted crystal model. Red the so-called "*ad-layer model*", Dashed blue: "*first-layer model*". On the left a simulated reflectivity profile normalized by Fresnel reflectivity with no appreciable difference in the models. Right the electron density profiles plot related to the reflectivity. The slightly different description of the interface gives the same result.

Reflection from a thin layer

In the previous sections, it has been introduced the reflection of an x-ray beam on an interface. Nevertheless, the behavior is different whenever there is a thin layer between the two phases.

As we know, the beam hitting the layer is partially transmitted and partially reflected. The transmitted part penetrates the layer and gets reflected from the phase below Figure 2.11. The coherent superposition of the two reflected waves leads to constructive and destructive interference, meaning oscillations in the reflectivity profile, due to the q_z dependence of the phase difference of both waves [105]. The oscillations are also called "Kiessig fringes". The thickness of the layer can be estimated by the period of the oscillations [94]:

$$\Delta d = \frac{2\pi}{\Delta q_z} \tag{2.38}$$

Therefore the period of the fringes is directly related to the thickness of the layer. Instead, the electron density contrast between layers determines their amplitude.

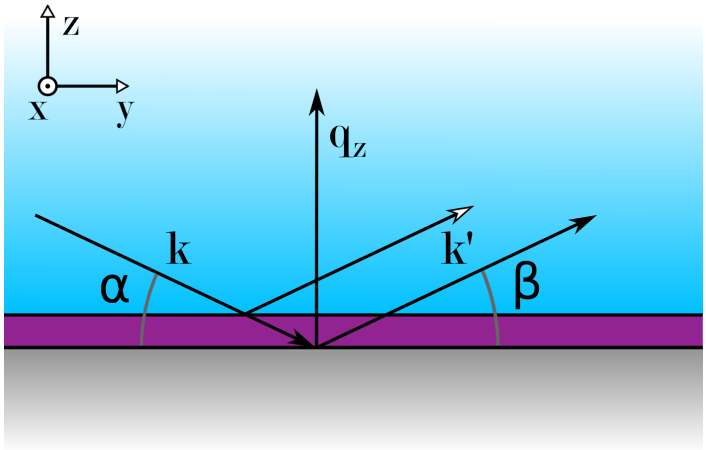

Figure 2.11: Representation of the scattering vectors on a surface when a thin layer is present.

2.3 Electrochemical principles and methods

This section will treat some of the basic principles of electrochemistry and the information needed for this thesis. For more extensive and in-depth information, refer to [106–108]

2.3.1 Electrochemical system

Electrochemistry is defined as the branch of chemistry that examines the phenomena resulting from combined chemical and electrical effects.
In an electrochemical system, the focus is to investigate the processes and factors affecting the reactions at the interface between chemical phases, for example, an electronic conductor (electrode) and an ionic conductor (electrolyte). The overall chemical reaction taking place in an electrochemical cell is made up of two independent half-reactions, one on the cathode and one on the anode; a general example is:
Oxidation half-reaction of an ion Z^-:

$$Z^- \rightarrow Z + e^- \tag{2.39}$$

Reduction half-reaction of an ion Y^+:

$$Y^+ + e^- \rightarrow Y \tag{2.40}$$

Usually, the interest is in only one of these reactions. The electrode where it occurs is called the working electrode (WE). The current flows between the working electrode and a second electrode, the counter electrode (CE). Charge transport in the electrodes occurs via the motion of electrons (or holes), instead charge transport in the electrolyte occurs via the movement of ions (positive and negative). It is possible

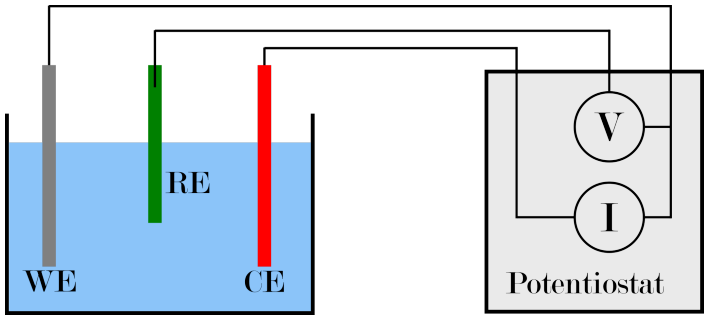

Figure 2.12: Scheme of an electrochemical cell in three electrode configuration.

to investigate the reactions as a function of potential by applying an external voltage.
The processes are usually strongly dependent on the potential, but the reactions can themselves influence the potential across the interface of the working electrode. Therefore a reference is needed. This role is covered by a third electrode called the reference electrode (RE). This electrode has a fixed chemical composition where the reactions occur at a constant potential. It has a role of reference in the potential of the reaction. The potential is applied between RE and WE through a potentiostat, able to control the voltage between the two electrodes. All these elements together form an electrochemical cell: three-electrode configuration like shown in Figure 2.12. Two electrode configuration is possible when the CE also acts as RE.

In this thesis, only the three-electrode setup was utilized. In general, in an electrochemistry cell, two types of electrochemical reactions can occur: *ion transfer reaction* and *electron transfer reaction*. In the fist one, the charge of an ion of the electrolyte is reduced at the interface of the electrode. As a result, the ion is adsorbed at the electrode or becomes part of an alloy with it, e.g., mercury amalgamation of metals (for more details see 2.3.6). The reverse process, in which the charge of a particle previously bound to the electrode is increased so that it is released into the electrolytes, it is also an ion transfer reaction. An example of an ion transfer process is the reduction of a species A during adsorption at the metal electrode where z electrons are involved:

$$A^{n+}(solution) + n\,e^- \rightleftharpoons A(WE) \tag{2.41}$$

Eq. 2.41 can lead also to a deposition. This technique is also called "electrodeposition". More details are explained in section 2.3.8.
In the *electron transfer reactions*, an ion exchanges one or more electrons with the electrode without being adsorbed:

$$A^{n+}(solution) + n\,e^- \rightleftharpoons A(solution) \tag{2.42}$$

Since electrons can bridge a certain distance through tunnel effects, the ion does not have to contact the electrode directly.
In general two families of the process can be described. One, in which charges are

transferred across the interface (electrode-electrolyte). The electron transfer causes reduction or oxidation to occur. This process is called "*faradaic processes*", where the amount of chemical reaction caused by the flow of current is proportional to the amount of electricity passed, governed by Faraday's law.
In other processes where the charge does not cross the interface, external currents can flow (at least transiently) when the potential, electrode area, or solution composition changes. These processes are called "*nonfaradaic processes*". Examples could be absorption and desorption. More complex reactions are also possible as a combination of them. Under equilibrium conditions, the resulting electrical current through the electrode is determined by the speed of the slowest sub-process.
Let us consider a faradaic process either eq. 2.41 or 2.42, given the concentration of A, $[A]$ and of A^{n+}, $[A^{n+}]$, with n electrons involved. The equilibrium potential, respect of the standard hydrogen electrode, can be calculated through the Nernst equation [106]:

$$E^{eq}_{A^{n+}/A} = E_0 - \frac{RT}{nF} \ln\left(\frac{[A]}{[A^{n+}]}\right) \tag{2.43}$$

E_0 is the equilibrium potential of the reaction under standard reaction conditions, usually tabulated as standard potential of a given reaction. T is the temperature, R the gas constant and F the Faraday constant. The deviation of the electrode potential from the equilibrium potential $E - E^{eq}_{A^{n+}/A}$ is called overpotential η. The existence of overpotential implies the cell requires more energy than thermodynamically expected to drive a reaction. Some reasons for the overpotential could come from the system's electrical resistance or the resistance of ion's ability to transfer to the surface due to diffusion or electrostatic forces at the interfaces. But commonly the most important reason rely in the charge transfer kinetics.

2.3.2 Electrochemical's interface structure

When an electrode is immersed in an electrolyte, the so-called "electrical double layer" is formed at the interface. The surface of the electrode is charged; consequently, the first layer of the electrolyte compensates the free charge with the opposite one. A series of layers could explain the structure formed. The first one is with solvent molecules and other species, ions or molecules, specifically adsorbed. This layer is called "Helmoltz" or "Stern layer". The place where the first layer is centered is called the "inner Helmoltz plane" (IHP). Solvated ions of the electrolyte are outside the IHP. The locus of these nearest solvated ions centers is called the outer Helmholtz plane (OHP). Beyond this plane, we have the region called "diffuse layer". The schematic description is reported in Figure 2.13.

The overall charge neutrality of the system can be described by $\sigma^S = \sigma^i + \sigma^d = -\sigma^M$ where σ^i and σ^d is the charge density ($\mu C/cm^2$) of the inner layer and of the outer layer respectively, σ_M the charge density of the electrode (Figure 2.13). This structure can be seen as a voltage-depended capacitor, called "double layer capacitor". As a

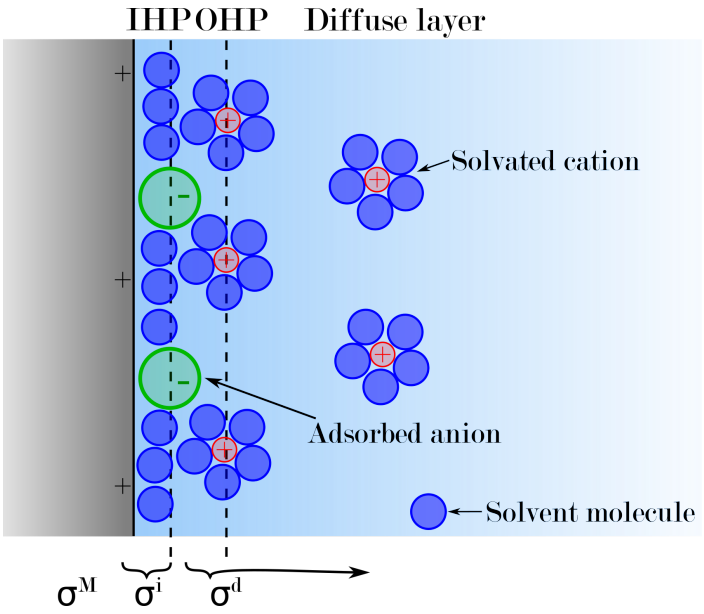

Figure 2.13: Representation of the electrical double layer

differential capacitance, it is defined as the derivative of the surface charge density σ^S with respect to the potential E: $C = \frac{d\sigma^S}{dE}$ [106].
The potential of zero charge (PZC) is the potential at which the capacitance of the double layer is zero (in particular $\sigma^S = 0$).

2.3.3 Electrocapillarity

Away from the PZC, anions or cations are attracted on the surface due to their polarization. That creates forces acting on the electrode surface, which for liquid electrodes, leads to a deformation of the interface, and thus a change of the surface energy γ. This effect can be described by the electrocapillary equation, considering a surface charge density σ, the surface excess of absorbed molecules at the interface Γ and the chemical potential of individual species at the interface μ [106]:

$$d\gamma(E,\mu) = \sigma dE - \sum_i \Gamma_i \mu_i^S \tag{2.44}$$

Eq. 2.44 can be derived from the Gibbs adsorption isotherm by taking into account the Gibbs-Duhem equation, which describes the relationship between the changes in the chemical potentials of different species of a thermodynamic system.
As described in eq 2.28 the capillary wave roughness is directly related to the surface tension, which means that the roughness changes as a function of potential.

2.3.4 Mass Transport Mechanisms

We have already introduced "faradaic processes" and described them. Nevertheless, it has not been considered that reactions occur locally on the electrode. The species

participating in the reaction need to be transported to the surface of the electrode. This process influences the current in a electrochemical system. In particular, it is dependent upon two things [109]:

1. the rate at which material travels from the bulk of the electrolyte to the electrode, "mass transport"
2. the rate at which electrons can transfer across the interface, or "charge transfer kinetics".

These processes are entangled together in the flow of current. Furthermore, there are three mass processes that could occur [106]:

- Diffusion: spontaneous movement of any substances due to a concentration gradient
- Migration: the movement of charged particles due to an electric field
- Convection: movement due to an imbalance of forces on the solution.

Convection processes in electrochemistry are essentially the movement of solution species, like stirring or flowing electrolyte. However, this process is not relevant for the experiments performed in this thesis since steady solutions was used.
The migration contribution is proportional to the charge of the ion, the ion concentration, the diffusion coefficient, and the magnitude of the electric field gradient present. Thus can be effectively eliminated by increasing the conductivity of the solution, namely the ion concentration. It is typically done by inserting a "supporting electrolyte", a substance that does not affect the reactions under investigation, but increase the conductivity of the solution.
The diffusion contribution is related to the concentration gradients that directly result from the reactions at the electrode's surface. At the interface, under reaction conditions, the concentration of the reactants decreases while the concentration of the products increases.Therefore, the overall reaction rate limit is the rate at which the reactants diffuse to the interface. In this case, the total mass transport or flux is described only by diffusion by Fick's laws [110].
The flux F can then be related to the observed current i at the working electrode with area A (cm^2) by [107]:

$$J = \frac{i}{A} = n\,F\,D\left(\frac{\partial C_i}{\partial x}\right)_{x=0} \tag{2.45}$$

Where D is the diffusion constant (cm^2/s), and C_i is concentration of the species (mol/cm^3). Such a reaction, in which the diffusion rate alone determines the course of the reaction, is called "*diffusion-limited*".
In this thesis, this process was predominant in the reactions treated.

2.3.5 Absorption

The process in which molecular, atomic, or ionic species of one substance accumulate at the surface is called adsorption. It is called adsorbate, the substance which gets absorbed and adsorbent the substance on which absorption occurs.
There are two types of absorption. When the excess charge at the interface is only caused by long-range electrostatic forces such as van der Waals forces and it is only dependent on the radius and the number of charges of the ions, but not depending on the chemical species, this is referred to as "non-specific adsorption", also called "physisorption".
The adsorbate is in solution, therefore surrounded by a solvation shell made of water molecules. The ions might strip off their solvation shell and form a chemical bond, i.e., a covalent or metallic bond with the electrode. In this case the process is known as "specific adsorption" or "chemisorption". It occurs preferentially with anions since they have comparatively low solvation energies [111]. But in an electrochemical environment, the strength of the chemical bond between the anion and the electrode can be adjusted by varying the electrode potential [112, 113].
Neutral molecules can also adsorb on an electrode surface and then directly or indirectly influence Faraday processes.
The ratio of occupied adsorption sites on the electrode to the total number of adsorption sites is determined by the degree of coverage Θ. Consider the adsorption of a species A with concentration c_A in the bulk of the solution. The variation of the coverage Θ with c_A, keeping all other variables fixed, is known as the adsorption isotherm. Adsorption isotherms can be described as the adsorption of substances at interfaces. In the simplest case, single species ions adsorb on the electrode, and the interaction between adsorbed particles can be neglected. Such a process can be described by Langmuir isotherms [107]. There are different types of isotherms. The description goes beyond the interests of this thesis.
In many cases, however, adsorption processes are more complex, e.g., the interaction of the adsorbed particles cannot be neglected, or adsorption of several species takes place simultaneously (so-called coadsorption).
Another example of coadsorption is the adsorption of one species, which is only possible through the previous adsorption of another species. Another situation could be when electrochemically inactive substances are adsorbed, an insulating layer forms on the electrode surface (inhibition) [114]. Nevertheless, redox reactions often occur even at such interfaces due to tunneling processes through the adsorbate layer or at defect sites.
On the other hand, an adsorbate layer can also catalyze other reactions, for example, the oxidation and reduction of many cations are accelerated by small amounts of adsorbed anions [115]. The ability of an ion or molecule to adsorb depends, among other things, on the electrode potential, the type of bond formed, the solvation shell, and the charge.

2.3.6 Amalagamation of metals in Mercury

Many metals can form an alloy with mercury [116]; notable exceptions are iron, platinum, and tungsten. These alloys are called amalgams. If we use mercury as an electrode, metal ions can diffuse into the liquid mercury under the surface. In an electrochemical cell, this could be controlled by the applied potential. For example, when a negative potential is applied to the mercury electrode, metal cations M^{n+} can pass through the electrochemical double layer and penetrate the mercury electrode, where they are reduced:

$$M^{n+} + n\,e^- \rightleftharpoons M_{Hg} \tag{2.46}$$

The amalgamation reaction described (eq 2.46) is nothing more than a redox reaction and can be characterized by cyclic voltammetry (details about this method are explained in the following section 2.3.7).
Another example of amalgamation is when ions dissolve in a liquid metal due to the solubility of the two components. Once inside the working electrode, the species could nucleate and start the growth process and only after emerging at the surface. This is a particular example that happens in the case of electrodeposition of Ge using a Hg or Hg-alloy as working electrode [12, 21, 117].

2.3.7 Cyclic voltammetry

Cyclic voltammetry (CV) is a powerful electrochemical technique commonly used to investigate the redox processes of molecular species. CV is also invaluable for studying electron transfer-initiated chemical reactions, including catalysis or synthesis, which provides information about the thermodynamics and kinetics of these reactions [106].
CV is performed by applying a repeated triangular shape potential oscillating between two turning points while monitoring the current flowing between electrodes. The essential parameters for a CV are the turning points and the scan rate: the rate of voltage change in the ramp. An example of a CV is reported in Figure 2.14.

The cyclic voltammogram shown in the Figure 2.14 describes a system in which a redox reaction occurs. The two symmetrical current maxima are characteristic of such a reaction. From the positions E_a of the anodic maximum and E_c of the cathodic maximum the equilibrium potential can be calculated [119] as $E^{eq} = \frac{1}{2}(E_a + E_c)$. In the case of a reversible reaction, the two current densities $J_{p,a}$ and $J_{p,c}$ are equal, and their amplitudes are not measured absolutely, but relative to the zero line of the scan direction, as shown in Figure 2.14. The current densities $J_{p,a}$ and $J_{p,c}$ depend on the scan rate and the processes. By systematically changing the scan rate, conclusions can be drawn about the type of processes taking place [120].
At room temperature the absolute difference between E_a and E_c for reversible one-electron reactions is about 58 mV [119], this value can be obtained from the Nernst equation 2.43. For a process in which n electrons are involved, the distance between the maxima peak-to-peak separation is 58 / n mV. However, this is only the case if

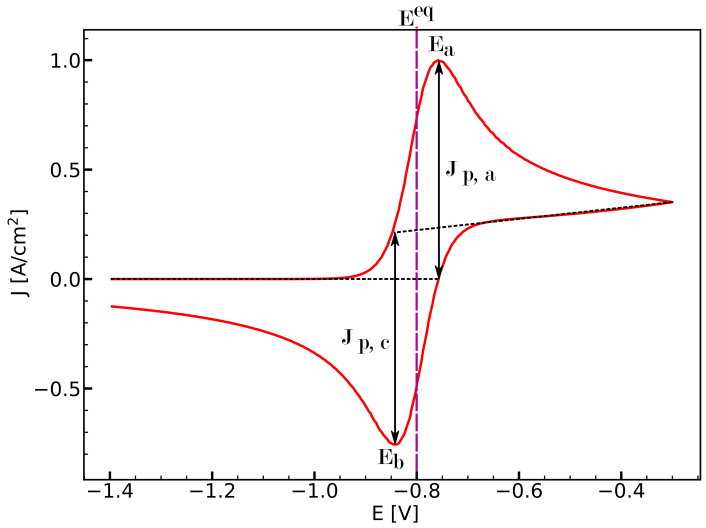

Figure 2.14: Cyclic voltammogram of a 1 electron redox reaction, simulated with [118]. On the graph are reported the current peaks $J_{p,a}$ and $J_{p,c}$ and equilibrium potential E^{eq}.

all parts of the reaction take place at the same potential. In the general case, a superposition of several maxima is obtained, whereby the distance between the cathodic and anodic maximum can no longer be specified [121].
A current not equal to zero can be observed positively and negatively of the redox maxima. The charging of the double-layer capacitance causes a small part of this current. However, the most significant contribution comes from the ongoing reduction or oxidation, which is limited in these areas by transporting the reacting species to the electrode interface. More details on CV can be found [119, 121, 122].

2.3.8 Electrodeposition

Electrodeposition denotes nucleation and crystal growth in electrochemical systems under the influence of an electric field [123]. Crystallization commonly occurs at the interface between an electronic conductive substrate and an ionic conductive electrolyte. Usually, it is possible to divide the process into three stages:

- Formation of adatoms on the substrate via absorption
- Nucleation: first stages of formation of two-dimensional and three-dimensional phase via phase transition
- Crystal growth of the 3D bulk phase of the deposit.

Contrary to other synthesis techniques like in vacuum (physical depositions) or chemical vapor deposition, the electrochemical synthesis is influenced by properties of the electrolyte phase that strongly affect the structure of the substrate/electrolyte interface and the kinetics of the process. Factor to consider are, for example, pH and concentration of solution.

The classical deposition mechanism is based on the interaction between deposit (D) and substrate (S). In particular, it can be divided into two main modes:

- The binding energy of the adatoms on the substrate is lower than the energy between the adatoms and D. Consequently, it is favorable to have an "island growth mode". The deposition starts on different substrate sites and eventually covers the working electrode. It is also called the "Volmer-Weber mechanism".
- The binding energy of the adatoms on S is higher than the energy between the adatoms and D. Then a two-dimensional phase can be formed. Multilayer arrangements could take place depending on the misfit between the 2D deposit and the substrate:
  - If the mismatch is negligible, the 3D crystallites are epitaxially oriented followed by a layer-by-layer growth or "Frank-van der Merwe mechanism".
  - If the misfit is significant, there is a considerable internal strain on the 2D structure. This leads to unstrained 3D crystallites (island) formation and growth on top of the 2D layer. This process is called the "Stranski-Krastanov" growth mode. Usually, the mismatch between 2D and 3D structures is removed by dislocations.

The process described depends on the kinetics of nucleation and growth and other parameters of the reactions. Therefore real physical systems may behave differently. New theories and considerations are still under investigation [124]. However, it is interesting to see how the Stranski-Krastanov mechanism cannot happen with a liquid substrate (from a strict point of view) since there is no mismatch between substrate and deposit. Moreover, for heterogeneous nucleations the possible nucleation sites on a solid substrate are steps, kinks, defects, vacancies. That would lead to defects in the deposit. This can be avoided on liquid working electrodes.
The growth on liquid substrates is a relatively new technique [12, 117], and a well-established theory is not developed. Further considerations have to be taken into account. Liquid metals can act as a solvent for precursors, and therefore adatoms can be found inside the liquid metal instead of on the surface. Nucleation, the first stage of growth, may start in the bulk of the substrate, as suggested in [12, 117]. This phenomenon is also treated in Chapter 6.
To perform electrodepositions, only an electrochemical cell is needed (either two or three electrodes). The working electrode acts as a substrate where the deposition occurs. The potential drives a reaction where an element M^{n+} in solution gets reduces:

$$M^{n+} + n\,e^- \rightarrow M_S^0 \tag{2.47}$$

As introduced before, the reaction 2.47 occurs at the potential E^0, the thermodynamic potential of the reaction. Like most of the electrochemical process, the reaction 2.47 occurs at the surface of the working electrode when M^{n+} is in contact with the substrate. For this reason, the reactions involved in the discharge process are the transport of hydrated ions towards the cathode surface, the diffusion in the Helmholtz layer, followed by adsorption of the ions as adatoms at the electrode surface and then the nucleation of the deposit [125].
As mentioned before, this effect is typical of a solid substrate, but for liquid metal substrates or liquid substrates in general, atoms or molecules can be dissolved into the working electrode, like an amalgamation of metals in mercury (see 2.3.6).
If during the deposition process there is no other reaction in parallel besides reaction 2.47, in principle, it is possible to calculate the amount of material deposited by just measuring the current in the electrochemical cell.
By assuming that all the M_S^0 ions reduced at the surface of the working electrode stick to this surface, the total amount of electrodeposited material can be calculated from the charge Q (in coulombs), which represents the product of the total amount of electrodeposited atoms N times the charge of n electrons $Q = N\,n\,e$. Where $e = -1.6 \times 10^{-19} C$ and Q can be calculated from the integral of the current $I = I(t)$ as a function of time:

$$Q = \int I(t)\, dt \tag{2.48}$$

In order to calculate the thickness of the deposit h, the surface area of the electrode A is need it. Then the thickness can be calculated as [126]:

$$h = \frac{M\,Q}{n\,d\,A\,N_a\,e} \tag{2.49}$$

Were M is atomic weight of the deposited elements, d is the density of the material, and N_a is Avogadro's number (the number of atoms in a mole, equal to 6.02×10^{23}). This calculation is a good approximation, but for more precise results, various factors have to be considered, for example, simultaneous reactions during the deposition (the most common the reduction of H^+), the porosity of the deposit, and possible non faradic processes.

3 Experimental details

3.1 Beamline P08

The beamline P08 is a High-Resolution Diffraction Beamline located at Petra III DESY (Hamburg) [127]. The X-ray energy available at the beamline P08 ranges from 5.4 to 29.4 keV, with a flux of 10^{11} to 10^{12} photons per second, a beam size between 1500×100 μm^2 and 20×2 μm^2. The beamline layout is shown in Figure 3.1. A tunable undulator provides a white beam. First, water-cooled high-power slits cut off the low-energy halo. Then the beam is monochromated at the liquid-nitrogen-cooled high heat load monochromator (HHLM). Following this, the beam is collimated or focused using compound refractive beryllium lenses (CRLs) and guided into the experimental hutch via the Large Offset Monochromator (LOM), which consists of two crystals. Depending on the energy range, a pair of Ge(331) or Ge(511) (or Si crystals) is used [127]. After the LOM, the beam enters the hutch through the beam shutter, a fast shutter (FS), a series of slits (sl), an attenuator (blatt), and further CRLs to focus the beam to the position of the experiment. Through the setup the beam is monitored by beam position monitors (BPMs). At this point, the beam reaches two possible diffractometers. A high precision 6-circle diffractometer (Kohzu) with Eulerial cradle dedicated for investigations at hard condensed matter samples, or Liquid Interfaces Scattering Apparatus (LISA).

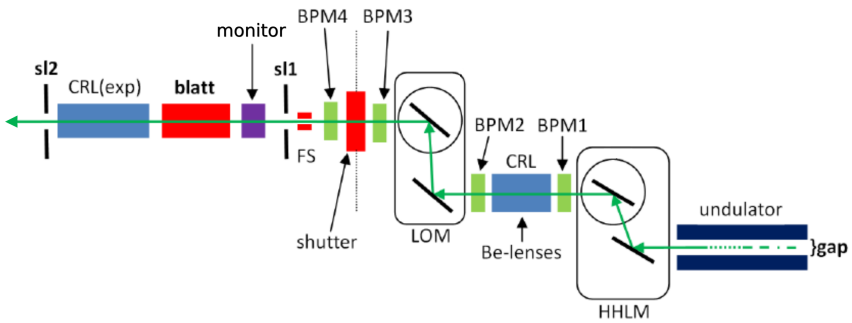

Figure 3.1: Setup of the optics of P08 beamline Petra III in DESY (Hamburg Germany). From right to left: high heat load monochromator (HHLM), beam position monitors (BPM1-BPM4), compound refractive beryllium lenses (CRL), large-offset monochromator (LOM), hutch shutter, fast shutter (FS), slits (sl1, sl2), beam monitor, attenuator (blatt). The green arrows is the beam path from the undulator to the diffractometers [128].

3.1.1 Liquid Interfaces Scattering Apparatus (LISA)

LISA is dedicated liquid surface diffractometer installed at P08, which has been constructed by University of Kiel [32, 129]. It was the first liquid diffractometer employs a tilting double-crystal monochromator in Bragg geometry. This diffractometer allows reflectivity, grazing-incidence scattering small angle scattering measurements of an immobile mechanically and completely decoupled liquid sample, providing high mechanical stability. The diffractometer acts as a beam tilter and directs the X-ray beam onto the horizontal interface of a liquid sample at different angles via two germanium crystals. Due to the use of two asymmetric crystals, the point of impact of the beam on the sample is fixed, which means that the sample does not need to tracked, as in the case where a single crystal is used [78, 130–133] This is made possible by mounting two germanium (or silicon) crystals on a common rotating stage. Their axis of rotation must coincide with the horizontal primary beam, with a very low sphere of confusion. The first crystal (Ge(111) plane) is mounted on the axis of rotation in such a way that it reflects the incident beam just at the angle of Bragg reflection θ_1. This reflected beam hits the second crystal ((Ge(220) plane) mounted on the axis of rotation, where it also in Bragg condition (at θ_2) to reflect the beam (see Figure 3.2).

By rotating the beam tilter (① in Figure 3.2), this double-reflected beam moves on a cone whose tip is located at the position of the sample (see Figure 3.2 top). The incident angle on the sample position varies between $\alpha_i = 0$ and a maximum angle $\alpha_{max} = 2(\theta_2 - \theta_1)$, which depends on the photon energy. Since all the components are motorized, the instrument can be used with the entire energy range of the beamline by just aligning the crystals properly, and a q_z range from 0 to $\sim$ 2.45 Å can be examined.
Due to the design, similar to the incident beam, also the reflected from the sample moves on a cone, so the detector must follow accordingly. Therefore the detector is mounted on a moveable detector stage (③ in Figure 3.2) decoupled from the sample stage, which can be rotated by two angles and moved along the vertical z-direction. The detector can move in a wide range of angles and distances behind the sample, allowing GID, small-angle X-ray scattering (SAXS) experiments are also possible in addition to reflectivity measurements.
The advantage of the set up shown in Figure 3.2, where the three elements ①, ②,③ are decoupled from each other, is to increase the stability of each module and to prevent unwanted vibrations from reaching the liquid sample during experiments.
A recent improvement of the set up is a second detector (EIGER2 1M) mounted closer to the sample stage ($\sim$ 30 cm). In such a way a wider reciprocal space can be accessed, without moving the detector arm. For experiment where more resolution is needed the other detector positioned at $\sim$ 110 cm can be used.

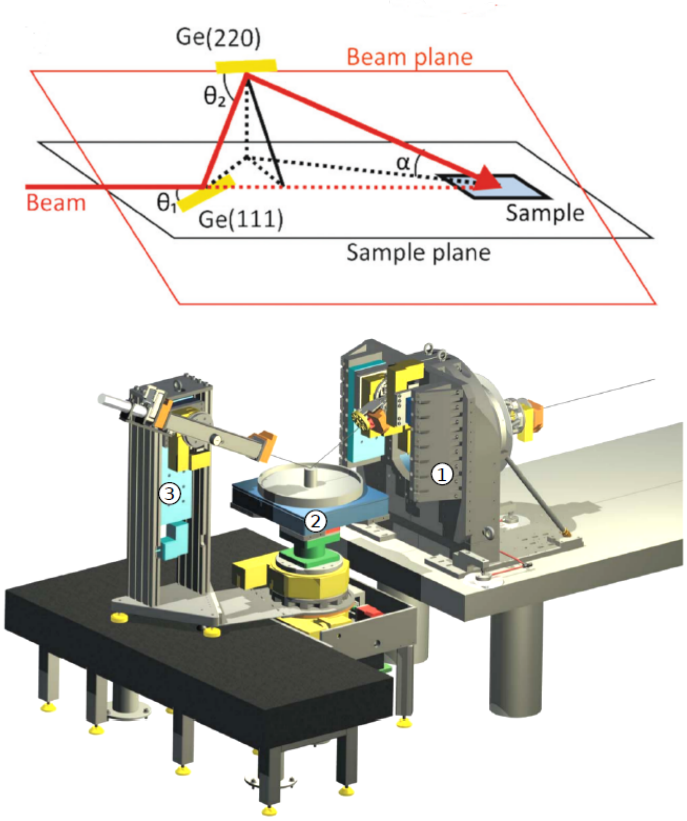

Figure 3.2: Top: Beam path through LISA double crystal beam tilter. At the first germanium crystal the X-ray beam is scattered upwards via reflection with a Bragg angle θ_1, then scattered downward using a second germanium crystal with a larger Bragg angle θ_2, defining a plane in which The beam is located [31]. Bottom: Drawing P08 beamline dedicated to liquid scattering experiment. 1 housing containing the beam tilter, 2 sample stage, 3 Detector arm [32].

LISA beam path

The beam reaches LISA after passing through sl2 (Figure 3.1), then the beam size is defined by a pair of horizontal and vertical slits (monochromator slits ms). The intensity is monitored with avalanche photodiodes (APD). The beam then enters the beam tilter, hits the first monochromator crystal (Ge(111)), and is deflected towards the second crystal (Ge(220)). The intensity at this point is monitored by an ion chamber (ion1), mainly for alignment purposes. From the second crystal, the beam is diffracted towards the sample. A sample slit (ss) is positioned behind the second crystal to reduce diffuse intensity around the beam. After that, an ion chamber (ion2) and avalanche photodiodes (APD) monitor the intensity; these monitors are used to normalize the data since they are the closest to the sample. An absorber wheel (abs) attenuates the beam before reaching the sample. The sample stage can be moved in all three dimensions (sx, sy and sz) and rotated around the vertical axis (sphi). After the sample, the beam is scattered towards the detector mounted on the detector stage that can be changed in position: rotation around horizontal axis

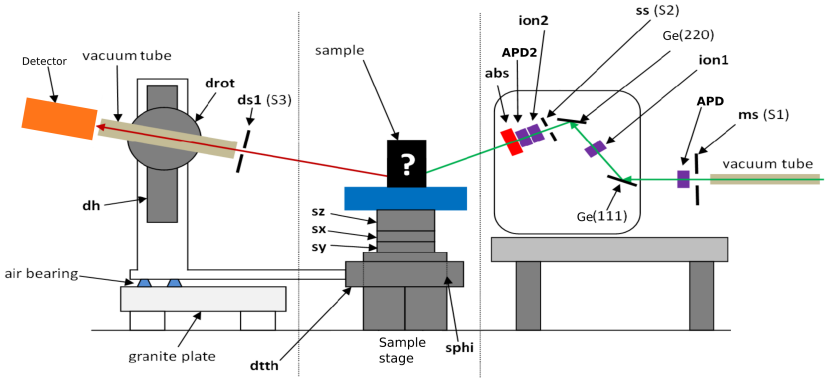

Figure 3.3: Scheme of the main modules of LISA[128]. The X-ray beam comes from the right (continuation of Figure 3.1). Full description reported in the text.

(drot), height (dh), and rotation around the vertical axis (dtth). A slit (ds1) is placed before the detector flying tube (vacuum tube) to reduce the background from the sample. The sketch in Figure 3.3 shows what is described in this subsection.

3.2 X-ray data collection and treatment

3.2.1 X-Ray Reflectivity

XRR data was collected with the XSpectrum Lambda detector, with a beam energy of 25 keV. A typical macro used to collect the data is reported in the appendix A.
The sample must be aligned before each X-ray measurement. The main goal is to have the beam hitting the center of the liquid metal pool. Therefore a scan in all three dimensions ($x - y - z$) is needed.
First, using the primary beam at $\alpha = 0$, the high of the sample is aligned, by finding half high intensity to center the sample in the beam. Then, the angle of incidence α is increased, and an x and a y scan are performed, in order to scan the sample profile. After an initial alignment of x, y, z the scans are repeated. When no appreciable change in sample position was detected, the experiment was ready to start.
In reflectivity measurements performed here, the angle of incidence α_i and α_f are gradually varied in a q_z range from 0 to about 2.45 Å^{-1}. The upper limit of the range was chosen so that the intensity maximum caused by the layering of the mercury at $\sim$ 2.2 Å^{-1} could be recorded. Since the measured intensity of the reflected beam ranges over a range of seven orders of magnitude, the intensity for small α_i, where the intensity is highest, had to be reduced to avoid damaging the detector. It is possible by using an aluminum wheel with different thicknesses (absorbers), which each one reduces the intensity of the beam by about one order of magnitude before it hits the sample. It is important to determine the exact absorber factor to normalize the beam intensity properly. For this purpose, overlapping points on the curve were recorded when the absorber was changed. The minimum integration time per point

was 1 s. In the course of the measurements, all absorbers were removed, and it was necessary to increase the integration time to up to 5 minutes at very high $\alpha_i > 4°$. As a result, to keep a reasonable duration of the experiment, the point density at the end of the reflectivity curve has been reduced.
The collected data were then reduced with a custom-written python code (see appendix). All the XRR data presented in this Thesis was treated the same way. First, the primary beam channel was localized (PBC) on the detector, then the specular beam was followed at high angles. If the specular beam moved in the process, a new PBC_{avg} was defined as the average of the positions recorded.
A minor misalignment of LISA could cause a shift of the specular beam on the detector, usually less than 4 pixels.
A ROI centered in the PBC_{avg} was set with 0.4 ° × 0.08 ° acceptance. The background was calculated by offsetting the ROI by 0.08 positive and negative in the parallel direction than the original ROI. The average of the background signal was then subtracted from the specular intensity. As described in the following equation:

$$I = I_{ROI} - \left(\frac{I_{bkg_+} + I_{bkg_-}}{2} \right) \tag{3.1}$$

The signal obtained from the extraction described above was normalized to plot R vs q_z with R∼1 at q_z=0. The primary beam intensity was often inaccurate due to the mismatch of absorber factors. A possible reason could be a slight shift of the beam on the absorber wheel when the incidence angle is changed; this effect was already observed in Runge studies with similar samples [128].
So a different approach was developed. The basic idea is to consider a low q_z-region, between $\sim 2 \times q_c$ and $q_z \sim 0.4 \text{Å}^{-1}$, where the behaviour of the reflected beam intensity normalized by the Fresnel reflectivity follows a decay $\propto \exp\left(q_z^2\right)$ (eq. 2.24). Therefore the data plotted as $\ln\left(I/I_{Fr}\right)$ vs q_z^2 should have linear behavior, and in particular, the intercept with the Y axes should be zero. This model implemented here to normalize the XRR data.
First the coefficient m (slope) of the line was obtained by a linear fit using the equation:

$$\begin{aligned} \ln\left(\frac{I(q_z)}{I_{Fr}(q_z)}\right) &= m\,x\, + k \\ x = q_z^2 \quad q_z &\in [2 \times q_c, 0.4] \end{aligned} \tag{3.2}$$

Once m wass obtained, the intercept k was set to zero. So from 3.2, the primary beam I_P was obtained by averaging the point as follow:

$$I_P = \left\langle \frac{I(q_z)/I_{Fr}(q_z)}{\exp\left(m\,x\right)} \right\rangle \tag{3.3}$$

This process was done for each curve during extraction. An average of I_P was calculated for each Beamtime and electrolyte to avoid artifacts during the process. The

beam intensity was normalized by the monitors to exclude intensity fluctuation coming from the instrumentation like PETRA ring of from LISA itself.

3.2.2 Grazing Incidence Diffraction

Also GID data were collected with XSpectrum Lambda detector and treated with custom-written Python codes (see C for details). Typical GID experiments were performed by scanning the horizontal 2θ angle with incidence angle fixed, typically to 80 % of the critical angle of the system. The detector images obtained in the scan were then converted from pixels in q-space coordinates. Then, the images were combined together and binned to obtained a single image with three data arrays q_z q and intensity. From these images also, a diffraction profile was possible to obtain by calculating the total $q = \sqrt{q_z^2 + q^2}$ and plotting the integrated intensity. The binning was unnecessary for a single detector image, and only a change of coordinates was needed. Typically, the same scan as blank (e.g., without deposition) was recorded before the diffraction experiment. Then it was subtracted to the data to reduce the noise, especially to remove the structure factor contribution of water.

3.3 Electrochemical experiments

Electrochemical experiments were performed with Ametek Solartron Analytical potentiostat (Modulab 2101A), with the controlling software *XM-studio ECS*.
Controlling the potential of the sample during the whole experiment is crucial. Losing the potential control could cause oxidation of the sample and/or irreversible reactions like a deposition. Therefore, to avoid open circuit potential (OCP), the software was programmed in advance with all the different measurements planned for the run. Furthermore, the software allows skipping to the next step when the user desires it. The voltage applied to the cell was implemented as a counter in SPOCK[1]. So it was possible to synchronize the electrochemical and X-ray data. In addition, the data was saved on the same file, simplifying the analysis post beamtime.

3.4 Sample cell

On the market there is no standard electrochemical cell dedicated to *in–situ* scattering experiments at liquid-liquid interface, therefore the implementation of a suitable sample cell is required. A new electrochemical cell was designed as part of this Thesis. The requirements are multiple:

The cell material needs to be resistant to a wide list of chemicals due to the variety of experiments performed.

[1]SPOCK is the the command-line interface for sardana to talk to the TANGO devices controlling the experiment at the beamline

A diameter big enough is necessary to achieve a flat surface of the liquid metal. A curved surface scatters the reflected beam at different exit angles due to the geometrical effect. This creates artefacts in the reflectivity profiles [134, 135]. The other way around, namely, a big diameter leads to an absorption of the X-ray beam and an increase of scattering due to the massive electrolyte volume. This would make the data quality drop. Previous experiments show great results with a diameter around 5 cm [22, 23, 59, 60]. Due to the footprint of the X-ray the meniscus effect affects angles lower than $\lesssim 0.1\,\text{Å}^{-1}$ for this diameter. The information used in this Thesis is based on higher angles. So the effect of curvature is negligible. Details information about the effect of curvature and cell size are described in [128, 136]. As reported in the literature, further analysis must be performed to tread low angle data on the curved surface [134, 135]. However, this is beyond the work presented here.

The X-ray windows aperture needs to match the angles spectrum utilized during the experiments, either normal or parallel to the sample's surface, to obtain a range of q_z up to $3\,\text{Å}^{-1}$ and of $q_{//}$ up to $5\,\text{Å}^{-1}$.

Observing the liquid metal surface during the experiment should be possible by mounting a microscope camera on top of it.

The possibility to exchange electrolytes *in situ* is necessary.

The liquid metal should avoid contact with the external environment once the setup is assembled. The reasons are to avoid heavy oxidation that compromises the experiment and for safety reasons. For example, Hg vapors are dangerous, so none of them should be present at the beamline or laboratory during an experiment.

The cells should have the possibility to be sealed for transportation. Moreover, in the case of a spill, it should be confined.

There should be the possibility of changing the temperature of the liquid metal pool in order to investigate metals not liquid at room temperature (e.g., Ga).

It should be easy to clean and assemble. During experiments, this process is repeated several times.

Our group worked on liquid metal in an electrochemical environment for a decade and designed and used different cells. However, all of them were missing the possibility of exchanging the electrolyte *in situ*, it was not possible to observe the liquid metal interface, and a vacuum pump was employed to free the cell from oxygen to avoid oxidation of the liquid metal. An improved cell that meets all the requirements was designed and built at the University of Kiel. The cell project is illustrated in the *Inventor* drawing in Figure 3.4.

As shown in 3.4 the apparatus has two main components:

- Inner cell: the actual electrochemical cell

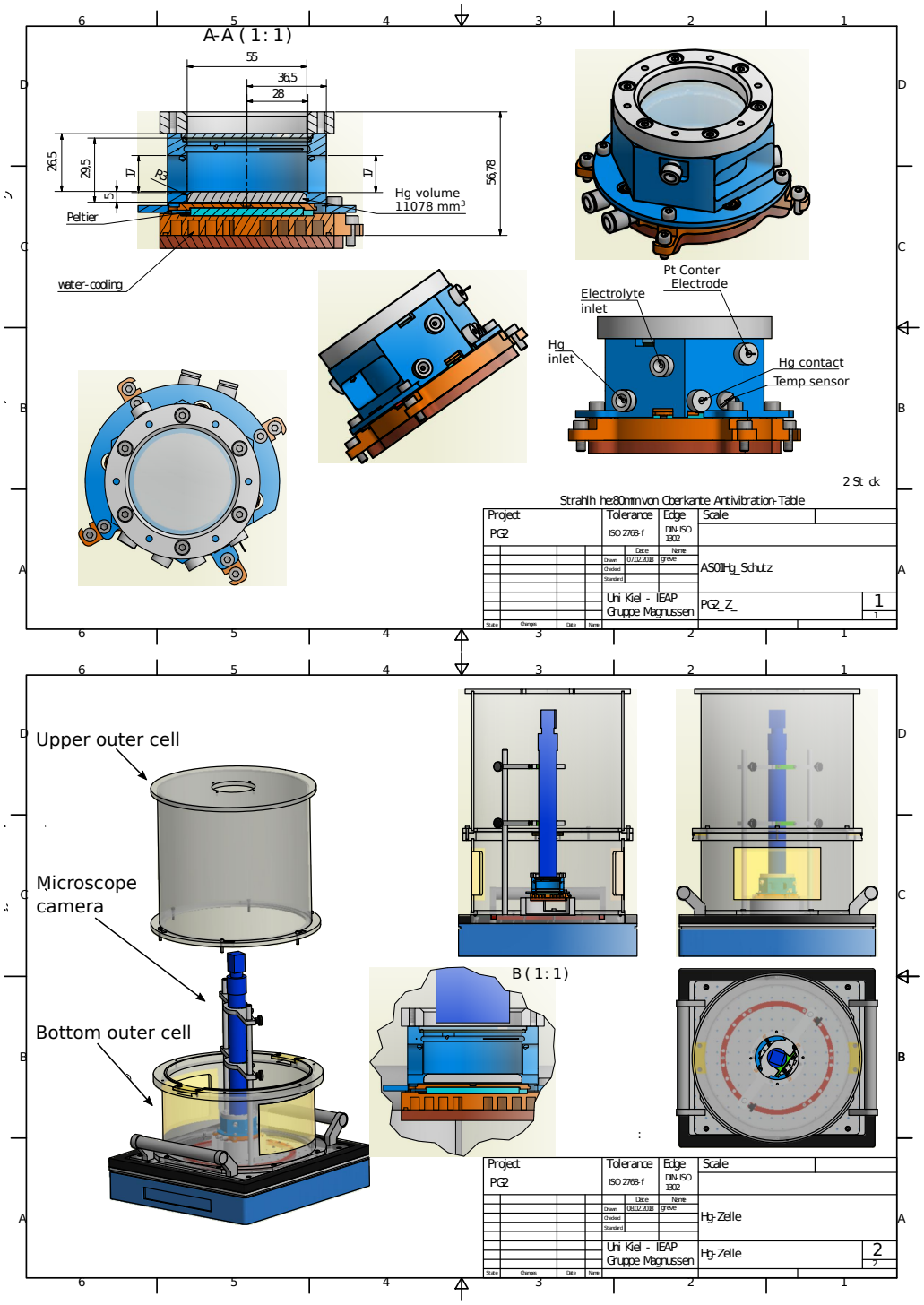

Figure 3.4: *Inventor* drawing of the liquid metals electrochemical cell for *in situ* X-ray experiment. Top: details of the inner cell. Bottom: Outer cell design. (Credit Dipl.Ing. Matthias Greve)

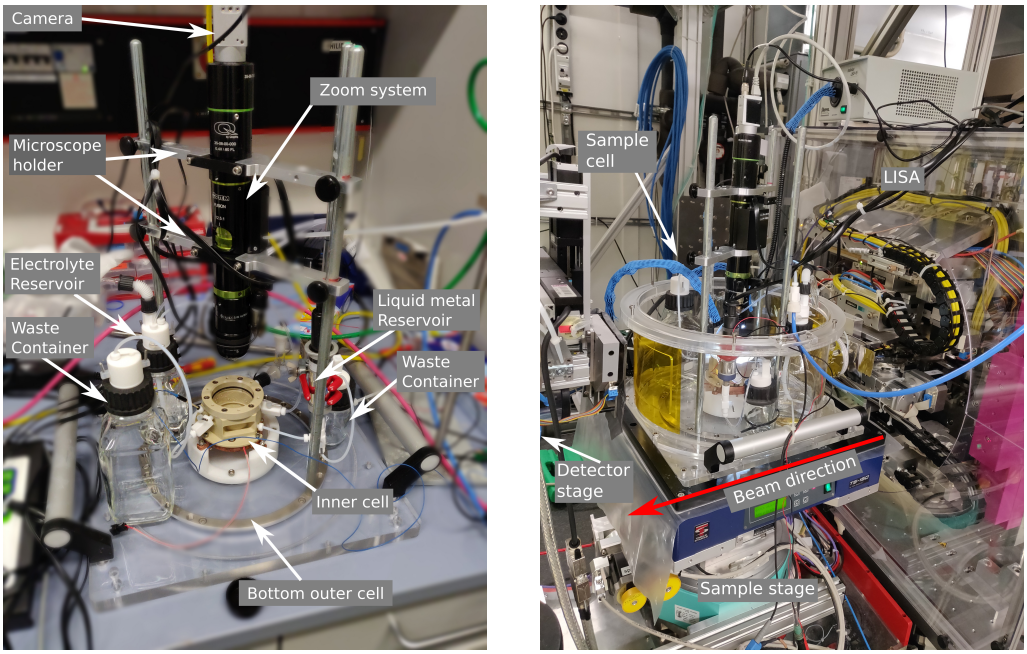

Figure 3.5: Liquid metals electrochemical cell photos. Left: arrows indicates the different component of the cell. Right: sample cell mounted on the sample stage of the beamline P08 at DESY.

- Outer cell: an external shell for safety

The inner cell made from PEEK, since the material has high chemical resistance and thanks to its hardness was possible to create threaded holes able to hold a sealed system. The inner diameter is 5.5 cm, and it is 3.45 cm tall. The volume of the liquid metals is around 10-15 ml, and for the electrolyte is therefore, $\sim$ 70 ml. Moreover, thanks to the properties of the material were possible to create very thin X-ray windows (0.5 mm) to avoid as much scattering as possible. Also, the bottom of the cell is the same thickness; this helps the heat transfer from the Peltier element beneath it. Thermoelectric cooling permits to tune the temperature of the sample, also remotely. However, in order to have correct functioning, the opposite side of the Peltier needs to be cooled/heated. Therefore, a hollow copper base was designed to allow water to flow inside of it.
As it can be seen in Figure 3.4, the diameter was chosen to the 5.5 cm. Considering the typical beam size used (0.4 $\times$ 0.1 mm) and energy (25 keV), the theoretical footprint matching the diameter is at the angle of 0.1 $^\circ$ (q= 0.044 Å^{-1}), even lower than the critical angle of Hg-water interface (at 25 keV) 0.145 $^\circ$ (q= 0.064 Å^{-1}). In reality, the liquid sample has a curvature higher, so the flat surface results to be around 20 mm. However, the diameter size is a good compromise between signal and amount of liquid metal and electrolyte to be used. Unfortunately, by increasing the diameter of the mercury surface, the beam path through the electrolyte increases too, and intensity will be lost due to absorption. So a compromise had to be found.
The top window is made of high-quality glass (quartz), but is possible to exchange

with other materials in case of highly alkaline solutions used, like Poly(methyl methacrylate) (PMMA), commonly known as plexiglass. Thanks to this design, an optical microscope or a surface optical reflectivity device were possible to be mounted on top of the cell. It allows to monitor *in situ* the evolution of the surface during different experiments, not only at the beamline facilities. The setup was designed to exchange electrolytes during the experiment, with an inlet connected to a reservoir and an outlet tube connected to a waste container. The electrolyte was exchanged by creating a controlled overpressure with an inert gas in the reservoir. The flow rate was tuned as desired by changing the gas flow rate and outlet valve. The electrolyte volume during the experiment is about 70 ml. A volume of 500 ml of the new solution was flown inside the cell to obtain the new target concentration. The procedure is designed to inject the liquid metal while avoiding contact with the external environment. First of all, before inserting any solution into the cell, the fresh electrolyte was purged with N_2 for at least 30 minutes to remove dissolved oxygen in it. A glass tube with a porous head connected to the gas line was used for this purpose (see 3.6). Then the cell is filled with the desired electrolyte, including filling all the tubes. To do that and avoiding trapped gas bubbles the cell is tilted up to 90 $^\circ$ with the outlet facing up. Once this step is fulfilled, some droplet of liquid metal is injected into the waste container to remove the small amount of the liquid metal that was in contact with air. At this point the liquid metal can be inserted into the electrochemical cell. This procedure is made manually with a 25 ml syringe acting as a reservoir of Hg. But a project to connect to a syringe pump controllable remotely, is currently in progress.
The electric contacts are platinum wire or tungsten with a diameter of 0.5 mm to connect the working electrode. The counter electrode is a platinum wire bend as a ring around the inner upper part of the cell.

The outer chamber has a diameter of 34 cm and 53 cm tall. It is mainly made of plexiglass. It is divided into three main parts. The base where a steel ring with threaded holes is embossed. The holes allow for mounting metal rods (commonly used in chemistry laboratories), it is possible to attach clamps to hold the different glassware, tubes, and camera. The base center is dedicated to placing the inner cell, the actual electrochemical cell described above. Furthermore there are also two practical handles for transportation. The other two main parts are hollowed plexiglass cylinders. These have the primary goal of safety. In the case of a spill, the material(s) is confided inside the outer cell. It can be removed during the assembly, but it must be present during experiments. Especially the bottom part. For this reason two wide Kapton windows were created to allow X-ray to pass through with less absorption and scattering possible. The upper one is necessary to remove it to operate the cell, like setting up the microscope camera, exchanging the electrolyte, tuning the liquid metal level, and connecting the potentiostat to the electrodes. Some photos of the cell are reported in Figure 3.5. The left one shows the setup mounted without the safety outer cell. On the right one, the cell is mounted on the sample stage at beamline P08

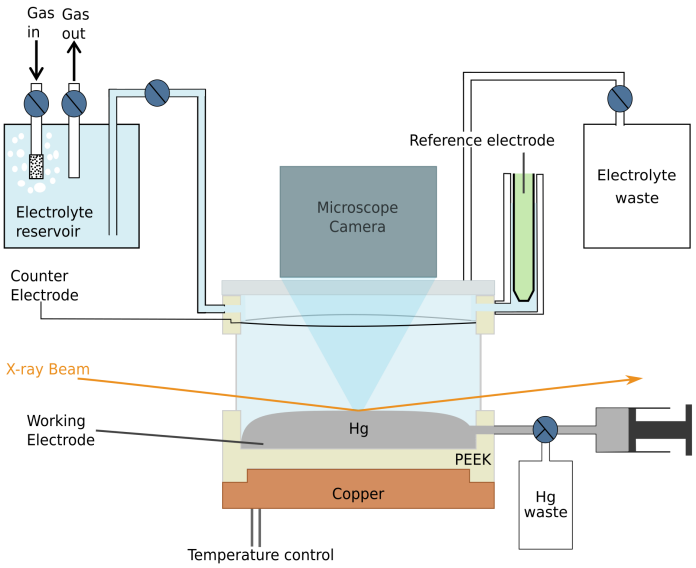

Figure 3.6: Electrochemical cell scheme. The electrolyte reservoir is connected with a gas line to bubble the solution, it has an exhaust valve and a third connection with the inner cell. A syringe acting as Hg reservoir is connected with a three-way stopcock to the cell and a waste container. The apparatus is also equipped with a electrolyte waste container, a temperature controller and a microscope camera.

at DESY.

Camera setup

The camera used is a Basler ACE acA1600-20gm with OPTEM Fusion motorized Zoom system 12.5:1 with Stepper Motor and 15mm Focus Lower Module with Stepper Motor equipped with a lower lens of 9 cm focal length. The software to record video and images was Pylon viewer. The setup was mounted on two aluminum arms specifically designed to hold the camera (Figure 3.5); those were then fixed on two metals rods. Thanks to the design, the high of de camera could be manually moved. However, for a more fine adjustment, the motorized system was used.

3.5 Sample preparation

3.5.1 Electrochemical cell cleaning

Before assembly, the sample cell components were cleaned individually. The main purpose of this procedure was to remove organic residues, which can have a major impact on electrochemical measurements and influence the liquid metal surface. Cell components made of glass, PTFE or PCTFE or PEEK that came into contact with the liquids metal or electrolyte along with the equipment required for the preparation (flasks, tweezers, beakers, glass syringes, etc.) were carefully cleaned with Caro's acid. To avoid dissolution of PEEK a lower concentration, around 40%, has

been used. Caro's acid (H_2SO_5), was prepared by mixing two to three parts hydrogen peroxide and one part sulfuric acid. The components were placed in the acid for at least six hours. The acid was removed by thorough ultrasonic cleaning and by rinsing at least ten times with ultrapure water (MilliQ water 18.2 MΩ cm).

3.5.2 Liquid metal preparation

The Hg used for all the experiments in this Thesis was Hg 99.999+ % purchased from ChemPur. To assure no contamination of liquid mercury, the final volume used was obtained by a series of cleaning steps. First, the metal was poured into a clean beaker. Then with a syringe, 3/4 of its volume was collected from the bottom (the bulk of the sample), and poured into a second container. From here, the mercury used in the experiment was taken, once again from the bottom of the container, with a clean syringe.
As mercury is denser than most of the possible contaminations, for example, organic compounds, oxide, dust; since they rise to the surface. Once in the syringe, the liquid metal stays sealed until the start of the experiment.

In the case of HgIn alloy preparation, the solid In shots were first weighted and then mechanically mixed with Hg to achieve the desired atomic ratio . The obtained sample was then collected with the syringe from the bulk in the middle of the container.

3.5.3 Electrolyte preparation

The electrolyte solution was prepared freshly for each experiment. The solvent was Milli-Q water (18.2 MΩ· cm). The solute in powder form with a purity of at least 99.995 % was used without further treatment.

4 Role of chemisorbing species in growth at liquid metal-electrolyte interfaces revealed by in situ X ray scattering

This chapter is based on a submitted manuscript in which investigation of growth at the interface of liquid mercury and lead-halides solutions was performed using a combination of X-ray scattering and electrochemical methods.

List of authors

Andrea Sartori[1], Rajendra P. Giri[1], Hiromasa Fujii[1], Svenja C. Hövelmann[1,3], Jonas E. Warias[1], Philipp Jordt[1], Chen Shen[3], Bridget M. Murphy[1,2], Olaf M. Magnussen[1,2]

[1] Institute for Experimental and Applied Physics, Kiel University, D-24118 Kiel, Germany

[2] Ruprecht-Haensel Laboratory, Kiel University, D-24118 Kiel, Germany

[3] Deutsches Elektronen-Synchrotron DESY, D-22607 Hamburg, Germany

4.1 Abstract

Liquid-liquid interfaces offer intriguing possibilities for nanomaterials growth. Especially, growth at liquid metal surfaces has recently received renewed interest. Here, fundamental interface-related mechanisms that control the growth behavior in these systems are studied for the case of Pb halide compound formation at the interface between liquid mercury electrode and aqueous salt solutions, using *in situ* X-ray reflectivity and grazing incidence X-ray diffraction, supplemented by electrochemical measurements and optical microscopy. The nucleation and growth of these compounds at potentials in the regime of Pb de-amalgamation was investigated in NaX + PbX_2 (X = F, Cl, Br) to systematically explore the role of the halide species. X-ray reflectivity studies reveal the rapid formation of well-defined ultrathin precursor adlayers in Cl- and Br-containing solution. This adlayer formation is followed by

subsequent quasi-epitaxial growth of Pb(OH)X bulk crystals, that are oriented with the c-axis along the surface normal. In contrast, growth in F-containing solution proceeds by slow formation of a more disordered deposit, resulting in random bulk crystal orientations on the Hg surface. A detailed structural analysis of the Pb(OH)Br and Pb(OH)Cl precursor adlayers reveals that they determine the orientation of the subsequently formed bulk crystals, with the arrangement in the adlayer providing a template. Together with our previous results on the pseudo-epitaxial growth of PbFBr on Hg (A. Elsen, et al., Proc.Nat.Acad.Sci., 2013, 110, 6663), these data reveal the decisive role of the interface chemistry, especially the strong chemisorption of the anions bromide and chloride, in steering the formation of these textured deposits at the liquid metal surface.

4.2 Introduction

Liquid metals have attracted large interest in the last years, not only for fundamental studies[1−3] but also for applications,[4−6] such as microfluidics,[7,8] electronics,[9] reconfigurable devices,[10,11] optics,[12,13] catalysis,[13,14] and materials synthesis.[15−18] Of particular interest is the use of liquid metals in growth processes, for example, in vapor-liquid-solid or electrochemical liquid-liquid-solid deposition.[19] Liquid metals possess major advantages over the use of solid substrates for such processes, including the high mobility of precursors on the surface, the absence of surface defects such as steps, and the inherent lack of strain, stress, and lattice mismatch that strongly affect the crystal growth process.[20] Moreover, many atomic species can be dissolved in liquid metals, allowing growth from both sides of the liquid interface, and the deposit can be easily separated from a liquid substrate. Recent achievements in this field are the controlled production of nanostructured materials,[5,21] including two-dimensional films[22,23] and crystalline nanowires.[24] Furthermore, the 'green' production of Ge, Si, and GaAs at low temperatures has been demonstrated. [15,19,25−30]

Despite these achievements, only little is known about the underlying nucleation and growth processes involved in the deposition at liquid metal interfaces, especially interfaces to other liquid phases. Most existing studies have been restricted to *ex-situ* characterization of the deposit. This is related to the experimental challenges in obtaining structural data from liquid-liquid interfaces by conventional materials science techniques. As a result, only very few *in situ* investigations of growth at liquid metal-solution interfaces have been reported so far.[31−33] Among the few structure-sensitive techniques that are capable of accessing liquid-liquid interfaces, X-ray scattering methods, such as X-ray reflectivity (XRR) and grazing incidence diffraction (GID) measurements, play a prominent role. XRR has been utilized extensively since the 1990s to study the atomic-scale structure of liquid metal-vapor interfaces, for example of Hg,[34,35] Ga,[36−38] In, [39] and liquid alloys.[26,40] These studies showed that liquid metals provide a nearly atomically flat substrate

with pronounced atomic layering in the near-surface region. More recent applications of XRR to liquid metal-electrolyte interfaces confirmed these general features of the liquid metal in the presence of aqueous electrolytes and provided fundamental insights into the dependence of surface layering and roughness on potential and temperature.[3,41]

In this work, we report a systematic *in situ* X-ray scattering study of the nucleation and growth of lead halide compounds at liquid Hg-electrolyte interface. The synthesis of lead halide compounds, especially perovskite, has lately received great interest, owning to their potential use in highly efficient solar cells.[42–45] In a previous study, our group reported the nucleation and growth of PbFBr on liquid Hg from $PbBr_2$-containing aqueous NaF solution.[32,33,46] This process was induced by electrochemical de-amalgamation of Pb from the Hg electrode and commenced with the rapid formation of a highly uniform 'precursor' adlayer with a thickness of one PbFBr unit cell on the Hg surface, followed by quasi-epitaxial growth of c-axis oriented bulk PbFBr crystals on top of it. This surprising nucleation and growth mechanism was observed over a wide range of growth rates[33] and indicates that, similar to growth on solid substrates, the initial interactions at the liquid substrate surface can steer the texture and morphology of the deposit. It was not clear, however, whether this phenomenon is specific to PbFBr or represents a more general growth mode at liquid metal interfaces.

Here, we present *in situ* X-ray scattering results for a series of deposition systems, in which only one halide anion is present at a time. The influence of the halide species is studied by deposition from aqueous electrolytes of composition NaX + PbX_2 with X = Br, Cl, F. We investigate by XRR the presence and structure of 'precursor' adlayers and correlate this with GID data on the formed bulk deposit as well as complementary electrochemical data and optical microscopy observations. Our results confirm the important role of the precursor layer in the nucleation and growth process at liquid metal interfaces and shed light on the influence of the halide species on this process.

4.3 Results

4.3.1 Electrochemical characterization of the Pb halide systems

Cyclic voltammograms (CVs) of freshly prepared samples in 0.01 M NaX + 0.25 mM PbX_2 (X = Br, Cl, F) are presented in Figure 4.1 (solid lines). All systems feature typical oxidation/reduction currents due to Pb dissolution/deposition, with an equilibrium potential $E_{Pb/Pb2+} \sim$ -0.80 V (as estimated from the midpoint potential between anodic and cathodic peaks in the CV). For potentials $E < E_{Pb/Pb2+}$ the Pb^{2+} ions amalgamate into Hg as Pb^0, whereas for $E > E_{Pb/Pb2+}$ de-amalgamation occurs, where Pb is released into the solution as Pb^{2+}. This process and the equilibrium potential do not depend on the halide species. The changes in $E_{Pb/Pb2+}$, the shape

of the CV, and the diffusion-limited current density follow the trend, expected for a simple Faradaic reaction (see Figure 4.1, bottom panel).

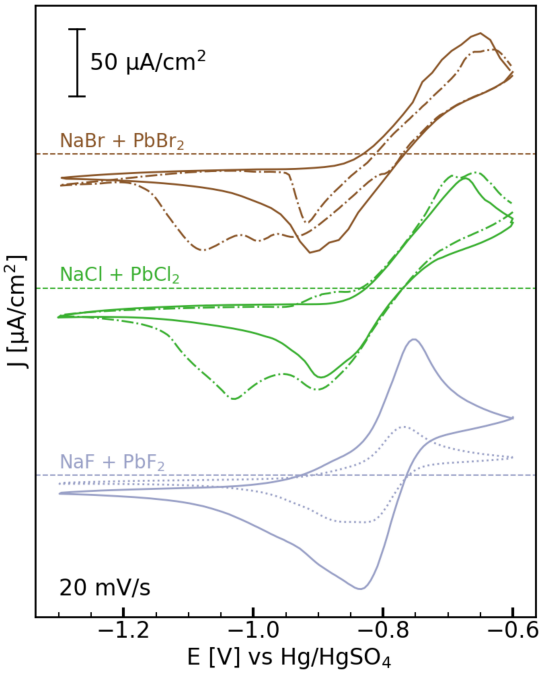

Figure 4.1: Cyclic voltammograms of Hg in 0.01 M NaBr + 0.25 mM PbBr2 (brown), 0.01 M NaCl + 0.25 mM PbCl2 (green), 0.01 M NaF + 0.25 mM PbF2, (blue solid line) and 0.01 M NaF + 0.12 mM PbF2 (blue dotted line). The CVs (offset for clarity with J = 0 indicated by dashed horizontal lines) were measured at 20 mV/s directly after immersion of the electrode into Pb-containing solution (solid lines) and after keeping the potential for more than one hour positive of -0.8 V (dotted dashed lines).

In CVs in Br- or Cl-containing solution that are measured after keeping the potentials for longer times positive of $E_{Pb/Pb^{2+}}$ (dotted-dashed lines) substantial changes are observed. In the presence of Br, the cathodic current in the positive going potential scan exhibits a sharp increase in the range -1.0 to -0.9 V (dependent on sample history), followed by a nearly linear change in the opposite direction. In Cl-containing electrolyte, a shoulder emerges in the positive scan at potentials >-0.95 V. Furthermore, a broad additional cathodic peak is found in the negative going scan at potentials that are ∼150 mV more negative than the original amalgamation peak. As shown below, these changes are caused by the formation of Pb halide compounds on the Hg surface in the potential regime of de-amalgamation. Because these ionic compounds dissolve only slowly by a chemical process that is coupled to the local Pb concentration, they partly remain on the surface during the CVs. The additional electrochemical features thus can be attributed to the presence of Pb halide at the interface (see below). In F-containing electrolyte, such effects are not observed. Here, no major changes in the CV are found after longer times at potentials $> E_{Pb/Pb^{2+}}$, indicating fundamental difference from the behavior in Br- and Cl-containing solution.

4.3.2 X-ray reflectivity studies of the Hg-electrolyte interface structure

The atomic-scale Hg interface structure was characterized in the different electrolytes by *in situ* XRR, which depends on the average electron density profile along the surface-normal direction. Figure 4.2 shows the obtained reflectivity curves of Hg immersed in the three different electrolytes, measured at potentials in the amalgamation (-1.20 V) and de-amalgamation (-0.70 to -0.90 V) regime. The XRR curves at -1.20 V (triangles) are identical to those measured in Pb-free 0.01 M NaX solution (Figure 4.8) and are independent of the halide species. They are characteristic for a pristine Hg-electrolyte interface without any adsorbed species from the electrolyte, as has been reported in previous studies.[3,26,32,33,41] Specifically, the measured reflectivity $R(q_z)$ is close to that of the Fresnel reflectivity $R_F(q_z)$ of a perfectly sharp interface over a wide range of the surface-normal scattering vector q_z, indicating a low interface roughness. With increasing q_z we observe first an initial decrease of $R(q_z)$ relative to $R_F(q_z)$, followed by an increase towards the so-called pseudo-Bragg peak at ~2.15 Å^{-1}. The latter is caused by the well-known stratification of the liquid Hg into atomic layers near its surface,[34,47] which decays exponentially into the Hg bulk within 10-20 Å. These data provide clear evidence that the amalgamated Pb atoms diffuse into the bulk liquid metal, leaving the Hg surface unmodified.

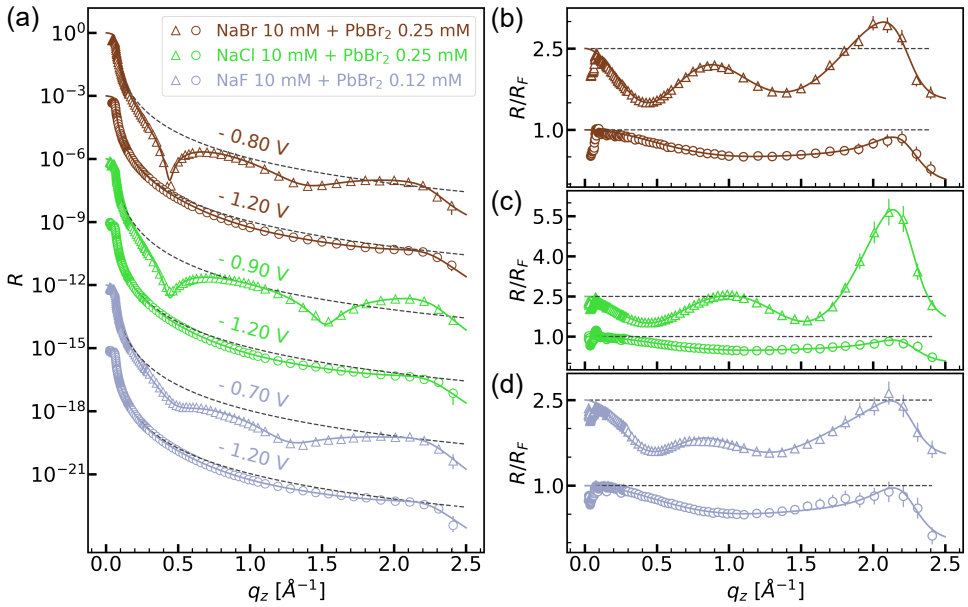

Figure 4.2: (a) X-ray reflectivity and (b-d) XRR normalized to the Fresnel reflectivity of Hg electrodes in 0.01 M NaBr + 0.25 mM $PbBr_2$ (brown symbols), 0.01 M NaCl + 0.25 mM $PbCl_2$ (green symbols), and 0.01 M NaF + 0.12 mM PbF_2 (blue symbols). Triangles indicate curves measured at -1.20 V, open circles curves were measured in the potential range of de-amalgamation, at -0.80 V (brown), -0.90V (green), and -0.70 V (blue). For clarity, the profiles in (a) are offset by a factor of 1000. Solid lines correspond to the best fits with the models discussed in the main text.

Quantitative fits of the XRR interface data at -1.20 V were performed by the distorted

crystal model, which is widely used to fit XRR of liquid metal interfaces (details on the fitting process are given in the supporting information).[3,32,34,36,39–41] Within the fit errors, the obtained structural parameters (Tables 4.1, 4.2, 4.3) depend neither on the halide species nor on the presence of Pb in the solution. Especially, the Hg layer spacing and the layer decay parameter, which essentially describe properties of the liquid Hg itself, had in all fits identical values of d = 2.76 Å and σ_b = 0.48 Å, respectively. These results indicate that at this negative potential the halide anion and the amalgamated Pb species do not influence the Hg-electrolyte interface structure, as already shown in our previous studies of the PbFBr system.[32]

A very different behavior is found at potentials in the de-amalgamation region (Figure 4.2, circles), where the XRR curves deviate strongly from those recorded at similar potentials in the corresponding Pb-free base electrolyte (Figure 4.8). Here, a pronounced modulation in the range $0 < q_z < 1.8$ Å^{-1} is observed for NaBr + $PbBr_2$, NaCl + $PbCl_2$, and NaF + PbF_2. This modulation corresponds to typical 'Kiessig fringes', which in XRR experiments indicate the presence of a defined layer on the probed surface. From the position of the first maxima, a characteristic layer thickness in the range of ∼7 Å can be estimated. The strong modulation observed in these XRR curves is only possible, if the layer contains strongly scattering species, which in this case has to be Pb. All other electrolyte species have scattering length densities that are ∼2.3 (Br), ∼5 (Cl), and ∼10 (F, H_2O) times smaller than Pb and thus can be neglected in the first order. These observations provide strong evidence that - similar to the behavior found in our previous studies of the nucleation and growth of the mixed-halide compound PbFBr - a Pb-containing adlayer forms on the surface in the de-amalgamation regime in all three studied systems. In addition, in Cl-based electrolyte the pseudo-Bragg peak is increased in comparison to the Pb-free electrolyte at this potential (see Figure 4.8), which indicates a reduced interface roughness. This phenomenon was also reported previously in the presence of the PbFBr precursor layer. It can be attributed to a damping of the capillary waves of the interface due to the mechanical rigidity of the precursor layer and indicates that this layer is crystalline.

In the F-containing electrolyte, the oscillations associated with precursor layer formation were less pronounced, indicating a less defined structure. Furthermore, XRR curves with noticeable 'Kiessig fringes' could only be observed at a lower PbF_2 concentration of 0.12 mM. Even in this electrolyte, however, the XRR curves were not stable in time but slowly changed in subsequently recorded XRRs (Figure 4.8). These changes can be attributed to a slow continuous growth of the deposit, which most likely is limited by the availability of Pb ions. This is supported by the measurements in electrolytes containing 0.25 mM PbF_2, where no 'Kiessig fringes' but only a bulk deposit could be observed (see below).

4.3.3 Potentiodynamic changes in the interface structure

In all systems, the formation of the precursor adlayer is directly linked to the de-amalgamation process. This is illustrated by experiments where the reflected X-ray intensity $I(t)$ was monitored during cyclic voltammograms at a fixed scattering vector q_z where the XRR curves have a pronounced minimum in the presence of the precursor adlayer (Figure 4.3). Upon sweeping the potential towards positive potentials, $I(t)$ starts to drop at $\sim$ -0.98 V in Br-containing, $\sim$ -0.93 V in Cl-containing electrolyte, and $\sim$ -0.80 V (depending on sample history) in F-containing solution, indicating adlayer formation on the Hg surface. This intensity change is reversible, i.e., the intensity fully recovers when the potential is swept back to a more negative region, albeit with some hysteresis. This reversible behavior indicates that the surface returns to the initial state of a clean Hg surface.

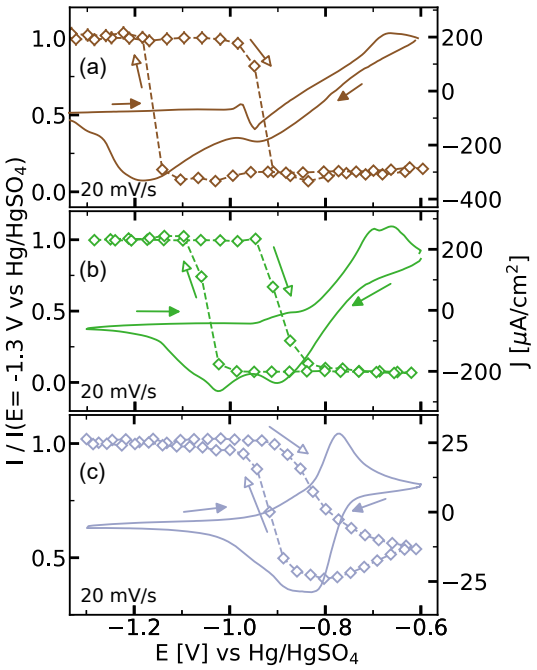

Figure 4.3: X-ray intensity (open symbols) at (a) $q_z = 0.50$ Å^{-1} and (b,c) $q_z = 0.45$ Å^{-1}, recorded during cyclic voltammograms (solid lines) of Hg at 20 mV/s in (a) 0.01 M NaBr + 0.25 mM $PbBr_2$, (b) 0.01 M NaCl + 0.25 mM $PbCl_2$, and (c) 0.01 M NaF + 0.12 mM PbF_2. Arrows indicate the directions of the potential sweeps.

According to the data in Figure 4.3, the adlayer formation occurs in a different manner and at different rate in the studied systems. In Br- and Cl-containing electrolyte, the drop in X-ray intensity is sharp and occurs within a small potential range of the sweep, corresponding to a time of several seconds. This potential range is in excellent agreement with that of the additional features in the CV that are found after longer residence times in the de-amalgamation region. The good correlation indicates that these features are caused by the presence of the precursor adlayer, which is further supported by the good agreement of the additional cathodic peak in the

negative sweep with the change back to the initial X-ray intensity. After each decrease and increase in X-ray intensity, respectively, a defined steady-state intensity is reached, indicating that a defined interface structure has formed and then remains stable.

In F-containing electrolyte, the intensity only starts to decrease positive of -0.90 V and then decreases much more gradually. Here, the intensity of the corresponding XRR curve in Figure 4.2 is never reached during the entire CV. Rather, $I(t)$ continues to decrease also in the subsequent negative potential sweep until $E_{Pb/Pb2+}$ is reached, where $I(t)$ gradually increases again. This behavior indicates that no well-defined precursor adlayer is formed. Instead, the data suggest a slower more continuous layer growth which is in agreement with the XRR observations and the slower growth of the bulk deposit in this system (see below).

The kinetics of the structural transitions at the Hg-electrolyte during such sweeps are complicated and depend on the precise conditions of the potential sweep and the sample history. The pronounced intensity changes in Br- and Cl-containing solution are only observed in potential sweeps where the sample was previously kept in the de-amalgamation regime. For CVs, starting on the pristine Hg electrode, corresponding intensity changes were found at similar potentials but of much smaller magnitude. Furthermore, in the transition region, $I(t)$ occasionally exhibited strong fluctuations. Similar observations were made in PbFBr nucleation and growth and could be explained by the lateral movement of deposit islands floating on the liquid Hg surface and electrocapillary effects, resulting in long-range mechanical deformation of the liquid electrode.[33]

4.3.4 Growth of bulk deposits at the liquid metal interface

Before we investigate the atomic-scale arrangement within the adlayer in more detail, we first discuss observations on thicker deposits, as they provide valuable clues to the adlayers composition and structure. Such deposits were formed after keeping the potential for longer times positive of $E_{Pb/Pb2+}$ and could be optically detected. Characteristic microscope images of the deposited film are shown in Figure 4.4. Clear differences in the deposit morphology formed in the three systems under identical conditions are found. In Br-containing electrolyte (Figure 4.4a), the deposit appears rough but uniform; in Cl-containing solution (Figure 4.4b), a smoother film is formed. In contrast to the two former cases, the deposit grown in F-containing electrolyte (Figure 4.4c) consists of isolated micrometer-sized crystals. From the image, an average crystal size of $\sim$35 μm was estimated. The individual crystals did not change their positions in subsequent microscope images, indicating that they were not mobile on the liquid surface but fixed in position relative to each other. This is attributed to the presence of a surrounding much thinner layer that cannot be detected by optical microscopy - most likely the initial adlayer. We note that no

visible bulk deposit (based on optical microscopy and GID data) could be observed in electrolytes containing only 0.12 mM PbF_2.

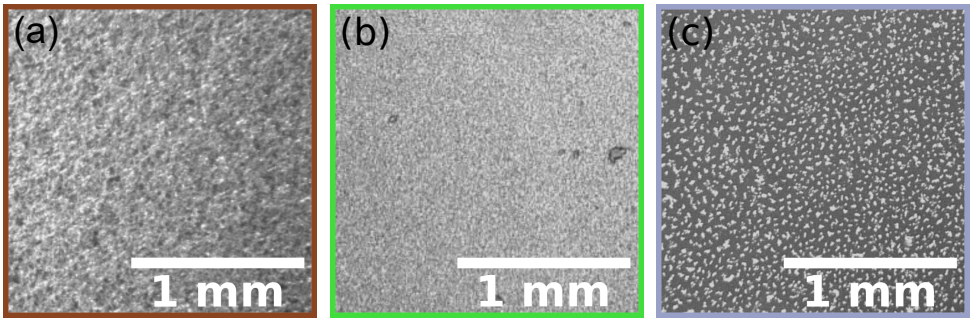

Figure 4.4: Optical microscopy images of the deposits on Hg electrodes formed by 1 h deposition at -0.60 V in 0.01 M NaX + 0.25 mM PbX_2 with X being (a) Br, (b) Cl, and (c) F, respectively.

XRR studies of these bulk deposits were not possible due to the high interface roughness. The deposits were therefore characterized by *in situ* GID measurements, whose results are displayed in Figure 4.5. For Br- and Cl-containing electrolytes, discrete Bragg peaks are observed, indicating that the films consist of crystals with a well-defined orientation along the surface-normal direction (see Figure 4.9).[33] In contrast, only powder rings are detected for deposits grown in F-containing electrolyte, indicating a random orientation of the formed crystals. By integration of the detector intensities at identical $q=\sqrt{q_z^2+q_{||}^2}$, with $q_{||}$ being the lateral wave transfer vector, powder spectra I(q) were generated (Figure 4.104.114.12), which were then used to identify the composition and structure of the crystallites. For this, the diffraction peak patterns were compared to the crystal structures of Pb halides and other Pb-containing compounds (see supporting information).

Based on this analysis, the crystal structures of the deposits in Br- and Cl-containing electrolyte could be unambiguously identified. For the case of Br, an excellent match with orthorhombic Pb(OH)Br (pnma, with a = 7.385 Å , b = 4.085 Å, c = 10.012 Å , ICSD 404573) was found (Figure 4.6). Pb(OH)Br formation in this solution was already reported in similar studies.[48] For Cl-containing solution, orthorhombic Pb(OH)Cl (pnma, with a = 7.111 Å, b = 4.020 Å, c = 9.699 Å, ICSD 28035) provides a good match to the GID data.[49,50] Orthorhombic Pb(OH)Br and Pb(OH)Cl exhibit the same crystal structure ('laurionite'), apart from small differences in the bond lengths due to the different halide species. Less clear is the structure formed in F-containing electrolyte. Cubic PbF_2 (fm3m, with a = b = c = 6.002 Å, ICSD 201114) shows a possible match but not all observed peaks could be attributed to this compound. Probably a hybrid Pb(OH)F and/or $Pb_xO_yH_z$ structure is present given the lower Gibbs energy for oxides and hydroxides.[51] However, in contrast to the case of Pb(OH)Cl and Pb(OH)Br, there is no Pb(OH)F structure reported in the literature up to date.

With the identified crystal structure in Br- and Cl-containing electrolyte, also the

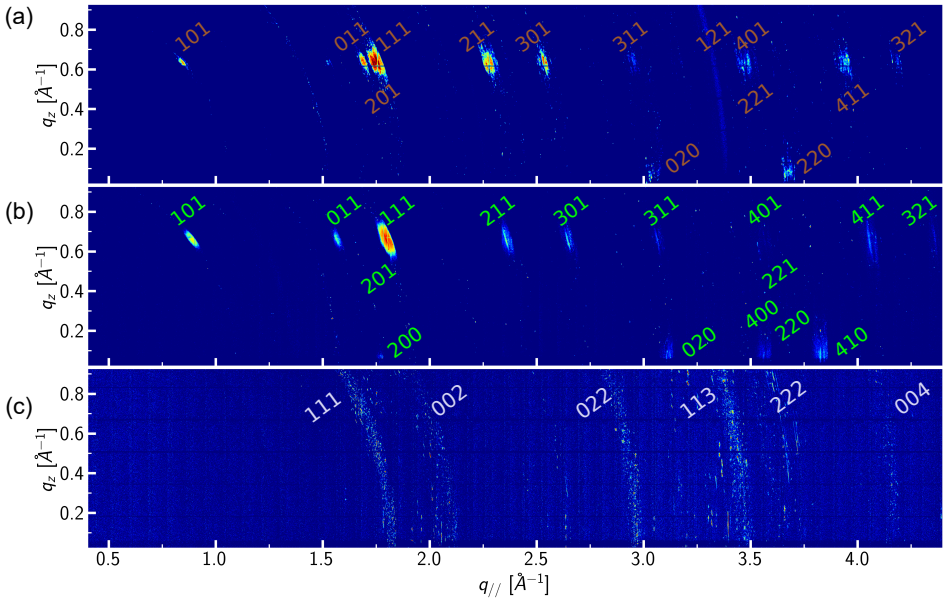

Figure 4.5: X-ray intensity maps of the deposits formed in (a) 0.01 M NaBr + 0.25 mM $PbBr_2$, (b) 0.01 M NaCl + 0.25 mM $PbCl_2$, and (c) 0.01 M NaF + 0.25 mM PbF_2. The GID data were measured at incidence angles of 0.122° and transformed into the reciprocal space coordinates q_z and $q_{//}$. All the experiments were recorded after 1 hour deposition at -0.60 V. The miller indexes of the diffraction peaks for the identified compounds (a) Pb(OH)Br, (b) Pb(OH)Cl, and (c) PbF_2 are given in the maps.

orientation of the crystals along the surface normal can be determined from the intensity maps in Figure 4.5. Here, all Bragg peaks were found at q_z values of 0 (partly cut off by the Hg substrate) and at ∼0.64 Å^{-1}. The latter value is in excellent agreement with that of the (001) peaks in Pb(OH)Br (q_z = 0.63 Å^{-1}) and Pb(OH)Cl (q_z = 0.65 Å^{-1}), indicating a film texture where the c-axis is oriented along the surface normal. All experimentally observed peaks can be assigned to the (*hk0*) and (*hk1*) peaks of crystals in this orientation (see labels in Figure 4.5a,b).

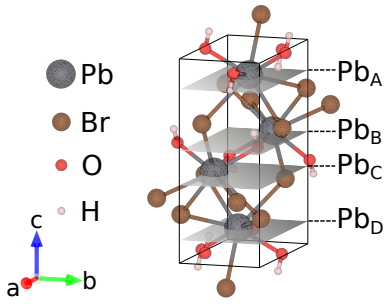

Figure 4.6: Laurionite crystal structure, illustrated for the case of Pb(OH)Br (generated by VESTA[65]).

4.3.5 Structure of the adlayer formed in the de-amalgamation regime

The results obtained on the structure and orientation of the bulk deposits provide a valuable starting point for the determination of the precise structure of the precursor adlayer from the XRR data. Specifically, we assume in the models employed to fit the XRR data that the precursor adlayer consists of the same material and has the quasi-epitaxial orientation as the bulk deposit, as was found in our previous studies of PbFBr growth.[32,33] The results obtained for the three systems are described in the following in the order Br-, Cl-, and F-containing electrolyte. In all fits, the Hg layer spacing d and the layer decay parameter σ_b were kept constant to reduce the number of free fit parameters.

For Br-containing electrolyte, we assume that the precursor adlayer consists of c-axis oriented Pb(OH)Br (see Figure 4.13). However, the modulation period $\Delta q_z \sim 0.95$ Å^{-1} in the XRR curves corresponds to a thickness of roughly $d = 2\ \pi/\Delta q_z \sim 6.6$ Å, which is clearly smaller than a complete Pb(OH)Br unit cell (c =10.012 Å) and indicates that the adlayer is only composed of a fraction of the unit cell. Preliminary fits show clearly that good fits of the XRR data require two pronounced peaks in the electron density profile of the adlayer (Figure 4.7a), which we attribute to 2 atomic planes containing Pb atoms. For a more precise structure determination, various models and structures were tested but only one was able to provide fits that are in excellent agreement with the experimental data (for fits by different models see supporting information). In this successful model, the majority of the adlayer consisted of a section of the Pb(OH)Br unit cell where the Pb planes denoted as A and B (see Figure 4.6 and S6) correspond to the electron density peaks in the adlayer (denoted as Pb(OH)Br$_{ad}$-I in Figure 4.7b). Fits with this adlayer phase alone could not fully describe the data (see Figure 4.14) but a second minority adlayer phase with a relative surface coverage of only 7% as compared to the majority phase was required (denoted as Pb(OH)Br$_{ad}$-II). This second phase had a different termination at the Hg surface, resulting in a smaller vertical distance between the two Pb layers.

The structural parameters obtained for the best fit by this two-phase model are given in Table 4.1.

Here, terminating anion layers of OH and Br were assumed in Pb(OH)Br$_{ad}$-I and Pb(OH)Br$_{ad}$-II, respectively (see Figure 4.7b). For Pb(OH)Br$_{ad}$-I, the distance to the Hg substrate was found to be $d_{Hg-O} = 2.86 \pm 0.03$ Å, which is comparable to typical Hg-O distances of 2.2 to 2.9 Å.[52,53] The distance for the halide-terminated Pb(OH)Br$_{ad}$-II phase was found to be $d_{Hg-Br} = 2.03 \pm 0.10$ Å. This value is slightly smaller than values reported in the literature (2.4 to 2.5 Å).[54,55] It is noted that the presence of these terminating OH or Br anions cannot be directly verified, because their contribution to the total electron density profile is small. Considering only the spacing between the first Pb and the Hg surface layer, which is a robust parameter in the fits, rather similar values are found for the two adlayer phases: 3.30 Å in Pb(OH)Br$_{ad}$-I

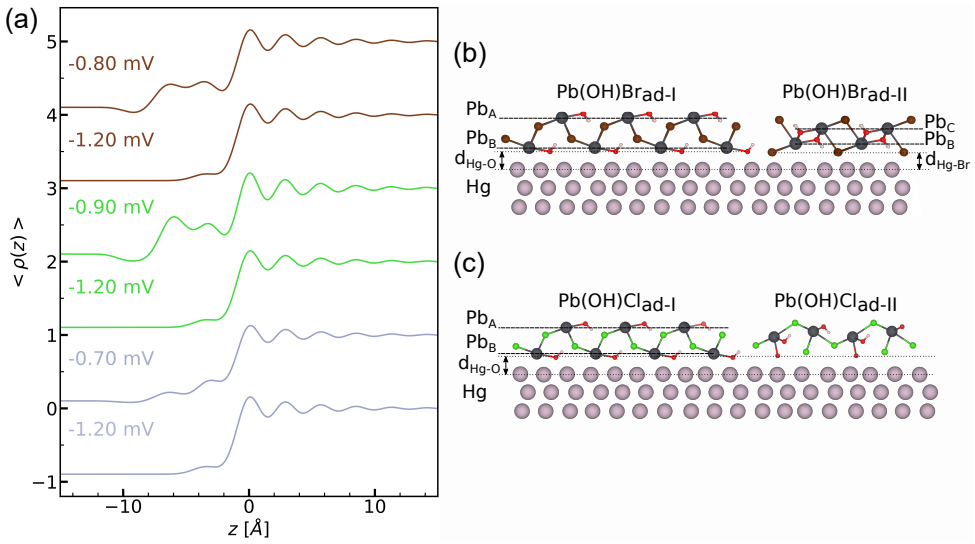

Figure 4.7: (a) Electron density profiles obtained from fits of the XRR measurements in Figure 4.2, corresponding to the interface structure in the potential regime of Pb de-amalgamation in Br (brown), Cl (green), and F (blue) containing electrolyte. (b,c) Structural models used to describe the Hg-electrolyte interface in the presence of Pb-containing adlayers for the case of (b) Br and (c) Cl anions.

and 3.00 Å in Pb(OH)Br$_{ad}$-II. These distances are sufficiently short to allow also for direct bonding of the Pb atoms to the Hg surface. The total surface coverage of the precursor layer (Pb(OH)Br$_{ad}$-I and Pb(OH)Br$_{ad}$-II) is 77% of the whole Hg electrode for the data shown in Figure 4.2 but varied by ±10% in different experiments. Such an incomplete coverage of the Hg surface was also observed for the case of PbFBr precursor adlayers.[32,56] In the remaining surface area, the Hg could either be free of the deposit or covered by three-dimensional Pb(OH)Br bulk deposits, which would not contribute to the features in the XRR. Considering that measurement of an XRR curve requires 60 min., the latter appears more likely.

Structural data on the precursor adlayer formed in Br-containing solution [a]

NaBr + $PbBr_2$	Parameter	-1.20 V	-0.80 V
Hg	σ_i [Å]	1.01±0.01	1.00±0.01
Pb(OH)Br$_{ad}$-I	θ_I		0.72±0.04
	d_{Hg-Br} [Å]		2.03±0.10
Pb(OH)Br$_{ad}$-II	θ_{II}		0.05±0.02
	d_{Hg-O} [Å]		2.86±0.03
Solution	σ_s [Å]		1.00±0.01

Table 4.1: [a] Results obtained from fits of the XRR data in 0.01 M NaBr + 0.25 mM $PbBr_2$ by the models described in the text. Given are the width of the Hg surface layer σ_i, the coverages and distance to the Hg surface layer of the precursor adlayer phases Pb(OH)Br$_{ad}$-I and Pb(OH)Br$_{ad}$-II, and the width of the interface to the electrolyte solution σ_s.

Structural data on the precursor adlayer formed in Cl-containing solution [a]

$NaBr + PbCl_2$	Parameter	-1.20 V	-0.90 V
Hg	σ_i [Å]	1.01±0.01	0.89±0.01
$Pb(OH)Cl_{ad}$-I	θ_I		0.84±0.02
	d_{Hg-O} [Å]		2.63±0.02
$Pb(OH)Cl_{ad}$-II	θ_{II}		0.16±0.02
	d_{Hg-O} [Å]		2.63±0.02
Solution	σ_s [Å]		0.89±0.02

Table 4.2: [a] Results obtained from fits of the XRR data in 0.01 M NaCl + 0.25 mM $PbCl_2$ by the models described in the text. Given are the width of the Hg surface layer σ_i, the coverages and distance to the Hg surface layer of the precursor adlayer phases $Pb(OH)Br_{ad}$-I and $Pb(OH)Br_{ad}$-II, and the width of the interface to the electrolyte solution σ_s.

For the adlayer formed in Cl-containing electrolyte, analogue results were obtained (Table 4.2).

Also here, a good fit was only possible by a mixture of two different surface phases (see supporting information). The phase with the larger coverage (denoted $Pb(OH)Cl_{ad}$-I) corresponds to the majority phase found in the Pb(OH)Br adlayer, i.e., c-axis oriented Pb(OH)Cl that is terminated by OH at the Hg surface (see Figure 4.7c and 4.15). In contrast to the case of Pb(OH)Br, the second phase cannot be described by a similar c-axis oriented Pb(OH)Cl phase with different surface termination. In particular, all successful fits of the corresponding XRR require that the peak in the electron density profile facing the electrolyte is more pronounced than the peak facing the Hg surface (see Figure 4.7a and 4.16). This can be accomplished by structures where the outer peak is composed of two closely spaced Pb layers. A phase that would fulfill this requirement is a Pb(OH)Cl adlayer that is oriented with the a-axis along the surface normal (Figure 4.7c, $Pb(OH)Cl_{ad}$-II). Excellent fits with this model are possible, with the distance between the terminating OH layer and the Hg surface layer being identical to that in $Pb(OH)Cl_{ad}$-I. However, also models where this $Pb(OH)Cl_{ad}$-II minority phase contains an additional Pb layer at the Hg surface (with d_{Pb-Hg} = 2.83 Å) or have different Hg-O distances describe the data well. It is further noted that a good fit can also be obtained by models that assume other crystalline materials as the minority phase, especially c-axis oriented $PbO(H_2O)$. However, the GID data exclude the presence of a similarly oriented $PbO(H_2O)$ bulk phase. Furthermore, formation of a $PbO(H_2O)$ adlayer would also be expected in the Br- and F-containing electrolyte, which was not observed. Thus, this alternative explanation does not seem likely.

Description of the adlayer formed in 0.1 M NaF + 0.12 mM PbF_2 was even more difficult than in the Cl- and Br-system. Since the crystal structure of the formed bulk deposit is unclear and the deposit is powder-like, it was not possible to model the adlayer by assuming the same composition and orientation as within the three-dimensional crystals. We therefore employed a more general approach describing

Structural data on the adlayer formed in F-containing solution [a]

$NaBr + PbF_2$	Parameter	-1.20 V	-0.70 V
Hg	σ_i [Å]	1.00±0.01	1.03±0.01
Pb Layer 1	ρ_1		0.96±0.06
	d_{Hg-1} [Å]		3.10±0.10
	σ_1 [Å]		1.10±0.15
Pb Layer 2	ρ_2		0.47±0.15
	d_{12} [Å]		3.09±0.11
	σ_2 [Å]		1.20±0.22
Pb Layer 3	ρ_3		0.13±0.06
	d_{23} [Å]		1.35±0.12
	σ_3 [Å]		1.28±0.23
Solution	σ_s [Å]		1.40±0.28

Table 4.3: [a] Results obtained from fits of the XRR data in 0.01 M FCl + 0.12 mM PbF_2 by the models described in the text. Given are the width of the Hg surface layer σ_i, the coverages, widths, and distances of the Gaussian layers assigned to Pb, and the width of the interface to the electrolyte solution σ_s.

the adlayer by simple Gaussian peaks in the electron density profile without any assumption of the corresponding chemical species. As discussed above, the main contribution to these peaks will come from the strongly scattering Pb atoms, whereas the contributions of O and F will be negligible. We thus denote these Gaussian peaks in the following as Pb layers. Reasonable fits of the experimental XRR curves could only be obtained by a series of three Pb layers that decayed in intensity (by a factor >7 from the first to the third Pb layer) and increased in width from the Hg surface towards the electrolyte (see Figure 4.7a, Table 4.3 and 4.17).

Deconvolution of the Pb layer by the width of the Hg surface layer σ_i, which is dominated by the capillary wave width, results in effective widths of 0.34 Å for the first, 0.62 Å for the second, and 0.76 Å for the third Pb layer. These observations indicate that in contrast to the Pb(OH)Br and Pb(OH)Cl adlayers, the ordering along the surface normal direction rapidly decays. The distance of the first Pb layer to the Hg surface (3.10 Å) is comparable to that in the two other systems. The distance between Pb layer 1 and 2 (3.09 Å) differs by only 3% from that of the Pb planes in a PbF_2 cubic structure, but the much shorter distance between Pb layers 2 and 3 cannot be explained by a PbF_2 phase. However, the two distances are similar to those found between the Pb layers in Pb(OH)Br and Pb(OH)Cl. The observed adlayer could hence correspond to a mixture of PbF_2 and of Pb(OH)F with laurionite crystal structure, although the latter phase has hitherto not been observed in the bulk.

As mentioned above, only the vertical position of the first Pb layer is reasonably well localized, whereas the following layers already have a rather large width. Thus, a coexistence of crystallites with different orientation is possible, which would be in agreement with the powder-like bulk deposit structure in F-containing electrolyte.

In total, the XRR data in electrolyte containing exclusively F anions suggest that instead of a well-defined precursor adlayer only thin crystallites of a three-dimensional deposit are formed in solution containing 0.12 mM PbF_2. This is supported by experiments showing that subsequently recorded XRR curves in this solution are not stable but continuously change with time (Figure4.18). This indicates slow, kinetically limited growth of the deposit, which is in accordance with the absence of bulk crystallite formation in the optical microscopy and GID studies. At higher PbF_2 concentration, no distinct adlayer formation but only bulk deposition was found, which further supports this scenario.

4.4 Discussion

4.4.1 Mechanism of Pb halide growth at the liquid Hg interface

The structural data obtained from the *in situ* X-ray scattering studies reveal fundamental differences in the phase formation processes found in the presence of Br and Cl anions as compared to those in the presence of F anions alone. Before discussing the origin of these differences, we first consider the general mechanism of Pb halide formation on the Hg surface. We assume that this occurs by a controlled precipitation of these ionic compounds that is triggered by electrochemically induced de-amalgamation, as suggested in our previous studies of PbFBr formation.[32,33] Here, at potentials negative of $E_{Pb/Pb2+}$, Pb^{2+} is first electrochemically reduced to Pb atoms on the Hg surface, which are then dissolved in the Hg bulk, resulting in accumulation of Pb in the near-surface region of the liquid metal. Upon increasing the potential into the de-amalgamation regime, the dissolved Pb is rapidly released into the electrolyte. This release leads to supersaturation of Pb^{2+} ions in the electrolyte close to the electrode surface, up to a point where the Pb^{2+} concentration exceeds the solubility product of the Pb halide compounds. As a result, nucleation and growth of crystallites of these compounds commence.

In principle, this growth occurs by a purely chemical mechanism in solution and the main role of the electrochemical process is to provide a sufficient local Pb^{2+} ion concentration. In the absence of specific interactions with the Hg-electrolyte interface, one would therefore expect a randomly oriented, powder-like deposit. This type of behavior seems indeed to be the case in NaF + PbF_2 solution, where our data indicate direct nucleation and growth of poorly ordered, three-dimensional crystallites. In the presence of Cl or Br anions in solution, however, Pb halide growth proceeds by a different route, as shown by our observations in NaCl + $PbCl_2$ and NaBr + $PbBr_2$ solution as well as our earlier results in NaF + $PbBr_2$ electrolyte[32,33]. Specifically, we find in all these systems a well-defined texture of the bulk deposit, where the crystals are oriented with the c-axis parallel to the surface normal direction. This quasi-epitaxial growth indicates a steering role of the Hg substrate in the crystal growth.

The XRR measurements demonstrate that the occurrence of oriented crystal growth is strongly linked to the formation of well-defined precursor adlayers in the initial stages of the deposition process. For Pb(OH)Br and PbFBr formation, the precursors are c-axis oriented crystalline films with a thickness of two Pb atomic layers, i.e., two formula units of the Pb halide compound. The subsequent quasi-epitaxial growth of c-axis oriented Pb(OH)Br and PbFBr, respectively, merely constitutes a continuation of these ultrathin crystals and thus is easily explained. For Pb(OH)Cl growth, the same reasoning holds true for the majority adlayer phase Pb(OH)Cl_{ad}-I, which is structurally analogue to the Pb(OH)Br_{ad}-I phase. The further vertical growth of the minority phase Pb(OH)Cl_{ad}-II seems to be kinetically hindered, as bulk crystallites with the same orientation as in Pb(OH)Cl_{ad}-II were not observed in the GID measurements. The precise reasons for that are not clear at present and require further studies. Based on the microscopy investigations, which show that the entire Hg surface is covered by the Pb(OH)Cl film after longer deposition times, the surface areas covered by the Pb(OH)Cl_{ad}-II phase are either converted into Pb(OH)Cl_{ad}-I or overgrown by lateral growth of the oriented Pd(OH)Cl bulk crystals. The preferred growth of certain crystal orientations on cost of less favorable oriented nuclei is a well-known phenomena in thin film deposition and encountered for example in columnar growth.

4.4.2 Role of the anion species in precursor adlayer formation

Having established that the existence of well-oriented precursor adlayers is the reason for quasi-epitaxial growth, we now address the origin of precursor adlayer formation. According to our data these adlayers form in the presence of Cl and Br anions but not in electrolytes containing only F (and OH) anions. Chloride and bromide are known as electronically polarizable ('soft') anion species that strongly chemisorb on metal surfaces. Specifically, the specific adsorption, i.e., chemical binding, of Cl and Br on Hg electrodes is known since the early days of interfacial electrochemistry.[57,58] In contrast, fluoride is a 'hard' anion with strongly bound hydration shell and known for its non-specific adsorption on Hg. Consequently, F anions only reside as hydrated, electrostatically bound species in the outer Helmholtz plane whereas Cl and Br form chemisorbed adlayers on Hg, which can reach considerable coverages at potentials positive of the potential of zero charge. In our previous studies,[32,33] we proposed that these chemisorbed anions stabilize coadsorbed Pb^{2+} counter ions on the surface. The latter carry twice the charge as the halide and thus attract further ions until charge neutrality is reached after in total five atomic layers, with the last one being a terminating anion layer.

For the systems studied in the present work, the scenario is in principle similar but the detailed explanation of the formed adlayer structure is more difficult. This is mainly caused by the more complex crystal structure of Pb(OH)Br and Pb(OH)Cl, which result from the presence of OH and cannot be understood from simple isotropic

ion-ion interactions alone. As an example, we briefly consider the majority adlayer phases, which will be most important phases for the subsequent quasi-epitaxial growth. Here, the Pb atoms in the two cation layers are interlinked by a buckled layer, composed of Br anions with an in-plane square arrangement (Figure 4.7b and Figure 4.13). This structure results from the space requirements of the Br-bound OH groups, which are located slightly above and below the Pb planes, respectively. The inner Pb layer appears to be directly adsorbed on the Hg surface layer rather than bound via an intermediate halide adlayer. In contrast, the minority phase Pb(OH)Br_{ad}-II involves adsorbed Br at the liquid Hg electrode.

Obviously, the stabilization of defined precursor adlayers by coadsorbed cations is possible in a variety of atomic arrangements on the liquid metal surface. This is in agreement with the well-known formation of mixed chemisorbed layers of anions and cations on solid metal electrodes (see Ref. [59] for an overview). Here, it has been shown that these species can mutually stabilize themselves on the electrode surface. Particularly insightful are *in situ* X-ray surface scattering studies of Wang and coworkers that reported the presence of mixed adlayers of halides with Tl or Pb on Au (111) electrodes in acidic electrolyte.[60–62] These systematic studies reported a complex potential-dependent sequence of differently ordered adlayer structures, in which the stoichiometry changed stepwise from a purely metallic adlayer to a pure halide layer. In an intermediate potential range, various mixed phases were found, including phases with a square 1:1 arrangement of halide and metal. The halide was either coadsorbed with the metal species on the Au surface or resided on top of the adsorbed metal layer. In both cases, the ad-metal is stabilized on the electrode surface at much more positive potentials as in halide-free electrolyte. For Pb in Br-containing solution the transition between the different mixed adlayer phases was slow, resulting in long-term coexistence of those phases.[62] All these observations closely resemble our findings for the precursor adlayers on liquid Hg electrodes. The main differences are the presence of a second anion species in the adlayer (F or OH) and its larger vertical extension, i.e., the presence of 2 Pb and several anion layers. The former difference can be related to the coexistence of two anions in the electrolyte and an apparently lower Gibbs energy of formation of these compounds as compared to more simple salts, such as $PbBr_2$ or $PbCl_2$.[32] The larger vertical extension was attributed in Ref. [32] to electrostatic effects, resulting from the different charges of the Pb^{2+} and the monovalent anions and the need to achieve charge neutrality in the adlayer. A similar reasoning can be applied to the precursor adlayer phases observed in this study.

Within the scenario described above, the tendency towards precursor adlayer formation should increase with increasing Gibbs energy of adsorption of the halide on

the Hg electrode, i.e., in the order F < Cl < Br. This is indeed found in potential-dependent XRR studies, which show that both formation and dissolution of the adlayer start to shift in the same order towards more negative potentials. For example, the onset of dissolution in the negative potential scans of the experiments in Figure 4.3 starts in F-containing solution at -0.80 V, i.e., directly at $E_{Pb/Pb2+}$, in Cl-containing solution at -1.0 V, and in Br-containing solution at -1.1 V. This supports our assumption that chloride and bromide stabilize Pb-containing precursor adlayers on the Hg surface in a wide potential range, from the Pb amalgamation up to the de-amalgamation regime, where Pb dissolution into the bulk Hg or Pb^{2+} desorption would be expected, respectively. In contrast, fluoride anions do not lead to any stabilization and therefore only bulk precipitates without a defined orientation towards the interface are formed. The kinetics of adlayer formation and dissolution exhibits this trend too, resulting in faster and more facile formation with increasing chemisorption strength of the halide anion.

4.5 Conclusion

Our *in situ* X-ray scattering studies show that in deposition at liquid metal - electrolyte interfaces, chemisorbing ions, such as chloride and bromide, can serve as surfactants that promote the growth of strongly textured deposits. This behavior can be linked to the formation of well-defined ultrathin precursor adlayers of the deposited compounds that serve as nuclei for the subsequent quasi-epitaxial growth of oriented crystals of the bulk phase. The mechanistic scenario proposed for this process should be valid for many materials, provided they contain species that chemisorb at the interface but are poorly solvable in the liquid metal. The stability and ease of formation of the precursor adlayers scales with the strength of the chemisorption. Even stronger tendencies for precursor adlayer formation and quasi-epitaxial growth are therefore expected in the presence of iodide or sulfide anions. This opens up interesting possibilities for the preparation of technologically interesting compound semiconductors. Already the Pb(OH)Br phase is interesting in that respect, as it was shown to be chemically convertible into a perovskite material for resistive memory devices;[63] for PbI perovskites an even larger range of potential applications exists.

The growth-steering effects at interfaces to liquid metals and the resulting deposit texture are stronger than those found at other liquid-liquid interfaces, such as interfaces between aqueous and non-aqueous solutions.[64] One important reason for this are the strong chemical interactions of many species with metal surfaces. These lead to strongly bound adsorbate layers with a high surface coverage, which promote the formation of oriented precursor adlayers. In addition, the high surface tension of liquid metals results in atomically smooth interfaces, providing ideal substrates. Because of these properties, growth at liquid metal interfaces is an interesting route for the formation of crystalline nanomaterials and thin films. The mechanistic insights

obtained in this work may help in developing these deposition processes and tuning them, e.g., towards higher crystallinity and optimized morphology. Specifically, precursor-mediated growth may also allow to further improve emerging methods employing liquid metals, such as electrochemical liquid-liquid-solid deposition.

4.6 Methods

X-ray reflectivity and GID studies were performed using the LISA liquid interface diffractometer at beamline P08 of PETRA III (DESY). An X-ray energy of 25 keV was chosen to have acceptable counts despite the strong X-ray absorption by the electrolyte. All data were collected with a two-dimensional X-ray detector with 55 μm pixel size (X-Spectrum Lambda 750k GaAs). The acceptance of the detector to integrate the intensity for XRR was 0.35° vertically and 0.06° horizontally, the background subtraction was calculated by offsetting the ROI horizontally with the same acceptance by 0.06°. For the GID studies of the bulk deposit structure, the incident angle was fixed at 0.122°, corresponding to 85 % of the critical angle for the system. An in-plane scan of the detector with 50 images was recorded (with 30 s counting time, 0.40° intervals). From each image, the background, obtained by an identical scan performed before the deposition, was subtracted, and the resulting 50 images were then binned with a $q_{//}$ resolution between $5{\cdot}10^{-3}$ and $5{\cdot}10^{-4}$ Å^{-1}.

The experiments were performed in a dedicated electrochemical sample environment, which is described in detail in the supplementary information. It consisted of a sealed PEEK cell, with an upper quartz window that provides optical access for the microscope camera (Basler ACE acA1600-20gm with OPTEM Fusion motorised Zoomsystem). The cell contains a liquid mercury pool (Chempur, 99.999+%) of 23.7 cm^2 surface area with a Pt wire contact and approximately 55 mL of the electrolyte. A Hg/Hg2SO4 (Schott) reference electrode, a Pt counter electrode, and a Ametek Solartron Analytical potentiostat (Modulab 2101A) were used for potential control. All potentials mentioned in this publication are given relative to Hg/Hg2SO4. The sample cell parts that were in contact with the sample were previously soaked for at least 6 hours in caroic acid, a 3:1 solution of sulfuric acid and hydrogen peroxide, and then sonicated and rinsed with Milli-Q water prior to sample preparation. To clean the PEEK components a 20-30% caroic solution was used to avoid dissolution of the cell material. The electrolyte solutions were prepared from NaF (Alfa Aesar Puratronic®, 99.995%), NaCl (ChemPur, 99.999 %), NaBr (Merck Suprapur® 99.995%), PbF_2 (abcr, Puratronic®, 99.997%), $PbCl_2$ (ChemPur, 99.999 %), $PbBr_2$ (Alfa Aesar Puratronic®, 99.998%), and Milli-Q water. They were purged with N_2 gas for at least 30 min before injecting them in the cell to remove O_2 dissolved in the electrolyte. After initial sample characterization in the pure NaX base electrolyte, the electrolyte was exchanged by flowing 500 ml of NaX + Pb_2X solution through the cell, i.e., more than 9 times the cell volume. All experiments were performed at room temperature (22.5 °C).

ASSOCIATED CONTENT

Additional information on experimental procedures and analysis methods, additional figures, and additional tables are given in the supporting information.

AUTHOR INFORMATION

Corresponding Author

* magnussen@physik.uni.kiel.de, murphy@physik.uni.kiel.de

Present Addresses

† Mitsubishi Electric Corporation, Advanced Technology R&D Center, 8-1-1 Tsukaguchi-Honmachi, Amagasaki 661-8661, Japan

Author Contributions

The manuscript was written through the contributions of all authors. All authors have given approval to the final version of the manuscript.

Funding Sources

The research was supported by the DFG through project MA 1618/18 and funding for LISA by the BMBF through project K16FK1/K19FK2.

Aknowledgment

The authors acknowledge financial support by the DFG through project MA 1618/18 and funding for LISA by the BMBF through project 05K16FK1/05K19FK2. We acknowledge DESY (Hamburg, Germany), a member of the Helmholtz Association HGF, for the provision of experimental facilities. Parts of this research were carried out at PETRA III and we would like to thank Florian Bertram and Rene Kirchhof for assistance in using P08 and Milena Lippmann for her assistance in using the PETRA III chemistry laboratory. Beamtime was allocated for proposals I-20200512, I-20180496 and II-20170014. Furthermore, we would like to thank Wulf Depmeier for his feedback on laurionite crystal structure.

4.7 References

(1) Shpyrko Oleg G.; Streitel Reinhard; Balagurusamy S. K. Venkatachalapathy; Grigoriev Y. Alexei; Deutsch Moshe; Ocko M. Benjamin; Meron Mati; Lin Binhua; Pershan S. Peter. Surface Crystallization in a Liquid AuSi Alloy. *SCIENCE* **2006**, *313*, 77-80.

(2) Cui, Y.; Liang, F.; Yang, Z.; Xu, S.; Zhao, X.; Ding, Y.; Lin, Z.; Liu, J. Metallic Bond-Enabled Wetting Behavior at the Liquid Ga/CuGa2 Interfaces. *ACS Applied*

Materials and Interfaces **2018**, *10* (11), 9203-9210.
https://doi.org/10.1021/acsami.8b00009.

(3) Elsen, A.; Murphy, B. M.; Ocko, B. M.; Tamam, L.; Deutsch, M.; Kuzmenko, I.; Magnussen, O. M. Surface Layering at the Mercury-Electrolyte Interface. *Physical Review Letters* **2010**, *104* (10), 105501.
https://doi.org/10.1103/PhysRevLett.104.105501.

(4) Dickey, M. D. Emerging Applications of Liquid Metals Featuring Surface Oxides. *ACS Applied Materials and Interfaces* **2014**, *6* (21), 18369-18379.
https://doi.org/10.1021/am5043017.

(5) Daeneke, T.; Khoshmanesh, K.; Mahmood, N.; de Castro, I. A.; Esrafilzadeh, D.; Barrow, S. J.; Dickey, M. D.; Kalantar-Zadeh, K. Liquid Metals: Fundamentals and Applications in Chemistry. *Chemical Society Reviews*. Royal Society of Chemistry June 7, 2018, pp 4073-4111.
https://doi.org/10.1039/c7cs00043j.

(6) Song, H.; Kim, T.; Kang, S.; Jin, H.; Lee, K.; Yoon, H. J. Ga-Based Liquid Metal Micro/Nanoparticles: Recent Advances and Applications. *Small* **2020**, *16* (12), 1903391.

(7) Siegel, A. C.; Tang, S. K. Y.; Nijhuis, C. A.; Hashimoto, M.; Phillips, S. T.; Dickey, M. D.; Whitesides, G. M. Cofabrication: A Strategy for Building Multicomponent Microsystems. *Accounts of Chemical Research* **2010**, *43* (4), 518-528.
https://doi.org/10.1021/ar900178k.

(8) Ma, K. Q.; Liu, J. Nano Liquid-Metal Fluid as Ultimate Coolant. *Physics Letters A* **2007**, *361* (3), 252-256.
https://doi.org/10.1016/J.PHYSLETA.2006.09.041.

(9) Hammock, M. L.; Chortos, A.; Tee, B. C. K.; Tok, J. B. H.; Bao, Z. 25th Anniversary Article: The Evolution of Electronic Skin (E-Skin): A Brief History, Design Considerations, and Recent Progress. *Advanced Materials* **2013**, *25* (42), 5997-6038.
https://doi.org/10.1002/adma.201302240.

(10) Rashed Khan, M.; Hayes, G. J.; So, J. H.; Lazzi, G.; Dickey, M. D. A Frequency Shifting Liquid Metal Antenna with Pressure Responsiveness. *Applied Physics Letters* **2011**, *99* (1).
https://doi.org/10.1063/1.3603961.

(11) Ren, L.; Zhuang, J.; Casillas, G.; Feng, H.; Liu, Y.; Xu, X.; Liu, Y.; Chen, J.; Du, Y.; Jiang, L.; Dou, S. X. Nanodroplets for Stretchable Superconducting Circuits. *Advanced Functional Materials* **2016**, *26* (44), 8111-8118.
https://doi.org/10.1002/adfm.201603427.

(12) Vetrovec, J.; Litt, A. S.; Copeland, D. A.; Junghans, J.; Durkee, R. Liquid Metal Heat Sink for High-Power Laser Diodes. In *High-Power Diode Laser Technology and*

Applications XI; SPIE, 2013; Vol. 8605, p 86050E.
https://doi.org/10.1117/12.2005357.

(13) Liang, S. T.; Wang, H. Z.; Liu, J. Progress, Mechanisms and Applications of Liquid-Metal Catalyst Systems. *Chemistry - A European Journal*. Wiley-VCH Verlag December 3, 2018, pp 17616-17626.
https://doi.org/10.1002/chem.201801957.

(14) Tan, S. C.; Gui, H.; Yang, X. H.; Yuan, B.; Zhan, S. H.; Liu, J. Comparative Study on Activation of Aluminum with Four Liquid Metals to Generate Hydrogen in Alkaline Solution. *International Journal of Hydrogen Energy* **2016**, *41* (48), 22663-22667.
https://doi.org/10.1016/J.IJHYDENE.2016.10.090.

(15) Carim, A. I.; Collins, S. M.; Foley, J. M.; Maldonado, S. Benchtop Electrochemical Liquid-Liquid-Solid Growth of Nanostructured Crystalline Germanium. *Journal of the American Chemical Society* **2011**, *133* (34), 13292-13295.
https://doi.org/10.1021/ja205299w.

(16) Gu, J.; M. Collins, S.; I. Carim, A.; Hao, X.; M. Bartlett, B.; Maldonado, S. Template-Free Preparation of Crystalline Ge Nanowire Film Electrodes via an Electrochemical Liquid-Liquid-Solid Process in Water at Ambient Pressure and Temperature for Energy Storage. *Nano Letters* **2012**, *12* (9), 4617-4623.
https://doi.org/10.1021/nl301912f.

(17) Fahrenkrug, E.; Gu, J.; Jeon, S.; Alexander Veneman, P.; S. Goldman, R.; Maldonado, S. Room-Temperature Epitaxial Electrodeposition of Single-Crystalline Germanium Nanowires at the Wafer Scale from an Aqueous Solution. *Nano Letters* **2014**, *14* (2), 847-852.
https://doi.org/10.1021/nl404228z.

(18) DeMuth, J.; Ma, L.; Lancaster, M.; Acharya, S.; Cheek, Q.; Maldonado, S. Eutectic-Bismuth Indium as a Growth Solvent for the Electrochemical Liquid-Liquid-Solid Deposition of Germanium Microwires and Coiled Nanowires. *Crystal Growth & Design* **2018**, *18* (2), 677-685.
https://doi.org/10.1021/acs.cgd.7b01036.

(19) Fahrenkrug, E.; Maldonado, S. Electrochemical Liquid-Liquid-Solid (Ec-LLS) Crystal Growth: A Low-Temperature Strategy for Covalent Semiconductor Crystal Growth. *Accounts of Chemical Research* **2015**, *48* (7), 1881-1890.
https://doi.org/10.1021/acs.accounts.5b00158.

(20) Zeng, M.; Tan, L.; Wang, J.; Chen, L.; H. Rümmeli, M.; Fu, L. Liquid Metal: An Innovative Solution to Uniform Graphene Films. *Chemistry of Materials* **2014**, *26* (12), 3637-3643.
https://doi.org/10.1021/cm501571h.

(21) Zeng, M.; Li, L.; Zhu, X.; Fu, L. A Liquid Metal Reaction System for Advanced Material Manufacturing. *Accounts of Materials Research* **2021**, *2* (8), 669-680. https://doi.org/10.1021/accountsmr.1c00101.

(22) Jankowski, M.; Saedi, M.; la Porta, F.; Manikas, A. C.; Tsakonas, C.; Cingolani, J. S.; Andersen, M.; de Voogd, M.; van Baarle, G. J. C.; Reuter, K.; Galiotis, C.; Renaud, G.; Konovalov, O. v.; Groot, I. M. N. Real-Time Multiscale Monitoring and Tailoring of Graphene Growth on Liquid Copper. *ACS Nano* **2021**, *15* (6), 9638-9648. https://doi.org/10.1021/acsnano.0c10377.

(23) Zavabeti, A.; Ou, J. Z.; Carey, B. J.; Syed, N.; Orrell-Trigg, R.; Mayes, E. L. H.; Xu, C.; Kavehei, O.; O'mullane, A. P.; Kaner, R. B.; Kalantar-Zadeh, K.; Daeneke, T. *A Liquid Metal Reaction Environment for the Room-Temperature Synthesis of Atomically Thin Metal Oxides*; 2017; Vol. 358.

(24) Carim, A. I.; Collins, S. M.; Foley, J. M.; Maldonado, S. Benchtop Electrochemical Liquid-Liquid-Solid Growth of Nanostructured Crystalline Germanium. *Journal of the American Chemical Society* **2011**, *133* (34), 13292-13295. https://doi.org/10.1021/ja205299w.

(25) Fahrenkrug, E.; Gu, J.; Maldonado, S. Electrodeposition of Crystalline GaAs on Liquid Gallium Electrodes in Aqueous Electrolytes. *Journal of the American Chemical Society* **2013**, *135* (1), 330-339. https://doi.org/10.1021/ja309476x.

(26) Pattadar, D.; Cheek, Q.; Sartori, A.; Zhao, Y.; Giri, R. P.; Murphy, B.; Magnussen, O.; Maldonado, S. Evidence for Facilitated Surface Transport during Ge Crystal Growth by Indium in Liquid Hg-In Alloys at Room Temperature. *Crystal Growth and Design* **2021**, *21* (3), 1645-1656. https://doi.org/10.1021/acs.cgd.0c01485.

(27) DeMuth, J.; Fahrenkrug, E.; Maldonado, S. Controlling Nucleation and Crystal Growth of Ge in a Liquid Metal Solvent. *Crystal Growth & Design* **2016**, *16* (12), 7130-7138. https://doi.org/10.1021/acs.cgd.6b01360.

(28) Zhang, T.; Fahrenkrug, E.; Maldonado, S. Electrochemical Liquid-Liquid-Solid Deposition of Ge at Hg Microdroplet Ultramicroelectrodes. *Journal of The Electrochemical Society* **2016**, *163* (9), D500-D505. https://doi.org/10.1149/2.0691609jes.

(29) DeMuth, J.; Ma, L.; Fahrenkrug, E.; Maldonado, S. Electrochemical Liquid-Liquid-Solid Deposition of Crystalline Gallium Antimonide. *Electrochimica Acta* **2016**, *197*, 353-361. https://doi.org/ https://doi.org/10.1016/j.electacta.2015.10.163.

(30) Downes, N.; Cheek, Q.; Maldonado, S. Electroreduction of Perchlorinated Silanes for Si Electrodeposition. *Journal of The Electrochemical Society* **2021**, *168* (2), 022503. https://doi.org/10.1149/1945-7111/abda58.

(31) Cheek, Q.; Fahrenkrug, E.; Hlynchuk, S.; Alsem, D. H.; Salmon, N. J.; Maldonado, S. In Situ Transmission Electron Microscopy Measurements of Ge Nanowire Synthesis with Liquid Metal Nanodroplets in Water. *ACS Nano* **2020**, *14* (3), 2869-2879.
https://doi.org/10.1021/acsnano.9b06468.

(32) Elsen, A.; Festersen, S.; Runge, B.; Koops, C. T.; Ocko, B. M.; Deutsch, M.; Seeck, O. H.; Murphy, B. M.; Magnussen, O. M. In Situ X-Ray Studies of Adlayer-Induced Crystal Nucleation at the Liquid-Liquid Interface. *Proceedings of the National Academy of Sciences of the United States of America* **2013**, *110* (17), 6663-6668.
https://doi.org/10.1073/pnas.1301800110.

(33) Festersen, S.; Runge, B.; Koops, C.; Bertram, F.; Ocko, B.; Deutsch, M.; Murphy, B. M.; Magnussen, O. M. Nucleation and Growth of PbBrF Crystals at the Liquid Mercury-Electrolyte Interface Studied by Operando X-Ray Scattering. *Langmuir* **2020**, *36* (37), 10905-10915.
https://doi.org/10.1021/acs.langmuir.0c01199.

(34) Magnussen, O. M.; Ocko, B. M.; Regan, M. J.; Penanen, K.; Pershan, P. S.; Deutsch, M. *X-Ray Reflectivity Measurements of Surface Layering in Liquid Mercury*; 1995; Vol. 74.

(35) Dimasi, E.; Tostmann, H.; Ocko, B. M.; Pershan, P. S.; Deutsch, M. *RAPID COMMUNICATIONS PHYSICAL REVIEW B 15 NOVEMBER 1998-II VOLUME*; Vol. 58.

(36) Regan, M. J.; Pershan, P. S.; Magnussen, O. M.; Ocko, B. M.; Deutsch, M.; Berman, L. E. *PHYSICAL REVIEW B 1 OCTOBER 1996-II VOLUME*; 1996; Vol. 54.

(37) Regan, M. J.; Tostmann, H.; Pershan, P. S.; Magnussen, O. M.; Dimasi, E.; Ocko, B. M.; Deutsch, M. *PHYSICAL REVIEW B 15 APRIL 1997-II VOLUME*; 1997; Vol. 55.

(38) Regan, M. J.; Kawamoto, E. H.; Lee, S.; Pershan, P. S.; Maskil, N.; Deutsch, M.; Magnussen, O. M.; Ocko, B. M.; Berman, L. E. *Surface Layering in Liquid Gallium: An X-Ray Reflectivity Study*; 1995; Vol. 75.

(39) Tostmann, H.; Dimasi, E.; Pershan, P. S.; Ocko, B. M.; Shpyrko, O. G.; Deutsch, M. *Surface Structure of Liquid Metals and the Effect of Capillary Waves: X-Ray Studies on Liquid Indium*.

(40) Regan, M. J.; Pershan, P. S.; Magnussen, O. M.; Ocko, B. M.; Deutsch, M.; Berman, L. E. *X-Ray Reflectivity Studies of Liquid Metal and Alloy Surfaces*; 1997.

(41) Runge, B.; Festersen, S.; Koops, C. T.; Elsen, A.; Deutsch, M.; Ocko, B. M.; Seeck, O. H.; Murphy, B. M.; Magnussen, O. M. Temperature- and Potential-Dependent

Structure of the Mercury-Electrolyte Interface. *Physical Review B* **2016**, *93* (16), 165408. https://doi.org/10.1103/PhysRevB.93.165408.

(42) Arya, S.; Mahajan, P.; Gupta, R.; Srivastava, R.; Tailor, N. kumar; Satapathi, S.; Sumathi, R. R.; Datt, R.; Gupta, V. A Comprehensive Review on Synthesis and Applications of Single Crystal Perovskite Halides. *Progress in Solid State Chemistry*. Elsevier Ltd December 1, 2020.
https://doi.org/10.1016/j.progsolidstchem.2020.100286.

(43) Yu, B. bin; Chen, Z.; Zhu, Y.; Wang, Y.; Han, B.; Chen, G.; Zhang, X.; Du, Z.; He, Z. Heterogeneous 2D/3D Tin-Halides Perovskite Solar Cells with Certified Conversion Efficiency Breaking 14%. *Advanced Materials* **2021**, *33* (36).
https://doi.org/10.1002/adma.202102055.

(44) Liu, X. K.; Xu, W.; Bai, S.; Jin, Y.; Wang, J.; Friend, R. H.; Gao, F. Metal Halide Perovskites for Light-Emitting Diodes. *Nature Materials*. Nature Research January 1, 2021, pp 10-21.
https://doi.org/10.1038/s41563-020-0784-7.

(45) Peña, M. A.; Fierro, J. L. G. Chemical Structures and Performance of Perovskite Oxides. *Chemical Reviews*. July 2001, pp 1981-2017.
https://doi.org/10.1021/cr980129f.

(46) Murphy, B. M.; Festersen, S.; Magnussen, O. M. The Atomic Scale Structure of Liquid Metal-Electrolyte Interfaces. *Nanoscale* **2016**, *8* (29), 13859-13866.
https://doi.org/10.1039/C6NR01571A.

(47) D'Evelyn, M. P.; Rice, S. A. A Study of the Liquid-Vapor Interface of Mercury: Computer Simulation Results. *The Journal of Chemical Physics* **1983**, *78* (8), 5081-5095.
https://doi.org/10.1063/1.445376.

(48) Yu, Y.; Hou, J.; Zhang, L.; Sun, Q.; Attique, S.; Wang, W.; Xu, X.; Xu, F.; Ci, Z.; Cao, B.; Qiao, X.; Xiao, X.; Yang, S. Ultrastable Laurionite Spontaneously Encapsulates Reduced-Dimensional Lead Halide Perovskites. *Nano Letters* **2020**, *20* (4), 2316-2325.
https://doi.org/10.1021/acs.nanolett.9b04730.

(49) Venetopoulos, C. CH.; Rentzeperis, P. J. The Crystal Structure of Laurionite, Pb(OH)Cl. *Zeitschrift für Kristallographie - Crystalline Materials* **1975**, *141* (1-6), 246-259.

(50) Lutz, H. D.; Beckenkamp, K.; Kellersohn, T.; Möller, H.; Peter, S. Neutron and X-Ray Structure Determination of Laurionite-Type Pb{O(H,D)}X, WithX= Cl, Br, and I, Hydrogen Bonds to Lead(II) Ions as a Hydrogen-Bond Acceptor. *Journal of Solid State Chemistry* **1996**, *124* (1), 155-161.
https://doi.org/10.1006/JSSC.1996.0219.

(51) Wagman, D. D.; Evans, W. H.; Parker, V. B.; Schumm, R. H.; Halow, I. *The NBS Tables of Chemical Thermodynamic Properties. Selected Values for Inorganic and C1 and C2 Organic Substances in SI Units*; National Standard Reference Data System, 1982.

(52) Weil, M.; Puchberger, M.; Baran, E. J. Preparation and Characterization of Dimercury(I) Monofluorophosphate(V), Hg2PO3F: Crystal Structure, Thermal Behavior, Vibrational Spectra, and Solid-State 31P and 19F NMR Spectra. *Inorganic Chemistry* **2004**, *43* (26), 8330-8335.
https://doi.org/10.1021/ic048741e.

(53) Amaro-Estrada, J. I.; Maron, L.; Ramírez-Solís, A. Aqueous Solvation of HgClOH. Stepwise DFT Solvation and Born-Oppenheimer Molecular Dynamics Studies of the HgClOH-(H2O)24 Complex. *Physical Chemistry Chemical Physics* **2014**, *16* (18), 8455-8464.
https://doi.org/10.1039/c3cp55339f.

(54) Frey, M.; Leligny, H.; Ledésert, M. Structure Cristalline Du Solvate Hg Br2 C4H8O. *Bulletin de la Société française de Minéralogie et de Cristallographie* **1971**, *94* (5), 467-470.
https://doi.org/10.3406/bulmi.1971.6610.

(55) Baghan, Z. N.; Salimi, A.; Eshtiagh-Hosseini, H.; Oliver, A. G. *Supporting Information Hydrogen Bond Synthons Affect Coordination Geometry of D10-Metal Halide Complexes: Synthetic Methods, Theoretical Studies and Supramolecular Architectures*; 2021.

(56) Festersen, S.; Runge, B.; Koops, C.; Bertram, F.; Ocko, B.; Deutsch, M.; Murphy, B. M.; Magnussen, O. M. Nucleation and Growth of PbBrF Crystals at the Liquid Mercury-Electrolyte Interface Studied by Operando X-Ray Scattering. *Langmuir* **2020**, *36* (37), 10905-10915.
https://doi.org/10.1021/acs.langmuir.0c01199.

(57) Grahame, C. D.; Parsons, R. Components of Charge and Potential in Inner Region of Electrical Double Layer - Aqueous Potassium Chloride Solutions in Contact with Mercury at 25 Degrees. *Journal of the American Chemical Society* **1961**, *83* (6), 1291-1296.

(58) Lawrence, J.; Parsons, R.; Payne, R. Adsorption of Halides at the Mercury-Water Interface. *Journal of Electroanalytical Chemistry and Interfacial Electrochemistry* **1968**, *16* (2), 193-206.
https://doi.org/10.1016/S0022-0728 (68) 80061-0.

(59) M. Magnussen, O. Ordered Anion Adlayers on Metal Electrode Surfaces. *Chemical Reviews* **2002**, *102* (3), 679-726.
https://doi.org/10.1021/cr000069p.

(60) R. Adžić, R.; X. Wang, J. Bromide Adsorption Induced Formation of Thallium Bromide Adlayers with Varying Composition and Structure on the Au (111) Electrode Surface. *The Journal of Physical Chemistry B* **1998**, *102* (33), 6305-6308.
https://doi.org/10.1021/jp980740i.

(61) Wang, J. X.; Robinson, I. K.; Adžić, R. R. Formation of Well-Ordered Surface Compounds by Coadsorption of Thallium and Bromide on the Au(111) Electrode Surface. *Surface Science* **1998**, *412-413*, 374-383.
https://doi.org/10.1016/S0039-6028(98)00450-6.

(62) X. Wang, J.; K. Robinson, I.; E. DeVilbiss, J.; R. Adžić, R. Structural Trends among Ionic Metal-Halide Adlayers on Electrode Surfaces. *The Journal of Physical Chemistry B* **2000**, *104* (33), 7951-7959.
https://doi.org/10.1021/jp000759x.

(63) Attique, S.; Ali, N.; Khatoon, R.; Ali, S.; Abbas, A.; Yu, Y.; Hou, J.; Cao, B.; Wu, H.; Yang, S. Aqueous Phase Fabrication and Conversion of Pb(OH)Br into a CH3NH3PbBr3perovskite and Its Application in Resistive Memory Switching Devices. *Green Chemistry* **2020**, *22* (11), 3608-3614.
https://doi.org/10.1039/d0gc00878h.

(64) Fan, D.; John Thomas, P.; O'Brien, P. Pyramidal Lead Sulfide Crystallites With High Energy {113} Facets. *Journal of the American Chemical Society* **2008**, *130* (33), 10892-10894.
https://doi.org/10.1021/ja804516q.

(65) Momma, K.; Izumi, F. VESTA 3 for Three-Dimensional Visualization of Crystal, Volumetric and Morphology Data. *Journal of Applied Crystallography* **2011**, *44* (6), 1272-1276.
https://doi.org/10.1107/S0021889811038970.

4.8 Supporting information

S1: Fitting process and model

In order to fit the experimental XRR data the distorted crystal model (DCM) was used. The DCM described the near surface region of a liquid metal by an infinite stack of layers that continuously broaden with increasing distance from the surface. Based on this model, the electron density profile of a simple Hg-electrolyte interface is described by the following equations:

$$\rho_{DCM}(z) = F_{Hg} \otimes \left(\sum_{n=0}^{\infty} \left(\frac{d\,\rho_{Hg}}{\sigma_n \sqrt{2\pi}} \exp\left(-\frac{(z-nd)^2}{2\sigma_n^2} \right) \right) + \frac{\rho_{ad}}{\sigma_{ad}\sqrt{2\pi}} \exp\left(-\frac{(z-z_{ad})^2}{2\,\sigma_{ad}^2} \right) \right) \tag{4.1}$$

with

$$\sigma_n = \sqrt{\sigma_i^2 + n\,\sigma_b^2} \tag{4.2}$$

$$\rho_{electrolyte}\ (z) = F_{H_2O} \otimes \left(\frac{\rho_{H_2O}}{2} \left(1 - \mathrm{erf}\left(\frac{z - z_{H_2O}}{\sigma_{H_2O}} \right) \right) \right) \tag{4.3}$$

$$\frac{\langle \rho(z) \rangle}{\rho_\infty} = \frac{\rho_{DCM}(z) + \rho_{electrolyte}\ (z)}{\rho_{Hg}} \tag{4.4}$$

Here, d describes the interatomic distance between the atomic layers of mercury, σ_i describes the intrinsic width common to all layers, which corresponds to the roughness of the Hg surface layer (n = 0), and σ_b determines the rate by which σ_n increases with n. The second term of the eq. 1 describes an additional Hg adlayer of lower density, which is a typical feature of Hg-vapor and Hg-liquid interfaces.[1–4] ρ_{Hg} and ρ_{H_2O} are the electron density of mercury and water respectively. F_{Hg} and F_{H_2O} are the Fourier transform of the atomic form factor of Hg and H_2O. Using the form factor of water for the description of the electrolyte is justified by the low concentration of the employed solutions.

In the fits of the reflectivity curves in the de-amalgamation potential regime, adlayers of Pb halide compounds were included in the electron density profiles. These typically consisted of several atomic layers of different ionic compounds (Pb, halides, OH) that were placed at defined distances. The electron density contribution of each of these atomic layers is given by:

$$\rho_n(z) = F_n \otimes \left(\frac{\theta}{\sigma_n\sqrt{2\pi}} \exp\left(-\frac{(z-z_n)^2}{2\,\sigma_n^2} \right) \right) \tag{4.5}$$

For the XRR data obtained in Br- or Cl-containing solution, the distances between the positions of the atomic layers z_n and the type of the atomic species (defined by the Fourier transform of the atomic form factor F_n) were fixed to those in the

corresponding bulk compounds described in the main manuscript. The layer widths σ_n were identical for all atomic layers and fixed to that of the Hg surface layer (i.e., $\sigma_n = \sigma_i$). Likewise, all layers were scaled by the same coverage factor θ. In the F-containing solution a more general approach was applied. Here, a sequence of up to three Gaussian with independently fitted densities ρ_n, widths σ_n, and positions z_n, was used (n = 1, 2, 3). The sum of all contribution

$$\frac{\langle \rho(z) \rangle}{\rho_\infty} = \frac{1}{\rho_{Hg}} \left(\rho_{DCM}(z) + \rho_{electrolyte}(z) + \sum_n \rho_n(z) \right) \tag{4.6}$$

was then inserted in the master formula:

$$\frac{R(q_z)}{R_F(q_z)} = \left| \frac{1}{\rho_\infty} \int \frac{d \langle \rho(z) \rangle}{dz} e^{iq_z z} dz \right|^2 \tag{4.7}$$

, where $R_F(q_z)$ is the Fresnel reflectivity of an ideally sharp interface and q_z the scattering vector in surface normal direction. This expression was used to fit the experimental data $R(q_z)$.

The fit model was implemented in a self-written Python code. The first stage of the fit procedure was to fit all the reflectivity of Hg in NaX (X=Br, Cl, F) where the interface is pristine. The average bulk parameters of mercury (σ_b, d) were then used to fit all the rest of the data presented in the manuscript. The first step of each fit was to set a wide range of boundaries for each parameter, by using a global optimization. The obtained values were then employed as starting point for a second fit with a local optimization algorithm. The error function describing the electrolyte solution has only a small effect on the fit of the Hg-electrolyte interface in the absence of a layer. Therefore, also the position of the error function was fixed to the average value.

System	Parameter	-1.20 V	-0.60 V
Common values	d [Å]	2.76	2.76
	σ_b[Å]	0.48	0.48
	z_{H_2O} [Å]	1.50	1.50
0.01 M NaBr	σ_i [Å]	1.01±0.01	0.97±0.01
	ρ_{ad}	0.27±0.01	0.37±0.01
	z_{ad}[Å]	3.51±0.03	3.25±0.04
0.01 M NaCl	σ_i[Å]	1.01±0.01	0.96±0.01
	ρ_{ad}	0.26±0.01	0.35±0.01
	z_{ad} [Å]	3.48±0.05	3.34±0.04
0.01 M NaF	σ_i[Å]	1.01±0.01	0.96±0.01
	ρ_{ad}	0.24±0.01	0.38±0.01
	z_{ad} [Å]	3.35±0.05	3.38±0.03

Table 4.4: Structural data on the Hg-electrolyte interface structure in Pb-free solutions

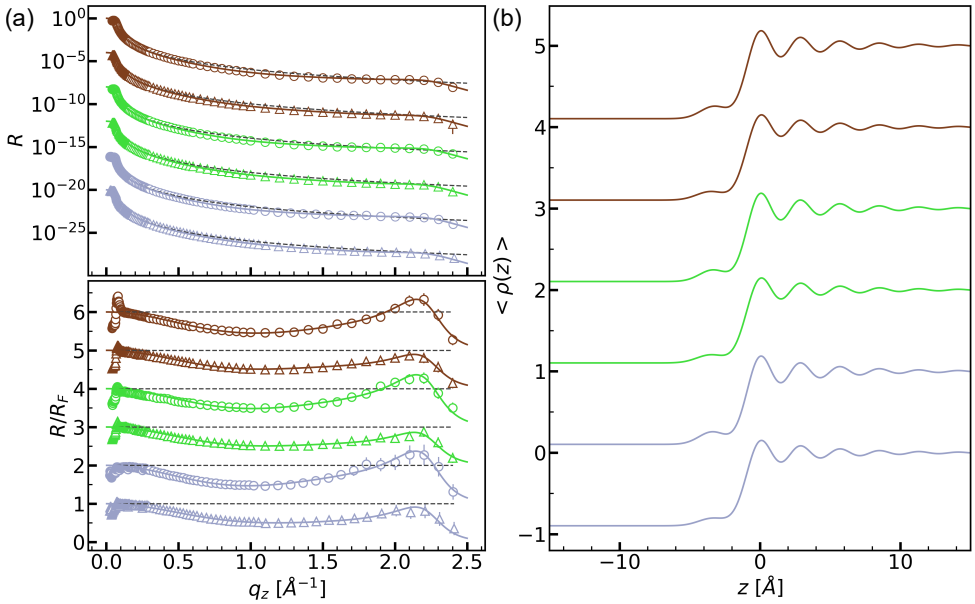

Figure 4.8: (a) Reflectivity profiles (top panel) and reflectivity normalized by the Fresnel reflectivity $R_F(q_z)$ (bottom panel) of the liquid Hg electrode in pure 0.01 M NaBr (brown), 0.01 M NaCl (green) and, 0.01 M NaF (blue) solution. Triangles indicate XRR curves measured at -1.20 V, circles XRR curves measured at -0.60 V. top: The grey dashed lines indicate the Fresnel reflectivity $R_F(q_z)$, solid lines correspond to the best fit of the XRR data. For clarity, the individual profiles are offset with respect to each other. (b) The electron density profiles corresponding to the best fits (detailed structural parameters are given in table S1).

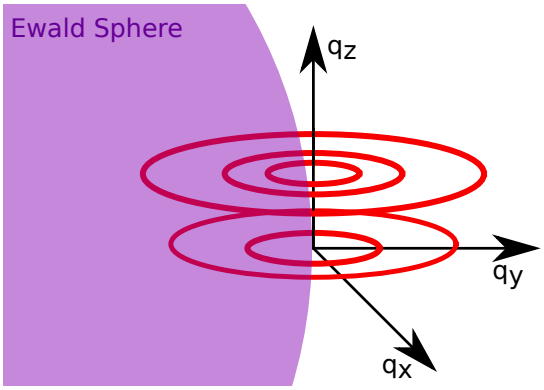

Figure 4.9: Schematic representation of reciprocal space diffraction geometry for a two-dimensional powder with the Ewald sphere shown in purple. Intersections of the ring-shaped arrangement of the Bragg reflections with the Ewald sphere manifest as diffraction peaks on the two-dimensional X-ray detector. In contrast, scattering from a three-dimensional powder (corresponding to spheres in reciprocal space) would result in powder rings on the detector.

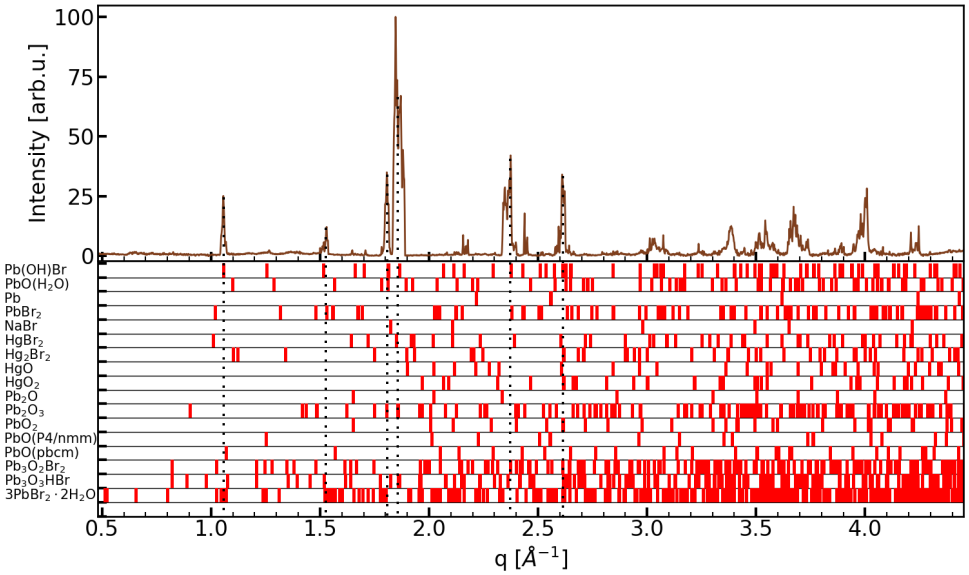

Figure 4.10: Powder diffraction pattern obtained by integration of the GID data of the deposit in Br-containing electrolyte (top), compared to the peak positions of listed crystal structures (bottom).

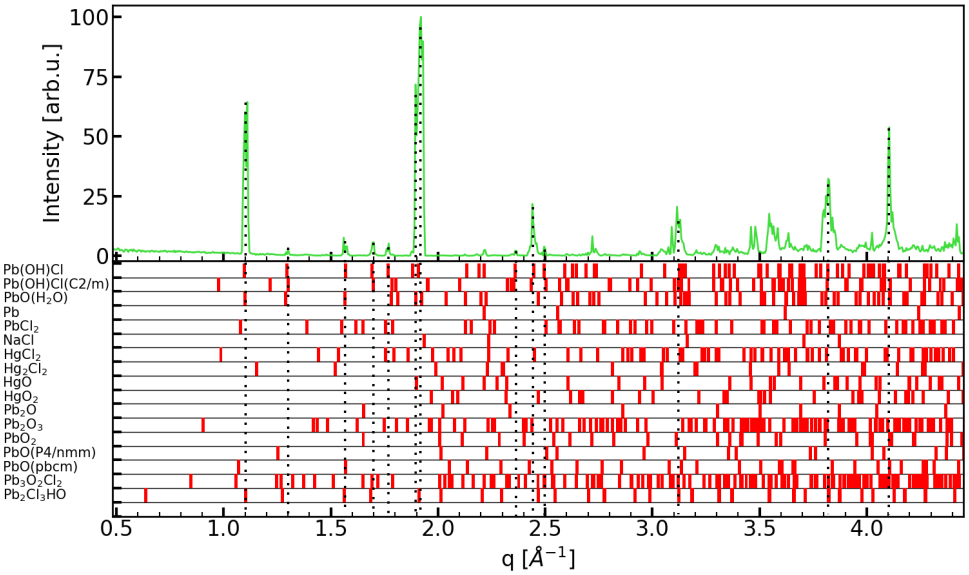

Figure 4.11: Powder diffraction pattern obtained by integration of the GID data of the deposit in Cl-containing electrolyte (top), compared to the peak positions of listed crystal structures (bottom).

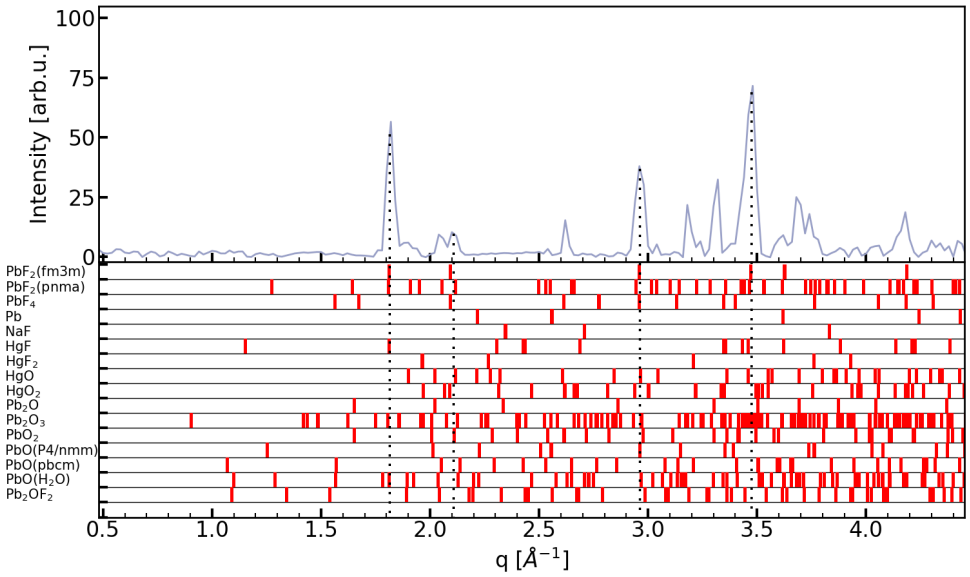

Figure 4.12: Powder diffraction pattern obtained by integration of the GID data of the deposit in F-containing electrolyte (top), compared to the peak positions of listed crystal structures (bottom).

S2: XRR modelling of the adlayer in Pb-containing solutions

This section describes the different models used in the fitting of the experimental data.For each system, we first considered an adlayer with a height of one full unit cell of the identified bulk material, as this was the adlayer structure found in the case of PbFBr.[5] That is, c-axis oriented Pb(OH)Br was used for Br-containing solution, c-axis oriented Pb(OH)Cl for Cl-containing solution, and PbF_2 for F-containing solution. Then we removed subsequently single Pb atomic layers (and their neighboring anion layers). For each of the XRR fits shown below (Figure 4.14,4.16, 4.17), the solid line is the best fit described in the main manuscript and identical to the fit displayed in Figure 4.2. The dashed line describes the best fit if only the majority phase Pb(OH)X_{ad-1}(X = Br, Cl) or only two Pb layers (X = F) are considered.

a) Adlayer in Br-containing solution

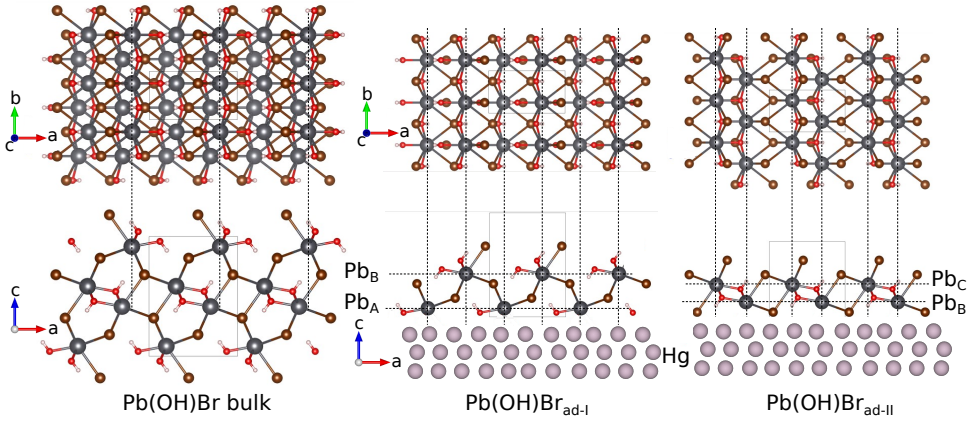

Figure 4.13: Top and side view of the Pb(OH)Br crystal structure. On the left hand side, the bulk structure is shown, on the right hand side, the precursor adlayer structures used to fit the experimental XRR data at -0.80 V.

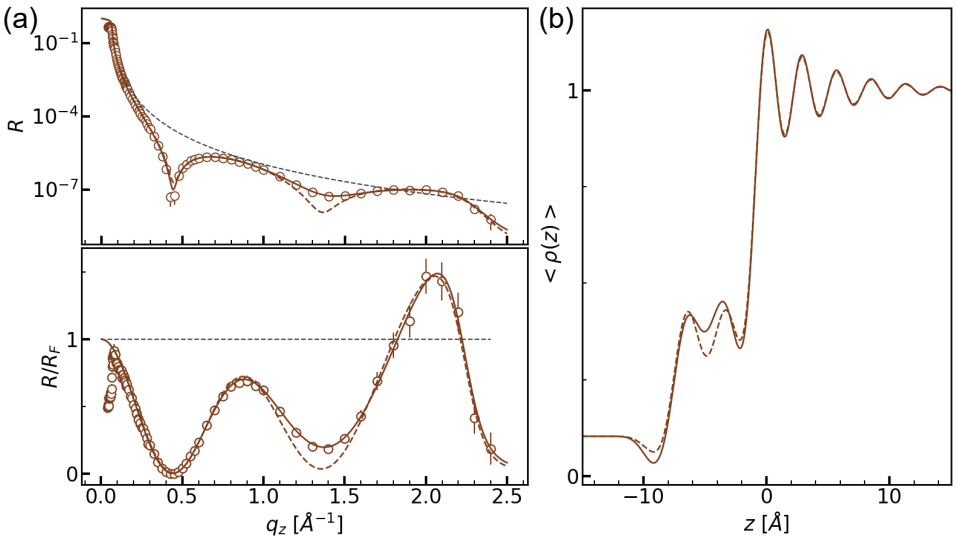

Figure 4.14: (a) X-ray reflectivity (top) and XRR normalized to the Fresnel reflectivity (bottom) of Hg electrodes in 0.01 M NaBr + 0.25 mM $PbBr_2$. The solid line describes the best fit by a model that includes two adlayer phases, Pb(OH)Br_{ad}-I and Pb(OH)Br_{ad}-II, the dashed line the best fit by a model with only Pb(OH)Br_{ad}-I. Obviously, fits with a Pb(OH)Br_{ad}-I adlayer phase alone cannot fully reproduce the oscillations in the XRR data, making the consideration of a second phase necessary. (b) Electron density profiles corresponding to the fits in (a).

b) Adlayer in Cl-containing solution

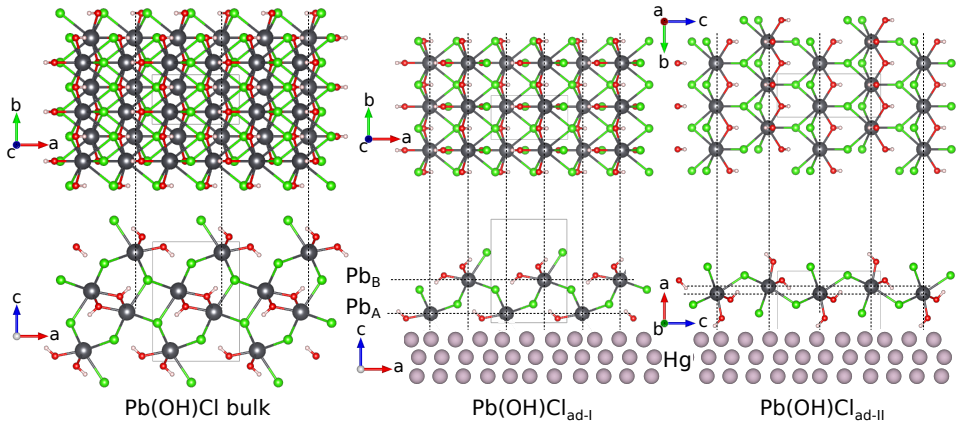

Figure 4.15: Top and side view of the Pb(OH)Cl crystal structure. On the left hand side, the bulk structure is shown, on the right hand side, the precursor adlayer structures used to fit the experimental XRR data at -0.90 V.

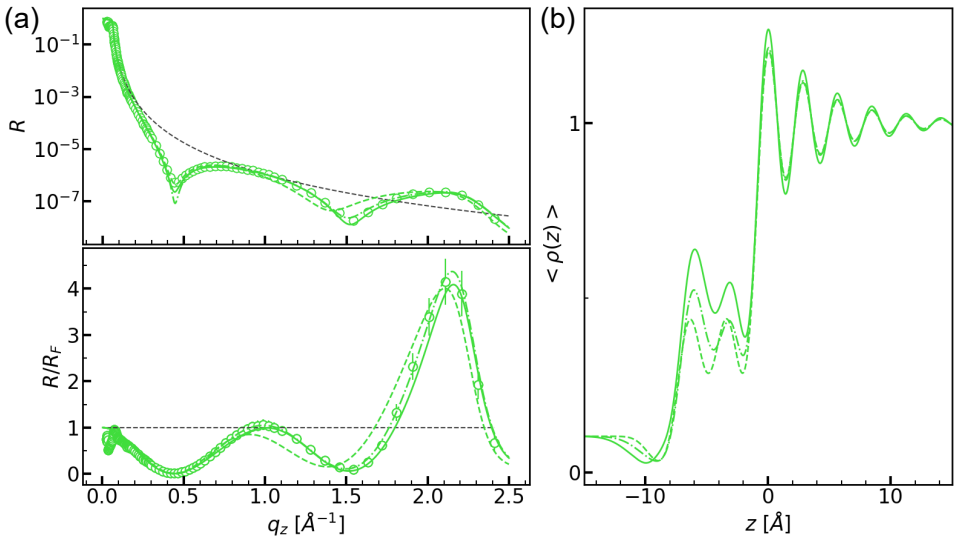

Figure 4.16: a) X-ray reflectivity (top) and XRR normalized to the Fresnel reflectivity (bottom) of Hg electrodes in 0.01 M NaCl + 0.25 mM $PbCl_2$. The solid line describes the best fit by a model that includes $Pb(OH)Cl_{ad-I}$ and $Pb(OH)Cl_{ad-II}$, the dashed line by a model with only $Pb(OH)Cl_{ad-I}$, and the dashed-dotted line by a model with $Pb(OH)Cl_{ad-I}$ and a c-axis oriented minority phase analogue to $Pb(OH)Br_{ad}$-II (but an unphysically large Cl-Hg distance of ∼4 Å). Obviously, the first model provides the best description of the experimental data. (b) Electron density profiles corresponding to the fits in (a).

c) Adlayer in F-containing solution

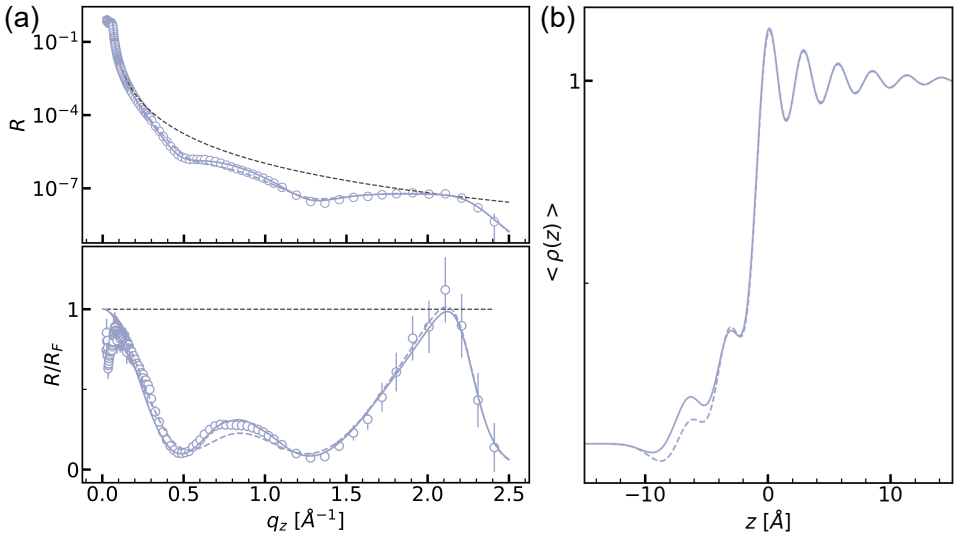

Figure 4.17: (a) X-ray reflectivity (top) and XRR normalized to the Fresnel reflectivity (bottom) of Hg electrodes in 0.01 M NaF + 0.12 mM PbF_2. The solid line describes the best fit by a model including three Gaussians, representing Pb atomic layers, the dashed line by a model with two Gaussians. (b) Electron density profiles corresponding to the fits in (a).

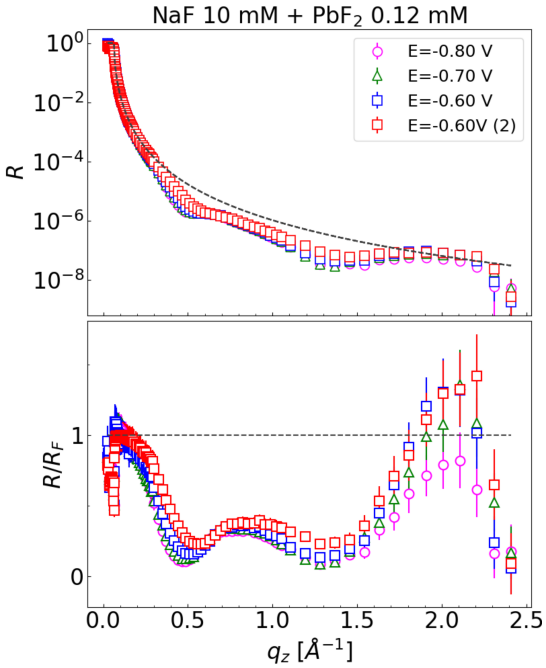

Figure 4.18: Series of XRR, recorded subsequently on Hg in 0.01 M NaF + 0.12 mM PbF_2 at -0.80 V, -0.70 V, -0.60 V, and again at -0.60 V. Prior to these measurements, the sample had been kept at -1.20 V for 15 minutes. The data indicate that the adlayer is not stable but slowly changes with time, even if the sample is kept at the same potential.

S3: Electrochemical cell for *in situ* XRR and GID studies

A custom-made electrochemical cell was used to collected the *in situ* XRR and GID data presented in the manuscript. The cell is made of PEEK and gas tight. Two opposite thin sections (0.5 mm) of the PEEK wall act as x-ray windows. Liquid Hg and electrolyte were inserted via connected PTFE tubings. A similar tubing connected a glass chamber with the reference electrode to the cell. The counter electrode was a ring of 0.5 mm thick Pt-wire along the inner circumference of the cell in order to have an homogeneous electric field at the working electrode. The electrolyte exchange was performed by applying an overpressure to the electrolyte reservoir, the replaced electrolyte was collected in a waste container. The flow was controlled by a series of valves. The microscope camera was mounted on top of the cell, where a quartz glass window provided an optical access. The cell also allows for temperature control but all measurements in this work were done at room temperature.

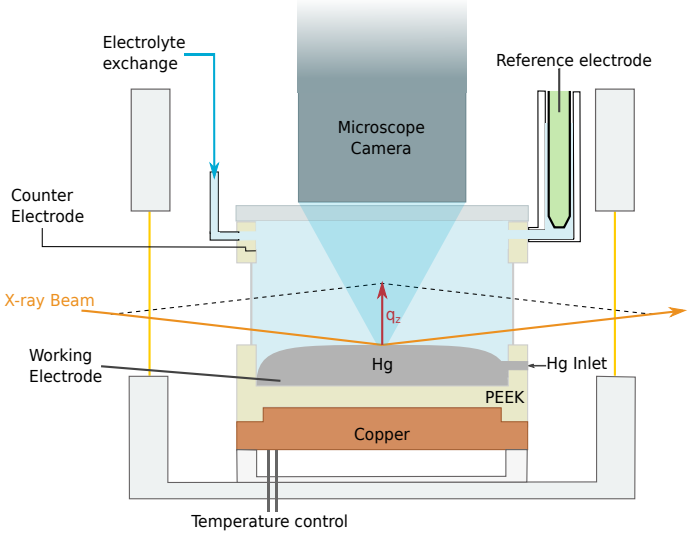

Figure 4.19: Sketch of the electrochemical cell used for the experiment.

References

(1) Magnussen, O. M.; Ocko, B. M.; Regan, M. J.; Penanen, K.; Pershan, P. S.; Deutsch, M. X-Ray Reflectivity Measurements of Surface Layering in Liquid Mercury. *Physical Review Letters* **1995**, *74* (22), 4444-4447.
https://doi.org/10.1103/PhysRevLett.74.4444.

(2) DiMasi, E.; Tostmann, H.; Ocko, B. M.; Pershan, P. S.; Deutsch, M. X-Ray Reflectivity Study of Temperature-Dependent Surface Layering in Liquid Hg. *Physical Review B* **1998**, *58* (20), R13419-R13422.
https://doi.org/10.1103/PhysRevB.58.R13419.

(3) Elsen, A.; Murphy, B. M.; Ocko, B. M.; Tamam, L.; Deutsch, M.; Kuzmenko, I.; Magnussen, O. M. Surface Layering at the Mercury-Electrolyte Interface. *Physical Review Letters* **2010**, *104* (10), 105501.
https://doi.org/10.1103/PhysRevLett.104.105501.

(4) Runge, B.; Festersen, S.; Koops, C. T.; Elsen, A.; Deutsch, M.; Ocko, B. M.; Seeck, O. H.; Murphy, B. M.; Magnussen, O. M. Temperature- and Potential-Dependent Structure of the Mercury-Electrolyte Interface. *Physical Review B* **2016**, *93* (16), 165408.
https://doi.org/10.1103/PhysRevB.93.165408.

(5) Elsen, A.; Festersen, S.; Runge, B.; Koops, C. T.; Ocko, B. M.; Deutsch, M.; Seeck, O. H.; Murphy, B. M.; Magnussen, O. M. In Situ X-Ray Studies of Adlayer-Induced Crystal Nucleation at the Liquid-Liquid Interface. *Proceedings of the National Academy of Sciences* **2013**, *110* (17), 6663.
https://doi.org/10.1073/pnas.1301800110.

5 Detection of Ge-Containing Adlayers at the Liquid Hg/Water Interface by In Situ X-Ray Reflectivity in Aqueous Borate Electrolytes Containing Dissolved GeO_2

This chapter is based on an published as an article in The Journal of Physical Chemistry C [137] obtained in collaboration with the Maldonado group (University of Michigan). Here is presented systematic X-Ray reflectivity investigation of mercury-$Na_2B_4O_7$ and Hg-$Na_2B_4O_7$+GeO_2 interface as a function of potential in a range where there are no faradaic redox reactions.

List of authors

Joshua P. Hazelnis,[1†] Andrea Sartori,[2†] Quintin B. Cheek,[1] Rajendra P. Giri,[2] Molly M. MacInnes,[1] Bridget M. Murphy,[2,3] Olaf M. Magnussen,[2,3] and Stephen Maldonado[1,4]

[1] Department of Chemistry, University of Michigan, 930 N University, Ann Arbor, Michigan 48109-1055

[2] Institute for experimental and Applied Physics, Kiel University, D-24118 Kiel, Germany

[3] Ruprecht Haensel Laboratory, Kiel University, D-24118 Kiel, Germany,

[4] Program in Applied Physics, University of Michigan, 930 N University, Ann Arbor, Michigan 48109-1055

[†] J. P. Hazelnis and A. Sartori contributed equal to this work

5.1 Abstract

The local structure of the liquid metal/electrolyte interface for Hg electrodes immersed in aqueous solutions suitable for crystalline Ge electrodeposition was probed by *in situ* X-Ray reflectivity. Series of X-Ray reflectivity measurements were collected in both pure 0.1 M $Na_2B_4O_7$ solution and 0.1 M $Na_2B_4O_7$ with 0.05 M GeO_2 at potentials where there are no faradaic redox reactions. Quantitative analysis of these data indicates that the interface structure in pure $Na_2B_4O_7$ solution is indistinguishable from that of Hg immersed in NaF solution, suggesting non-specific adsorption of the borate ions. In GeO_2-containing electrolyte, the presence of Ge species could be detected over a wide potential regime. Between -0.9 and -0.5 V vs SCE, the reflectivity data revealed the adsorption of dissolved H_2GeO_3 and/or $HGeO_3^-$ at a coverage that appears to be independent of potential. At potentials more positive than -0.5 V, an incomplete ultrathin film of a condensed phase forms via slow nucleation and growth at the Hg surface. This solid phase is consistent with a form of GeO_2 and tentatively assigned to polygermanates. This film likely forms through a condensation reaction driven by the concentration of $HGeO_3^-$ at the liquid Hg/electrolyte interface at positive potentials.

5.2 Introduction

Room temperature liquid metal interfaces are potent reaction sites for the syntheses of inorganic, crystalline materials.[1-8] In general, the ductility of a liquid metal facilitates mechanical removal of material from its surface.[2,9-10] For the preparation of ultra-thin oxides, the surface tension of the liquid metal alloys helps dictate the surface oxide composition.[2] For electrodeposition of crystalline metals, metal salts, and covalent semiconductors, liquid metals are advantageous because they can serve as reaction solvents for species electroreduced at the solution/electrode interface.11-16

Further development of liquid-metal-based material growth and processing requires detailed insight into the underlying interface structure and interface processes, similar to that obtained for growth at the solid-vapor and solid-liquid interface.[17-18] However, atomic-scale data on liquid metal interfaces is currently scarce, mostly because these interfaces are difficult to access by structure-sensitive experimental techniques.

One of the few methods that is capable of interrogating liquid metal interfaces is X-ray reflectivity (XRR). From XRR data, the interface structure along the surface normal can be directly determined with up to atomic resolution.[19] Historically, XRR measurements were essential in confirming atomic layering within the near surface region of liquid metals in contact with their vapor.[20-23] More recently, *in situ* XRR methods that probe liquid solution-liquid metal interfaces have been realized.[24-26] These methods employ high photon energies, which allow to access these deeply buried liquid-liquid interfaces due to their penetration depth. XRR measurements of pristine Hg electrodes in aqueous electrolytes were used to corroborate the electrocapillarity law, i.e. the maximum in surface tension and, consequently, the minimum in roughnesses of liquid metals at the potential of zero charge (E_{pzc}), as well as the polarization of the surface electron density profile according to the Schmickler-Henderson theory.[27] Similarly, the temperature-dependences of factors that govern the interfacial structure at water/liquid Hg contacts have been identified by XRR.[27] Two more recent sets of studies have illustrated the value of XRR in studying electrodeposition processes at water/liquid metal interfaces. XRR measurements combined with grazing incidence X-ray diffraction elucidated the initial steps in the nucleation and growth of lead halide crystals at liquid Hg electrolyte interfaces.[8,28] Other XRR data have separately identified the surface composition and structure of liquid Hg-In alloy electrodes used to grow Ge crystals.[29]

This study utilizes XRR to determine *in situ* the interface between liquid Hg and aqueous $Na_2B_4O_7$ containing dissolved GeO_2. This electrolyte is of interest since electrodeposition of Ge nanowires,[14] microwires,[30] and epitaxial films[31] is possible with a variety of liquid metals. Still, little is known about the nature of these water/liquid metal contacts, particularly when under potential control. Given the wealth of information on Hg interfaces, XRR analysis of liquid Hg electrodes in this solution is an ideal starting point. Accordingly, the results from a series of potential-dependent XRR experiments and accompanying electrochemical measurements are presented that provide atomic-scale details on the Hg electrode surface in $Na_2B_4O_7(aq)$, both with and without dissolved GeO_2. Notably, persistent adsorption of a Ge species is identified for the first time on Hg in solutions containing dissolved GeO_2. As demonstrated below, at sufficiently positive potentials, this adsorbate unexpectedly undergoes a transformation to a condensed phase at the water/Hg interface at positive potentials.

5.3 Experimental

5.3.1 Materials

Germanium (IV) oxide (99.999%, ChemPur), sodium tetraborate (99.998%, ChemPur), and mercury (99.999+%, ChemPur) were used as received. Water with a resistivity >18.2 MΩ·cm was used throughout.

5.3.2 Potential of Zero Charge Measurement

Measurements of E_{pzc} were performed using a custom-built, pendant-drop optical measurement system consisting of a digital camera (640 x 480p resolution) positioned perpendicular to a pendant Hg droplet (r = 695.2 um) immersed in an electrochemical cell with a flat optical window. A white-light, LED microscope ring light with a diffuser was placed opposite to the camera for illumination. Images were collected and processed with a custom ImageJ script using an algorithm[32-33] for the surface tension as a function of the drop shape. Estimates of E_{pzc} were then obtained from the maximum of parabolic fits of the potential-dependent surface tension data. Cell temperature was monitored throughout the course of the experiment (25$\pm$ 1 $^\circ$ C). All reported values were performed in triplicate and the error bars represent the sample standard deviation.

5.3.3 X-Ray Reflectivity Measurements

XRR measurements of the liquid metal-liquid electrolyte interfaces were performed using the Liquid Interface Scattering Apparatus (LISA) diffractometer 25 at beamline P08 of the PETRA III synchrotron source at DESY in Hamburg, Germany. A photon energy of 25 keV with a beam size of 0.4 mm (horizontal) and 0.1 mm (vertical) was chosen. Data were collected with a GaAs Lambda detector (1536 x 512 array of pixels with a pixel height of 55 μm). Beam attenuators were used to ensure that the count intensity was $\leq 10^5$ counts per pixel. Reflectivities were measured as a function of the incidence and exit angle $\alpha = \beta$ of the X-rays impinging on the interface, as shown schematically in Figure 5.1.

The measured XRR intensity was obtained from integration of a detector area corresponding to a vertical and horizontal acceptance of 0.4^o and 0.08^o, respectively. The background intensity from X-ray scattering from bulk Hg and the electrolyte was determined at a 0.08^o horizontal offset and subtracted from the main signal. The XRR curves were obtained by normalizing the background-subtracted detector signal by the direct beam intensity and are presented as a function of q_z, where $q_z = (4\pi/\lambda)$ sin α and λ is the wavelength of the X-rays.

The sample was kept in a custom-designed electrochemical X-ray scattering cell similar to that described previously,[26] where the X-ray beam passed through thin PEEK

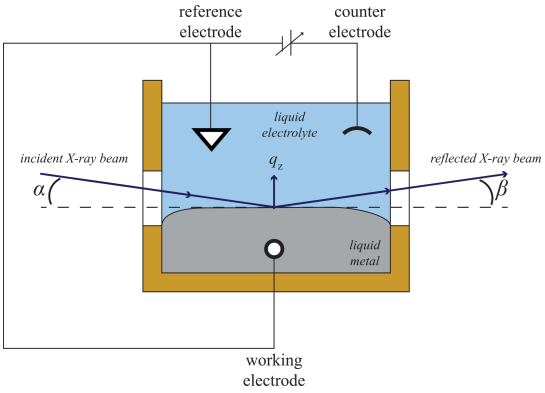

Figure 5.1: Schematic illustration of the electrochemical cell and the X-ray beam path used for *in situ* X-ray reflectivity measurements.

windows and the liquid metal electrode was a 2.75 cm radius Hg pool (Figure 5.1). Electrolyte solutions were purged with $N_2(g)$ for at least 30 minutes prior to injection into the cell. Upon assembly, the Hg electrode was held at a constant potential with respect to a saturated calomel electrode (SCE) for at least 15 minutes before the reflectivity measurements to ensure a stable interface. A digital, computer-controlled potentiostat (Ametek Modulab) was used throughout. Electrochemical data are presented in the polarographic ('Texas') convention, i.e. cathodic currents are plotted as positive and more negative potentials plotted to the right. All potentials are reported here with respect to SCE.

For XRR measurements collected at a constant applied potential, at least two XRR scans were taken. In these experiments, a random sequence of the applied potential values was used to eliminate the possibility of cumulative, systematic bias. A full set of angle-dependent XRR data from small (0.04 $Å^{-1}$) to large (2.5 $Å^{-1}$) values of the surface-normal scattering vector, q_z, took between 0.6 to 1.5 hours to collect, depending on the angle resolution at large q_z and signal integration time.

Fitting of XRR data was performed in a sequential process through custom-written python scripts. The first round of fitting focused on global optimization, using pre-defined upper and lower bounds for each fitting parameter. Subsequent fitting rounds were performed to refine the value of each parameter individually. The uncertainties in the reported fit parameters were calculated from a least squares analysis and denote the precision of that parameter towards the total fit rather than a sample standard deviation.

5.4 Modelling of XRR Data

The experimental X-ray reflectivity curves, $R(q_z)$, were normalized by the Fresnel reflectivity, $R_F(q_z)$, of a perfectly sharp interface between Hg and the aqueous electrolyte. The deviations of $R(q_z)$ from $R_F(q_z)$ contain information on the interface

structure, in particular the distance-dependent electron density normal to the surface plane,$\rho_e(z)$. The relation between electron density profile and reflectivity is given by the so-called master formula,[34]

$$\frac{R(q_z)}{R_F(q_z)} = \left| \frac{1}{\rho_\infty} \int \frac{d\rho_e(z)}{dz} e^{izq_z} dz \right|^2 \tag{5.1}$$

where ρ_∞ is equal to the difference in the electron densities of the bulk solvent and the bulk Hg.

The simplest model employed here to describe $\rho_e(z)$throughout the electrolyte, interface, and Hg electrode is described by *eq* 5.2,

$$\rho_e(z) = \rho_{electrolyte}(z) + \rho_{DCM,Hg}(z) \tag{5.2}$$

where $\rho_{electrolyte}(z)$ and $\rho_{DCM,\ Hg}(z)$ represent the distance-dependent contributions of the electrolyte solution and the Hg electrode, respectively. The electrolyte term is given by a complementary error function. The near-surface region of the liquid Hg was described by the 'adlayer'[35] form of the 'distorted crystal model'.[19,23] Here, the outermost atomic Hg layer is given by a discrete Gaussian term and the subsequent Hg layers by a decay function resulting from an infinite series of Gaussians with increasing width, [8, 23-24, 27, 36]

$$\rho_{electrolyte}(z) = \frac{1}{2}\rho_{e,H_2O}\left(\text{erfc}\left(\frac{z - z_{H_2O}}{\sigma_{H_2O}\sqrt{2}}\right)\right) \tag{5.3}$$

$$\rho_{DCM,Hg}(z) = F_{Hg}(z) \otimes \left[\frac{\rho_{e,ad-Hg}}{\rho_{e,Hg}} \frac{1}{\sigma_{ad}\sqrt{2\pi}} e^{\frac{-(z-z_{ad})^2}{2\sigma_{ad}^2}} + \sum_{n=0}^{\infty} \frac{d}{\sqrt{\sigma_i^2 + n\sigma_b^2}\sqrt{2\pi}} e^{\frac{-(z-nd)^2}{2\left(\sigma_i^2+n\sigma_b^2\right)}}\right] \tag{5.4}$$

where z_{H_2O}, σ_{H_2O} , ρ_{H_2O} describe the position, width, and electron density of the electrolyte front. $\rho_{e,ad-Hg}$, σ_{ad} , z_{ad} are respectively the amplitude, root mean square displacement and position of the low density Hg adlayer, d is the spacing between the atomic layers of Hg, F_{Hg}(z) is the Fourier transform of the Hg atomic form factor, σ_i is the surface roughness (i.e. the combination of the intrinsic roughness and the effect of capillary waves),[27] and σ_b describes how the roughness of each atomic layer increases with increasing layer number n.[19, 23] In this presentation, the ratio of adlayer and bulk electron densities corresponds to a fractional monolayer coverage, i.e. number of adlayer units per Hg atom on the surface.

Inserting *eq* 5.2, 5.3 and 5.4 into *eq* 5.1, we obtain an explicit dependence of $\frac{R(q_z)}{R_F(q_z)}$ with q_z.

$$\frac{R\left(q_z\right)}{R_F\left(q_z\right)} = \left| \left(\frac{1}{\rho_{e,Hg} - \rho_{e,H_2O}}\right) \left(\begin{array}{l} \left(\frac{f^0_{Hg}(q_z)+f^{'}_{Hg}}{Z_{Hg}+f^{'}_{Hg}}\right) \left(iq_z d \frac{e^{\frac{-q_z^2\sigma_i^2}{2}}}{\left(1-e^{iq_z d-\frac{q_z^2\sigma_b^2}{2}}\right)} + iq_z \frac{\rho_{e,ad-Hg}}{\rho_{e,Hg}} e^{-\left(iq_z z_{ad}-\frac{q_z^2\sigma_{ad}^2}{2}\right)} \right) \\ -\rho_{e,H_2O} e^{-\left(iq_z z_{H_2O}-\frac{q_z^2\sigma_{H_2O}^2}{2}\right)} \end{array} \right) \right|^2 \tag{5.5}$$

where $f^0_{Hg}\left(q_z\right)$ and $f^{'}_{Hg}$ are the angle-dependent Hg atomic form factor and the dispersion correction, respectively, and Z_{Hg} is the atomic number of Hg.

As discussed in the next section, fitting XRR data collected in solutions with dissolved GeO_2 and potentials more negative than -0.2 V with *eq* 5.2 yielded notably larger values of $\rho_{e,ad-Hg}$. Accordingly, *eq* 5.2 was refined to include a set of additional Gaussian terms, $\rho_{HGeO_3^-}(z)$, that constituted an 'adlayer' of $H_2GeO_3/HGeO_3^-$ (*eq* 5.13, Supporting Information). H_2GeO_3 and $HGeO_3^-$ are the predominant forms of dissolved GeO_2 at the solution pH of 9.13.[37-38] In these fits, the terms that pertained to the Hg 'adlayer' were fixed at the values determined from the fits of the XRR data in the blank 0.1 M $Na_2B_4O_7$ electrolyte and corresponding potential.

The XRR data collected in the electrolyte with dissolved GeO_2 at -0.2 V could not be adequately fit in the same way even allowing for simple refinements to *eq* 5.2. Instead, a two-step approach was adopted for fitting. First, a preliminary model was generated by adding multiple Gaussian terms without specific atomic form factors to *eq* 5.2.

$$\rho_e(z) = \rho_{electrolyte}(z) + \sum_{m=1}^{3} \frac{\rho_{ad,m}}{\sigma_{ad}\sqrt{2\pi}} e^{\frac{-\left(z-z_{ad,m}\right)^2}{2\sigma^2_{ad,m}}} + \rho_{DCM,Hg}(z) \tag{5.6}$$

The intent of these general Gaussian terms was to assess where excess electron density was needed to yield a good match to the data to inform a subsequent, structure-specific model. *Eq* 5.6 represents the fewest Gaussian terms necessary. Second, a more structure-specific model was explored based on the formation of GeO_2 at the water/Hg interface (*vide infra*). For brevity, the full expression of the electron density profile normal to the surface plane and of the resulting $\frac{R(q_z)}{R_F(q_z)}$ for this second model is given by *eq* 5.21 in the *Supporting Information*. *Eq* 5.7 is presented here to summarize the essence of this second model,

$$\begin{aligned} \rho_e(z) = \rho_{electrolyte}(z) + \rho_{DCM,Hg}(z) + \theta_{GeO_2}\left(\rho_{ad,Ge/GeO_2}(z) + \rho_{e,GeO_2}(z)\right) \\ + (1-\theta_{GeO_2})\rho_{ad,Ge/Hg}(z) \end{aligned} \tag{5.7}$$

Eq 5.7 describes the Hg surface composition as the sum of two separate surface types. One fraction of the surface, θ_{GeO2}, was considered as having a solid bilayer of GeO_2 deposited on the Hg surface. In this part of the surface, the electron density was

modeled by 2 additional Gaussian terms with Ge form factors and 6 additional Gaussian terms with O form factors. Based on the results of the preliminary model, the distances between these Gaussians were chosen to correspond to rutile GeO_2 oriented with the [110] direction along the surface normal. Furthermore, a third set of Gaussian terms with Ge and O atomic form factors that described specifically the accumulation of (solvated) $H_2GeO_3/HGeO_3^-$ at the water/GeO_2 interface was included. In the remaining surface fraction (i.e. '1- θ_{GeO2}'), an identical structure as Hg at the more negative potentials was assumed. This part of the surface was modeled by a set of Gaussians with Ge and O atomic form factors that described the adsorption of $H_2GeO_3/HGeO_3^-$ on the bare Hg surface.

5.5 Results

Figure 5.2 presents the voltammetric behavior of Hg immersed in either aqueous 0.1 M $Na_2B_4O_7$ or aqueous 0.1 M $Na_2B_4O_7$ with 0.05 M dissolved GeO_2. In the potential range from -0.1 to -0.9 V, Hg is neither electrochemically oxidized nor does it readily support H^+ reduction, as shown by the dashed line in Figure 5.2a. Repeated scanning of Hg in the blank electrolyte over this potential range effected no change in voltammetric response. Although the potential range in Figure 5.2 was not sufficiently negative to support the $4e^-$ reduction of dissolved GeO_2, addition of dissolved GeO_2 to the $Na_2B_4O_7$ electrolyte results in a clear change in the voltammogram (solid line). A sizeable increase in oxidative current at potentials more positive than -0.2 V was noted in the presence of dissolved GeO_2. Similarly, there was a notable increase in reductive current in the potential range between -0.1 and -0.6 V of the potential sweep to more negative values. The corresponding anodic and cathodic charge densities (corrected for the contribution of double layer charging) were of comparable magnitude, i.e. 6.9 μC cm^2 and 10.5 μC cm^2 , respectively. The pronounced hysteresis between anodic and cathodic charge transfer rules out a simple reversible pseudo-capacitive process, such as electrochemical adsorption, and suggest a more complex behavior that involves nucleation and growth.

To determine the potential-dependent structure of the electrolyte/Hg interface, *in situ* XRR measurements were performed. First, XRR data were obtained in the blank aqueous $Na_2B_4O_7$ electrolyte and compared with data collected within the same synchrotron experiment in aqueous NaF. The NaF (*aq*)/Hg system is arguably the best studied liquid metal electrochemical system and considered as the prototypical case of a non-specifically adsorbing electrochemical double layer.[39-42] The extant XRR literature on this system supports this view and suggests that the interface is atomically abrupt [24,27] and exhibits a similar surface layering as the vacuum/Hg interface.[23,43]

The characteristic electron density profile along the surface normal, $\rho_e(z)$, for NaF

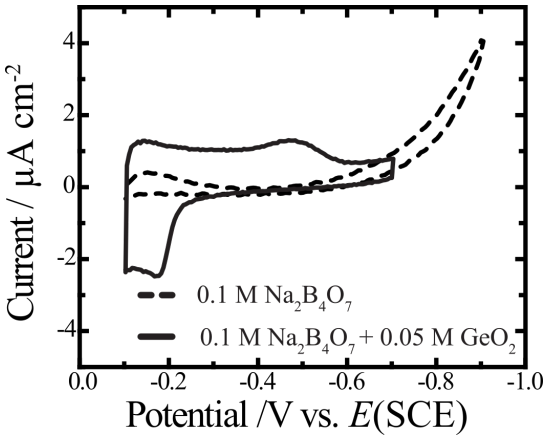

Figure 5.2: Voltammetric responses for a mercury electrode immersed in 0.1 M $Na_2B_4O_7$ (*aq*) (dashed line) and 0.1 M $Na_2B_4O_7$ + 0.05 M GeO_2 (*aq*) (solid line). Scan rate: 0.02 V s^{-1}.

(*aq*)/Hg (and similar interfaces between liquid metals and non-specifically adsorbing electrolyte) as shown in Figure 5.3a. $\rho_e(z)$ contains contributions from the atomic surface layering in the Hg bulk (gray), a lower density Hg adlayer (green), and the electrolyte solution (blue). For low-Z ions, such as Na^+ and F^-, the X-ray scattering cross sections are similar to water and the electrolyte can thus be described by a single complementary error-function profile. Furthermore, Figure 5.3a depicts characteristic positions and widths that are employed as structural parameters in the models used to fit the data.

In the following, the XRR data are presented in the form of normalized reflectivity curves, R/R_F, plotted versus the surface normal scattering vector q_z (the corresponding experimentally measured X-ray reflectivities, $R(q_z)$, are presented in Figure 5.9 of the *Supporting Information*). Figure 5.3b illustrates the characteristic shape of these XRR curves for Hg immersed in either 0.01 M NaF (*aq*) or 0.1 M $Na_2B_4O_7$(*aq*) at the identical potential of -0.2 V. As clearly visible, the two curves are equivalent within the measurement errors over the entire q_z range. This observation is in accordance with the weak X-ray scattering of $Na_2B_4O_7$ and indicates a negligible influence of these electrolyte species on the Hg surface structure, suggesting the absence of strong chemisorption. R/R_F first decays up to $q_z \approx 1\ ^{-1}$, reflecting the finite roughness of the interface, and then increases up to a peak at $q_z \approx 2.2\ ^{-1}$. The latter is the 'pseudo-Bragg' peak, caused by the atomic Hg surface layering. [8, 20, 24, 27]

Quantitative structural data were obtained by fitting the R/R_F curves by the model function given by *eq* 5.5, which resulted in the structure parameters given in Table 5.1. We first performed fits of the XRR data for Hg immersed in 0.01 M NaF (*aq*). Here, the electrolyte parameters z_{H_2O}, ρH_2O) and the atomic layering distance in Hg (d) were set to established values for this system27 while the parameters for the Hg adlayer (ρ_{ad}, z_{ad}) and the atomic roughnesses (σ_b and σ_i) were fitted. The subsequent

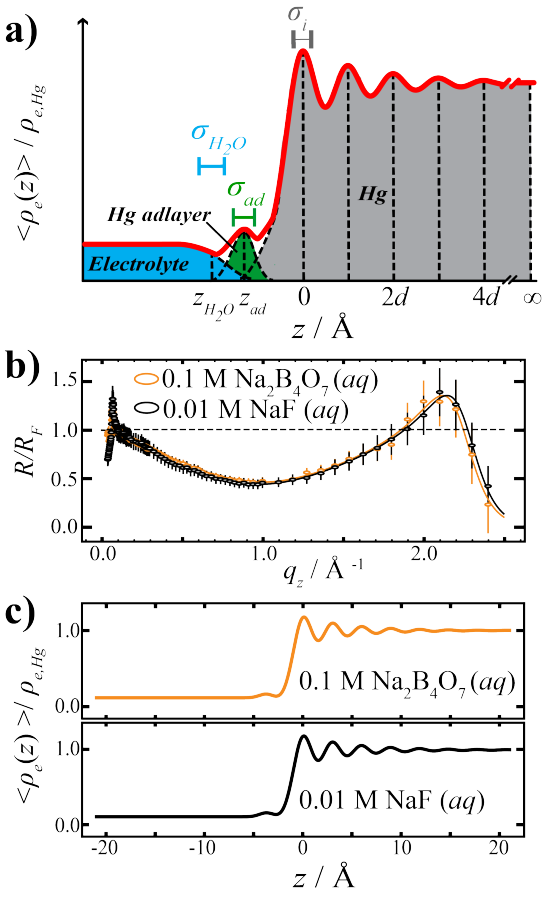

Figure 5.3: a) Schematic depiction of the model function for the electron density profile along the surface normal that was employed in the fitting of the XRR data. Contributions from the electrolyte, the Hg 'adlayer', and bulk Hg as well as the central fit parameters are indicated. b) Plot of the X-ray reflectivity normalized to the Fresnel reflectivity, R/R_F, vs. surface-normal momentum transfer, q_z, for a Hg electrode immersed in deaerated 0.1 M $Na_2B_4O_7(aq)$ (orange) or 0.01 M NaF(aq) (black) at -0.2 V. Solid lines denote best fits of the data with the model given by *eq* 5.5. The resulting values of the model parameters are listed in Table 5.1. The corresponding electron density profiles are shown in c).

fit of the XRR data for Hg immersed in 0.1 M $Na_2B_4O_7(aq)$ was performed in a similar fashion but with the position of the Hg adlayer fixed at the value obtained in NaF. Unsurprisingly, the fit parameters (Table 5.1) and the corresponding electron density profiles (Figure 5.3c) for the NaF and $Na_2B_4O_7$ datasets are statistically indistinguishable. More importantly, the fit parameters here are in good agreement with a previous detailed XRR study of the NaF (aq)/Hg system.[27] Together with the voltammetric data, this point verifies that the measurements reported here are sound and free of contaminations. The data in Figure 5.3b,c imply the $Na_2B_4O_7(aq)$/Hg interface is structurally similar to the NaF (aq)/Hg system despite differences in anion identity, ionic strength, and pH. As a result, these data support the contention that XRR data for Hg immersed in $Na_2B_4O_7(aq)$ afford a suitable reference point when

Electrolyte	*Potential*	σ_{H2O} /Å	σ_i /Å	σ_b /Å	$\rho_{e,ad\text{-}Hg}/\rho_{e,Hg}$ /Å	σ_{ad} /Å	z_{ad} /Å
0.01 M NaF							
	-0.2 V	-0.95 ± 0.01	0.95 ± 0.01	0.48 ± 0.01	0.21 ± 0.01	0.95 ± 0.01	-3.64 ± 0.23
0.1 M $Na_2B_4O_7$							
	-0.2 V	-0.94 ± 0.01	-0.94 ± 0.01	0.49 ± 0.01	0.24 ± 0.01	0.94 ± 0.01	-3.64[b]
	-0.5 V	-0.97 ± 0.01	-0.97 ± 0.01	0.49[c]	0.21 ± 0.01	0.97 ± 0.01	-3.64[b]
	-0.7 V	-1.00 ± 0.01	-1.00 ± 0.01	0.49[c]	0.16 ± 0.01	1.00 ± 0.01	-3.64[b]
	-0.9 V	-1.01 ± 0.01	-1.01 ± 0.01	0.49[c]	0.10 ± 0.01	1.01 ± 0.01	-3.64[b]
0.1 M $Na_2B_4O_7$ + 0.05 M GeO_2							
	-0.5 V	-1.00 ± 0.01	-1.00 ± 0.01	0.49[c]	0.31 ± 0.01	1.00 ± 0.01	-3.64[b]
	-0.7 V	-1.01 ± 0.01	-1.01 ± 0.01	0.49[c]	0.27 ± 0.01	1.01 ± 0.01	-3.64[b]
	-0.9 V	-1.01 ± 0.01	-1.01 ± 0.01	0.49[c]	0.21 ± 0.01	1.01 ± 0.01	-3.64[b]

Table 5.1: Parameters of the best fits of the XRR data by *eq* 5.5[a,b,c]. a. The data collected in 0.01 M NaF (*aq*) and in 0.1 M $Na_2B_4O_7$(*aq*) based electrolyte were modelled using *eq* 5.2 and $\rho_{e,ad-Hg}$ =0.1 $\rho_{e,Hg}$, z_{H_2O} = -1.00 Å , and d = 2.75 Å based on Reference 27. The data in 0.1 M $Na_2B_4O_7$+ 0.05 M GeO_2 (*aq*) at -0.2 V could not be described by this model and is thus not included here. b. For data collected in 0.1 M $Na_2B_4O_7$(*aq*) base electrolyte, z_{ad} was not a free fit parameter, but kept constant at its value obtained in fits of the data in 0.01 M NaF(*aq*) at-0.2 V.[27] c. For data collected in 0.1 M $Na_2B_4O_7$ (*aq*) base electrolyte, σ_b was obtained from the data in 0.1 M $Na_2B_4O_7$(*aq*) at -0.2 V and then used as a constant value for the fits of the data at potentials $<$ -0.2 V.

changes are made to the electrolyte composition.

Subsequently, we assessed the potential dependence of the XRR curves in 0.1 M $Na_2B_4O_7$ (*aq*). Figure 5.4a shows the R/R_F data collected at several applied potentials. The best fits by *eq* 5.5are presented as solid black lines. They were performed using the same procedure described above but with the same Hg layering decay (i.e., fixed σ_b) as at -0.2 V. The latter was motivated by previous studies that showed that this decay is a Hg bulk property and not affected by the potential.8 In the corresponding electron density profiles (Figure 5.4b) a characteristic behavior is apparent. The position of the 'pseudo-Bragg' peak at $\approx$ 2.2 $^{-1}$ is potential-independent but its intensity decreases towards more negative potentials. A similar behavior was observed previously in the NaF (*aq*)/Hg system.[27] All of the data are well fit by *eq* 5.5 using parameters for bulk Hg, bulk electrolyte, and the water/Hg interface that are in good agreement with the parameters reported in the literature for NaF (*aq*)/Hg.24, 27 On the basis of these fits, the change in the intensity of the layering peak at different potentials can be attributed to changes in the interface roughness, σ_i, and $\rho_{e,ad-Hg}$ (Figure 5.4b, inset),[24,27] in accord with previous XRR measurements of Hg immersed in NaF (*aq*).[36]

Figure 5.5 shows normalized X-ray reflectivity data collected at the same potentials as in Figure 5.4 but with dissolved GeO_2 added to the $Na_2B_4O_7$(*aq*) electrolyte. At

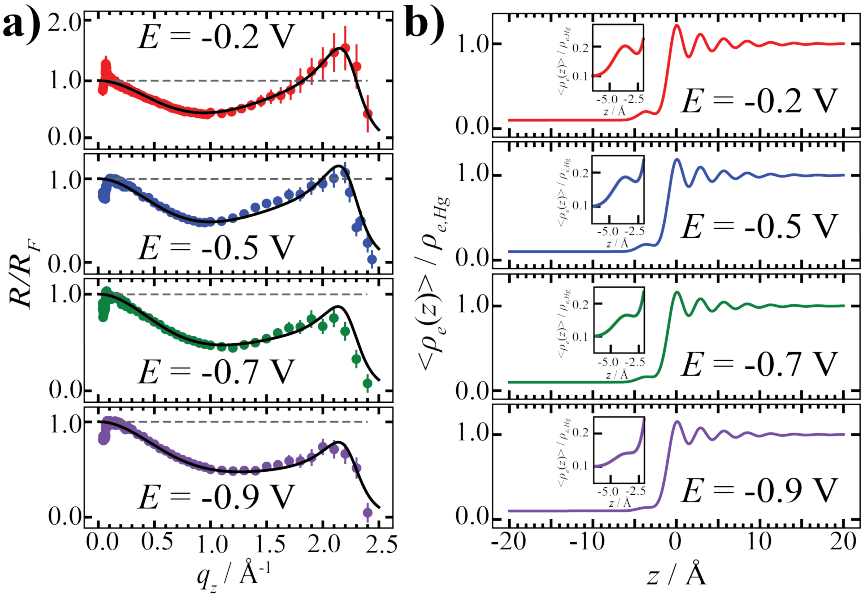

Figure 5.4: a) Plots of the normalized X-ray reflectivity curves for a Hg electrode immersed in 0.1 M $Na_2B_4O_7(aq)$ at -0.2 V (red), -0.5 V (blue), -0.7 V (green), -0.9 V (purple). Solid black lines denote the corresponding best fits of the data. Data were normalized to the Fresnel reflectivity. b) Electron density profiles corresponding to the best fits of the data in (a). Insets show an enlarged view of the electron density profile in the adlayer region (-5 $Å^{-1}$ $\leq z \leq$ -2 $Å^{-1}$).

potentials equal to or more negative than -0.5 V, the R/R_F curves had the same general features as those shown in Figure 5.4. That is, they exhibited a smooth decay and subsequent rise to the 'pseudo-Bragg' peak with increasing q_z and are well described by the model function given by *eq* 5.5. However, the measured data differed quantitatively from the measurements performed in the absence of dissolved GeO_2.

Figure 5.6 illustrates this point more directly. At applied potentials of -0.5, -0.7, and -0.9 V (Figure 5.6a), the differences in the XRR data measured in the absence and in the presence of dissolved GeO_2 are larger than the measurement standard deviations at $q_z \leq 1$ $Å^{-1}$. The fits to *eq* 5.5 indicate that the differences in the data can largely be ascribed to an increase in the electron density of the 'adlayer' component (Figure 5.6b, Table 5.1). Figure 5.6b shows the fitted $\rho_{e,ad-Hg}$ values from the data in the presence and absence of dissolved GeO_2 as a function of potential. The two datasets have the same profile but the values in the presence of dissolved GeO_2 are uniformly higher. Assuming that the increased electron density results from the enrichment of some Ge-containing species at the Hg interface, the data collected in the presence of dissolved GeO_2 were fit again but with a modified version of *eq* 5.5 (*Supporting Information*). This modified model includes an additional 'adlayer', which corresponds to a molecule of H_2GeO_3 or $HGeO_3^-$ (i.e. the dominant species in bulk solution)38 adsorbed at the interface through a hydrogen bond with the Hg surface. This modified model can not distinguish between H_2GeO_3 and $HGeO_3^-$ but for simplicity

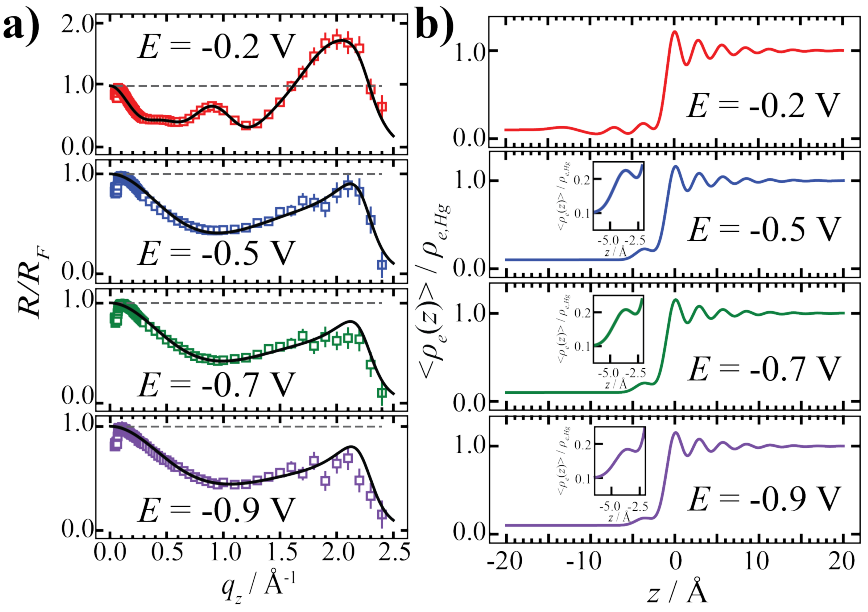

Figure 5.5: a)Plots of the normalized X-ray reflectivity curves for a Hg electrode immersed in deaerated electrolyte containing 0.1 M $Na_2B_4O_7$ + 0.05 M GeO_2 (*aq*) at -0.2 V (red), -0.5 V (blue), -0.7 V (green), and -0.9 V (purple). The XRR data at -0.2 V were recorded after keeping the potential for 15 min. at this value. The solid black lines denote the corresponding best fit of the data. b) Electron density profiles corresponding to the fitted data shown in (a). Insets show an enlarged view of the electron density profile in the adlayer region (-5 $Å^{-1} \leq z \leq$ -2 $Å^{-1}$).

we refer to this 'adlayer' as describing adsorbed $HGeO_3^-$. In this refined model, $\rho_{e,ad-Hg}$ was set to the value obtained from the fit of the corresponding XRR data in neat 0.1 M $Na_2B_4O_7$(*aq*) at the identical potential. Accordingly, the difference in electron density of the Hg 'adlayer' in Figure 5.6b can be re-interpreted as a coverage of $HGeO_3^-$ adsorbed at the Hg interface ($\theta_{HGeO3-/Hg}$). Over this range, $\theta_{HGeO3-/Hg}$ remains constant at a value of 0.20±0.01 monolayers.

The premise of adsorbed $HGeO_3^-$ at the Hg interface was further supported by separate estimates of E_{pzc} through surface tension measurements of Hg pendant drops (Figure 5.6b). The E_{pzc} value in 0.1 M $Na_2B_4O_7$(*aq*) was -0.49±0.09 V, in close agreement with the reported value of E_{pzc}=-0.441 V in 0.01 M NaF (*aq*).[39] The apparent E_{pzc} value shifted negatively to -0.56±0.06 V when GeO_2 was dissolved in the $Na_2B_4O_7$ electrolyte, consistent with additional negative charge localized at the solution/Hg interface.

At -0.2 V, the XRR data are distinctly different. An additional peak is evident, centered at q_z = 0.85 $Å^{-1}$, that is less intense than the surface layering peak at q_z= 2.2 $Å^{-1}$. The prominence of the peak at q_z = 0.85 $Å^{-1}$ depended somewhat on the duration the potential was held at ≥-0.2 V but was consistently observed when the applied potential was ≥ -0.2 V. However, independently of the duration, the R/R_F value at the center of this new peak was consistently below 1. The presence of the

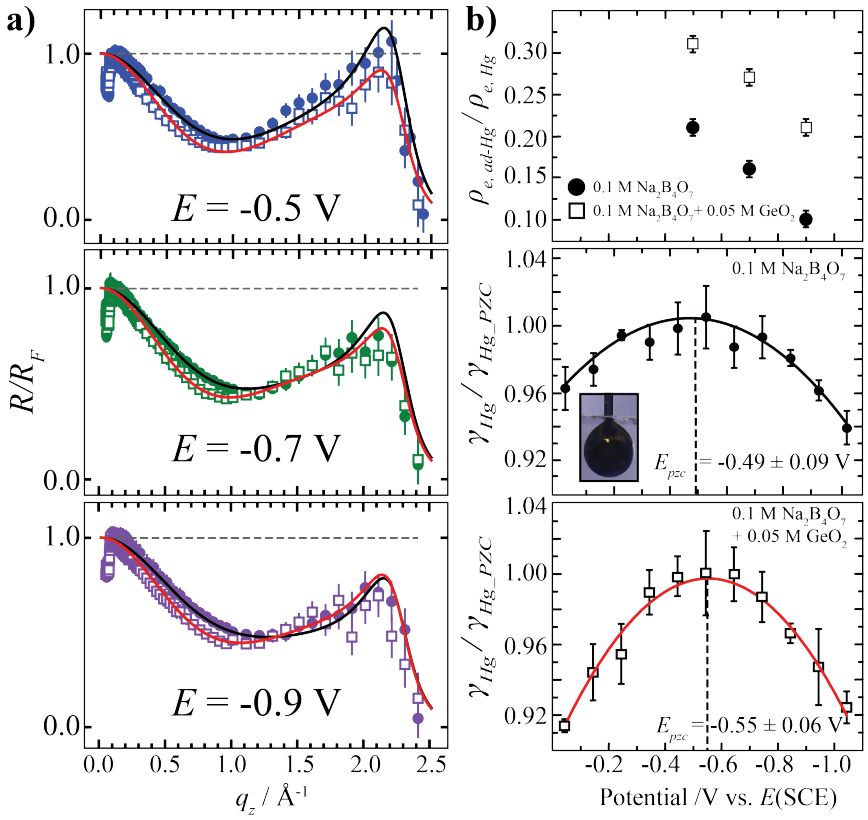

Figure 5.6: a) Comparison of the normalized X-ray reflectivity curves and corresponding fits for Hg electrodes immersed in either 0.1 M $Na_2B_4O_7$ (*aq*) (solid circles and black solid lines) or 0.1 M $Na_2B_4O_7$ + 0.05 M GeO_2(*aq*) (hollow squares and red solid lines) at -0.50 V, -0.70 V, and -0.90 V. b) (top) Potential-dependent adlayer density determined from fits of the data in (a). (middle) Normalized surface tension, γ, measurements for Hg pendant drop electrodes (inset) in 0.1 M $Na_2B_4O_7$ (*aq*). (bottom) Normalized surface tension measurements for Hg pendant drop electrodes in 0.1 M $Na_2B_4O_7$ + 0.05 M GeO_2 (*aq*).

new peak implies the formation of a new structural feature at the interface on a length scale of $2\pi/0.85^{-1} \approx 7$ Å along the surface normal.

Dynamic XRR measurements were recorded during the course of a voltammetric experiment to determine if the differences in the data in Figures 5.4 and 5.5 occurred instantly or evolved slowly over time. Figure 5.7 shows a cyclic voltammetric sweep from -0.7 to -0.2 V and back to -0.7 V. In the steady-state experiments shown in Figures 5.4 and 5.5, the XRR recorded at q_z = 0.3 Å^{-1} was significantly reduced in the presence of dissolved GeO_2 when the potential was changed from -0.5 to -0.2 V (by a factor of 1.5). Figure 5.7 shows a similar behavior in the XRR signal intensity at q_z = 0.3 Å^{-1} during the voltammetric sweep. Specifically, the potential started to decrease in the negative going scan (red symbols) below -0.4 V, parallel to the increasing current in the CV. In the subsequent scan in positive direction (blue symbols), the XRR signal intensity increased again and reached the original intensity value at ≈-0.5 V.

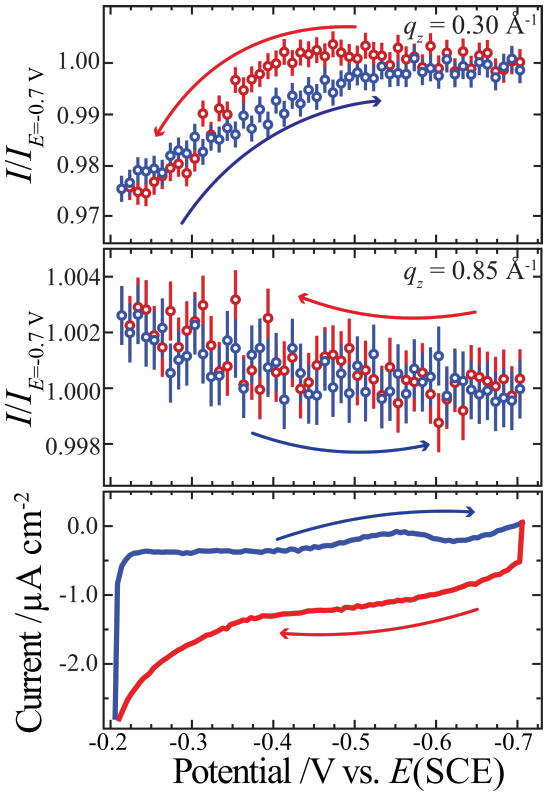

Figure 5.7: Plots depicting the reflected X-ray intensity at (top) q_z = 0.30 Å^{-1} and (middle) 0.85 Å^{-1}, recorded concurrently with (bottom) the electrochemical current during a voltammetric scan at 0.05 V s^{-1} for a Hg electrode immersed in 0.1 M $Na_2B_4O_7$ + 0.05 M GeO_2 (*aq*). The arrows denote the voltammetric sweep direction.

The noticeable hysteresis between negative and positive scan mirrors the hysteresis in the charge transfer observed in the CV indicates the surface transformation and restoration processes were kinetically distinct. XRR data were also recorded at q_z=0.85 Å^{-1}, at the local maximum in Figure 5.5b. At this q_z value, the XRR intensity is expected to increase at more positive potentials according to the steady-state observations. Despite the poorer signal to noise at this q_z, which is caused by the lower XRR, this behavior is indeed observed in the potential sweep experiments. In total, these data indicated that the initial changes in the interface structure occur rapidly upon biasing the Hg electrode. However, the relative intensity changes are at both q_z positions much lower than those that would be expected from a comparison of the steady-state XRR curves at -0.5 and -0.2 V in Figure 5.5a. This point indicates that the formation of the interface structure that is responsible for the altered XRRs is a slow process and is in accordance with the observation that XRRs with a pronounced peak at q_z=0.85 Å^{-1}are only found after longer waiting times at -0.2 V.

To obtain insight into the atomic-scale origin of the structural changes at the positive potential limit, several strategies were explored to fit the XRR data in GeO_2-containing electrolyte at -0.2 V. No satisfactory fits could be obtained with *eq* 5.5 as

written or by adding a $HGeO_3^-$ 'adlayer' as discussed above. This may be expected, as the presence of additional features in the R/R_F curve indicates that more complex interface structures are required to properly describe the data. For this purpose, a two-tiered fitting approach was adopted to identify the general and specific features of this solution/Hg interface structure. Based on the qualitative behavior of the XRR and the electrochemical data we attribute the structural changes to the formation of an ultrathin layer of a Ge compound at the Hg electrode surface.

$\rho_e(z)$ described by *eq 6*				$\rho_e(z)$ described by *eq 7*			
Model Component	**Parameter**	**Value**	**Units**	**Model Component**	***Parameter***	***Value***	***Units***
Distorted Crystal Model	$\rho_{e,ad\text{-}Hg}/\rho_{e,Hg}$	0.22 ± 0.01	Å	Distorted Crystal Model	$\rho_{e,ad\text{-}Hg}/\rho_{e,Hg}$	0.22 ± 0.01	Å
	$\sigma_{ad,Hg}$	0.93 ± 0.01	Å		$\sigma_{ad,Hg}$	0.92 ± 0.01	Å
	$z_{ad,Hg}$	-3.64	Å		$z_{ad,Hg}$	-3.64	Å
	σ_b	0.49	Å		σ_b	0.49	Å
	σ_i	-0.93 ± 0.01	Å		σ_i	-0.92 ± 0.01	Å
	d	2.75	Å		d	2.75	Å
Electrolyte	$\rho_{e,H2O}/\rho_{e,Hg}$	0.10	-	Electrolyte	$\rho_{e,H2O}/\rho_{e,Hg}$	0.10	-
	z_{H2O}	-9.52 ± 0.37	Å		z_{H2O}	-6.55 ± 0.15	Å
	σ_{H2O}	-2.90 ± 0.10	Å		σ_{H2O}	-0.92 ± 0.01	Å
1st Gaussian	$\rho_{e,ad\text{-}1}/\rho_{e,Hg}$	0.18 ± 0.01	Å	$HGeO_3^-$ 'adlayer' on Hg	$z_{Ge,1}$	-3.75 ± 0.15	Å
	$z_{ad,1}$	-3.79 ± 0.13	Å		$z_{O,1}$	-2.09 ± 0.15	Å
	$\sigma_{ad,1}$	0.92 ± 0.08	Å		$z_{O,2}$	-4.60 ± 0.15	Å
2nd Gaussian	$\rho_{e,ad\text{-}2}/\rho_{e,Hg}$	0.25 ± 0.02	Å		$\sigma_{Ge} = \sigma_O$	0.92 ± 0.01	Å
	$z_{ad,2}$	-7.05 ± 0.03	Å		$\Theta_{HGeO3^-/Hg}$	0.07 ± 0.02	Å
	$\sigma_{ad,2}$	0.92 ± 0.05	Å	GeO_2 Bilayer	$z_{Ge,1}$	-3.44 ± 0.25	Å
3rd Gaussian	$\rho_{e,ad\text{-}3}/\rho_{e,Hg}$	0.15 ± 0.02	Å		$z_{Ge,2}$	-6.61 ± 0.25	Å
	$z_{ad,3}$	-13.00 ± 0.13	Å		$z_{O,1\text{-}1}$	-2.19 ± 0.25	Å
	$\sigma_{ad,3}$	1.50 ± 0.14	Å		$z_{O,1\text{-}2}$	-3.44 ± 0.25	Å
					$z_{O,1\text{-}3}$	-4.69 ± 0.25	Å
					$z_{O,2\text{-}1}$	-5.36 ± 0.25	Å
					$z_{O,2\text{-}2}$	-6.61 ± 0.25	Å
					$z_{O,2\text{-}3}$	-7.86 ± 0.25	Å
					σ_{GeO2}	0.92 ± 0.01	Å
				$HGeO_3^-$ 'adlayer' on GeO_2	$z_{Ge,1}$	-12.60 ± 0.12	Å
					$z_{O,1}$	-10.94 ± 0.12	Å
					$z_{O,2}$	-13.45 ± 0.12	Å
					$\sigma_{Ge} = \sigma_O$	0.92 ± 0.01	Å
					$\Theta_{HGeO3^-/GeO2}$	0.22 ± 0.02	Å
					θ_{GeO2}	0.27 ± 0.03	-

Table 5.2: Parameters of the best fits of the XRR data collected in 0.1 M $Na_2B_4O_7$ + 0.05 M GeO_2 at -0.2 V[a]. a. The full expressions for $\frac{R}{R_F}$ vs q_z using *eqs 6* or *7* are detailed in the Supporting information as *eqs S2* and *S11*, respectively.

The results of the fits with *eq* 5.6 for the data collected at -0.2 V are shown in Figure 5.5 and Table 5.2. This generic fit provided no direct information on the specific identity of species accumulating at the solution/Hg interface but was useful in identifying where additional electron density, caused by Ge species at the surface, must be localized to produce the observed XRR curve (the contribution of oxygen species is much lower due to the lower Z and can be neglected in this first approach). Specifically, the fit implied a small Ge-Ge spacing of 3.26±0.13 Å (Table 5.2) near the Hg surface, consistent with rutile GeO_2 that is oriented with the [110] direction along

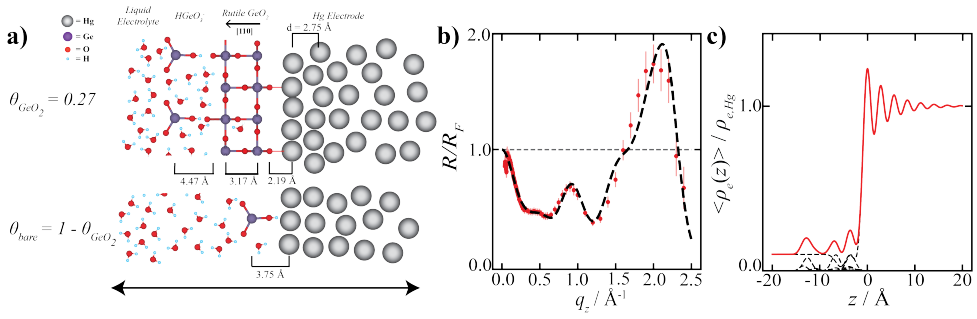

Figure 5.8: Interface structure of Hg electrodes in 0.1 M $Na_2B_4O_7$ + 0.05 M GeO_2(*aq*) at -0.2 V. a) Schematic depiction of the three-component model (*eq* 5.7) used to fit the XRR data at this potential, consisting of a surface fraction with a bilayer of solid GeO_2 (top) and a Hg surface with adsorbed $HGeO_3^-$ (bottom). The best fits were obtained with a rutile-like bilayer structure, oriented with the [110] direction along the surface normal, and a layer of adsorbed $HGeO_3^-$ on top. b) XRR curve shown in Figure 5.5a together with best fit by this model (dashed black line), corresponding to a bilayer coverage of θ_{GeO2} = 0.27 ±0.01. c) Electron density profile corresponding to the fit shown in (b).

the surface normal (3.17 Å).[44-47] A rutile crystal structure seems reasonable, since this phase is the thermodynamically stable polymorph at ambient temperature and pressure.[48] Attempts to verify the presence of a rutile phase at -0.2 V by in-plane X-ray diffraction studies were unsuccessful, however. This is not surprising, as the total amount of material is low (see below) and the crystals would be arranged in arbitrary in-plane orientation on the liquid Hg surface (i.e., form a two-dimensional powder), which would result in very weak diffraction peaks. Considering these aspects, the second phase of fitting for these data focused on a separate model with a presumed atomic structure based on GeO_2 in form of a (110)-oriented rutile polymorph (Figure 5.8a).

Fits with a GeO_2 bilayer that completely covered the Hg surface did provide qualitatively reasonable simulated XRR curves but the quantitative agreement was poor, particularly in the q_z ranges of 0.25 – 0.75 $Å^1$ and 1.0 – 1.5 $Å^{-1}$ (*Supporting Information*). However, a suitable fit was obtained when the surface was modelled with a partial coverage of rutile GeO_2 (Figure 5.8a). In this model, only a fraction θ_{GeO2} of the surface was considered to be covered by a film of solid, crystalline rutile GeO_2. This film was modelled as a rutile bilayer with a layer of adsorbed $HGeO_3^-$ on top. The remaining surface (i.e. '1 - θ_{GeO2}') was assumed to consist of an Hg electrode with adsorbed $HGeO_3^-$, as employed for modelling the XRR data at potentials negative of -0.2 V. This model satisfactorily fits the XRR data in GeO_2-containing solution at -0.2 V, resulting in a rutile coverage θ_{GeO2} = 0.27 ± 0.01 for the R/R_F curve shown in Figure 5.8b (Table 5.2). Analogous models where the atomic Ge and O positions reflected *a*-quartz or other rutile crystalline directions could not be absolutely ruled out but generally yielded slightly poorer fits.

The data collectively support the premise that adsorbed Ge species are present on Hg electrodes immersed in solutions with dissolved GeO_2. However, the adsorbed species are not the same at all potentials. At comparatively negative potentials, the evidence points to the accumulation of solvated H_2GeO_3 and/or $HGeO_3{}^-$ at the Hg interface. At more positive potentials, the data implicate the growth of a condensed phase from the $HGeO_3{}^-$ adlayer. The condensation does not appear redox-based but instead the consequence of $HGeO_3^-$ accumulation on the Hg surface far from E_{pzc}. These points are elaborated below.

5.5.1 Hg/Electrolyte Interface at $<$ -0.2 V Potentials

Our studies show that Hg immersed in 0.1 M $Na_2B_4O_7(aq)$ has a similar E_{pzc} as in NaF(aq), exhibits only featureless double layer charging in voltammograms, and has an identical atomic layering within Hg. These observations are consistent with the premise that $Na_2B_4O_7(aq)$ is not forming strong chemical bonds with the Hg surface atoms. While fortuitous, this point could not be assumed *a priori*. Extensive adsorption of $B_4O_7^{2-}$ on solid metal electrodes is known.[49]1 The reasons for the relative inertness of $B_4O_7^-$ anions towards Hg were not explored. Nevertheless, the XRR argue directly against any complicating chemistry between Hg and $B_4O_7^{2-}$ within the potential range explored here, making the $Na_2B_4O_7(aq)$ a suitable base electrolyte for studies on the adsorption of Ge species.

The changes in the electrochemical behavior upon addition of GeO_2 to the electrolyte indicate adsorption of a $H_2GeO_3/HGeO_3^-$ species. The negative shift of E_{pzc} would be consistent with specific anion adsorption but chemisorption of a neutral species can also not be excluded. At the more negative potentials in the range explored here, the XRR data provide clear evidence that there is excess electron density at the water/Hg interface when GeO_2 is dissolved in the electrolyte. Although the XRR data are not definitive on the identity of the species, enrichment of the double layer with $HGeO_3^-$ and/or H_2GeO_3 is consistent with the cumulative observations. The chemisorption of $H_2GeO_3/HGeO_3^-$ at metal electrodes has been noted previously. At this same pH, molecular adlayers were previously observed on single crystalline Au electrodes by electrochemical scanning tunneling microscopy.[50] Ge-containing adsorbates in this electrolyte were separately identified on polycrystalline Au by surface-enhanced Raman measurements.[51] In the work here, the specific binding mode of $H_2GeO_3/HGeO_3^-$ to the Hg surface could not be unambiguously determined. However, the best fits were obtained with a separation distance of 2.09 Å between the O and Hg electron densities at the interface, suggestive of a bridging Ge-O-Hg bond. The $HGeO_3^-$ coverage of 0.20 ML (corresponding to a surface area per molecule of 45 $Å^2$) was less than the 0.33 ML (surface area per molecule of 20 $Å^2$) found previously on Au(111).[50] Considering that the coverage is constant over a wide potential range from -0.35 V below to 0.05 V more positive of E_{pzc}, adsorption of a neutral species (H_2GeO_3) appears more likely than adsorption of $HGeO_3^-$.

Unambiguous clarification of the adsorbed species is difficult, however, because of the assumptions involved in determination of the coverage from the adlayer peak in the electron density profile (see above). Overall, the XRR data here indicate that the role of chemisorbed $H_2GeO_3/HGeO_3^-$ should be considered when determining the mechanism(s) of Ge electrodeposition with Hg electrodes in this electrolyte.

5.5.2 Hg/Electrolyte Interface at $\geq$ -0.2 V

In the presence of dissolved GeO_2, the XRR and CV data provide clear evidence for a structural transition at the Hg surface as the potential approaches -0.2 V. This transition has to be related to a surface phase containing Ge. However, neither Hg nor $HGeO_3{}^-$ are redox active at this potential, so a direct, redox-based oxide growth is difficult to rationalize. One possible interpretation of the voltammetric features in Figure 5.2 is a potential-dependent change in the protonation state of the adsorbate. That is, the Bronsted acid/base character of $H_2GeO_3/HGeO_3{}^-$ can be expressed as follows,[38]

$$OH^- + H_2GeO_3 \rightleftharpoons HGeO_3^- + H_2O \tag{5.8}$$

In homogeneous solution, this reaction favors the products (i.e. deprotonation of $HGeO_3^-$, pK_A = 8.52) only at more alkaline pH values.[38] However, if localized at an electrode surface, the equilibrium of this acid/base reaction will couple to the electrostatic potential drop across the diffuse layer.[52] If the rates of protonation/deprotonation are sufficiently fast and the potential drop between the electrode surface and the adsorbate is negligible, the surface concentrations of H_2GeO_3 and $HGeO_3^-$ ($[H_2GeO_3]_s$ and $[HGeO_3^-]_s$, respectively) become dependent on the applied potential in the following manner, [52]

$$\ln\left(\frac{[HGeO_3^-]_s}{[H_2GeO_3]_s}\right) \approx \ln 10\,(pH - pK_A) + \frac{F}{RT}\left(E - E_{pzc}\right) \tag{5.9}$$

where F is the Faraday constant and R is the ideal gas constant.

If both H_2GeO_3 and $HGeO_3^-$ do not desorb from the electrode surface as a result of deprotonation/protonation, differentiating *eq* 5.9 with respect to potential describes the rate at which the deprotonation/protonation of the adsorbate occurs as the potential is changed. This rate has the same underlying mathematical form[53-54] as the reduction/oxidation of a redox adsorbate and will elicit an electrochemical current that describes when the net charge of the adsorbate transitions through protonation/deprotonation states. That is, when the potential relative to E_{pzc} is positive enough, the adsorbed species will deprotonate, producing a current that is not associated with a redox reaction but has the same principle features.[55-57] This point is well known for self-assembled monolayers featuring terminal acid groups.[52, 55, 58] Accordingly, *eq* 5.9 predicts that $HGeO_3^-$ will be the dominant species at sufficiently positive potentials, irrespective of solution pH. For example, a potential of 300 mV

more positive than E_{pzc} will increase the surface concentration of $HGeO_3^-$ by a factor of $\sim 10^5$ at pH = 9.13 and T = 25 ° C.

Although *eq* 5.9 provides a possible rationale for the electrochemical data, changes in just the protonation state of the adsorbate would not elicit the observed XRR data. However, the following chemical equilibrium is known for $HGeO_3^-$, [38]

$$HGeO_3^-(aq) GeO_2(s) + OH^-(aq) \tag{5.10}$$

Eq 5.10 describes the conversion (precipitation) of solvated $HGeO_3^-$ into of solid GeO_2. Mechanistically, such a process involves the formation of a Ge-O-Ge linkage between neighboring monomers of $HGeO_3^-$ (or a cogener).[59] We posit that a surface with predominantly adsorbed $HGeO_3^-$ would be subject to such a condensation reaction and would be consistent with the presented XRR data. That is, when adsorbed H_2GeO_3 is de-protonated because of a positive applied potential, the neighboring and newly formed $HGeO_3^-$ adsorbates undergo *eq* 5.10 and form a new, defined phase at the Hg surface.

An electrochemically-coupled acid/base reaction that produces a film by precipitation would likely be limited to small thicknesses. The potential drop across the double layer would necessarily decrease when a dielectric (GeO_2) accumulates at the surface, thereby stopping the products of *eq* 5.10 from being favored. Two facts support this premise. First, the relative dielectric constant of GeO_2 (5.2) is much smaller than that of water (80.4).[60-61] Second, extremely long experiments (biasing at -0.2 V for days) were attempted to grow thicker films of GeO_2. In every trial, no macroscopic quantity of material was produced. This is in accordance with the XRR studies that find much less than a monolayer coverage even after keeping the potential for 15 min. at -0.20 V.

The XRR data argue against a description of extended rutile GeO_2 sheets for the phase identified by the XRR data, as they show clearly that the condensed phase formed at -0.2 V is readily removed by moving the electrode potential more negative than -0.5 V. Bulk rutile GeO_2 is relatively insoluble in water,[38] so simply shifting the electrode potential more negative would not necessarily be expected to remove or dissolve rutile GeO_2 from the Hg interface. In addition, it is not clear why hypothetical rutile GeO_2 sheets would be limited to a low incomplete surface coverage, as indicated by the data. These points suggest that an alternate form of GeO_2 is more likely under the investigated conditions.

Polygermanates are a class of macromolecular germanium oxyanions composed of edge-sharing GeO_6 octahedra and GeO_4 tetrahedra.[62-65] These oxyanions can exhibit a variety of sizes and structures, i.e. from linear chains to porous networks.[64-65] In the solid-state, polygermanates are charge-stabilized by small cations. If the positive surface charge at an electrode surface, kept at potentials positive of E_{pzc}, similarly stabilizes polygermanate anions, polygermanates may be the relevant species

indicated by the XRR data. Several points support this general premise. First, multiple polygermanates feature the same six-coordinate Ge arrangement as in rutile GeO_2, e.g. $Ge_7O_{15}^{2-}$,[64,66-67] consistent with the fitting results reported here. Second, the dissolution/removal of a charge-stabilized polygermanate anion at the Hg interface would be expected at more negative potentials, as observed here. Third, the XRR fits were consistent with both an incomplete surface coverage and defined bilayer structures, i.e. defined stoichiometry between the first and second Ge-O layers. Porous and cyclic polygermanates are known[64] that, if adsorbed, could conceivably still leave a significant fraction of an electrode surface exposed while still maintaining defined positions of the constituent Ge atoms.

Although the formation mechanism of polygermanates was not interrogated directly in this work, the possibility of their synthesis at liquid metal electrode surfaces is intriguing. Typically, polygermanates (and oxocondensates more generally) are prepared by heating saturated solutions of dissolved precursors in a closed vessel.[63] Elevated temperatures are necessary to increase solubility and lower activation barriers of formation. The data here could indicate that an alternative reaction route that doesn't require high temperatures is possible if the precursor species are adsorbed onto an electrode. If so, XRR features such as the hysteresis in Figure 5.7 should also contain information on the energetic barriers of formation, in analogous fashion to hysteresis analysis in the voltammetry of conventional electrodeposition.[68] The known activation barrier for Ge-O-Ge linkage formation (36 kJ mol^{-1})[59] in homogeneous solution is sufficient to suggest that polygermanate formation/deconstruction at an electrode surface would not necessarily occur instantly following deprotonation of H_2GeO_3. The difference in the rates of deposition vs removal indicated by the hysteresis in the time-dependent XRR data are consistent with a strongly kinetically hindered nucleation and growth.[69-70] More work is needed to develop these points further. Nevertheless, the innate value of XRR for such studies is clear.

5.6 Conclusions

The work presented here provide insights how Ge species in aqueous solution interact with liquid Hg electrodes as a function of potential. Clear evidence for the adsorption of Ge species at the electrolyte-liquid metal interface over a wide potential range is found in electrolyte containing dissolved GeO_2. The collected XRR profiles atomic-scale data on the interface structure significantly go beyond that obtainable by electrochemical studies alone. Specifically, the work here illustrates that at least two different types of adlayers form on Hg in solutions containing dissolved GeO_2. At more negative potentials, adsorbed $H_2GeO_3/HGeO_3^-$ persists at Hg electrodes. At the most positive potentials, a condensed phase forms with atomic spacing consistent with polygermanates with a rutile GeO_2 sub-structure. The presented data

suggest accumulation of oxyanions at a liquid metal electrode could present an alternative synthetic route for oxocondensates that are otherwise only obtained by hydrothermal reactions.[63] Thus, these observations incentivize further *in-situ* studies of Hg and other liquid metal electrodes in this electrolyte to elucidate the operative surface species during material syntheses. In total, the results presented here provide specific new insights on the surface chemistry of Hg in this electrolyte and illustrate the advantages of XRR as a tool for *in situ* studies of liquid metal electrode interfaces.

Acknowledgements

We acknowledge generous financial support from the National Science Foundation (CHE-1807755) for S. M. and by the Deutsche Forschungsgemeinschaft (Ma1618/18) and the German Federal Ministry for Science and Education (05K16FK2 and 05K19K2) for A.S., R.P.G., O.M.M. and B.M.M. We also thank the beamline staff Florian Bertram and Chen Shen at P08 of PETRA III for experimental support and DESY for the beam time.

Supporting Information

Additional detail on the XRR models as well as the raw XRR data prior to normalization are presented in the Supporting Information.

5.7 References

1. Martin, A.; Du, C.; Chang, B.; Thuo, M., "Complexity and Opportunities in Liquid Metal Surface Oxides." Chemistry of Materials 2020, 32 (21), 9045-9055.

2. Zavabeti, A.; Ou, J. Z.; Carey, B. J.; Syed, N.; Orrell-Trigg, R.; Mayes, E. L. H.; Xu, C.; Kavehei, O.; O'Mullane, A. P.; Kaner, R. B.; Kalantar-zadeh, K.; Daeneke, T., "A liquid metal reaction environment for the room-temperature synthesis of atomically thin metal oxides." Science 2017, 358 (6361), 332.

3. Daeneke, T.; Khoshmanesh, K.; Mahmood, N.; de Castro, I. A.; Esrafilzadeh, D.; Barrow, S. J.; Dickey, M. D.; Kalantar-zadeh, K., "Liquid metals: fundamentals and applications in chemistry." Chemical Society Reviews 2018, 47 (11), 4073-4111.

4. Dong, R.; Zhang, T.; Feng, X., "Interface-Assisted Synthesis of 2D Materials: Trend and Challenges." Chemical Reviews 2018, 118 (13), 6189-6235.

5. Zavabeti, A.; Zhang, B. Y.; de Castro, I. A.; Ou, J. Z.; Carey, B. J.; Mohiuddin, M.; Datta, R.; Xu, C.; Mouritz, A. P.; McConville, C. F.; O'Mullane, A. P.; Daeneke, T.; Kalantar-Zadeh, K., "Green Synthesis of Low-Dimensional Aluminum Oxide Hydroxide and Oxide Using Liquid Metal Reaction Media: Ultrahigh Flux Membranes." Advanced Functional Materials 2018, 28 (44), 1804057.

6. Ghasemian, M. B.; Mayyas, M.; Idrus-Saidi, S. A.; Jamal, M. A.; Yang, J.; Mofarah, S. S.; Adabifiroozjaei, E.; Tang, J.; Syed, N.; O'Mullane, A. P.; Daeneke, T.; Kalantar-Zadeh, K., "Self-Limiting Galvanic Growth of MnO2 Monolayers on a Liquid Metal—Applied to Photocatalysis." Advanced Functional Materials 2019, 29 (36), 1901649.

7. Alkathiri, T.; Dhar, N.; Jannat, A.; Syed, N.; Mohiuddin, M.; Alsaif, M. M. Y. A.; Datta, R. S.; Messalea, K. A.; Zhang, B. Y.; Khan, M. W.; Elbourne, A.; Pillai, N.; Ou, J. Z.; Zavabeti, A.; Daeneke, T., "Atomically thin TiO2 nanosheets synthesized using liquid metal chemistry." Chemical Communications 2020, 56 (36), 4914-4917.

8. Elsen, A.; Festersen, S.; Runge, B.; Koops, C. T.; Ocko, B. M.; Deutsch, M.; Seeck, O. H.; Murphy, B. M.; Magnussen, O. M., "In situ X-ray studies of adlayer-induced crystal nucleation at the liquid–liquid interface." Proceedings of the National Academy of Sciences 2013, 110 (17), 6663.

9. Kochat, V.; Samanta, A.; Zhang, Y.; Bhowmick, S.; Manimunda, P.; Asif Syed Asif, S.; Stender Anthony, S.; Vajtai, R.; Singh Abhishek, K.; Tiwary Chandra, S.; Ajayan Pulickel, M., "Atomically thin gallium layers from solid-melt exfoliation." Science Advances 2018, 4 (3), e1701373.

10. Tao, P.; Yao, S.; Liu, F.; Wang, B.; Huang, F.; Wang, M., "Recent advances in exfoliation techniques of layered and non-layered materials for energy conversion and storage." Journal of Materials Chemistry A 2019, 7 (41), 23512-23536.

11. Benbow, E. M.; Dalal, N. S.; Latturner, S. E., "Crystal growth and magnetic behavior of R6T13-xAlxMy phases (R=La, Nd; T=Mn, Fe; M=main group) grown from lanthanide-rich eutectic fluxes." Journal of Solid State Chemistry 2009, 182 (11), 3055-3062.

12. He, H.; Tyson, C.; Saito, M.; Bobev, S., "Synthesis and structural characterization of the ternary Zintl phases AE3Al2Pn4 and AE3Ga2Pn4 (AE=Ca, Sr, Ba, Eu; Pn=P, As)." Journal of Solid State Chemistry 2012, 188, 59-65.

13. Stojanovic, M.; Latturner, S. E., "Growth of new ternary intermetallic phases from Ca/Zn eutectic flux." Journal of Solid State Chemistry 2007, 180 (3), 907-914.

14. Carim, A. I.; Collins, S. M.; Foley, J. M.; Maldonado, S., "Benchtop Electrochemical Liquid–Liquid–Solid Growth of Nanostructured Crystalline Germanium." Journal of the American Chemical Society 2011, 133 (34), 13292-13295.

15. Kanatzidis, M. G.; Pöttgen, R.; Jeitschko, W., "The Metal Flux: A Preparative Tool for the Exploration of Intermetallic Compounds." Angewandte Chemie International Edition 2005, 44 (43), 6996-7023.

16. Sebastian, C. P.; Malliakas, C. D.; Chondroudi, M.; Schellenberg, I.; Rayaprol, S.; Hoffmann, R.-D.; Pöttgen, R.; Kanatzidis, M. G., "Indium Flux-Growth of Eu2AuGe3:

A New Germanide with an AlB2 Superstructure." Inorganic Chemistry 2010, 49 (20), 9574-9580.

17. Budevski, E.; Staikov, G.; Lorenz, W. J., Electrochemical Phase Formation and Growth: An Introduction to the Initial Stages of Metal Deposition. VCH Verlagsgesellschaft mbH: Weinheim, 1996.

18. King, D. A.; Woodruff, D. P., Growth and Properties of Ultrathin Epitaxial Layers. El Sevier Ltd.: 1997; Vol. 8.

19. Pershan, P. S.; Schlossman, M., Liquid Surfaces and Interfacs: Synchrotron X-ray Methods. Cambridge University Press: Cambridge, 2012.

20. Magnussen, O. M.; Ocko, B. M.; Regan, M. J.; Penanen, K.; Pershan, P. S.; Deutsch, M., "X-Ray Reflectivity Measurements of Surface Layering in Liquid Mercury." Physical Review Letters 1995, 74 (22), 4444-4447.

21. DiMasi, E.; Tostmann, H.; Ocko, B. M.; Pershan, P. S.; Deutsch, M., "X-ray reflectivity study of temperature-dependent surface layering in liquid Hg." Physical Review B 1998, 58 (20), R13419-R13422.

22. Regan, M. J.; Pershan, P. S.; Magnussen, O. M.; Ocko, B. M.; Deutsch, M.; Berman, L. E., "X-ray reflectivity studies of liquid metal and alloy surfaces." Physical Review B 1997, 55 (23), 15874-15884.

23. Regan, M. J.; Kawamoto, E. H.; Lee, S.; Pershan, P. S.; Maskil, N.; Deutsch, M.; Magnussen, O. M.; Ocko, B. M.; Berman, L. E., "Surface Layering in Liquid Gallium: An X-Ray Reflectivity Study." Physical Review Letters 1995, 75 (13), 2498-2501.

24. Elsen, A.; Murphy, B. M.; Ocko, B. M.; Tamam, L.; Deutsch, M.; Kuzmenko, I.; Magnussen, O. M., "Surface Layering at the Mercury-Electrolyte Interface." Physical Review Letters 2010, 104 (10), 105501.

25. Murphy, B. M.; Greve, M.; Runge, B.; Koops, C. T.; Elsen, A.; Stettner, J.; Seeck, O. H.; Magnussen, O. M., "A novel X-ray diffractometer for studies of liquid-liquid interfaces." Journal of Synchrotron Radiation 2014, 21 (1), 45-56.

26. Murphy, B. M.; Festersen, S.; Magnussen, O. M., "The Atomic scale structure of liquid metal–electrolyte interfaces." Nanoscale 2016, 8 (29), 13859-13866.

27. Runge, B.; Festersen, S.; Koops, C. T.; Elsen, A.; Deutsch, M.; Ocko, B. M.; Seeck, O. H.; Murphy, B. M.; Magnussen, O. M., "Temperature- and potential-dependent structure of the mercury-electrolyte interface." Physical Review B 2016, 93 (16), 165408.

28. Festersen, S.; Runge, B.; Koops, C.; Bertram, F.; Ocko, B.; Deutsch, M.; Murphy, B. M.; Magnussen, O. M., "Nucleation and Growth of PbBrF Crystals at the Liquid Mercury–Electrolyte Interface Studied by Operando X-ray Scattering." Langmuir 2020, 36 (37), 10905-10915.

29. Pattadar, D.; Cheek, Q.; Sartori, A.; Zhao, Y.; Giri, R. P.; Murphy, B.; Magnussen, O.; Maldonado, S., "Evidence for Facilitated Surface Transport during Ge Crystal Growth by Indium in Liquid Hg–In Alloys at Room Temperature." Crystal Growth & Design 2021, 21 (3), 1645-1656.

30. Zhang, T.; Fahrenkrug, E.; Maldonado, S., "Electrochemical Liquid-Liquid-Solid Deposition of Ge at Hg Microdroplet Ultramicroelectrodes." Journal of The Electrochemical Society 2016, 163 (9), D500-D505.

31. Demuth, J.; Fahrenkrug, E.; Ma, L.; Shodiya, T.; Deitz, J. I.; Grassman, T. J.; Maldonado, S., "Electrochemical Liquid Phase Epitaxy (ec-LPE): A New Methodology for the Synthesis of Crystalline Group IV Semiconductor Epifilms." Journal of the American Chemical Society 2017, 139 (20), 6960-6968.

32. Hansen, F. K.; Rødsrud, G., "Surface tension by pendant drop: I. A fast standard instrument using computer image analysis." Journal of Colloid and Interface Science 1991, 141 (1), 1-9.

33. Daerr, A.; Mogne, A., "Pendant Drop: An ImageJ Plugin to Measure the Surface Tension from an Image of a Pendant Drop." Journal of Open Research Software, 4(1), p.e3. DOI: http://doi.org/10.5334/jors.97 2016, 4 (1), e3.

34. Als-Nielsen, J.; McMorrow, D., Refraction and Reflection from Interfaces. In Elements of Modern X-ray Physics, Wiley: 2011; pp 69-112.

35. D'Evelyn, M. P.; Rice, S. A., "A study of the liquid–vapor interface of mercury: Computer simulation results." The Journal of Chemical Physics 1983, 78 (8), 5081-5095.

36. Duval, J. F. L.; Bera, S.; Michot, L. J.; Daillant, J.; Belloni, L.; Konovalov, O.; Pontoni, D., "X-Ray Reflectivity at Polarized Liquid-Hg–Aqueous-Electrolyte Interface: Challenging Macroscopic Approaches for Ion-Specificity Issues." Physical Review Letters 2012, 108 (20), 206102.

37. Isac-García, J.; Dobado, J. A.; Calvo-Flores, F. G.; Martínez-García, H., Chapter 13 - Green Chemistry Experiments. In Experimental Organic Chemistry, Isac-García, J.; Dobado, J. A.; Calvo-Flores, F. G.; Martínez-García, H., Eds. Academic Press: 2016; pp 417-484.

38. Pourbaix, M., Atlas of electrochemical equilibria in aqueous solutions. 2d English ed.; National Association of Corrosion Engineers: Houston, Tex., 1974; p 644 p.

39. Grahame, D. C., "The Electrical Double Layer and the Theory of Electrocapillarity." Chemical Reviews 1947, 41 (3), 441-501.

40. Grahame, D. C.; Larsen, R. P.; Poth, M. A., "The Potential of the Electrocapillary Maximum of Mercury." Journal of the American Chemical Society 1949, 71 (9), 2978-2983.

41. Grahame, D. C., "Differential Capacity of Mercury in Aqueous Sodium Fluoride Solutions. I. Effect of Concentration at 25°." Journal of the American Chemical Society 1954, 76 (19), 4819-4823.

42. Grahame, D. C., "Capacity of the Electrical Double Layer between Mercury and Aqueous Sodium Fluoride. II. Effect of Temperature and Concentration." Journal of the American Chemical Society 1957, 79 (9), 2093-2098.

43. Tostmann, H.; DiMasi, E.; Pershan, P. S.; Ocko, B. M.; Shpyrko, O. G.; Deutsch, M., "Surface structure of liquid metals and the effect of capillary waves: X-ray studies on liquid indium." Physical Review B 1999, 59 (2), 783-791.

44. https://www.cryst.ehu.es/.

45. Bradlyn, B.; Elcoro, L.; Cano, J.; Vergniory, M. G.; Wang, Z.; Felser, C.; Aroyo, M. I.; Bernevig, B. A., "Topological quantum chemistry." Nature 2017, 547 (7663), 298-305.

46. Vergniory, M. G.; Elcoro, L.; Felser, C.; Regnault, N.; Bernevig, B. A.; Wang, Z., "A complete catalogue of high-quality topological materials." Nature 2019, 566 (7745), 480-485.

47. Vergniory, M. G.; Wieder, B. J.; Elcoro, L.; Parkin, S. S. P.; Felser, C.; Bernevig, B. A.; Regnault, N., "All Topological Bands of All Stoichiometric Materials." arXiv:2105.09954 [cond-mat.mtrl-sci] 2021.

48. Hill, V. G.; Chang, L. L. Y., "Hydrothermal investigation of GeO2." American Mineralogist 1968, 53 (9-10), 1744-1748.

49. Stevenson, K. J.; Gao, X.; W. Hatchett, D.; White, H. S., "Voltammetric measurement of anion adsorption on Ag(111)." Journal of Electroanalytical Chemistry 1998, 447 (1), 43-51.

50. Liang, X.; Kim, Y.-G.; Gebergziabiher, D. K.; Stickney, J. L., "Aqueous Electrodeposition of Ge Monolayers." Langmuir 2010, 26 (4), 2877-2884.

51. Carim, A. I.; Gu, J.; Maldonado, S., "Overlayer Surface-Enhanced Raman Spectroscopy for Studying the Electrodeposition and Interfacial Chemistry of Ultrathin Ge on a Nanostructured Support." ACS Nano 2011, 5 (3), 1818-1830.

52. Smith, C. P.; White, H. S., "Voltammetry of molecular films containing acid/base groups." Langmuir 1993, 9 (1), 1-3.

53. Waelder, J.; Maldonado, S., "Beyond the Laviron Method: A New Mathematical Treatment for Analyzing the Faradaic Current in Reversible, Quasi-Reversible, and Irreversible Cyclic Voltammetry of Adsorbed Redox Species." Anal. Chem. 2021, 93 (37), 12672-12681.

54. Myland, J. C.; Oldham, K. B., "Quasireversible cyclic voltammetry of a surface confined redox system: a mathematical treatment." Electrochemistry Communications 2005, 7 (3), 282-287.

55. White, H. S.; Peterson, J. D.; Cui, Q.; Stevenson, K. J., "Voltammetric Measurement of Interfacial Acid/Base Reactions." The Journal of Physical Chemistry B 1998, 102 (16), 2930-2934.

56. Burgess, I.; Seivewright, B.; Lennox, R. B., "Electric Field Driven Protonation/Deprotonation of Self-Assembled Monolayers of Acid-Terminated Thiols." Langmuir 2006, 22 (9), 4420-4428.

57. Luque, A. M.; Mulder, W. H.; Calvente, J. J.; Cuesta, A.; Andreu, R., "Proton Transfer Voltammetry at Electrodes Modified with Acid Thiol Monolayers." Analytical Chemistry (Washington, DC, United States) 2012, 84, 5778-5786.

58. Calvente, J. J.; Luque, A. M.; Andreu, R.; Mulder, W. H.; Olloqui-Sariego, J. L., "Analytical Expressions for Proton Transfer Voltammetry: Analogy to Surface Redox Voltammetry with Frumkin Interactions." Analytical Chemistry 2013, 85 (9), 4475-4482.

59. Trinh, T. T.; Rozanska, X.; Delbecq, F.; Tuel, A.; Sautet, P., "The mechanism of the initial step of germanosilicate formation in solution: a first-principles molecular dynamics study." Physical Chemistry Chemical Physics 2016, 18 (21), 14419-14425.

60. Murad, S. N. A.; Baine, P. T.; McNeill, D. W.; Mitchell, S. J. N.; Armstrong, B. M.; Modreanu, M.; Hughes, G.; Chellappan, R. K., "Optimisation and scaling of interfacial GeO2 layers for high-κ gate stacks on germanium and extraction of dielectric constant of GeO2." Solid-State Electronics 2012, 78, 136-140.

61. Lee, C. H.; Tabata, T.; Nishimura, T.; Nagashio, K.; Kita, K.; Toriumi, A., "Ge/GeO2 Interface Control with High Pressure Oxidation for Improving Electrical Characteristics." ECS Transactions 2019, 19 (1), 165-173.

62. Smart, M. M.; McMillen, C. D.; Ivey, K.; Kolis, J. W., "Chemistry of Metal Silicates and Germanates: The Largest Metal Polygermanate, K11Mn21Ge32O86(OH)9(H2O), with a 76 Å Periodic Lattice." Inorganic Chemistry 2020, 59 (23), 16804-16808.

63. Everest, D. A.; Salmon, J. E., "Studies in the chemistry of quadrivalent germanium. Part II. The depolymerisation of the pentagermanate ion with change of pH, and ion-exchange studies of germanate solutions containing sulphate and orthophosphate." Journal of the Chemical Society (Resumed) 1955, (0), 1444-1449.

64. Qin, C.; Gao, L.; Wang, E., "Germanium: Inorganic Chemistry Based in part on the article Germanium: Inorganic Chemistry by Frank Glockling which appeared in the Encyclopedia of Inorganic Chemistry, First Edition." Encyclopedia of Inorganic Chemistry 2005.

65. Ingri, N., "Equilibrium Studies of Polyanions. 12. Polygermanates in Na(Cl) Medium." Acta Chemica Scandinavica 1963, 17, 597-617.

66. Vegas, A.; Jenkins, H. D. B., "A revised interpretation of the structure of (NH4)2Ge7O15 in the light of the Extended Zintl-Klemm Concept." Acta Crystallographica Section B 2017, 73 (1), 94-100.

67. Ingri, N.; Lundgren, G., "The Crystal Structure of Na4Ge9O20." Acta Chemica Scandinavica 1963, 17, 617-633.

68. Emery, S. B.; Hubbley, J. L.; Roy, D., "Voltammetric and amperometric analyses of electrochemical nucleation: electrodeposition of copper on nickel and tantalum." Journal of Electroanalytical Chemistry 2004, 568, 121-133.

69. Guo, L.; Searson, P. C., "On the influence of the nucleation overpotential on island growth in electrodeposition." Electrochimica Acta 2010, 55 (13), 4086-4091.

70. Guo, L.; Oskam, G.; Radisic, A.; Hoffmann, P. M.; Searson, P. C., "Island growth in electrodeposition." Journal of Physics D: Applied Physics 2011, 44 (44), 443001.

5.8 Supporting Information

Detection of Ge-Containing Adlayers at the Liquid Hg/Water Interface by In Situ X-Ray Reflectivity in Aqueous Borate Electrolytes Containing Dissolved GeO_2

S1. Contents

This document contains supporting information for the manuscript entitled *Detection of Ge-Containing Adlayers at the Liquid Hg/Water Interface by In Situ X-Ray Reflectivity in Aqueous Borate Electrolytes Containing Dissolved GeO_2.'* Section S2 collects the raw XRR data shown in Figures 5.3, 5.4, and 5.5 in the main text prior normalization by the Fresnel reflectivity. Section S3 summarizes the explicit form of the 'master formula' using *eq* 5.6 of the main text for $\rho_e(z)$. Section S4 presents the explicit form of the 'master formula' using *eq* 5.7 of the main text for $\rho_e(z)$ to describe adsorbed $H_2GeO_3/HGeO_3^-$. Section S5 presents the full expression for the distance-dependent electron density profile normal to the surface plane for a Hg surface featuring a partial coating of GeO_2. Section S6 presents an alternate the fit of data collected at -0.2 V in a solution containing 0.1 M $Na_2B_4O_7$ and 0.05 M GeO_2.

S2. XRR Data Without Normalization

The XRR data presented in the main text are reproduced below as absolute X-ray reflectivity. In these plots, the dark grey dashed lines indicate the Fresnel reflectivity of an interface with a monotonic electron density profile with no surface roughness. The colored dashed lines correspond to the Fresnel reflectivity of an interface with a monotonic electron density profile with a nominal roughness of 1.00 . These Fresnel reflectivities were used to normalize the data in Figures 5.3, 5.4, and 5.5 of the main text.

S3. Refinement to *eq* 5.2 to Describe Enrichment Hg Interface with General Gaussian Terms

The following expressions constitute a refinement to the model described by *eq* 5.5 in the main text. In the approach presented below, additional Gaussian terms were included to account for the possibility of additional electron density throughout the solution/Hg interface. These new Gaussian terms do not pertain to any specific element and so they cannot give precise information of composition or structure. Instead, the intent of these general Gaussian terms was to assess where excess electron density was needed to yield a good match to the data. This information was used to

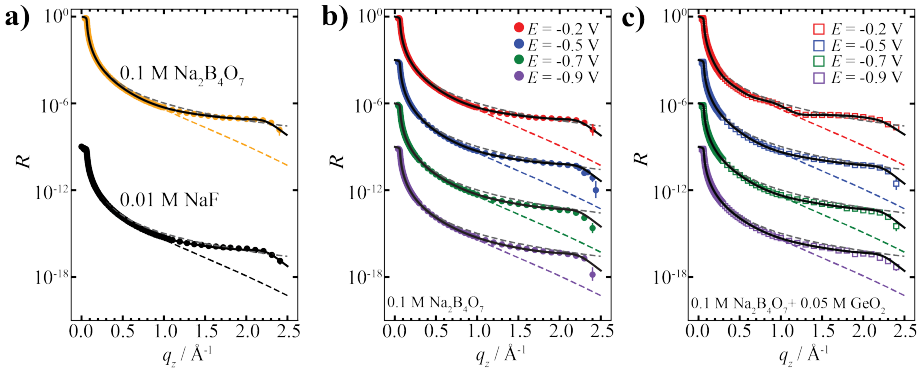

Figure 5.9: a) Plots of the absolute X-ray reflectivity vs. momentum transfer perpendicular to the surface for a Hg electrode immersed in deaerated electrolyte containing either 0.1 M $Na_2B_4O_7(aq)$ or 0.01 M NaF(aq). These data were normalized in Figure 5.3 of the main text. b) Plots of the absolute X-ray reflectivity vs. momentum transfer perpendicular to the surface in 0.1 M $Na_2B_4O_7(aq)$ at four different potentials: E = -0.2 V (red circles), -0.5 V (blue circles), -0.7 V (green circles), and -0.9 V (purple circles). These data were normalized in Figure 5.4 of the main text. c) Plots of the absolute X-ray reflectivity vs. momentum transfer perpendicular to the surface in 0.1 M $Na_2B_4O_7(aq)$ and 0.05 M GeO_2. For the data at $E <$ -0.2 V, the solid black lines denote the corresponding best fit of the data using *eq* 5.2, For the data at E = -0.2 V, the solid black lines indicate the best fit following the model of *eq* 5.5. These data were normalized in Figure 5.5 of the main text. In all panels, curves are offset for visual clarity.

generate the structure-specific model described in the next section.

$$\begin{aligned}\rho_e(z) =& \frac{1}{2}\rho_{e,H_2O}\left(\operatorname{erfc}\left(\frac{z-z_{H_2O}}{\sigma_{H_2O}\sqrt{2}}\right)\right) \\ &+ F_{Hg}(z) \otimes \left[+\frac{\rho_{e,ad-Hg}}{\rho_{e,Hg}}\frac{1}{\sigma_{ad,Hg}\sqrt{2\pi}}e^{\frac{-\left(z-z_{ad,Hg}\right)^2}{2\sigma_{ad,Hg}^2}} + \sum_{n=0}^{\infty}\frac{d}{\sqrt{\sigma_i^2+n\sigma_b^2}\sqrt{2\pi}}e^{\frac{-(z-nd)^2}{2\left(\sigma_i^2+n\sigma_b^2\right)}}\right] \\ &+ \left[\sum_{m=1}^{3}\rho_{ad,m}\frac{1}{\sigma_m\sqrt{2\pi}}e^{\frac{-(z-z_m)^2}{2\sigma_m^2}}\right]\end{aligned} \tag{5.11}$$

Inserting *eq* 5.11 into *eq* 5.1 of the main text yields the following result.

$$\frac{R(q_z)}{R_F(q_z)} = \left|\frac{1}{\rho_{e,Hg}-\rho_{e,H_2O}}\left(\begin{array}{l}\frac{f_{Hg}^0(q_z)+f_{Hg}'}{Z_{Hg}+f_{Hg}'}\left[iq_z d\frac{e^{-\frac{q_z^2\sigma_i^2}{2}}}{\left(1-e^{iq_z d-\frac{q_z^2\sigma_b^2}{2}}\right)}+\frac{iq_z\rho_{ad}}{\rho_{e,Hg}}e^{-iq_z z_{ad}-\frac{q_z^2\sigma_{ad}^2}{2}}\right] \\ -\rho_{e,H_2O}\,e^{iq_z z_{H_2O}-\frac{q_z^2\sigma_{H_2O}}{2}} \\ +\sum_{m=1}^{3} iq_z\rho_{ad,m}\,e^{-iq_z z_m-\frac{q_z^2\sigma_m^2}{2}}\end{array}\right)\right|^2 \tag{5.12}$$

S4. Refinement to *eq* 5.2 to Describe Enrichment of H_2GeO_3/$HGeO_3^-$ at Hg Interface

The following expressions constitute a refinement to the model described by *eq* 5.5 in the main text. In the approach presented below, additional Gaussian terms were added that collectively describe a separate 'adlayer' of $HGeO_3^-$ in addition to the Hg 'adlayer' term. Figure 6.3 describes the employed model.

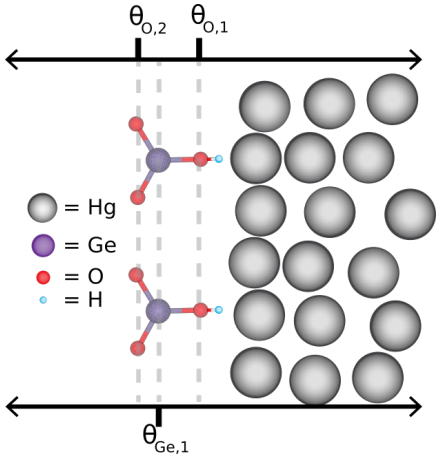

Figure 5.10: Pictorial representation of an 'adlayer' of $HGeO_3^-$ ions. The gray dashed lines indicate the layers of atoms that are described by a Gaussian term with the atomic form factors of either Ge or O, respectively.

In the following expressions, the term θ_{HGeO3-} corresponds to the fractional coverage of this 'adlayer'.

$$\begin{aligned}\rho_e(z) = {} & \frac{1}{2}\rho_{e,H_2O}\left(\operatorname{erfc}\left(\frac{z-z_{H_2O}}{\sigma_{H_2O}\sqrt{2}}\right)\right) \\ & + F_{Hg}(z) \otimes \left[\frac{\rho_{e,ad-Hg}}{\rho_{e,Hg}}\frac{1}{\sigma_{ad,Hg}\sqrt{2\pi}}e^{\frac{-\left(z-z_{ad,Hg}\right)^2}{2\sigma_{ad,Hg}^2}} + \sum_{n=0}^{\infty}\frac{d}{\sqrt{\sigma_i^2+n\sigma_b^2}\sqrt{2\pi}}e^{\frac{-(z-nd)^2}{2\left(\sigma_i^2+n\sigma_b^2\right)}}\right] \\ & + F_{Ge}(z) \otimes \left[\Theta_{HGeO_3^-/Hg}\frac{1}{\sigma_{ad}\sqrt{2\pi}}e^{\frac{-\left(z-z_{ad,Ge_j}\right)^2}{2\sigma_{ad,Ge}^2}}\right] \\ & + F_O(z) \otimes \left[\sum_{k=1}^{2}\Theta_{HGeO_3^-/Hg}\frac{1}{k\sigma_{ad,O}\sqrt{2\pi}}e^{\frac{-\left(z-z_{ad,O_k}\right)^2}{2\sigma_{ad,O}^2}}\right]\end{aligned} \tag{5.13}$$

In this expression, $F_{Ge}(z)$ and $F_O(z)$ are the Fourier transforms of the Ge and O atomic form factors, respectively. The term $\Theta_{HGeO3-/Hg}$ has units of and describes the fractional coverage of the $HGeO_3^-$ adlayer on bare Hg. Notably, the outer O atoms are twice as numerous as the inner O atoms.

The result of inserting *eq* 5.12 in *eq* 5.1 of the main text is given in *eq* 5.14, where $f^0_{Ge}(q_z)$ and $f^{'}_{Ge}$ are the angle-dependent Ge atomic form factor and the dispersion correction, respectively, and $f^0_O(q_z)$ and $f^{'}_O$ are the angle-dependent O atomic form factor and the dispersion correction, respectively.

Electrolyte	*E* /V	σ_{H2O} /Å	σ_i /Å	σ_b /Å	$\rho_{e,ad\text{-}Hg}$ /Å	$\sigma_{ad,Hg}$ /Å	$z_{ad,Hg}$ /Å	$\sigma_{Ge,1}$ /Å	$z_{Ge,1}$ /Å	$\sigma_{O,1}$ /Å	$z_{O,1}$ /Å	$\sigma_{O,2}$ /Å	$z_{O,2}$ /Å	$\Theta_{HGeO3^-\text{-}Hg}$ /Å
0.01 M NaF														
	-0.2	-0.95 ± 0.01	0.95 ± 0.01	0.48 ± 0.01	0.21 ± 0.01	0.95 ± 0.01	-3.64 ± 0.23	-	-	-	-	-	-	-
0.1 M $Na_2B_4O_7$														
	-0.2	-0.94 ± 0.01	-0.94 ± 0.01	0.49 ± 0.01	0.24 ± 0.01	0.94 ± 0.01	-3.64	-	-	-	-	-	-	-
	-0.5	-0.97 ± 0.01	-0.97 ± 0.01	0.49	0.21 ± 0.01	0.97 ± 0.01	-3.64	-	-	-	-	-	-	-
	-0.7	-1.00 ± 0.01	-1.00 ± 0.01	0.49	0.16 ± 0.01	1.00 ± 0.01	-3.64	-	-	-	-	-	-	-
	-0.9	-1.01 ± 0.01	-1.01 ± 0.01	0.49	0.10 ± 0.01	1.01 ± 0.01	-3.64	-	-	-	-	-	-	-
0.1 M $Na_2B_4O_7$ + 0.05 M GeO_2														
	-0.5	-1.00 ± 0.01	-1.00 ± 0.01	0.49	0.21 ± 0.01	1.00 ± 0.01	-3.64	1.00 ± 0.01	-3.75	1.00 ± 0.01	-4.60	1.00 ± 0.01	-2.09	0.20 ± 0.01
	-0.7	-1.01 ± 0.01	-1.01 ± 0.01	0.49	0.16 ± 0.01	1.01 ± 0.01	-3.64	1.01 ± 0.01	-3.75	1.01 ± 0.01	-4.60	1.01 ± 0.01	-2.09	0.20 ± 0.01
	-0.9	-1.01 ± 0.01	-1.01 ± 0.01	0.49	0.10 ± 0.01	1.01 ± 0.01	-3.64	1.01 ± 0.01	-3.75	1.01 ± 0.01	-4.60	1.01 ± 0.01	-2.09	0.20 ± 0.01

Table 5.3: S1. Fit Parameters Used for XRR Data in Figures 5.3, 5.4, and 5.5 Using *Eq S4*[a,b,c] a. The data collected in 0.01 M NaF (*aq*) and in 0.1 M $Na_2B_4O_7$ (*aq*) based electrolyte were modelled using *eq* 5.2 and $\rho_{e,ad-Hg} = 0.1\ \rho_{e,Hg}$, z_{H2O} = -1.00 , and d = 2.75 based on Reference 26. The data in 0.1 M $Na_2B_4O_7$ + 0.05 M GeO_2 (*aq*) at -0.2 V could not be described by this model and is thus not included here. b. For data collected in 0.1 M $Na_2B_4O_7$ (*aq*) base electrolyte, z_{ad} was not a free fit parameter, but kept constant at its value obtained in fits of the data in 0.01 M NaF(*aq*) at-0.2 V.27 c. For data collected in 0.1 M $Na_2B_4O_7$ (*aq*) base electrolyte, σ_b was obtained from the data in 0.1 M $Na_2B_4O_7$ (*aq*) at -0.2 V and then used as a constant value for the fits of the data at potentials < -0.2 V.

$$\frac{R(q_z)}{R_F(q_z)} = \left| \frac{1}{\rho_{e,Hg}-\rho_{e,H_2O}} \left(\begin{array}{l} \frac{f^0_{Hg}(q_z)+f'_{Hg}}{Z_{Hg}+f'_{Hg}} \left[iq_z d \frac{e^{-\frac{q_z^2\sigma_i^2}{2}}}{\left(1-e^{iq_z d-\frac{q_z^2\sigma_b^2}{2}}\right)} + \frac{iq_z\rho_{ad,e-Hg}}{\rho_{e,Hg}} e^{-iq_z z_{ad}-\frac{q_z^2\sigma_{ad}^2}{2}} \right] - \rho_{e,H_2O}\, e^{iq_z z_{H_2O}-\frac{q_z^2\sigma_{H_2O}}{2}} \\ + \frac{f^0_{Ge}(q_z)+f'_{Ge}}{Z_{Hg}+f'_{Ge}} iq_z \Theta_{HGeO_3^-/Hg}\, e^{-iq_z z_{ad,\,Gej}-\frac{q_z^2\sigma_{ad,Ge}^2}{2}} + \frac{f^0_O(q_z)+f'_O}{Z_{Hg}+f'_O} \sum_{k=1}^{2} \frac{1}{k} iq_z \Theta_{HGeO_3^-/Hg}\, e^{-iq_z z_{ad,\,O_k}-\frac{q_z^2\sigma_{ad,O}^2}{2}} \end{array} \right) \right|^2 \tag{5.14}$$

S5. Description of the Distance-Dependent Electron Density Profile for a Hg interface Featuring a Partial Coverage of GeO_2

The explicit terms in each component of *eq* 5.7in the main text (reproduced here as *eq* 5.15) are presented below in *eqs* 5.6, 5.7, 5.8, 5.9, 5.10. The general definitions for each term follow the description in the main text, except that subscripts j and i denote distinct Ge and O atoms, respectively.

$$\rho_e(z) = \rho_{e,electrolyte} + \rho_{DCM,Hg} + (1-\theta_{GeO_2})\,\rho_{ad,Ge/Hg} + \theta_{GeO_2}\rho_{ad,Ge/GeO_2} + \theta_{GeO_2}\rho_{e,GeO_2} \tag{5.15}$$

$$\rho_{e,electrolyte} = \frac{1}{2}\rho_{e,H_2O}\left(\operatorname{erfc}\left(\frac{z - z_{H_2O}}{\sigma_{H_2O}\sqrt{2}}\right)\right) \tag{5.16}$$

$$\rho_{DCM,Hg} = F_{Hg}(z) \otimes \left[\frac{\rho_{e,ad-Hg}}{\rho_{e,Hg}}\frac{1}{\sigma_{ad,Hg}\sqrt{2\pi}}e^{\frac{-\left(z-z_{ad,Hg}\right)^2}{2\sigma_{ad,Hg}^2}} + \sum_{n=0}^{\infty}\frac{d}{\sqrt{\sigma_i^2+n\sigma_b^2}\sqrt{2\pi}}e^{\frac{-(z-nd)^2}{2\left(\sigma_i^2+n\sigma_b^2\right)}}\right] \tag{5.17}$$

$$\begin{aligned}\rho_{ad,HGeO_3^-/Hg} = {} & F_{Ge}(z) \otimes \left[\Theta_{HGeO_3^-/Hg}\frac{1}{\sigma_{ad,Ge}\sqrt{2\pi}}e^{\frac{-\left(z-z_{ad,Ge_j}\right)^2}{2\sigma_{ad,Ge}^2}}\right] \\ & + F_O(z) \otimes \left[\sum_{k=1}^{2} k\Theta_{HGeO_3^-/GeO_2}\frac{1}{\sigma_{ad,O}\sqrt{2\pi}}e^{\frac{-\left(z-z_{ad,O_i}\right)^2}{2\sigma_{ad,O}^2}}\right]\end{aligned} \tag{5.18}$$

$$\begin{aligned}\rho_{ad,HGeO_3^-/GeO_2} = {} & F_{Ge}(z) \otimes \left[\Theta_{HGeO_3^-/GeO_2}\frac{1}{\sigma_{ad,Ge}\sqrt{2\pi}}e^{\frac{-\left(z-z_{ad,Ge_j}\right)^2}{2\sigma_{ad,Ge}^2}}\right] \\ & + F_O(z) \otimes \left[\sum_{k=1}^{2} k\Theta_{HGeO_3^-/GeO_2}\frac{1}{\sigma_{ad,O}\sqrt{2\pi}}e^{\frac{-\left(z-z_{ad,O_i}\right)^2}{2\sigma_{ad,O}^2}}\right]\end{aligned} \tag{5.19}$$

$$\rho_{e,GeO_2} = \sum_{j=1}^{2} \left(F_{Ge}(z) \otimes \left[\Theta_{\text{Ge bi } j} \frac{1}{\sigma_{ad}\sqrt{2\pi}} e^{\frac{-\left(z-z_{ad,Ge_j}\right)^2}{2\sigma_{ad,Ge}^2}} \right] + F_O(z) \otimes \left[\sum_{k=1}^{3} \Theta_{\text{O bi } j,k} \frac{1}{\sigma_{ad,O}\sqrt{2\pi}} e^{\frac{-\left(z-z_{ad,O_i}\right)^2}{2\sigma_{ad,O}^2}} \right] \right) \tag{5.20}$$

In these expressions, $\Theta_{HGeO3-/Hg}$, $\Theta_{HGeO3-/GeO2}$, $\Theta_{Ge\ bi,\ j}$, and $\Theta_{O\ bi,\ j,k}$ have units of . The first terms describe the fractional coverages of the $HGeO_3^-$ adlayer on bare Hg and on GeO_2, respectively. The last two terms describe the individual coverages of Ge and O atoms, respectively, that constitute a GeO_2 bilayer film with a rutile structure.

The result of the master formula in this case is given in *eq* 5.21,

$$
\begin{aligned}
\frac{R(q_z)}{R_F(q_z)} = \frac{1}{\rho_{e,Hg}-\rho_{e,H_2O}} \Bigg(& \left(\frac{f^0_{Hg}(q_z)+f'_{Hg}}{Z_{Hg}+f'_{Hg}} \left[iq_z d \, \frac{e^{-\frac{q_z^2\sigma_1^2}{2}}}{\left(1-e^{iq_z d-\frac{q_z^2\sigma_b^2}{2}}\right)} + iq_z \frac{\rho_{e,ad-Hg}}{\rho_{e,Hg}} e^{-iq_z z_{ad}-\frac{q_z^2\sigma_{ad}^2}{2}} \right] - \rho_{H_2O}\, e^{iq_z z_{H_2O}-\frac{q_z^2\sigma_{H_2O}}{2}} \right. \\
& + (1-\theta_{GeO_2}) \left(\frac{f^0_{Ge}(q_z)+f'_{Ge}}{Z_{Hg}+f'_{Ge}} iq_z \Theta_{HGeO_3^-/Hg} e^{-iq_z z_{ad,\,Ge\,j}-\frac{q_z^2\sigma_{ad,Ge}^2}{2}} + \frac{f^0_O(q_z)+f'_O}{Z_{Hg}+f'_O} \sum_{k=1}^{2} \frac{iq_z \Theta_{HGeO_3^-/Hg}}{k} e^{-iq_z z_{ad,\,Oj}-\frac{q_z^2\sigma_{ad,O}^2}{2}} \right) \\
& + \theta_{GeO_2} \left(\frac{f^0_{Ge}(q_z)+f'_{Ge}}{Z_{Hg}+f'_{Ge}} iq_z \Theta_{HGeO_3/GeO_2} e^{-iq_z z_{ad,\,Gej}-\frac{q_z^2\sigma_{ad,Ge}^2}{2}} + \frac{f^0_O(q_z)+f'_O}{Z_{Hg}+f'_O} \sum_{k=1}^{2} iq_z \Theta_{HGeO_3/GeO_2} e^{-iq_z z_{ad,\,Ok}-\frac{q_z^2\sigma_{ad,O}^2}{2}} \right) \\
& \left. + \theta_{GeO_2} \sum_{j=1}^{2} \left(\frac{f^0_{Ge}(q_z)+f'_{Ge}}{Z_{Hg}+f'_{Ge}} iq_z \Theta_{Ge\ \mathrm{bi}\ j} e^{-iq_z z_{ad,\,Gej}-\frac{q_z^2\sigma_{ad,Ge}^2}{2}} + \frac{f^0_O(q_z)+f'_O}{Z_{Hg}+f'_O} \sum_{k=1}^{3} iq_z \Theta_{O\ \mathrm{bi}\ jk} e^{-iq_z z_{ad,\,Ok}-\frac{q_z^2\sigma_{ad,O}^2}{2}} \right) \right)^2
\end{aligned}
\tag{5.21}
$$

Eqs eqs 5.6, 5.7, 5.8, 5.9, feature coverage parameters ($\Theta_{HGeO3-/Hg}$ and $\Theta_{HGeO3-/GeO2}$) that are necessarily linked by the rutile structure as shown in Figure 5.11.

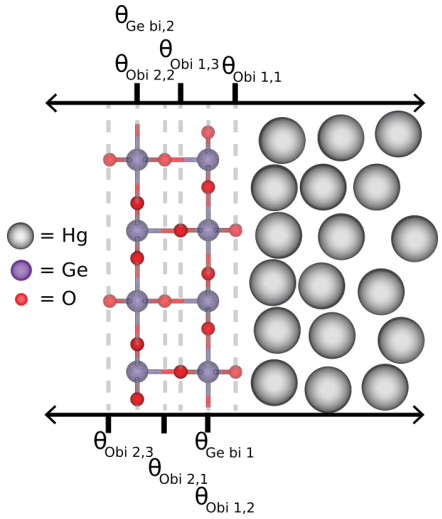

Figure 5.11: Pictorial representation of a rutile bilayer of GeO_2 along the <110> direction used in fitting the data collected at E = -0.2 V. The gray dashed lines indicate the layers of atoms within each of the respective structures which are described by Gaussian terms with the atomic form factors of Ge or O, respectively. Each layer is defined by a coverage (Θ), position (z), and roughness (σ). The relative positions of atoms within this structure are determined by the lattice bond distances and orientation.

Individual layers of atoms that together constitute GeO_2 are thus described with Gaussian terms for each atom in each layer that have fixed relative coverages (Θ) and positions (z). Roughness values for all Gaussian terms ($\sigma_{ad,Ge}$ and $\sigma_{ad,O}$) are set equal in magnitude to σ_i. The proportionalities for the Θ terms are determined by taking the ratio of Ge or O atoms in a given layer (as denoted by the gray dashed lines) to the Ge or O atoms in another. From Figure 5.11, the proportionalities of each coverage term are described in the following expressions.

$$\Theta_{Gebi1} = \Theta_{Gebi2} = \Theta_{Obi1,2} = \Theta_{Obi2,2} \tag{5.22}$$

$$\frac{1}{2}\Theta_{Gebi1} = \Theta_{Obi1,1} = \Theta_{Obi1,3} = \Theta_{Obi2,1} = \Theta_{Obi2,3} \tag{5.23}$$

S6. XRR Fit Assuming a Complete Monolayer Coverage of GeO_2

The XRR data collected at -0.2 V in the solution containing 0.1 M $Na_2B_4O_7$ and 0.05 M GeO_2 was also fit with a model where a full monolayer of GeO_2 was assumed, *i.e.* θ_{GeO2} = 1. Figure 5.10 shows the result of this fit, keeping all other model parameters identical to the values listed in the main text. As seen in Figure 5.12, a high coverage of GeO_2 predicts more pronounced local maxima and minima than what is seen in the experimental data. The quality of the fit is noticeably worse in the q_z ranges of 0.25 – 0.75 $^{-1}$ and 1.0 – 1.5 $^{-1}$.

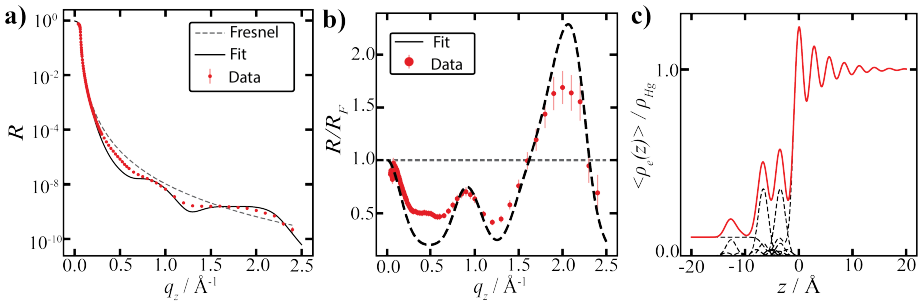

Figure 5.12: a) Plot of the absolute X-ray reflectivity vs. momentum transfer perpendicular to the surface for a Hg electrode immersed in deaerated electrolyte containing 0.1 M $Na_2B_4O_7$ (*aq*) and a formal concentration of 0.05 M GeO_2 at E = -0.2 V (closed red circles). The fit of the data using *eq* 5.6 assuming Θ_{GeO2} = 1 and all other parameters listed in Table 3 is shown (black line). The Fresnel reflectivity of an interface with a monotonic electron density profile with no surface roughness is also presented (grey dashed line). b) The same XRR data as in (a) but normalized to the Fresnel reflectivity. c) Electron density profiles corresponding to the fitted data shown in (b).

6 Evidence for Facilitated Surface Transport during Ge Crystal Growth by Indium in Liquid Hg-In Alloys at Room Temperature

This chapter is based on an published as an article in Crystal Growth & Design [21].
Reprinted with permission from Andrea Sartori, Dhruba Pattadar, Quintin Cheek, Yifan Zhao, Rajendra P. Giri, Bridget Murphy, Olaf Magnussen, and Stephen Maldonado. The article is available via the internet at
https://doi.org/10.1021/acs.cgd.0c01485

This publication was obtained by the collaboration with the group of Stephen Maldonado from the University of Michigan.
One of the focus of prof. Maldonado is the investigation of synthesis of semiconductor in particular Groups IV and III-V semiconductors on liquid metals. His group obtained incredible success and they were able to synthesize one step crystalline semiconductors like GaAs, Ge and Si, with different shapes and size [19, 138, 139].
One of the recent work was the characterization of Ge crystallites on HgIn alloy substrates. In particular by changing potential and composition of the working electrode as main parameters.
The full description of the system was missing of an essential piece of the puzzle, the surface structure of the bare working electrode immersed in the buffer solution used for the process. Access in buried liquid liquid interface is complex and many techniques are not suitable, especially with atomic resolution. X-ray reflectivity is one of the best candidates.
Our group in collaboration with the Maldonado team collected a series of X-ray scattering data, as a function of working electrode and electrolyte composition and applied potential. A set of data was analyzed and used for this publication [21]. The remaining data are still incomplete and they are not part of this thesis.

List of authors

Dhruba Pattadar,[1] Quintin Cheek,[1] Andrea Sartori,[2] Yifan Zhao,[1] Rajendra P. Giri,[2] Bridget Murphy,[2,3], Olaf Magnussen,[2,3] and Stephen Maldonado[1,4],

[1] Department of Chemistry, University of Michigan, 930 N University, Ann Arbor, Michigan 48109-1055
[2] Institute for experimental and Applied Physics, Kiel University, D-24118 Kiel, Germany
[3] Ruprecht Haensel Laboratory, Kiel University, D-24118 Kiel, Germany,
[4] Program in Applied Physics, University of Michigan, 930 N University, Ann Arbor, Michigan 48109-1055

6.1 Abstract

Room-temperature electrodeposition of Ge crystallites was investigated by the electrochemical liquid-liquid-solid (ec-LLS) process using a family of Hg1-xInx alloys. The objective was to determine whether different liquid metal alloys with nominally the same bulk solubility towards Ge but potentially different surface character would yield any differences in the resultant Ge crystallites. Variation of the In fraction in the these alloys was the control variable. The following details were ascertained from the cumulative data. First, in accord with thermodynamic predictions, the surface of Hg_xIn_{1-x} alloys was strongly enriched with Hg according to X-ray specular reflectivity data. These data further indicated that the surface enrichment was confined exclusively to a single atomic layer at the liquid metal surface. These properties of the Hg_xIn_{1-x} / electrolyte interface structure facilitated the first two steps of the ec-LLS process. Second, the presence of In influenced the morphology of the resultant Ge crystallites from ec-LLS, in accord with mediated transport of the Ge upon initial electroreduction. Specifically, X-ray diffraction, Raman, and microscopy data suggest that a strong affinity between In and Ge that affects the crystal morphology. This study thus motivates further exploration of both In as a component in liquid metal solvents to facilitate grain size and more general studies detailing how the surface structure and composition of liquid metals influence crystal growth. These findings significantly advance the prospect for preparing technologically-relevant inorganic crystalline semiconductors at low temperatures.

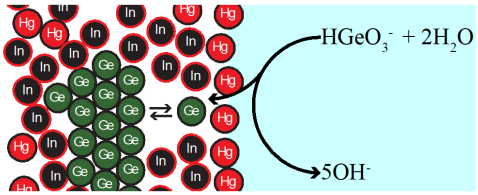

6.2 Introduction

Liquid metals are natural media for growing inorganic crystals.[1-5] For crystalline inorganic semiconductors, elemental liquid metals in vapor-liquid-solid (VLS) and liquid phase epitaxy (LPE) processes have been explored and utilized successfully.[6-9] In this regard, the choice of the liquid metal is known to strongly influence how the inorganic solute becomes a crystalline material. So far, the overwhelming majority of studies have focused largely on just unary liquid metals and the corresponding binary solvent/solute mixtures. Comparatively few studies have focused explicitly on exploring the composition space of liquid metal alloys to identify more optimal solvents for crystal growth. Accordingly, although the chemistry and metallurgy of liquid metal alloys have been studied intensely and even recently,[10-34] strategies that exploit this knowledge to design optimal liquid metal alloy solvents for the growth of target, crystalline inorganic materials are still lacking.

In both VLS and LPE, it is widely understood that crystal growth in a given elemental liquid metal can be improved by adding a second alloying metal to increase the solubility of the target solute.[35] The guiding rationale has been that adding elements with higher bulk solute solubilities (i.e. type A metals) into liquid metals with low bulk solute solubilities (i.e. type B metals) lowers the supersaturation attained during nucleation and crystal growth in the bulk liquid metal alloy. According to classical nucleation theory and crystal growth models,[36-37] controlling the supersaturation is the most direct way to obtain more pristine, larger solute crystals with fewer defects. This premise has been described sporadically but it is not clear if it represents the only or most impactful strategy for designing liquid metal crystal growth solvents. Specifically in VLS, it is widely accepted that the interfacial properties during the crystal growth process are important and potentially control is well established.[38-40]

Previously, identification of how a specific component alters the properties of a molten alloy during a crystal growth process was complicated by the need for high temperatures. However, a new liquid-metal-based process for growing crystalline inorganic semiconductors introduced this past decade offers a simpler alternative.[41] By utilizing electrochemical gradients rather than thermal gradients, the electrochemical liquid-liquid-solid (ec-LLS) strategy mirrors the nucleation and crystal growth aspects of VLS and LPE but without any heating or extensive support apparatus. Simply, a liquid metal acts as the working electrode where oxidized species can be reduced and then dissolved into the liquid metal at rates dictated by the electrochemical reduction reaction, surface chemistry, and rates of dissolution.[42-45] Recent studies have shown that the liquid metal alloy composition affects the resultant crystal size and morphology,[46-47] but clear design rules for the liquid metal have yet to be identified.

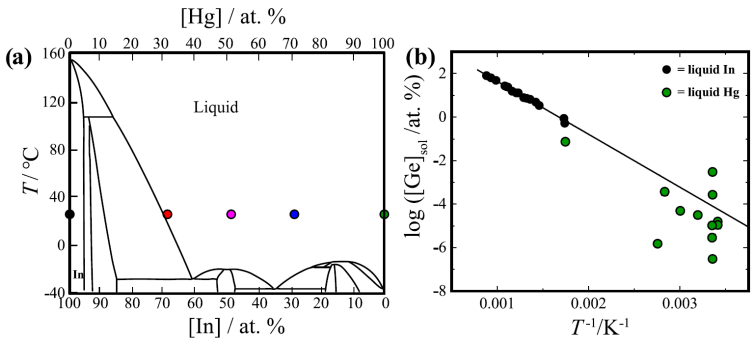

Figure 6.1: a) Binary phase diagram for the Hg-In binary system. The colored dots represents the specific compositions of Hg-In alloys used for ec-LLS deposition of Ge in this work. Adapted with permission from Chiarenzelli, R. V. and Brown, O. L. I *Journal of Chemical and Engineering Data*, **1962**, 7(4), 477-478. Copyright 1962 b) A plot of the known solubilities of Ge in (black dots) liquid In and in (green dots) liquid Hg as a function of reciprocal temperature. Data adapted from references 49 and 50, respectively. The linear regression represents the best fit line for the In-solubility data only.

In this study, the liquid Hg-In alloy system is a useful testbed for exploring and identifying aspects that may be relevant to crystal growth in ec-LLS and, by extension, to other related processes that rely on liquid metal solvents using alloys of only 'type B' metals. The $Hg_{1-x}In_x$ alloy system is notable since In is a solid at room temperature but can be uniformly dissolved in Hg as a homogeneous liquid phase up to concentrations of ~70 at.% at room temperature (Figure 6.1a).[48]

A wide composition range of molten, liquid $Hg_{1-x}In_x$ alloys are readily accessible at room temperature just by mixing predefined amounts of each metal. Here, we use Ge as the test solute for this family of liquid metals since Ge ec-LLS by the electrochemical reduction of dissolved GeO_2 in water is known for both pure Hg and In nanodroplets.[41, 47] Based on the available metallurgical for each metal,[49-50] the solubility of Ge in both pure In and pure Hg at room temperature is roughly of the order of 10^{-4} at. % (Figure 6.1b). Although there is some uncertainty in these data, both from extrapolation in the case of In and from Hg in the spread of the available experimental measurements,[50-51] the data clearly show that neither metal would be expected to appreciably increase the solubility of Ge in the other. Moreover, neither In nor Hg form germanicides at any temperature, and the atomic size of each metal is roughly similar (Table 6.1).[48, 52-53]

Accordingly, if bulk solute solubilities are the only important factors in designing liquid metal solvents, the expectation is that the crystallographic properties of Ge formed within every composition in the Hg-In alloy family would be the same. In contrast, these two metals differ notably in their surface properties. For example, liquid/air surface tensions for Hg and In in Table 6.1 differ noticeably.[54-55] More importantly, the wettability of these liquid metals towards Ge differs noticeably. Hg

	Hg	In
atomic mass/g mol^{-1}	200.59	114.81
gravimetric density/g cm^{-3}	13.53	7.02
molar density/mol cm^{-3}	0.067	0.061
atomic radius[a] /Å	1.71	1.56
surface tension[b] / N m^{-1}	0.47	0.57
melting point[c] / °C	-38.3	156.6
Ge solubility[d] / atom %	4.6×10^{-5},[e]	8.5×10^{-5} ,[f]

Table 6.1: [a] Data from ref 53. [b] Data are reported at the melting point in air. [c] Data from ref 48. [d] Data from refs 49,50. [e] Average value from data reported between 20 and 25 ° C. [f] Determined by linear extrapolation of data to 25 ° C.

does not readily wet a solid Ge surface while molten In readily wets Group IV semiconductor surfaces.[56-57] In fact, molten In at elevated temperatures has been used previously to grow crystalline Ge by liquid phase epitaxy and by VLS.[56-58] Accordingly, if surface wetting of the liquid metal to solid Ge is relevant, a change in the observable crystal growth would be expected as the liquid $Hg_{1-x}In_x$ alloy composition is varied.

Herein, a series of electrochemical, materials characterization, and surface characterization data are presented to describe the Ge ec-LLS process using electrode compositions spanning the $Hg_{1-x}In_x$ family. The purpose of this work is to evaluate the hypothesis that adding In into liquid Hg will effect no change in the crystalline properties of the resultant Ge. Direct insight into the liquid metal / electrolyte interface at which the solute atoms are formed is achieved. We accomplish this by X-ray reflectivity (XRR) measurements, which provide detailed data on the local atomic structure (e.g. atomic layering)[59-61] and composition of the interface. Specifically, the angle-dependent specular X-ray reflectivities of the two central systems under study, pure liquid Hg and liquid $Hg_{0.3}In_{0.7}$ (i.e., the alloy with the highest dissolved In content) in contact with the 0.1 M NaB_4O_7 electrolyte solution were collected in the potential range of Ge electrodeposition. The cumulative findings are significant in the context of developing improved strategies to grow technologically important semiconductors at low temperatures.

6.3 Experimental

6.3.1 Materials and Chemicals

Acetone (ACS grade, Fisher Scientific), Hg (triply distilled, D. F. Goldsmith), indium (99.99% Gallium Source), germanium dioxide (99.998% Sigma-Aldrich), sodium borate (>99.5% Sigma-Aldrich), Indium foil (99.998 %, Alfa Aesar), and Pt wire (0.25 mm diameter, Alfa Aesar) were used as received. Nanopure water with a resistivity > 18.2 MΩ cm^{-1} (Barnstead Nanopure) was used throughout.

6.3.2 Electrochemical Details

Both a CH Instruments 420A and a Solarton 1176A potentionstat were used to perform cyclic voltammetry and chronocoulometry experiments. A dual compartment, three-electrode cell was used for all electrodepositions and consisted of a 200 μL liquid metal pool housed within a bowl and contacted from the top by an insulated Pt wire (working electrode), a graphite rod (counter electrode), and an anodized Ag wire with a AgCl coating immersed in sat. KCl in a separate fritted compartment (reference electrode). All potentials in this work are given with respect to this reference electrode. For experiments featuring solid In as the working electrode, the Pt wire contact was not used. Voltammetry experiments were performed in solutions containing either 0.01 M NaB_4O_7 or 0.01 M NaB_4O_7 with 0.05 M GeO_2. After electrodeposition, the electrolyte was suctioned off by hand with a pipette. Following, the liquid metal pool electrode $\sim$ was washed $\sim$ with nanopure water multiple times until residual salt crystals were no longer visible. Then, electrodeposited Ge was collected carefully from the liquid pool electrode with a clean plastic spatula, dried under N_2, and then characterized.

6.3.3 Materials Characterization

Scanning electron microscopy (SEM) images were obtained using a JEOL JSM-7800FLV field emission scanning electron microscope (FESEM) operating at an accelerating voltage of 10.00 kV using an in-lens ion annular secondary electron detector. X-ray diffraction spectra were collected with a Bruker D8 Advance diffractometer equipped with a Cu Kα source, parallel beam optics and a LynxEye detector. Raman spectra were obtained with a Tescan RISE SEM equipped with a Raman spectrometer featuring a 532 nm Ar^+ laser at a radiant power of 50 μW on the sample.

6.3.4 X-Ray Reflectivity Measurements

X-ray reflectivity (XRR) measurements of the liquid metal/liquid electrolyte interfaces were performed using the Liquid Interface Scattering Apparatus (LISA) diffractometer[62] at beamline P08 of the PETRA III synchrotron source at DESY in Hamburg, Germany.[63] All experiments utilized a beam energy of 25 keV, corresponding to a wavelength of λ = 0.4959 $Å^{-1}$. The reflected intensity was recorded with a two-dimensional GaAs X-ray detector (Lambda from X-Spectrum). The detector was composed of $\sim$1536 X 512 pixels with 55 μm pixel size providing a resolution of 3.3 x 10^{-4} $Å^{-1}$ in both the horizontal q_x and vertical q_z directions. The background, due to scattering by the Hg and electrolyte bulks, was measured by offsetting the detector by 0.08 $^\circ$ horizontally out of the plane of reflection, and subtracting an area with 0.08° horizontal and 0.4° vertical angular acceptance, from the specular signal. A custom designed electrochemical X-ray scattering cell with 5 cm diameter was used throughout the experiments, allowing for the injection of the $Hg_{1-x}In_x$ alloy as well as the electrolyte

solution. Solutions were purged with N_2 ~ gas for at least 30 minutes prior to injection into the cell. Liquid metal electrodes were biased for at least 15 minutes before each reflectivity measurement to ensure a stable interface.

In the XRR data analysis, first the background-subtracted detector signal was normalized by the direct beam intensity and plotted versus the surface-normal scattering vector, q_z (= $4\pi\lambda^{-1} \sin\alpha$). The resulting experimental X-ray reflectivity, $R(q_z)$, was normalized by the Fresnel reflectivity, $R_F(q_z)$, of a perfectly sharp interface between the liquid metal sample ($Hg_{0.3}In_{0.7}$ or Hg, respectively) and the aqueous electrolyte. Here, the critical scattering vector, q_c, for total external reflection at the liquid metal/electrolyte interface was determined from the difference of the total electron densities of the bulk liquid metals, $\rho_{e,Me}$, which are 3.24 ~ $e_0Å^{-3}$ for Hg and 2.24 $e_0Å^{-3}$ for $Hg_{0.3}In_{0.7}$, and for the bulk electrolyte ($\rho_{e,H2O}$ = 0.33 $e_0Å^{-3}$). From these values scattering length densities of $8.177 \cdot 10^{-5}$ $Å^{-2}$ for Hg/0.1 M NaB_4O_7 and $5.364 \cdot 10^{-5}$ $Å^{-2}$ for $Hg_{0.3}In_{0.7}$ / 0.1 M NaB_4O_7, are calculated, resulting in q_c values of 0.064 and 0.052 $Å^{-1}$, respectively. R/R_F at each q_z is a function of the laterally averaged electron density, , profile along the surface-normal according to the master equation.[64-65] R/R_F values were fitted by a modification of the distorted crystal model,[61, 64] which was previously employed for the interface between liquid Hg and NaF solution.[66-67] This first layer model treats of the liquid electrolyte/liquid metal junction (normalized by the bulk metal density) as a function of three independent terms, with the first describing the electrolyte, the second representing an explicit atomic layer at the interface, and the third summation term representing the decaying atomic layering in the near-surface region of the liquid metal:

$$\frac{\langle\rho_e(z)\rangle}{\rho_{e,Me}} = \frac{1}{2}\frac{\rho_{e,H_2O}}{\rho_{e,Me}}\left(1 - erf\left(\frac{z - z_{H_2O}}{\sigma_{H_2O}\sqrt{2}}\right)\right) + \frac{d\,\rho_f}{\rho_{e,Me}\,\sigma_f\sqrt{2\pi}} e^{-\frac{(z-z_f)^2}{2\sigma_f^2}} + \sum_{n=1}^{\infty}\frac{d}{\sigma_n\sqrt{2\pi}} e^{-\frac{(z-nd)^2}{2\sigma_2^2}} \tag{6.1}$$

Here, z_{H2O} and σ_{H2O} describe the position and width of the electrolyte front, ρ_f and σ_f are the amplitude and root mean square displacement of the first layer, respectively, d is the atomic layer spacing after the second metal layer, z_f is the position of the first layer, and 'd - z_f' is the distance between the first and second liquid metal layers. σ_n is the root mean displacement of the nth layer which increases with z towards the liquid metal bulk and is given by $\sigma_n = \sqrt{\sigma_i^2 + n\,\sigma_b^2}$, where σ_i is the intrinsic width common to all sub-surface layers and σ_b describes the rate by which σ_n increases.[61, 64]

The model was fitted to the experimental XRRs in a two stage process, using a custom python script. First, a global optimization was performed, with defined upper and lower bounds for each fitting parameter. Then, the resulting values were used as starting point for a local refinement. The parameters describing the electrolyte,

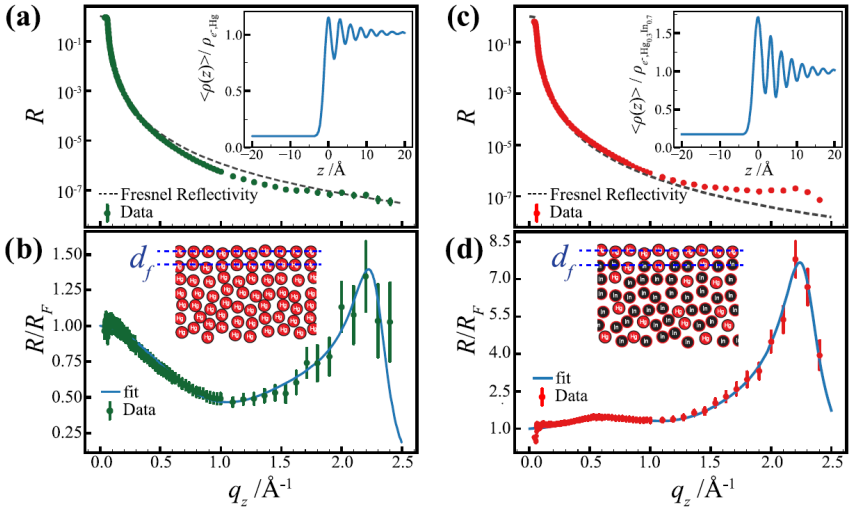

Figure 6.2: a) Measured and b) RF-normalized X-ray reflectivity of (a,b) liquid Hg and (c,d) liquid $Hg_{0.3}In_{0.7}$ in 0.1 M NaB_4O_7 at a potential of -1.4 V. The dashed lines in (a,c) indicates the Fresnel reflectivity, the solid lines in (b,d) the best fit by the model described in the text. Insets (a,c): the real-space profiles of the total electron density along the surface normal vector. Insets (b,d): Schematic presentations of the interface structure for each liquid metal.

and , had little influence on the resulting fit and thus were kept at the same values as for Hg in NaF solution.[67] The final fit was determined when χ^2 was minimized below a threshold value of 0.1.

6.4 Results

6.4.1 X-Ray Reflectivity

Representative XRR curves are shown in Figure 6.2 a and c.

At low q_z, the measured data (circles) closely follow the corresponding Fresnel reflectivities (dashed lines), indicating that the interfaces are atomically smooth. At $q_z \geqslant 2 \sim$ Å^{-1} a characteristic maximum is observed in both samples, which corresponds to the well-known quasi-Bragg peak associated with the atomic layering in the near-surface region of the liquid metal. [61, 64, 66-67]

The detailed behavior is more easily discernible after normalizing the XRR data by the Fresnel reflectivity (Figure 6.2b and d). For the case of pure Hg, the XRR curves in 0.1 M NaB_4O_7 strongly resemble those observed for the Hg/0.01 $\sim$ M NaF interface.[66-67] Specifically, $R(q_z)$ initially decreases up to q_z = 1.2 Å^{-1} and then increases again towards the quasi-Bragg peak at q_z = 2.22 Å^{-1}. Quantitative fits to the model described in the experimental section provide very similar structural parameters and electron density profiles as in NaF solution at the most negative potentials

(see Figure 6.2b and Table 6.2 of the Supporting Information). In particular, the first layer density $\rho_f/\rho_{e,Me}$ is very similar for Hg in NaB_4O_7 and in NaF.

In contrast, a very different behavior is found for the XRR of liquid $Hg_{0.3}In_{0.7}$. Here, the normalized X-ray reflectivity values initially increase, leading to a local maximum near q_z = 0.6 Å^{-1}. Furthermore, the quasi-Bragg peak is much more pronounced. The initial increase to an $R/R_f > 1$ is indicative of a higher electron density at the surface relative to that in the bulk. Similar effects were reported for the free surfaces of other liquid metal alloys and could be explained by surface segregation of the higher-Z element.[68-70] Accordingly, the X-ray reflectivity data indicates a Hg-rich surface. This point is supported by the best fit (Figure 6.2d, Table 6.2 of the Supporting Information), which corresponded to a liquid metal surface featuring a surface layer that consists almost exclusively of Hg on top of a surface-layered bulk liquid with a composition of $Hg_{0.3}In_{0.7}$, as depicted schematically in the inset of Figure 6.2d. In the surface layer, the concentration of In is no greater than 0.01, whereas all following atomic layers correspond to the nominal In concentration of 0.7. This result is also in accordance with the layer spacings. At the depth of second layer and below, the fitted parameters are identical to that at the surface of molten In at 443 $\sim$ K, [63] which is understandable taking into account thermal expansion effects and the high In content of the $Hg_{0.3}In_{0.7}$ alloy. In contrast, the spacing of the surface layer to the subsequent layer is much larger, as expected for a layer consisting of the more bulky Hg atoms.[59, 71] The decay of the atomic layering towards the liquid metal bulk is comparable to that found in pure liquid Hg and In, albeit a detailed comparison with the latter is difficult due to the differences in sample temperatures.

6.4.2 Electrochemical Responses

The voltammetric responses of Hg, $Hg_{1-x}In_x$, and In electrodes in 0.01 M NaB_4O_7 were examined in detail at a slow scan rate of 0.01 V s^{-1} (Figure 6.3).

Hg pool electrodes show a featureless steady-state current response when scanned between -0.4 V and -1.9 V (solid green line, Figure 6.3a). Figure 6.3a also shows the response when the scan is limited to -0.9 V and -1.9 V (dashed green line). H_2 evolution leads to some mechanical movement of the liquid metals that introduce noise in the data but the two traces are otherwise identical. Figure 6.3b shows similar voltammetry for $Hg_{0.7}In_{0.3}$. In this case, initiating the scan at -0.4 V resulted in a large cathodic wave with a maximum at -1.09 V and a peak current density of 0.24 mA cm^{-2}. Integration of this peak corresponded to a charge density of 3.86 mC cm^{-2}. On the return wave, anodic current onset at -0.87 V with a peak at -0.81 V and a steady—state anodic current of 0.10 mA cm^{-2} at more positive potentials. Integration of this anodic current corresponded to a charge density of 0.78 mC cm^{-2}. When the electrode scan was initiated at -0.9 V, i.e. the electrode potential as never allowed to drift more positive than -1.0 V, the cathodic wave disappeared. Further, the current for H_2 evolution was consistently higher. Similar observations were noted for

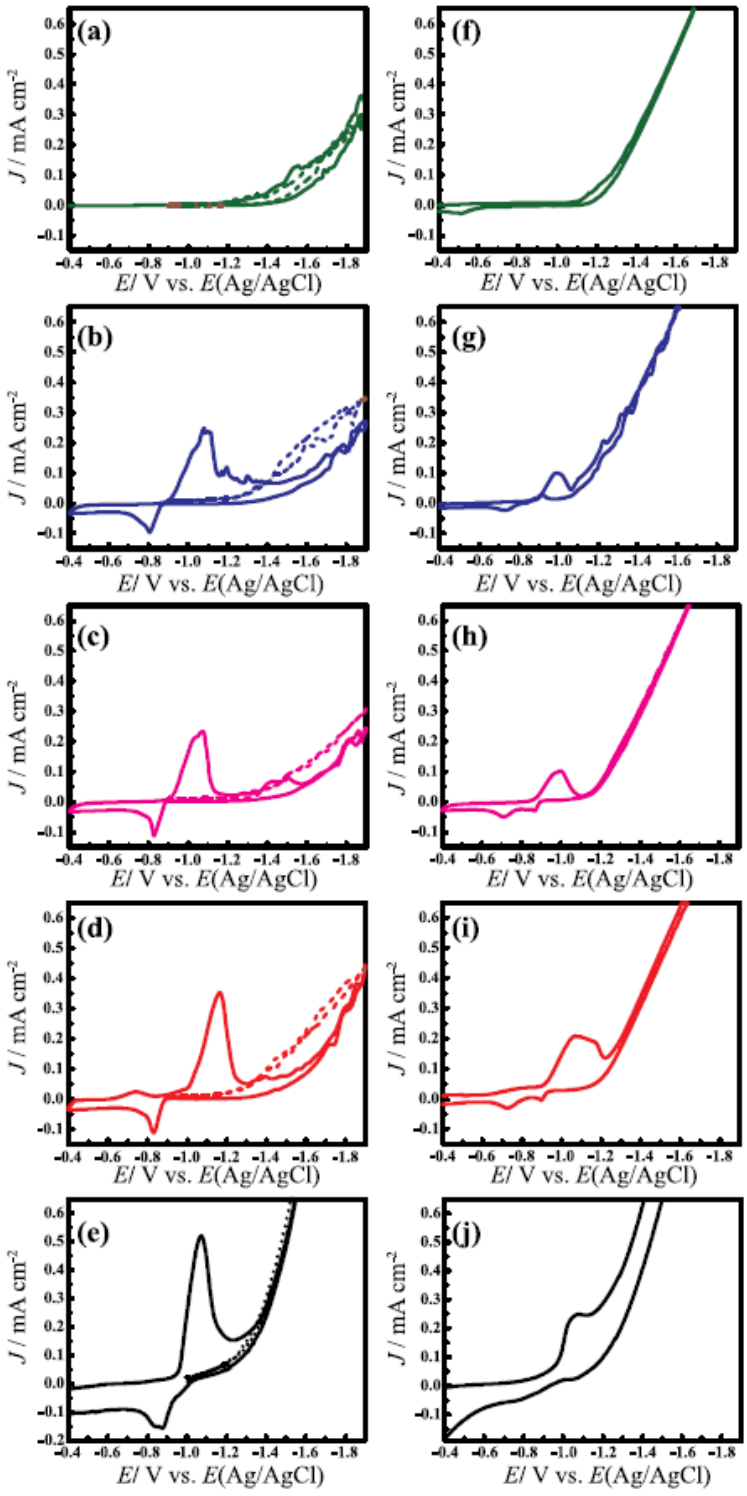

Figure 6.3: Voltammetric responses of Hg1-xInx electrode immersed in 0.01 M sodium tetraborate (A, B, C, D, and E) and a mixture of 0.01 M sodium $Na_2B_4O_7$ plus 0.05 M GeO_2 solution (F, G, H, I and J) at a scan rate of 0.01 Vs^{-1}. Green, blue, magenta, red and black graph represents the Hg, $Hg_0.7In_0.3$, $Hg_0.5In_0.5$, $Hg_0.3In_0.7$ and indium foil electrode respectively.

$Hg_{0.5}In_{0.5}$ and $Hg_{0.3}In_{0.7}$ (Figures 6.3d and 6.3e, respectively). The peak current densities and integrated charge densities of the cathodic wave that preceded the current onset for H_2 evolution when the voltammetric scan was initiated at -0. 4 V did not track monotonically with bulk In content (Table 6.3, Supporting Information). Data were also recorded using solid In foil as an electrode (Figure 6.3e). In this case, a more prominent cathodic wave was observed that again was absent when the potential was held more negative than the onset of anodic current (i.e. -1.3 V in this case). Notably, although H_2 bubbles were visibly observed, the current-potential response lacked any appreciable noise.

The voltammetric responses for these same electrodes at the same scan rate and initiated at -0.4 V were recorded after introduction of dissolved GeO_2 at a formal concentration of 0.05 M (Figures 6.3f-j). The principle observation was that the current at potentials more negative than -1.1 V were consistently higher, in accord with additional current for the reduction of dissolved GeO_2 (i.e., $HGeO_3^- + 4e^- + 2H_2O \rightarrow Ge + 5OH^-$). From these data, a cursory estimation of the faradaic efficiency for GeO_2 reduction at -1.4 V and -1.9 V was determined (Table 6.3). The faradaic efficiencies for GeO_2 reduction with $Hg_{1-x}In_x$ alloys was consistently higher than for solid In electrodes. A second observation in these data was that the cathodic wave at more positive potentials for electrodes containing In was consistently attenuated and shifted towards more negative potential. Similarly, the anodic current profile was altered.

Figure 6.10 in the Supporting Information contains the amperometric responses of these electrodes for Ge ec-LLS performed in the same electrolyte at -1.4 and -1.9 V, respectively. In every case, after the initial charging current dissipated within 100 s, the faradaic current slowly decayed to different quasi-steady state current densities. To obtain the target charge density, a total ec-LLS time between 12,500 to 75,000 s at E = -1.4 V and between 3,000 to 12,000 s at E = -1.9 V was necessary. Notably, electrodes with lower In content took longer to reach the target charge density.

6.4.3 Raman Spectral Analyses

A black particulate Ge film completely covered the electrode surface after all Ge ec-LLS trials. Figure 6.4 highlights representative Raman spectra for the as-deposited Ge crystallites collected with each type of electrode. The LO phonon mode for crystalline Ge near but substantially less than 300 cm^{-1} was observed for every sample.

Table 6.4 in the Supporting Information collects and summarizes the peak position and full widths at half maximum (*fwhm*) for each ec-LLS experiment. Three general features were apparent. First, for a given electrode material, the Ge produced at -1.4 V exhibited a smaller *fwhm* value than the corresponding material produced at -1.9 V. Second, the phonon peak position for crystalline Ge prepared with pure Hg was at a larger frequency than the phonon peak positions for crystalline Ge prepared with

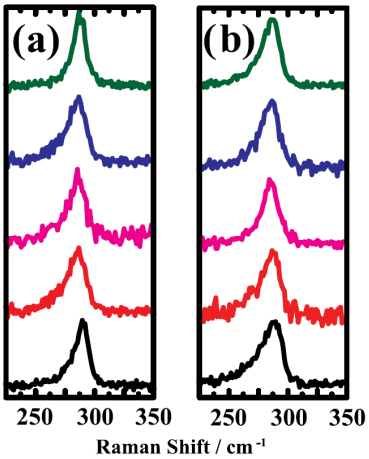

Figure 6.4: First-order Raman spectra for Ge electrodeposited on Hg1-xInx electrodes immersed in 0.01 M $Na_2B_4O_7$ and 0.05 M GeO_2 solution and biased at -1.4 V (a) and -1.9 V (b) with respect to an Ag/AgCl reference electrode. Green, blue, magenta, red and black graph represents the Hg, $Hg_0.7In_0.3$, $Hg_0.5In_0.5$, $Hg_0.3In_0.7$ and indium foil electrode respectively. The spectra have been offset for clarity.

$Hg_{1-x}In_x$. Third, the phonon peak positions tracked with In content for $Hg_{1-x}In_x$ and In electrodes.

6.4.4 X-ray Diffraction Analyses

Figure 6.5 shows representative power X-ray diffractograms of the ec-LLS deposited Ge crystal.

The strong diffraction pattern of the as prepared Ge crystal exhibited the reflection of diamond cubic lattice structure of crystalline Ge. Table 6.5 in the Supporting Information collect and summarizes the diffraction peak positions, full widths at half maximum (*fwhm*), corresponding crystal size and average crystal size, peak intensity ratio and lattice parameter for Hg, $Hg_{1-x}In_x$, and In electrodes at two different applied potential. Two general characteristics were clearly visible. First, the relative intensities of the peaks in the diffractograms were not the same, indicating some change in crystal orientation or possible preferred growth direction. Second, the lattice constant for Ge was clearly a function of In increasing with the increasing amounts of In (Figure 6.6).

6.4.5 Scanning Electron Microscopy Analyses

Representative scanning electron micrographs of as-deposited Ge crystallites for each film are presented in Figure 6.7.

As reported previously,[41] a leaf-like microstructure was observed on the Hg pool electrode (Figure 6.7 a) at less negative potentials and a bundle of nanofibers at more negative potentials (Figure 6.7f).[41] However, with increasing In content in the

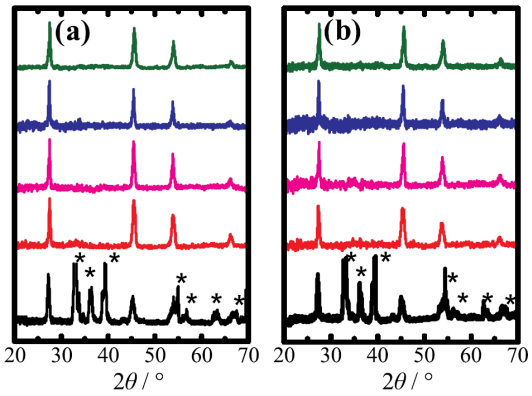

Figure 6.5: Powder X-ray diffractograms of Ge electrodeposited on Hg, $Hg_{1-x}In_x$, and In electrodes at potential a) -1.4 V and b) -1.9 V under the same reaction condition as described in Figure 6.5. Peaks denoted with * denote signals from crystalline In. The diffraction patterns are offset for clarity.

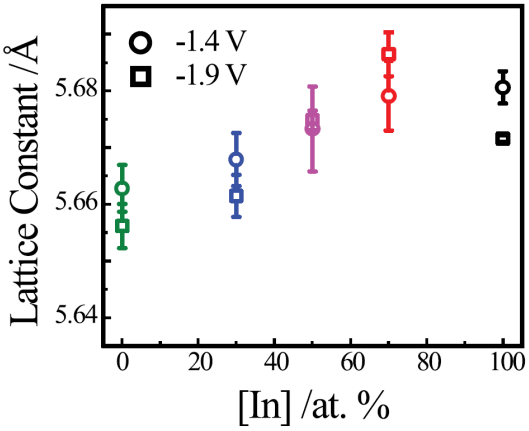

Figure 6.6: Lattice constant value of the crystalline Ge as a function of indium content (at. %) synthesized on Hg, $Hg_{1-x}In_x$, and In electrodes at potential -1.4 V (circular dot) and -1.9 V (square dot).

$Hg_{1-x}In_x$ alloys (Figures 6.7b-d,g-i), these morphologies were not conserved. For $Hg_{0.7}In_{0.3}$, the leaf-like shape was observed at both potentials, with no evidence of nanofibers. For $Hg_{0.5}In_{0.5}$, faceted grains appeared ~5 μm in size and their structure was not leaf-like at -1.4 V and only somewhat at -1.9 V. Additionally, sporadically interspersed in the Ge grains were smooth nanowires. For $Hg_{0.3}In_{0.7}$, the Ge grains were larger (>10 μm) at both potentials. Again, a minority fraction of Ge nanowires were intermixed throughout the ec-LLS product material. These features were in contrast with the morphologies observed with solid In electrodes (Figure 6.7 e,j), where there were no faceted grains. Instead, the surface was coated with a contiguous, granular film with particles of ~0.2 μm at both potentials. Smaller Ge nanowires were heterogeneously located on top of the granular surface coating. The contrasting crystalline Ge morphologies obtained with $Hg_{0.5}In_{0.5}$ and $Hg_{0.3}In_{0.7}$ are particularly notable since the total reaction time required to pass the target charge was comparable, indicating that the operative growth rates in these two cases were essentially

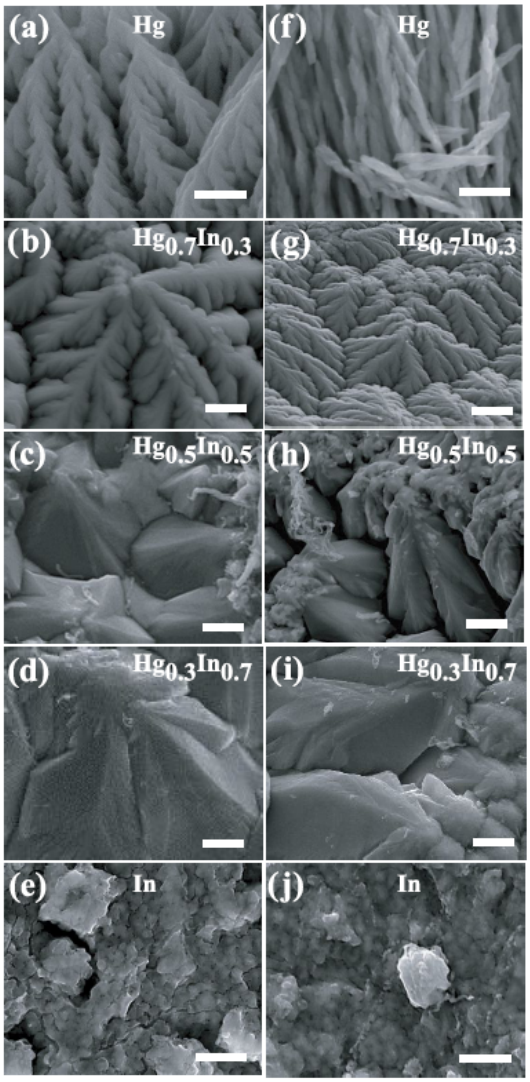

Figure 6.7: Scanning electron micrographs of as-prepared crystalline Ge electrodeposited with Hg, $Hg_{1x}In_x$, and In electrodes from solutions containing 0.05 M GeO_2 and 0.01 M $Na_2B_4O_7$. Micrographs show crystalline Ge obtained at (a-e) E = -1.4 V and (f-j) E = -1.9 V vs E(Ag/AgCl). Scale bars:(a, f, e, j) 0.5 μm; (b, c, d, g, h, i) 1 μm.

identical but the crystal morphology was patently different.

Figure 6.8 shows scanning electron micrographs specifically detailing the Ge nanowires observed with the $Hg_{0.5}In_{0.5}$, $Hg_{0.3}In_{0.7}$, and In electrodes.

With the liquid $Hg_{1-x}In_x$ alloys, the Ge nanowires were several microns in length and could approach 1 micron in diameter. Additionally, these nanowires were often kinked multiple times and sometimes coiled. Almost uniformly, these nanowires featured an obvious round liquid metal cap on the tip. Elemental analysis indicated the composition of these caps were 52.6% In, 14.5 % Hg, 20.2 % Ge and 12.6 % O. For crystalline Ge electrodeposited with solid In electrodes, the nanowires were noticeably shorter and much smaller in diameter (~0.1 μm) but still exhibited numerous

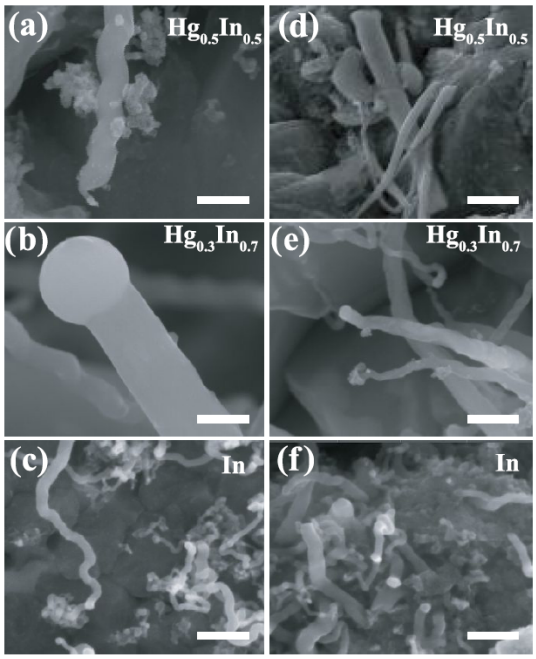

Figure 6.8: SEM micrographs of as-synthesized Ge crystal electrodeposited on $Hg_{1-x}In_x$ from the 0.1 M $Na_2B_4O_7$ and 0.05 M GeO_2 solution. Left side column image (a-c) obtained at potential -1.4 and right-side column image (d-f) obtained at -1.9 V vs Ag/AgCl. Scale bars: 0.5 μm.

kinks.

6.5 Discussion

The presented data support two primary points. First, the surface of $Hg_{1-x}In_x$ alloys is enriched by Hg but only in the topmost atomic layer of the liquid metal. Second, the presence of In during Ge ec-LLS did not alter the nucleation and crystal growth rates but did accelerate the diffusion of Ge along the growing crystal surface, greatly impacting the resultant crystal morphology. These points are discussed below.

6.5.1 Surface Composition of Liquid $Hg_{1-x}In_x$ Alloys

The surface composition of an ideal liquid metal mixture can be determined from the Gibbs adsorption isotherm. Specifically, in an ideal mixture, the component with the higher surface energy will have a more dilute fractional composition on the surface relative to its fractional composition in the bulk mixture,[72]

$$x_s = \frac{1}{\frac{1-x_b}{x_b} e^{-\frac{A}{k_b T}\left(\gamma_{Hg}-\gamma_{In}\right)} + 1} \tag{6.2}$$

where x_b is the bulk composition of In in the binary alloy, γ_{In} and γ_{Hg} are the surface tensions for In and Hg, respectively, A is the average area per atom in the

binary liquid alloy, k_B is the Boltzmann constant, and T is the temperature. To estimate accurately the surface composition of $Hg_{1-x}In_x$ alloys immersed in aqueous sodium tetraborate, the potential dependence of the surface tensions for each pure liquid metal in this electrolyte is required. Nevertheless, from surface tensions of In and Hg relative to vacuum (Table 6.1), the general expectation is that the surface of $Hg_{1-x}In_x$ alloys should be largely composed of Hg (e.g. $x_s \sim 0.3$ when $x_b = 0.7$).[73] The X-ray reflectance data directly confirm this concept, i.e. even the HgIn alloy with the highest bulk In content is Hg-rich at the electrolyte/liquid metal interface. Additionally, the collected XRR data provide further structural insight, i.e. the bulk composition is maintained just beneath the outer, Hg-rich surface layer.

Although XRR data were collected at a single electrolyte composition, the observed surface features of $Hg_{1-x}In_x$ should not depend strongly on the concentration of the supporting electrolyte. The best fit of the XRR data showed no evidence that adsorption of the supporting electrolyte occurs at the negative potentials of interest. No suitable fit was possible that included an explicit adlayer at potentials relevant to ec-LLS. Moreover, the background ion concentration does not appreciably change the electron density of the electrolyte, further limiting the impact of concentration on the XRR interpretation. The electrochemical data corroborate the inferences from the X-ray data. In the blank electrolyte without dissolved GeO_2, all the liquid $Hg_{1-x}In_x$ alloy electrodes exhibited H^+ reduction current-potential profiles consistent with the behavior of pure Hg rather than In electrodes. Since the electrochemical reduction of H^+ to H_2 is an inner-sphere redox process that depends strongly on the electronic character of the electrode surface, these data are fully in line with these liquid metals possessing a surface layer of predominantly/exclusively Hg atoms.

The electrochemical data separately indicate that In atoms are still able to participate in interfacial processes. The appearance of the cathodic redox wave near -1.1 V for $Hg_{1-x}In_x$ alloys strongly mirrors the reduction of the surface oxide on pure In,[74] even for $Hg_{0.7}In_{0.3}$. The integrated charge under these curves constituted several monolayers worth of indium oxide, indicating that the sub-surface In atoms are readily oxidized in these $Hg_{1-x}In_x$ liquid metal alloys. The exact mechanism of how sub-surface In atoms are oxidized is not presently clear but the occurrence and reoccurrence of indium oxidation suggests $x_s \neq 0$, in line with the estimate of $x_s \leqslant 0.02$ from the X-ray data. In this case, the oxidation of In atoms 'getters' In^0 from the surface, which are then rapidly replaced by the ample supply of sub-surface In. If the supply rate of In atoms to the electrolyte/liquid metal surface influences the rate of In oxide formation, then a difference in electrochemical behaviors at positive potentials would be expected. However, the return sweeps in the voltammetry in Figures 6.4 b-d exhibit oxidation peaks with equivalent positions and profiles. Accordingly, the exchange rate between surface and sub-surface atomic layers is not assumed to be limiting in the reactivity of In atoms at the electrolyte/electrode interface.

The collective data highlight beneficial properties of the $Hg_{1-x}In_x$/electrolyte interface structure for the electrochemical reduction of dissolved GeO_2 and Ge incorporation into the liquid metal, i.e. the first two steps of the ec-LLS process. Because of the strong Hg surface segregation, the electrode surface is Hg-like, substantially reducing the hydrogen evolution current density and facilitating higher coulombic efficiency of the ec-LLS process. The limitation of the Hg enrichment to a single atomic layer at the surface is likewise advantageous relative to a shallow gradient in the liquid metal composition. The steep Hg enrichment only at the surface ensures a high In-content already very near to the surface. Thus, the beneficial influence of In on the Ge transport (*vide infra*) becomes effective directly following Ge entering the sub-surface of the liquid metal phase. In addition, our observations indicate that the surface segregation layer is highly dynamic and apparently does not represent a barrier for the transfer of species between the interior of the liquid metal and the electrode/electrolyte interface.

6.5.2 Influence of $Hg_{1-x}In_x$ Composition on Ge Crystal Growth by ec-LLS

The cumulative microscopic, Raman, and X-ray diffraction data separately suggest that inclusion of In in liquid Hg specifically changed the fate of Ge atoms after initial electroreduction of dissolved GeO_2. Ge crystals grown with pure Hg exhibited clear dendritic structures, consistent with fast nucleation and crystal growth occurring at a large supersaturation. That is, because the solubility of Ge in Hg is small at room temperature, any appreciable amount of Ge dissolved in the liquid metal likely resulted in a large supersaturation, as observed in related ec-LLS processes.[75-76] Since the rates of nucleation and crystal growth are typically proportional to the extent of supersaturation,[77-79] the subsequent crystal growth rates are expected to be correspondingly fast.

When In was included in liquid Hg, especially at low concentrations, the dendritic structure of the resultant Ge crystals was still evident. This feature is consistent with the fact that the supersaturation attained during ec-LLS remained unchanged because In did not increase the bulk solubility of Ge in the liquid metal. However, the electron micrographs are clear that each Ge dendritic branch became progressively thicker with increasing In content. Eventually, the apparent grain size still had the outer profile of the dendrite 'leafs' but effectively with the inner void space filled in.

As described in Figure 6.9, we posit this observation arises because In can access the crystal growth front and because the presence of In specifically enhances the mobility of Ge along the solid Ge surface. The precedent for In acting as a surface transporter is not known in electrochemical settings but is well established in the field of vapor deposition of semiconductor films.[80-81] In this latter context, In has been identified as a 'surfactant' that specifically facilitates Ge surface diffusion in the case of vapor phase deposition of Ge on Si substrates.[82-84] A notable difference

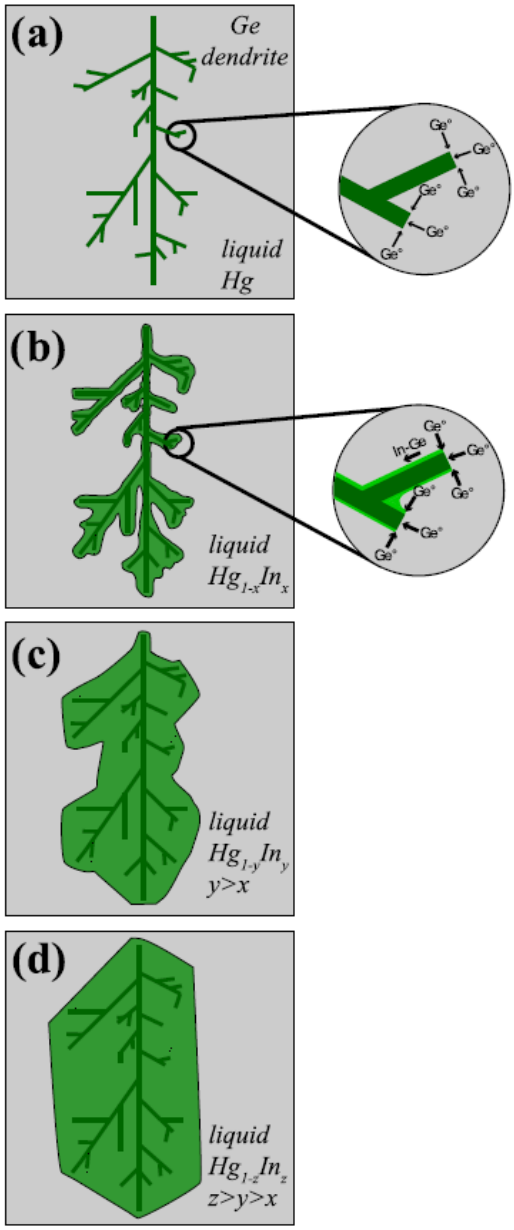

Figure 6.9: Schematic depiction of the influence of In on the surface diffusion of Ge on the resultant morphology of the Ge crystallites as a function of the In concentration.

between this prior precedence of In as a surface transporting agent and the work shown here is the operating temperatures. For vapor phase deposition, the action of In at a surface is typically understood at elevated temperatures. For the work shown here, the influence of In as a surface transporting agent was observed at room temperature.

The notion of In as an agent that affects/catalyzes the surface transport of Ge is consistent with the other materials characterization data. Specifically, the inferred crystallite sizes from the X-ray diffraction data do not appreciably change when In is dissolved in Hg, consistent with the idea that In is not changing the supersaturation level of Ge in the liquid metal and the corresponding crystal growth rate. Similarly, the Raman spectra are consistently red-shifted for all liquid metals, indicating that even though large apparent Ge grains are obtained with higher In content, the Ge grains are polycrystalline with crystallite domains remaining below the Bohr exciton radius of Ge (i.e. 25 nm).[85]

Presumably, the mediated transport of Ge by In involves a strong interaction between In and Ge. There are no known stable In-Ge complexes in the reported binary phase diagram[49] that would predict the formation of a strong In-Ge bond. However, molten In at elevated temperatures completely wets crystalline Ge,[57-58] indicating that the surface tension of the In/Ge interface is small. Although no direct measurement of the surface tension at this interface is available, an estimate of 0.58 N m^{-1} at T = 25 °C is possible through Young's equation and Eötvös' rule.[57] By comparison, the surface tension of the Hg/Ge interface at room temperature is in excess of 1.1 N m^{-1}, since the solid/vapor surface tensions of crystalline Ge are uniformly in excess of this value[86] and the wetting contact angle between Hg and a Ge wafer is significantly greater than 90 °. These liquid/solid surface tensions, by eq 2, would now predict an accumulation of In at the liquid metal/Ge crystal interface. Accordingly, the obvious trend in increasing Ge lattice constants with increasing In content in liquid $Hg_{1-x}In_x$ alloys in the X-ray diffraction patterns is consistent with the premise that the crystal growth plane is In-rich. Separately, the observation that the liquid metal droplets on the observed Ge nanowires consistently had a decreased fraction of In relative to the bulk pool alloy composition, in conjunction with the measurable In concentrations in these Ge nanowires, indicating that In had a high affinity for Ge.

The action of In as a surface transporting agent is also in accord with a recent and separate observation from our group on the growth mechanism of Ge nanowires using molten In nanodroplets.[46] In that work, the cumulative data indicated that Ge crystal growth was limited by the surface transport of Ge to the growth interface. That work also implied that electrodeposition of crystalline Ge using solid, rather than liquid, In electrodes may be possible. Here, in this work, we in fact did detect some accumulation of crystalline Ge with solid In foil electrodes. This observation stands in stark contrast to our and other groups' past attempts to perform crystalline

Ge electrodeposition with solid metal electrodes.[41, 87-88] However, the size of these Ge crystallites were smaller than for the liquid metal electrodes, their arrangement was a thin, compact film, and the total quantity was small. Hence, although fast mobility of electrodeposited Ge atoms on an In surface may still occur, this feature alone is not sufficient to mimic the crystal growth process in ec-LLS.

6.6 Conclusions

This work rejects the hypothesis that bulk solubilities of solutes are the only relevant factors in choosing components in the design of a liquid metal solvent for growing tailored inorganic crystals. Instead, this work demonstrates that the inclusion of In in binary $Hg_{1-x}In_x$ liquid metal alloys strongly impacts the morphology of the resultant Ge crystals grown by ec-LLS. In pure Hg, the dendritic structure of the resultant Ge crystals reflects the low Ge solubility and high operative supersaturations during nucleation and growth. Upon addition of In into Hg, the dendritic structures still form initially but then are 'filled in' with more Ge crystallites. The separate voltammetric and X-ray reflective data indicate that Hg is strongly enriched in the first atomic layer of $Hg_{1-x}In_x$ but that the alloy beneath this surface layer maintains the bulk composition, enabling In to still participate in interfacial processes while surficial Hg otherwise facilitates the initial electroreduction step for ec-LLS over H_2 generation. The inferred take away is that once Ge is dissolved beneath the first atomic layer of the liquid metal, In acts to accelerate Ge diffusion along the solid Ge/liquid metal interface. These data suggest that In as a liquid metal component specifically can dictate the crystalline grain morphology by effecting transport at the growth interface rather than by changing the solute solubility. More generally, the data argue for further development of liquid metal alloys as optimal solvents since surface segregation can improve the interfacial properties relevant for crystal growth.

Acknowledgements

We acknowledge generous financial support from the National Science Foundation (CHE-1807755) for S. M. and by the Deutsche Forschungsgemeinschaft (Ma1618/18) and the German Federal Ministry for Science and Education (05K16FK2 and 05K19K2) for O.M.M. and B.M.M. We also thank the beamline staff at P08 of PETRA III for experimental support and DESY for the beamtime.

Supporting Information

Additional information including chronoamperometric responses for Hg, Hg1-xInx, and In electrodes immersed in 10 mM $Na_2B_4O_7$ and 50 mM GeO_2 solution, a tabulated collection of the fitting parameters used in the first layer model for analysis of the X-ray reflectivity data presented in the main text as well as the corresponding

values for two relevant comparison fits for liquid Hg and liquid In previously reported in the literature, a tabulated summary of the voltammetric features of the data shown in the main text, a tabulated summary of the Raman spectral features shown in the main text, and a tabulated summary of the X-ray diffraction data are available. This material is available free of charge via the internet at ∼ http://pubs.acs.org.

6.7 References

1. Kanatzidis, M. G.; Pöttgen, R.; Jeitschko, W., The Metal Flux: A Preparative Tool for the Exploration of Intermetallic Compounds. Angew. Chem. Int. 2005, 44, 6996-7023.

2. Stojanovic, M.; Latturner, S. E., Growth of New Ternary Intermetallic Phases from Ca/Zn Eutectic Flux. J. Solid State Chem 2007, 180, 907-914.

3. Benbow, E. M.; Dalal, N. S.; Latturner, S. E., Crystal Growth and Magnetic Behavior of R6t13-Xalxmy Phases (R=La, Nd; T=Mn, Fe; M=Main Group) Grown from Lanthanide-Rich Eutectic Fluxes. J. Solid State Chem 2009, 182, 3055-3062.

4. Sebastian, C. P.; Malliakas, C. D.; Chondroudi, M.; Schellenberg, I.; Rayaprol, S.; Hoffmann, R.-D.; Pöttgen, R.; Kanatzidis, M. G., Indium Flux-Growth of Eu2auge3: A New Germanide with an Alb2 Superstructure. Inorg. Chem. 2010, 49, 9574-9580.

5. He, H.; Tyson, C.; Saito, M.; Bobev, S., Synthesis and Structural Characterization of the Ternary Zintl Phases Ae3al2pn4 and Ae3ga2pn4 (Ae=Ca, Sr, Ba, Eu; Pn=P, as). J. Solid State Chem 2012, 188, 59-65.

6. Seifner, M. S.; Sistani, M.; Zivadinovic, I.; Bartmann, M. G.; Lugstein, A.; Barth, S., Drastic Changes in Material Composition and Electrical Properties of Gallium-Seeded Germanium Nanowires. Cryst. Growth Des. 2019, 19, 2531-2536.

7. Ouyang, L.; Maher, K. N.; Yu, C. L.; McCarty, J.; Park, H., Catalyst-Assisted Solution-Liquid-Solid Synthesis of Cds/Cdse Nanorod Heterostructures. J. Am. Chem. Soc. 2007, 129, 133-138.

8. Trentler, T. J.; Hickman, K. M.; Goel, S. C.; Viano, A. M.; Gibbons, P. C.; Buhro, W. E., Solution-Liquid-Solid Growth of Crystalline Iii-V Semiconductors: An Analogy to Vapor-Liquid-Solid Growth. Science 1995, 270, 1791-1794.

9. Schmidt, V.; Wittemann, J. V.; Gösele, U., Growth, Thermodynamics, and Electrical Properties of Silicon Nanowires. Chem. Rev. 2010, 110, 361-388. 10. Sar, F.; Gasser, J. G., Electronic Transport Properties of Liquid Ga-Zn Alloys. Intermetallics 2003, 11, 1369-1376.

11. Turchanin, A.; Freyland, W., Surface Freezing and Wetting in Ga-Pb Alloy: Second Harmonic and Plasma Generation Study. Physical Chemistry Chemical Physics 2003, 5, 5285-5290.

12. Scharmann, F.; Cherkashinin, G.; Breternitz, V.; Knedlik, C.; Hartung, G.; Weber, T.; Schaefer, J. A., Viscosity Effect on Gainsn Studied by Xps. Surface and Interface Analysis 2004, 36, 981-985.

13. Xi, Y.; Zu, F. Q.; Li, X. F.; Yu, J.; Liu, L. J.; Li, Q.; Chen, Z. H., High-Temperature Abnormal Behavior of Resistivities for Bi-in Melts. Physics Letters A 2004, 329, 221-225.

14. Shpyrko, O. G.; Grigoriev, A. Y.; Streitel, R.; Pontoni, D.; Pershan, P. S.; Deutsch, M.; Ocko, B.; Meron, M.; Lin, B. H., Atomic-Scale Surface Demixing in a Eutectic Liquid Bisn Alloy. Physical Review Letters 2005, 95.

15. Yazdanpanah, M. M.; Harfenist, S. A.; Safir, A.; Cohn, R. W., Selective Self-Assembly at Room Temperature of Individual Freestanding Ag2ga Alloy Nanoneedles. Journal of Applied Physics 2005, 98.

16. Shpyrko, O. G.; Streitel, R.; Balagurusamy, V. S. K.; Grigoriev, A. Y.; Deutsch, M.; Ocko, B. M.; Meron, M.; Lin, B. H.; Pershan, P. S., Surface Crystallization in a Liquid Ausi Alloy. Science 2006, 313, 77-80.

17. Dickey, M. D.; Chiechi, R. C.; Larsen, R. J.; Weiss, E. A.; Weitz, D. A.; Whitesides, G. M., Eutectic Gallium-Indium (Egain): A Liquid Metal Alloy for the Formation of Stable Structures in Microchannels at Room Temperature. Advanced Functional Materials 2008, 18, 1097-1104.

18. Yatsenko, S. P.; Sabirzyanov, N. A.; Yatsenko, A. S., Dissolution Rates and Solubility of Some Metals in Liquid Gallium and Aluminum. In 13th International Conference on Liquid and Amorphous Metals, 2008; Vol. 98, pp U654-U660.

19. Cheng, S.; Rydberg, A.; Hjort, K.; Wu, Z., Liquid Metal Stretchable Unbalanced Loop Antenna. Applied Physics Letters 2009, 94.

20. Egry, I.; Ricci, E.; Novakovic, R.; Ozawa, S., Surface Tension of Liquid Metals and Alloys - Recent Developments. Advances in Colloid and Interface Science 2010, 159, 198-212.

21. Khalouk, K.; Mayoufi, M.; Gasser, J. G., Are There Phase Transitions in Liquid Metallic Alloys? Philosophical Magazine 2010, 90, 2695-2709.

22. Wang, L.-M.; Tian, Y.; Liu, R., Dependence of Glass Forming Ability on Liquid Fragility: Thermodynamics Versus Kinetics. Applied Physics Letters 2010, 97.

23. Deshpande, R. D.; Li, J.; Cheng, Y.-T.; Verbrugge, M. W., Liquid Metal Alloys as Self-Healing Negative Electrodes for Lithium Ion Batteries. Journal of the Electrochemical Society 2011, 158, A845-A849.

24. Jeyakumar, M.; Hamed, M.; Shankar, S., Rheology of Liquid Metals and Alloys. Journal of Non-Newtonian Fluid Mechanics 2011, 166, 831-838.

25. Liu, T.; Sen, P.; Kim, C.-J. C. J., Characterization of Nontoxic Liquid-Metal Alloy Galinstan for Applications in Microdevices. Journal of Microelectromechanical Systems 2012, 21, 443-450.

26. Thelen, J.; Dickey, M. D.; Ward, T., A Study of the Production and Reversible Stability of Egain Liquid Metal Microspheres Using Flow Focusing. Lab on a Chip 2012, 12, 3961-3967.

27. Agarwal, R.; Samui, P.; Kulkarni, S. G., Thermodynamic Investigations of (Bi+Ni) System - Part Ii. Journal of Chemical Thermodynamics 2013, 57, 477-484.

28. Kramer, R. K.; Majidi, C.; Wood, R. J., Masked Deposition of Gallium-Indium Alloys for Liquid-Embedded Elastomer Conductors. Advanced Functional Materials 2013, 23, 5292-5296.

29. Boley, J. W.; White, E. L.; Chiu, G. T. C.; Kramer, R. K., Direct Writing of Gallium-Indium Alloy for Stretchable Electronics. Advanced Functional Materials 2014, 24, 3501-3507.

30. Foettinger, K.; Rupprechter, G., In Situ Spectroscopy of Complex Surface Reactions on Supported Pd-Zn, Pd-Ga, and Pd(Pt)-Cu Nanoparticles. Accounts of Chemical Research 2014, 47, 3071-3079.

31. Wang, K.; Jiang, K.; Chung, B.; Ouchi, T.; Burke, P. J.; Boysen, D. A.; Bradwell, D. J.; Kim, H.; Muecke, U.; Sadoway, D. R., Lithium-Antimony-Lead Liquid Metal Battery for Grid-Level Energy Storage. Nature 2014, 514, 348-+.

32. Melchakov, S. Y.; Yamshchikov, L. F.; Osipenko, A. G.; Pozdeev, P. A.; Rusakov, M. A., Solubility and Excessive Thermodynamic Characteristics of Pr and Nd in the Ga-Sn Eutectic Alloy. Russian Metallurgy 2015, 595-598.

33. Zavabeti, A., et al., A Liquid Metal Reaction Environment for the Room-Temperature Synthesis of Atomically Thin Metal Oxides. Science 2017, 358, 332-335.

34. Zhao, X.; Xu, S.; Liu, J., Surface Tension of Liquid Metal: Role, Mechanism and Application. Frontiers in Energy 2017, 11, 535-567.

35. Biswas, S.; O'Regan, C.; Petkov, N.; Morris, M. A.; Holmes, J. D., Manipulating the Growth Kinetics of Vapor–Liquid–Solid Propagated Ge Nanowires. Nano Lett. 2013, 13, 4044-4052.

36. Kubota, N.; Yokota, M.; Mullin, J. W., Supersaturation Dependence of Crystal Growth in Solutions in the Presence of Impurity. Journal of Crystal Growth 1997, 182, 86-94.

37. Vekilov, P. G., Nucleation. Crystal Growth & Design 2010, 10, 5007-5019.

38. Jacobsson, D.; Panciera, F.; Tersoff, J.; Reuter, M. C.; Lehmann, S.; Hofmann, S.; Dick, K. A.; Ross, F. M., Interface Dynamics and Crystal Phase Switching in Gaas Nanowires. Nature 2016, 531, 317-322.

39. Tornberg, M.; Maliakkal, C. B.; Jacobsson, D.; Dick, K. A.; Johansson, J., Limits of Iii–V Nanowire Growth Based on Droplet Dynamics. The Journal of Physical Chemistry Letters 2020, 11, 2949-2954.

40. Wen, C. Y.; Tersoff, J.; Hillerich, K.; Reuter, M. C.; Park, J. H.; Kodambaka, S.; Stach, E. A.; Ross, F. M., Periodically Changing Morphology of the Growth Interface in Si, Ge, and Gap Nanowires. Physical Review Letters 2011, 107, 025503.

41. Carim, A. I.; Collins, S. M.; Foley, J. M.; Maldonado, S., Benchtop Electrochemical Liquid–Liquid–Solid Growth of Nanostructured Crystalline Germanium. J. Am. Chem. Soc. 2011, 133, 13292-13295.

42. Zhang, T.; Fahrenkrug, E.; Maldonado, S., Electrochemical Liquid-Liquid-Solid Deposition of Ge at Hg Microdroplet Ultramicroelectrodes. J. Electrochem. Soc. 2016, 163, D500-D505.

43. Fahrenkrug, E.; Gu, J.; Jeon, S.; Veneman, P. A.; Goldman, R. S.; Maldonado, S., Room-Temperature Epitaxial Electrodeposition of Single-Crystalline Germanium Nanowires at the Wafer Scale from an Aqueous Solution. Nano Lett. 2014, 14, 847-852.

44. Fahrenkrug, E.; Biehl, J.; Maldonado, S., Electrochemical Liquid–Liquid–Solid Crystal Growth of Germanium Microwires on Hard and Soft Conductive Substrates at Low Temperature in Aqueous Solution. Chem. Mater. 2015, 27, 3389-3396.

45. Ma, L.; Fahrenkrug, E.; Gerber, E.; Crowe, A. J.; Venable, F.; Bartlett, B. M.; Maldonado, S., High-Performance Polycrystalline Ge Microwire Film Anodes for Li Ion Batteries. ACS Energy Lett. 2017, 2, 238-243.

46. Cheek, Q.; Fahrenkrug, E.; Hlynchuk, S.; Alsem, D. H.; Salmon, N. J.; Maldonado, S., In Situ Transmission Electron Microscopy Measurements of Ge Nanowire Synthesis with Liquid Metal Nanodroplets in Water. ACS Nano 2020, 14, 2869-2879.

47. Mahenderkar, N. K.; Liu, Y.-C.; Koza, J. A.; Switzer, J. A., Electrodeposited Germanium Nanowires. ACS Nano 2014, 8, 9524-9530.

48. Okamoto, H., Hg-in (Mercury-Indium). Journal of Phase Equilibria and Diffusion 2012, 33, 159-160.

49. Olesinki, R. W.; Kanani, N.; Abbaschian, G. J., The Ge-in (Germanium-Indium) System. Bulletin of Alloy Phase Diagrams 1985, 6, 536-539.

50. Guminski, C., The Ge-Hg (Germanium-Mercury) System. J. Phase Equilib. 1999, 20, 344.

51. Keck, P. H.; Broder, J., The Solubility of Silicon and Germanium in Gallium and Indium. Phys. Rev. 1953, 90, 521-522.

52. Grosse, A. A. V., The Relationship between Surface Tension and Energy of Liquid Metals and Their Heat of Vaporization at the Melting Point. Journal of Inorganic and Nuclear Chemistry 1964, 26, 1349-1361.

53. Clementi, E.; Raimondi, D. L.; Reinhardt, W. P., Atomic Screening Constants from Scf Functions. Ii. Atoms with 37 to 86 Electrons. The Journal of Chemical Physics 1967, 47, 1300-1307.

54. White, D. W. G., The Surface Tensions of Indium and Cadmium. Metallurgical and Materials Transactions B 1972, 3, 1933-1936.

55. Wilkinson, M. C., The Surface Properties of Mercury. Chemical Reviews 1972, 72, 575-625.

56. Zolper, J. C.; Barnett, A. M., Selective Area Solution Growth of Ge and Gaas on Si. Journal of Applied Physics 1989, 66, 210-214.

57. Teubner, T.; Boeck, T.; Schmidt, K., Modelling of Solution Growth of Silicon from Small Indium Droplets – Homogeneous Nucleation. Journal of Crystal Growth 1999, 198-199, 425-429.

58. Maruyama, T.; Matsuda, K.; Naritsuka, S., Multinuclear Layer-by-Layer Growth on Ge(111) by Lpe. Journal of Crystal Growth 2005, 275, e2155-e2160.

59. DiMasi, E.; Tostmann, H.; Ocko, B. M.; Pershan, P. S.; Deutsch, M., X-Ray Reflectivity Study of Temperature-Dependent Surface Layering in Liquid Hg. Physical Review B 1998, 58, R13419-R13422.

60. Elsen, A.; Festersen, S.; Runge, B.; Koops, C. T.; Ocko, B. M.; Deutsch, M.; Seeck, O. H.; Murphy, B. M.; Magnussen, O. M., In Situ X-Ray Studies of Adlayer-Induced Crystal Nucleation at the Liquid–Liquid Interface. Proceedings of the National Academy of Sciences 2013, 110, 6663.

61. Magnussen, O. M.; Ocko, B. M.; Regan, M. J.; Penanen, K.; Pershan, P. S.; Deutsch, M., X-Ray Reflectivity Measurements of Surface Layering in Liquid Mercury. Physical Review Letters 1995, 74, 4444-4447.

62. Murphy, B. M.; Greve, M.; Runge, B.; Koops, C. T.; Elsen, A.; Stettner, J.; Seeck, O. H.; Magnussen, O. M., A Novel X-Ray Diffractometer for Studies of Liquid-Liquid Interfaces. Journal of Synchrotron Radiation 2014, 21, 45-56.

63. Seeck, O. H., et al., The High-Resolution Diffraction Beamline P08 at Petra Iii. Journal of Synchrotron Radiation 2012, 19, 30-38.

64. Pershan, P. S.; Schlossman, M., Liquid Surfaces and Interfacs: Synchrotron X-Ray Methods.; Cambridge University Press: Cambridge, 2012.

65. Robinson, L. K., Structure Factor Determination in Surface X-Ray Diffraction. Australian Journal of Physics 1988, 41, 359-368.

66. Elsen, A.; Murphy, B. M.; Ocko, B. M.; Tamam, L.; Deutsch, M.; Kuzmenko, I.; Magnussen, O. M., Surface Layering at the Mercury-Electrolyte Interface. Physical Review Letters 2010, 104, 105501.

67. Runge, B.; Festersen, S.; Koops, C. T.; Elsen, A.; Deutsch, M.; Ocko, B. M.; Seeck, O. H.; Murphy, B. M.; Magnussen, O. M., Temperature- and Potential-Dependent Structure of the Mercury-Electrolyte Interface. Physical Review B 2016, 93, 165408.

68. Yang, B.; Li, D.; Rice, S. A., Structure of the Liquid-Vapor Interface of a Dilute Ternary Alloy: Pb and in in Ga. Physical Review B 2003, 67, 054203.

69. Tostmann, H.; Dimasi, E.; Shpyrko, O. G.; Pershan, P. S.; Ocko, B. M.; Deutsch, M., Ii. Surface and Interfacial Phenomena: Surface Phases in Binary Liquid Metal Alloys: An X-Ray Study. Berichte der Bunsengesellschaft für physikalische Chemie 1998, 102, 1136-1141.

70. Regan, M. J.; Pershan, P. S.; Magnussen, O. M.; Ocko, B. M.; Deutsch, M.; Berman, L. E., X-Ray Reflectivity Studies of Liquid Metal and Alloy Surfaces. Physical Review B 1997, 55, 15874-15884.

71. Tostmann, H.; DiMasi, E.; Pershan, P. S.; Ocko, B. M.; Shpyrko, O. G.; Deutsch, M., Surface Structure of Liquid Metals and the Effect of Capillary Waves: X-Ray Studies on Liquid Indium. Physical Review B 1999, 59, 783-791.

72. Dumke, M. F.; Tombrello, T. A.; Weller, R. A.; Housley, R. M.; Cirlin, E. H., Sputtering of the Gallium-Indium Eutectic Alloy in the Liquid Phase. Surface Science 1983, 124, 407-422.

73. Oguchi, Y.; Itami, T.; Shimoji, M., Surface Tension of the Liquid Hg-in Alloys. Physics and Chemistry of Liquids 1981, 10, 315-325.

74. Metikoš-Huković, M.; Omanović, S., Thin Indium Oxide Film Formation and Growth: Impedance Spectroscopy and Cyclic Voltammetry Investigations. J. Electroanal. Chem. 1998, 455, 181-189.

75. Cheek, Q.; Fahrenkrug, E.; Hlynchuk, S.; Alsem, D. H.; Salmon, N. J.; Maldonado, S., In Situ Transmission Electron Microscopy Measurements of Ge Nanowire Synthesis with Liquid Metal Nanodroplets in Water. ACS Nano 2020, 14, 2869-2879.

76. DeMuth, J.; Fahrenkrug, E.; Maldonado, S., Controlling Nucleation and Crystal Growth of Ge in a Liquid Metal Solvent. Crystal Growth & Design 2016, 16, 7130-7138.

77. De Yoreo, J. J.; Vekilov, P. G., Principles of Crystal Nucleation and Growth. Reviews in Mineralogy and Geochemistry 2003, 54, 57-93.

78. Kodambaka, S.; Tersoff, J.; Reuter, M. C.; Ross, F. M., Germanium Nanowire Growth Below the Eutectic Temperature. Science 2007, 316, 729.

79. Senthil Pandian, M.; Verma, S.; Pareek, P.; Ramasamy, P.; Bartwal, K. S., Laser Shadowgraphy and Mach-Zehnder Interferometric Imaging of Convection, Concentration and Growth Kinetics During Unidirectional Solution Growth of Benzophenone Crystal. Optics & Laser Technology 2020, 132, 106491.

80. Won, D.; Weng, X.; Redwing, J. M., Effect of Indium Surfactant on Stress Relaxation by V-Defect Formation in Gan Epilayers Grown by Metalorganic Chemical Vapor Deposition. J. Appl. Phys. 2010, 108, 093511.

81. Won, D.; Weng, X.; Redwing, J. M., Metalorganic Chemical Vapor Deposition of N-Polar Gan Films on Vicinal Sic Substrates Using Indium Surfactants. Appl. Phys. Lett. 2012, 100, 021913.

82. Eaglesham, D. J.; Unterwald, F. C.; Jacobson, D. C., Growth Morphology and the Equilibrium Shape: The Role of "Surfactants" in Ge/Si Island Formation. Phys. Rev. Lett 1993, 70, 966-969.

83. Minoda, H.; Tanishiro, Y.; Yamamoto, N.; Yagi, K., In Situ Tem Observations of Surfactant-Mediated Epitaxy: Growth of Ge on an Si(111) Surface Mediated by In. Surf. Sci. 1996, 357-358, 418-421.

84. Voigtländer, B.; Zinner, A.; Weber, T.; Bonzel, H. P., Modification of Growth Kinetics in Surfactant-Mediated Epitaxy. Physical Review B 1995, 51, 7583-7591.

85. Vadavalli, S.; Valligatla, S.; Neelamraju, B.; Dar, M. H.; Chiasera, A.; Ferrari, M.; Desai, N. R., Optical Properties of Germanium Nanoparticles Synthesized by Pulsed Laser Ablation in Acetone. Front. Phys. 2014, 2.

86. Zhang, J.-M.; Ma, F.; Xu, K.-W.; Xin, X.-T., Anisotropy Analysis of the Surface Energy of Diamond Cubic Crystals. Surface and Interface Analysis 2003, 35, 805-809.

87. Bui, N. N.; Ledina, M.; Reber, T. J.; Jung, J.; Stickney, J. L., Electrochemical Scanning Tunneling Microscopic Study of the Potential Dependence of Germanene Growth on Au(111) at Ph 9.0. ACS Nano 2017, 11, 9481-9489.

88. Liang, X.; Kim, Y.-G.; Gebergziabiher, D. K.; Stickney, J. L., Aqueous Electrodeposition of Ge Monolayers. Langmuir 2010, 26, 2877-2884.

6.8 Supporting Information

Introduction

This document contains chronoamperometric responses for Hg, Hg1-xInx, and In electrodes immersed in 10 mM $Na_2B_4O_7$ and 50 mM GeO_2 solution, a tabulated collection of the fitting parameters used in the first layer model for analysis of the X-ray reflectivity data presented in the main text as well as the corresponding values for two relevant comparison fits for liquid Hg and liquid In previously reported in

the literature, a tabulated summary of the voltammetric features of the data shown in the main text, a tabulated summary of the Raman spectral features shown in the main text, and a tabulated summary of the X-ray diffraction data presented in the main text.

Chronoamperometric Responses

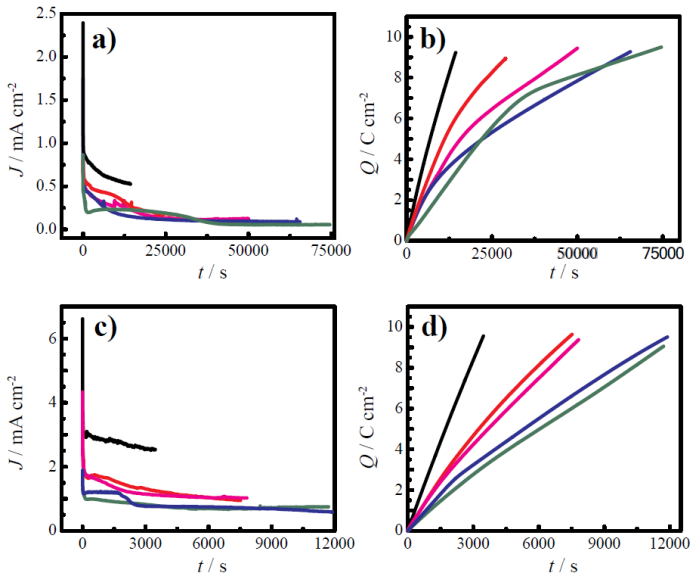

Figure 6.10: Amperometric responses for Hg, $Hg_{1-x}In_x$, and In electrodes immersed in 10 mM $Na_2B_4O_7$ and 50 mM GeO_2 solution at **a)** -1.4 V and **c)** -1.9 V vs E(Ag/AgCl). The corresponding charge passed over time profiles are shown in **b)** and **d)**, respectively. Green, blue, magenta, red and black lines represents the Hg, $Hg_0.7In_0.3$, $Hg_0.5In_0.5$, $Hg_0.3In_0.7$ and In electrodes, respectively.

Tabulated Data

The parameters resulting from fits of the normalized XRR data using the first layer modified-distorted crystal model as described in equation 1 in the main paper are tabulated in Table 6.2. In addition, XRR fit parameters from previously published XRR data for liquid Hg and liquid In are presented for comparison. The data for Hg immersed in NaF(aq) are reported for -0.85 V at 294 K are comparable to the experimental measurements reported here within the error margin. The data for liquid In in vacuum at the melting point are presented since bulk liquid In in water at standard pressure is not tenable.

Fitting Parameter	Unit	Hg in 0.1 M NaB_4O_7 (aq)[a]	$Hg_{0.3}In_{0.7}$ (aq)[b]	Hg in 0.01 M NaF (aq)[c]	In [d]
σ_i	Å	1.03 ± 0.01	0.76 ± 0.01	1.09 ± 0.08	0.61 ± 0.06
σ_b	Å	0.42 ± 0.02	0.43 ± 0.01	0.43 ± 0.08	0.54 ± 0.06
σ_f	Å	set to be same as σ_i	1.16 ± 0.02	set to be same as σ_i	-
σ_{H_2O}	Å	0.66	0.66	0.66	-
d	Å	2.70 ± 0.03	2.71 ± 0.01	2.74 ± 0.06	2.69 ± 0.05
d_f	Å	2.92 ± 0.03	3.27 ± 0.04	2.87 ± 0.09	2.69
ρ_f /$\rho_{e,Me}$	-	0.95 ± 0.01	1.44 ± 0.02	0.93 ± 0.05	1
ρ_{H_2O} /$\rho_{e,Me}$	-	0.1	0.17	0.1	-
z_{H_2O}	Å	-0.12	-0.12	-0.13 ± 0.07	-

Table 6.2: [a] E=-1.4 V (this work)
[b] E=-1.4 V (this work)
[c] Mean values determined from the values reported in the SI of *Temperature- and potential-dependent structure of the mercury-electrolyte interface*, Phys. Rev. B, 2016, 93, 165408
[d] Data reported for In in vacuum at T = 443 K in *Surface structure of liquid metals and the effect of capillary waves: X-ray studies on liquid indium*, Phys. Rev. B, 1999, 59, 783

Electrode composition	Cathodic peak potential / V	Cathodic peak current density / mA cm^{-2}	Integrated cathodic charge density / mC cm^{-2}	Anodic peak potential / V	Anodic peak current density / mA cm^{-2}	Integrated anodic charge density mC cm^{-2}	Faraday Efficiency for GeO_2 Reduction at E = -1.4 V / %	Faraday Efficiency for GeO_2 Reduction at E = -1.9 V / %
Hg	–	0	0	–	0	0	97.6	66.1
$Hg_{0.7}In_{0.3}$	-1.09	0.24	3.86	-0.81	0.10	0.78	81.6	76.7
$Hg_{0.5}In_{0.5}$	-1.08	0.23	3.33	-0.83	0.12	0.81	80.7	77.8
$Hg_{0.3}In_{0.7}$	-1.15	0.36	4.94	-0.83	0.12	0.83	78.5	59.2
In	-1.07	0.52	7.71	-0.86	0.16	1.88	56.6	4.7

Table 6.3: Summary of Voltammetric Features for GeO_2 Reduction on Hg, $Hg_{1-x}In_x$, and In Electrodes

Electrode composition	-1.4 V Peak position /cm^{-1}	-1.4 V fwhm /cm^{-1}	-1.9 V Peak position /cm^{-1}	-1.9 V fwhm /cm^{-1}
Hg	287.4	12.3	285.9	17.6
$Hg_{0.7}In_{0.3}$	284.5	18.1	284.7	18.4
$Hg_{0.5}In_{0.5}$	285.4	15.4	285.1	15.9
$Hg_{0.3}In_{0.7}$	286.9	17.9	285.4	18.9
In	289.3	12.9	288.1	19.8

Table 6.4: Raman Features for As-Prepared Ge from ec-LLS

Electrode composition	-1.4 V Peak position /2θ	Grain size /nm	Average Grain size /nm	Peak intensity ratio	Lattice constant /Å	-1.9 V Peak position /2θ	Grain size /nm	Average Grain size /nm	Peak intensity ratio	Lattice constant /Å
Hg	27.45 (0.37)	21.8	15.2 ± 4.6	1.00	5.6628 ± 0.0041	27.45 (0.54)	15.1	13.1 ± 1.7	1.00	5.6562 ± 0.0039
	45.58 (0.60)	14.3		1.27		45.58 (0.61)	13.9		1.22	
	53.97 (0.66)	13.3		0.87		53.97 (0.73)	12.1		0.83	
	66.34 (0.83)	11.4		0.19		66.35 (0.85)	11.1		0.23	
$Hg_{0.7}In_{0.3}$	27.37 (0.33)	24.4	18.1 ± 5.3	1.00	5.6679 ± 0.00465	27.37 (0.35)	23.1	17.2 ± 5.1	1.00	5.6615 ± 0.0037
	45.42 (0.44)	19.2		1.07		45.42 (0.46)	18.3		1.16	
	53.81 (0.51)	17.3		0.75		53.81 (0.53)	16.8		0.77	
	66.10 (0.82)	11.5		0.21		66.12 (0.89)	10.6		0.26	
$Hg_{0.5}In_{0.5}$	27.41 (0.41)	19.8	16.1 ± 3.0	1.00	5.6733 ± 0.00748	27.39 (0.47)	17.1	14.2 ± 2.5	1.00	5.6748 ± 0.0017
	45.45 (0.51)	16.8		1.54		45.47 (0.55)	15.4		1.35	
	53.83 (0.56)	15.7		1.03		53.86 (0.67)	13.2		0.95	
	66.11 (0.77)	12.3		0.37		66.18 (0.84)	11.2		0.38	
$Hg_{0.3}In_{0.7}$	27.46 (0.38)	21.3	14.8 ± 4.4	1.00	5.6791 ± 0.0061	27.33 (0.47)	17.3	13.5 ± 2.7	1.00	5.6865 ± 0.0039
	45.51 (0.64)	13.3		1.88		45.37 (0.73)	11.7		1.55	
	53.91 (0.72)	12.2		1.46		53.75 (0.77)	11.4		1.03	
	66.23 (0.77)	12.3		0.48		66.06 (0.70)	13.5		0.26	
In	27.21 (0.49)	16.6	9.7 ± 5.0	1.00	5.6806 ± 0.0028	27.19 (0.53)	15.2	10.1 ± 3.5	1.00	5.6716 ± 0.0006
	45.22 (0.85)	10.1		0.87		45.17 (0.85)	10.1		0.75	
	54.24 (1.73)	5.1		0.70		54.28 (1.17)	7.6		0.73	
	66.95 (1.37)	6.9		0.46		66.92 (1.21)	7.8		0.71	

Table 6.5: Summary of X-ray Diffraction Data for As-Prepared Ge from ec-LLS

7 Conclusion

The main aim of this thesis was to investigate *in-situ* electrochemical induced crystal growth at liquid metals-electrolyte interface and understand how physical and chemical interface properties affect the synthesis process. The goal was achieved by combining X-ray scattering, electrochemical methods, and optical microscope imaging. X-ray reflectivity and grazing incidence diffractions are powerful techniques since they allow structure information at the atomic scale with possible milli-second time resolution. However, high brilliance is required for a buried liquid interface; therefore, synchrotron radiation is necessary. Furthermore, given the unfeasibility to tilt liquid samples, a dedicated instrument such as LISA at beamline P08 PETRA III (DESY) is required.

To perform such challenging experiments, a suitable sample environment is necessary. Therefore, an improved electrochemical sample cell was developed, with all the principal characteristics needed for *in-situ* x-ray experiment, allowing the exchange of electrolyte and liquid metals, visible access to the interface for a microscope, ease of assembly, and flexible design to suit different beamlines.
For growth studies, a range of liquid metal electrodes combined with electrolytes containing metal ions was chosen.
One of these was liquid mercury electrode in aqueous salt solutions containing Pb halide, with the main focus on understanding how the different halides influence crystal growth. The Hg electrode was investigated while immersed in a different solution of 0.01 M of NaX (X=Br, Cl, F) in an electrochemical cell. All three samples showed features as previously seen for similar electrolyte solutions [59, 60], namely a change of interfacial roughness as a function of potential due to the capillarity effect. Notable changes in the behavior were observed once a precursor of PbX_2 was introduced to the electrolyte. First, electrochemical current red-ox peaks appeared due to the reduction and oxidation of Pb^{2+} ions in the solution. Once the potential was held at a more negative potential of the reduction potential, the Hg electrode exhibited the same surface structure of a pristine Hg electrode. A stable adlayer was formed when the potential moved close to the oxidation threshold. That behavior was common for all the three systems; the same behavior was observed in a previous study of our group where with a similar system (Hg - NaBr + NaF + $PbBr_2$) [22]. For even more positive potentials, crystal growth occurred. The nature of the crystals was attributed to a highly oriented, along the surface normal, structure of Pb(OH)X for the Br and Cl containing solution. However, for the F-containing solution, the

crystals were associated with a powder-like cubic form of PbF_2. The combination of X-ray scattering and electrochemical methods could successfully characterize the systems and explain the general behavior of liquid Hg immersed in lead-halides solutions. Adlayer formation prior to the crystal deposition appears to be a common phenomenon. These experiments show how an adlayer acts as a template for quasi-epitaxial growth of crystals with the same orientation as the adlayer beneath them. This study also shows the importance of interface chemistry in deposition on liquid metal, particularly for strong chemisorption anions such as bromide and chloride. This opens up exciting possibilities for preparing technologically interesting compound semiconductors such as perovskites. In addition, the strong chemical interactions of many species with metal surfaces lead to strongly bound adsorbate layers with a high surface coverage, which promotes the formation of oriented precursor adlayers.

To gain an understanding of growth on liquid Hg immersed in GeO_2 solution, systematic studies of the interface were performed. GeO_2 is a potent precursor often used to synthesize crystalline Ge on a liquid metal substrate. However, there is a lack of *in-situ* investigation on how the presence of this precursor influences the interface of the liquid metals itself. Here, the structure of Hg in a buffer solution of $Na_2B_4O_7$ was characterized as a function of potential and compared with Hg-$Na_2B_4O_7$+ GeO_2. The Hg interface shows no change in the structure once immersed in the buffer (compared to NaF solution), suggesting non-specific adsorption of the borate ions. However, the interface structure was altered once the precursor was added to the solution. Specifically, an adsorbate (most likely described by $HGeO^{3-}$) was present at the Hg surface. Interestingly, when the potential was held positive enough, a condensed layer was observed, attributed to polygermanates with a rutile GeO2 sub-structure. The process was shown to be reversible once the potential was swept to more negative values. The XRR data suggest accumulation of oxyanions at the liquid metal electrode substrate. This could present an alternative synthetic route for oxocondensates that are otherwise usually obtained by hydrothermal reactions [140]. The results here provide new insights on the surface chemistry of Hg in this electrolyte and how this might affect Ge synthesis on the system.

Liquid metal alloys are of interest for the synthesis of crystalline materials, but knowledge of how to design optimal liquid metal alloy solvents for the growth of inorganic crystals, such as semiconductors, is still lacking. With our collaborators from the University of Michigan, we examined the synthesis of Ge in different Hg-In alloy compositions. Notably, we observed different crystal morphology as a function of alloy composition and potential applied. Investigation of the bare working electrode (pure Hg and $Hg_{0.3}In_{0.7}$ in borate solution) clarifies the nature of the interface and thus the mechanism of growth of the crystallites. The data show that nucleation and growth cannot start at the interface as the topmost atomic layer of the alloy is shown to be of Hg. Therefore, the precursor must dissolve into the substrate and

organize the growth process through diffusion. This work shows how considerations for electrochemical synthesis should not only focus on the solute composition but also on the substrate, in particular, if the latter is liquid and it could act as a solvent and therefore affect the structure of the deposit. Moreover, the data presented suggest that indium as a liquid metal component can dictate the crystalline grain morphology by affecting transport at the interface rather than changing only the solute solubility. Liquid metal alloys are shown to be optimal for crystal growth since they act as solvents, and surface segregation can improve the interfacial properties relevant for material synthesis.

This thesis presents how electrochemical growth at liquid-liquid interfaces has unique properties and a wide field of application. Furthermore, it is shown the importance of understanding the surface processes that directly affect crystal growth, which is an essential step for developing upscale production.

Studies of Hg-$Na_2B_4O_7$+ GeO_2 during and post-deposition have been collected to understand the nucleation, growth process, and kinetics of Ge synthesis in liquid mercury. The analysis is in progress.
Our group has already started a deep investigation of the potential and composition-dependent behavior of liquid mercury-indium alloy. On the same system *in-situ* x-ray diffraction experiment during germanium deposition is planned to study the interface pre, during, and post-synthesis, and how it affects the final deposit.
Preliminary data on *in-situ* investigation on the liquid gallium-electrolyte interface has been collected. Since Ga is not toxic and it has a vast interest in industrial applications [141–143]. The challenge is even more ambitious here since an oxide-free surface is difficult to obtain. Moreover, in a chemical condition where gallium oxide is not present, such as an acidic environment, liquid gallium is not stable and dissolves in solution. Further investigation is therefore needed it.
Preliminary perovskite synthesis data, e.g., $CsPbBr_3$ on liquid mercury, has already been successfully collected at beamline P08 in DESY. However, even more, significant interest is in in-situ studies of PbI perovskites synthesis due to the extensive potential application.

A X-ray Reflectivity Macro

During the years the beamline P08 changed controlling language, from SPEC to SPOCK. Therefore slightly different macros has been used

A.1 SPEC

An example of macro used to record a XRR profile is the following:

```
\# === primary beam ==============
umv abs 4
umk 0 0 0
umvr sz -1
point 1
umvr sz 1

\# === reflectivity curve ========
umk 0 0 0.03
umv abs 3 \#stepsize 0.002 (20s)
lscan .04 .08 20 1

umv abs 2 \#stepsize .004 (22s)
lscan .072 .16 22 1

umv abs 1 \#stepsize  .01 (10s)
lscan .14 .24 10 1

umv abs 0
lscan .22 .29 7 1 \#stepsize  .01 (7s)
lscan .3 .6 12 1 \#(12s)
lscan 0.65 1.0 7 20 \#(140s)
lscan 1.1 1.9 8 120 \#(960s)
lscan 2.0 2.4 4 240 \#(960s)



umv abs 4
umk 0 0 0
```

```
\# === primary beam 2==
umvr sz -1
point 1
umvr sz 1
umv abs 6
```

It's worth notice that the macro was checked and changed if needed it every time. To assure that the detector linear behaviour of the detector. To do so at each angle where we swap the absorber the counts per pixels were checked to avoid to exceed 60-70 k counts per pixel.

A.2 SPOCK

The following it is an example of macro for XRR for SPOCK. Macros are written directly in Python.

```
@macro()
def lisa_refl_diff_25keV_hgin(self):

    self.execMacro('umv', 'atten', 1)
    '''
    sz scan
    '''
    self.execMacro('umv', 'abs', 4)
    self.execMacro('umvq', 0, 0, 0)
    self.execMacro('dscan', 'sz', -.15, .15, 20, 1)
    self.execMacro('mvsa', 'stepc', 0)
    '''
    primary beam
    '''
    self.execMacro('umv', 'abs', 4)
    self.execMacro('umvq', 0, 0, 0)
    self.execMacro('umvr', 'sz', -1)
    self.execMacro('pointy',1)
    self.execMacro('umvr', 'sz', 1)

    '''
    reflectivity
    '''
    self.execMacro('umv',[['abs',4]])
    self.execMacro('qscan',0,0, 0,0, 0.025, 0.075, 33, 1)
    self.execMacro('umv',[['abs',3]])
    self.execMacro('qscan',0,0, 0,0, 0.065, 0.11, 20, 1)
```

```
self.execMacro('umv',[['abs',2]])
self.execMacro('qscan',0,0, 0,0, 0.09, 0.21, 30, 1)
self.execMacro('umv',[['abs',1]])
self.execMacro('qscan',0,0, 0,0, 0.18, 0.38, 30, 1)
self.execMacro('umv',[['abs',0]])
self.execMacro('qscan',0,0, 0,0, 0.3, 0.6, 15, 2)
self.execMacro('qscan',0,0, 0,0, 0.625, 1, 13, 20)  #0.029
self.execMacro('qscan',0,0, 0,0, 1.1, 1.8, 8, 120)  #0.1
self.execMacro('qscan',0,0, 0,0, 1.9, 2.4, 5, 240)  #0.1

'''
primary beam
'''
self.execMacro('umv', 'abs', 4)
self.execMacro('umvq', 0, 0, 0)
self.execMacro('umvr', 'sz', -1)
self.execMacro('pointy',1)
self.execMacro('umvr', 'sz', 1)

'''
safety first
'''
self.execMacro('umv', 'abs', 6)
self.execMacro('umv', 'atten', 1)
```

The same rules mentioned before apply here. The macro was adapted every time. The counting time and step size were also adjusted to optimize time or focus on particular effects of the profile.

B Data used

The data used are from different beamtimes, all of them at LISA at P08 beamline (DESY):

B.1 Hg-NaX + PbX_2 X= Br Cl, F (Chapter 4)

- September 2018 Beamtime ID 11005498
- November 2019 Beamtime ID 11007116
- December 2020 Beamtime ID 11009676

B.2 Hg-$Na_2B_4O_7$ + GeO_2 (Chapter 5)

- May 2018 Beamtime ID 11004537
- November 2019 Beamtime ID 11007023

B.3 HgIn (Chapter 6)

- November 2019 Beamtime ID 11007023

C Software for data analysis

The data analysis was mainly performed with scripts written in *Python* programming language. The essential codes used in this thesis are updated on Gitlab.

C.1 XRR extraction

The LISA team developed Python code to reduce the detector images of a reflectivity profile. Each team member added the part needed for the different experiments. The code optimized to extract XRR at liquid Hg-electrolyte interface can be found at:

https://gitlab.physik.uni-kiel.de/sartori/xrr-extraction

C.2 XRR fit

Fitting XRR profiles of liquid metal-electrolyte interface can be challenging, and there is no commercial software available for this scope. So a self-written code was used. The basic code was developed by a former researcher of the group Sven Festersen. During the years, the code has been partly rewritten and adapted for different tasks, thanks to the help of students like Henning Vogt and Lukas Petersdorf.
The tasks for the software could be even more challenging when an ad-layer at the interface of the two liquids is present. An example of the software is at:

https://gitlab.physik.uni-kiel.de/sartori/xrr-fit

C.3 GID data treatment

As mentioned in 3.2.2, a scan in 2θ with multiple detector images was reduced to a big detector image by binning the detector pixels. First of all, the detector images were converted from pixels coordinates in q space and then binned together. Then the data was saved in a different file; in such a way, it is easier to re-plot the data without reducing them every time. From a 2θ scan, it is also possible to obtain a diffraction pattern such as intensity as a function on q (or 2θ).
The different codes can be found at:

https://gitlab.physik.uni-kiel.de/sartori/gid-plot

Bibliography

1. Dickey, M. D. Emerging applications of liquid metals featuring surface oxides. *ACS applied materials & interfaces* **6,** 18369–18379 (2014).
2. Daeneke, T. *et al.* Liquid metals: fundamentals and applications in chemistry. *Chemical Society Reviews* **47,** 4073–4111 (2018).
3. Liang, S.-T., Wang, H.-Z. & Liu, J. Progress, Mechanisms and Applications of Liquid-Metal Catalyst Systems. *Chemistry–A European Journal* **24,** 17616–17626 (2018).
4. Booth, S. G. & Dryfe, R. A. Assembly of nanoscale objects at the liquid/liquid interface. *The Journal of Physical Chemistry C* **119,** 23295–23309 (2015).
5. Hammock, M. L., Chortos, A., Tee, B. C.-K., Tok, J. B.-H. & Bao, Z. 25th anniversary article: the evolution of electronic skin (e-skin): a brief history, design considerations, and recent progress. *Advanced materials* **25,** 5997–6038 (2013).
6. Piradashvili, K., Alexandrino, E. M., Wurm, F. R. & Landfester, K. Reactions and polymerizations at the liquid–liquid interface. *Chemical reviews* **116,** 2141–2169 (2016).
7. Platt, M., Dryfe, R. A. & Roberts, E. P. Controlled deposition of nanoparticles at the liquid–liquid interface. *Chemical communications,* 2324–2325 (2002).
8. Dang, F. *et al.* Characteristics of CeO2 nanocubes and related polyhedra prepared by using a liquid- liquid interface. *Crystal growth & design* **10,** 4537–4541 (2010).
9. Krishnaswamy, R. & Sood, A. Growth, self-assembly and dynamics of nanoscale films at fluid interfaces. *Journal of Materials Chemistry* **20,** 3539–3552 (2010).
10. Zhou, D., Tan, X., Wu, H., Tian, L. & Li, M. Synthesis of C- C Bonded Two-Dimensional Conjugated Covalent Organic Framework Films by Suzuki Polymerization on a Liquid–Liquid Interface. *Angewandte Chemie* **131,** 1390–1395 (2019).
11. Miyazawa, K. *et al.* Structural characterization of C60 nanowhiskers formed by the liquid/liquid interfacial precipitation method. *Surface and Interface Analysis: An International Journal devoted to the development and application of techniques for the analysis of surfaces, interfaces and thin films* **35,** 117–120 (2003).
12. Carim, A. I., Collins, S. M., Foley, J. M. & Maldonado, S. Benchtop electrochemical liquid–liquid–solid growth of nanostructured crystalline germanium. *Journal of the American Chemical Society* **133,** 13292–13295 (2011).

13. Sakaguchi, H., Ohmura, R. & Mori, Y. H. Effects of kinetic inhibitors on the formation and growth of hydrate crystals at a liquid–liquid interface. *Journal of Crystal Growth* **247,** 631–641 (2003).
14. Basu, M. *et al.* Evolution of hierarchical hexagonal stacked plates of CuS from liquid- liquid interface and its photocatalytic application for oxidative degradation of different dyes under indoor lighting. *Environmental science & technology* **44,** 6313–6318 (2010).
15. Kadota, K., Shirakawa, Y., Matsumoto, I., Shimosaka, A. & Hidaka, J. Formation and morphology of asymmetric NaCl particles precipitated at the liquid-liquid interface. *Advanced Powder Technology* **18,** 775–785 (2007).
16. Dumke, M., Tombrello, T., Weller, R., Housley, R. & Cirlin, E. Sputtering of the gallium-indium eutectic alloy in the liquid phase. *Surface Science* **124,** 407–422 (1983).
17. Metaferia, W., Schulte, K. L., Simon, J., Johnston, S. & Ptak, A. J. Gallium arsenide solar cells grown at rates exceeding 300 μm h- 1 by hydride vapor phase epitaxy. *Nature communications* **10,** 1–8 (2019).
18. Tang, C., Fan, S., Lamy de la Chapelle, M., Dang, H. & Li, P. Synthesis of gallium phosphide nanorods. *Advanced Materials* **12,** 1346–1348 (2000).
19. Fahrenkrug, E., Gu, J. & Maldonado, S. Electrodeposition of crystalline GaAs on liquid gallium electrodes in aqueous electrolytes. *Journal of the American Chemical Society* **135,** 330–339 (2013).
20. Siegfried, M. J. & Choi, K.-S. Directing the architecture of cuprous oxide crystals during electrochemical growth. *Angewandte Chemie* **117,** 3282–3287 (2005).
21. Pattadar, D. *et al.* Evidence for Facilitated Surface Transport during Ge Crystal Growth by Indium in Liquid Hg–In Alloys at Room Temperature. *Crystal Growth & Design* **21,** 1645–1656 (2021).
22. Elsen, A. *et al.* In situ X-ray studies of adlayer-induced crystal nucleation at the liquid–liquid interface. *Proceedings of the National Academy of Sciences* **110,** 6663–6668 (2013).
23. Festersen, S. *et al.* Nucleation and Growth of PbBrF Crystals at the Liquid Mercury–Electrolyte Interface Studied by Operando X-ray Scattering. *Langmuir* **36,** 10905–10915 (2020).
24. Cheek, Q. *et al.* In situ transmission electron microscopy measurements of ge nanowire synthesis with liquid metal nanodroplets in water. *ACS nano* **14,** 2869–2879 (2020).
25. Booth, S. G. *et al.* In situ XAFS Study of palladium electrodeposition at the liquid/liquid interface. *Electrochimica Acta* **235,** 251–261 (2017).
26. Maiti, S. *et al.* Evidence of contact epitaxy in the self-assembly of HgSe nanocrystals formed at a liquid–liquid interface. *Journal of Physics: Condensed Matter* **29,** 095101 (2017).
27. Booth, S. G. *et al.* Gold deposition at a free-standing liquid/liquid interface: evidence for the formation of Au (I) by microfocus X-ray spectroscopy (μXRF

and μXAFS) and cyclic voltammetry. *The Journal of Physical Chemistry C* **119,** 16785–16792 (2015).

28. Zhang, Z., Gekhtman, D., Dresselhaus, M. S. & Ying, J. Y. Processing and characterization of single-crystalline ultrafine bismuth nanowires. *Chemistry of Materials* **11,** 1659–1665 (1999).
29. Zhou, K. *et al.* Characterization and properties of Zn/Co zeolitic imidazolate frameworks vs. ZIF-8 and ZIF-67. *Journal of Materials Chemistry A* **5,** 952–957 (2017).
30. Inkson, B. in *Materials characterization using nondestructive evaluation (NDE) methods* 17–43 (Elsevier, 2016).
31. Murphy, B., Festersen, S. & Magnussen, O. The atomic scale structure of liquid metal–electrolyte interfaces. *Nanoscale* **8,** 13859–13866 (2016).
32. Murphy, B. M. *et al.* A novel X-ray diffractometer for studies of liquid–liquid interfaces. *Journal of synchrotron radiation* **21,** 45–56 (2014).
33. DeMuth, J., Fahrenkrug, E. & Maldonado, S. Controlling nucleation and crystal growth of Ge in a liquid metal solvent. *Crystal Growth & Design* **16,** 7130–7138 (2016).
34. Fahrenkrug, E. *et al.* Room-temperature epitaxial electrodeposition of single-crystalline germanium nanowires at the wafer scale from an aqueous solution. *Nano letters* **14,** 847–852 (2014).
35. Lautrup, B. *Physics of continuous matter: exotic and everyday phenomena in the macroscopic world* (CRC press, 2011).
36. De Gennes, P.-G., Brochard-Wyart, F., Quéré, D., *et al. Capillarity and wetting phenomena: drops, bubbles, pearls, waves* (Springer, 2004).
37. Pershan, P. S. Review of the highlights of X-ray studies of liquid metal surfaces. *Journal of Applied Physics* **116,** 222201 (2014).
38. Rice, S. A. Research overview: The liquid-vapor interface of a metal as a vehicle for studying the atomic, electronic, and optical properties of an inhomogeneous liquid. *Proceedings of the National Academy of Sciences of the United States of America* **84,** 4709 (1987).
39. Penfold, J. The structure of the surface of pure liquids. *Reports on Progress in Physics* **64,** 777 (2001).
40. D'Evelyn, M. P. & Rice, S. A. Structure in the density profile at the liquid-metal-vapor interface. *Physical Review Letters* **47,** 1844 (1981).
41. Braslau, A. *et al.* Surface roughness of water measured by x-ray reflectivity. *Physical review letters* **54,** 114 (1985).
42. Ocko, B., Wu, X., Sirota, E., Sinha, S. & Deutsch, M. X-ray reflectivity study of thermal capillary waves on liquid surfaces. *Physical review letters* **72,** 242 (1994).
43. Rowlinson, J. S. & Widom, B. *Molecular theory of capillarity* (Courier Corporation, 2013).
44. Gryko, J. & Rice, S. The structure of the liquid-vapour interface of sodium-caesium alloys. *Journal of Physics F: Metal Physics* **12,** L245 (1982).

45. D'Evelyn, M. P. & Rice, S. A. A study of the liquid–vapor interface of mercury: Computer simulation results. *The Journal of chemical physics* **78,** 5081–5095 (1983).
46. Go, M., Chaco, E., *et al.* Structure and surface tension of the liquid-vapor interface of simple metals: A theoretical approach. *Physical Review B* **46,** 723 (1992).
47. Chekmarev, D. S., Zhao, M. & Rice, S. A. Computer simulation study of the structure of the liquid-vapor interface of mercury at 20, 100, and 200° C. *Physical Review E* **59,** 479 (1999).
48. Zhao, M. & Rice, S. A. Density distribution in the liquid-vapor interface of a dilute alloy of Pb in Ga. *Physical Review B* **63,** 085409 (2001).
49. Mo, H. *et al.* Observation of surface layering in a nonmetallic liquid. *Physical review letters* **96,** 096107 (2006).
50. Sloutskin, E. *et al.* Surface layering in ionic liquids: an X-ray reflectivity study. *Journal of the American Chemical Society* **127,** 7796–7804 (2005).
51. Shpyrko, O. *et al.* X-ray study of the liquid potassium surface: Structure and capillary wave excitations. *Physical Review B* **67,** 115405 (2003).
52. Sluis, D., D'Evelyn, M. P. & Rice, S. A. Experimental and theoretical studies of the density profile in the liquid–vapor interface of Cs. *The Journal of Chemical Physics* **78,** 1611–1613 (1983).
53. Regan, M. *et al.* Surface layering in liquid gallium: An X-ray reflectivity study. *Physical review letters* **75,** 2498 (1995).
54. Regan, M. *et al.* Oxidation of liquid gallium surfaces: X-ray reflectivity study. *Phys. Rev. B* **55,** 10786–10790 (1997).
55. Tostmann, H. *et al.* Surface structure of liquid metals and the effect of capillary waves: X-ray studies on liquid indium. *Physical Review B* **59,** 783 (1999).
56. Magnussen, O. *et al.* X-ray reflectivity measurements of surface layering in liquid mercury. *Physical review letters* **74,** 4444 (1995).
57. Magnussen, O. *et al.* X-ray reflectivity studies of the surface structure of liquid metals. *Physica B: Condensed Matter* **221,** 257–260 (1996).
58. DiMasi, E., Tostmann, H., Ocko, B., Pershan, P. S. & Deutsch, M. X-ray reflectivity study of temperature-dependent surface layering in liquid Hg. *Physical Review B* **58,** R13419 (1998).
59. Elsen, A. *et al.* Surface layering at the mercury-electrolyte interface. *Physical review letters* **104,** 105501 (2010).
60. Runge, B. *et al.* Temperature-and potential-dependent structure of the mercury-electrolyte interface. *Physical Review B* **93,** 165408 (2016).
61. Regan, M. *et al.* X-ray reflectivity studies of liquid metal and alloy surfaces. *Physical Review B* **55,** 15874 (1997).
62. Lei, N., Huang, Z. & Rice, S. A. Surface segregation and layering in the liquid–vapor interface of a dilute bismuth: gallium alloy. *The Journal of chemical physics* **104,** 4802–4805 (1996).

63. Tostmann, H., DiMasi, E., Ocko, B., Deutsch, M. & Pershan, P. S. X-ray studies of liquid metal surfaces. *Journal of non-crystalline solids* **250,** 182–190 (1999).
64. DiMasi, E., Tostmann, H., Ocko, B., Pershan, P. S. & Deutsch, M. Competition between Surface Layering and Surface Phase Formation in Dilute Liquid Hg-Au Alloys. *The Journal of Physical Chemistry B* **103,** 9952–9959 (1999).
65. Yang, B., Gidalevitz, D., Li, D., Huang, Z. & Rice, S. A. Two-dimensional freezing in the liquid–vapor interface of a dilute Pb: Ga alloy. *Proceedings of the National Academy of Sciences* **96,** 13009–13011 (1999).
66. DiMasi, E. *et al.* Surface-induced order in liquid metals and binary alloys. *Journal of Physics: Condensed Matter* **12,** A209 (2000).
67. Tostmann, H. *et al.* Microscopic surface structure of liquid alkali metals. *Physical Review B* **61,** 7284 (2000).
68. DiMasi, E. *et al.* Pairing interactions and Gibbs adsorption at the liquid Bi-In surface: a resonant x-ray reflectivity study. *Physical Review Letters* **86,** 1538 (2001).
69. Tolan, M. & Tolan, M. *X-ray scattering from soft-matter thin films: materials science and basic research* (Springer, 1999).
70. Lamb, H. *Hydrodynamics* (Cambridge University Press, 1994).
71. Seeck, O. H. & Murphy, B. *X-ray Diffraction: Modern Experimental Techniques* (CRC Press, 2015).
72. Pershan, P. X-ray scattering from liquid surfaces: Effects of thermal capillary waves. *Synchrotron Radiation News* **12,** 10–16 (1999).
73. Stanton, A. Wilhelm Conrad Röntgen on a new kind of rays: translation of a paper read before the Würzburg Physical and Medical Society, 1895. *Nature* **53,** 274–276 (1896).
74. Friedrich, W., Knipping, P. & Laue, M. Interferenzerscheinungen bei roentgenstrahlen. *Annalen der Physik* **346,** 971–988 (1913).
75. Laue, M. v. Eine quantitative Prüfung der Theorie für die Interferenzerscheinungen bei Röntgenstrahlen. *Annalen der Physik* **346,** 989–1002 (1913).
76. Bragg, W. H. & Bragg, W. L. The reflection of X-rays by crystals. *Proceedings of the Royal Society of London. Series A, Containing Papers of a Mathematical and Physical Character* **88,** 428–438 (1913).
77. Als-Nielsen, J. & McMorrow, D. *Elements of modern X-ray physics* (John Wiley & Sons, 2011).
78. Pershan, P. S. & Schlossman, M. *Liquid surfaces and interfaces: synchrotron x-ray methods* (Cambridge University Press, 2012).
79. Kittel, C. *Introduction to Solid State Physics* (Wiley ISBN, 2004).
80. Ashcroft, N. W. & Mermin, N. D. *Solid state physics* (Brooks/Cole, Cengage Learning, 1976).
81. Yager, K. *Ewald sphere, X-Ray Interactions with Matter* `http://gisaxs.com/index.php/Ewald_sphere`.

82. Dinnebier, R. E. & Billinge, S. J. *Powder diffraction: theory and practice* (Royal society of chemistry, 2008).
83. Baker, J. L. *et al.* Quantification of thin film crystallographic orientation using X-ray diffraction with an area detector. *Langmuir* **26,** 9146–9151 (2010).
84. Renaud, G., Lazzari, R. & Leroy, F. Probing surface and interface morphology with grazing incidence small angle X-ray scattering. *Surface Science Reports* **64,** 255–380 (2009).
85. Born, M. & Wolf, E. *Principles of optics: electromagnetic theory of propagation, interference and diffraction of light* (Elsevier, 2013).
86. Dosch, H., Batterman, B. & Wack, D. Depth-controlled grazing-incidence diffraction of synchrotron X radiation. *Physical review letters* **56,** 1144 (1986).
87. Robinson, I. & Tweet, D. Surface X-ray diffraction. *Reports on Progress in Physics* **55,** 599 (1992).
88. Marra, W., Eisenberger, P. & Cho, A. X-ray total-external-reflection–Bragg diffraction: A structural study of the GaAs-Al interface. *Journal of Applied Physics* **50,** 6927–6933 (1979).
89. Vineyard, G. H. Grazing-incidence diffraction and the distorted-wave approximation for the study of surfaces. *Physical Review B* **26,** 4146 (1982).
90. Segmüller, A. Characterization of epitaxial films by grazing-incidence X-ray diffraction. *Thin Solid Films* **154,** 33–42 (1987).
91. Ashcroft, N. & March, N. Structure factor and direct correlation function for a classical hard sphere fluid. *Proceedings of the Royal Society of London. Series A. Mathematical and Physical Sciences* **297,** 336–350 (1967).
92. Soper, A. & Phillips, M. A new determination of the structure of water at 25 C. *Chemical Physics* **107,** 47–60 (1986).
93. Soper, A. On the determination of the pair correlation function from liquid structure factor measurements. *Chemical physics* **107,** 61–74 (1986).
94. Daillant, J. & Gibaud, A. (*X-ray and Neutron Reflectivity: Principles and Applications* (Springer Berlin Heidelberg, 2009).
95. Sinha, S., Sirota, E., Garoff, S & Stanley, H. X-ray and neutron scattering from rough surfaces. *Physical Review B* **38,** 2297 (1988).
96. Nevot, 1. & Croce, P. Caractérisation des surfaces par réflexion rasante de rayons X. Application à l'étude du polissage de quelques verres silicates. *Revue de Physique appliquée* **15,** 761–779 (1980).
97. Parratt, L. G. Surface studies of solids by total reflection of X-rays. *Physical review* **95,** 359 (1954).
98. Pershan, P. S. X-ray or neutron reflectivity: limitations in the determination of interfacial profiles. *Physical Review E* **50,** 2369 (1994).
99. Of Crystallography, I. U., Ibers, J. A. & Hamilton, W. C. *International Tables for X-ray Crystallography: Revised and Supplementary Tables to Volumes 2 and 3/Editors James A. Ibers and Walter C. Hamilton* (Kynoch Press, 1974).

100. *NIST, X-Ray Attenuation Databases* https://physics.nist.gov/PhysRefData/FFast/html/form.html.
101. *CXRO, X-Ray Interactions with Matter* https://henke.lbl.gov/optical_constants/index.html.
102. Duval, J. F. *et al.* X-ray reflectivity at polarized liquid-Hg–Aqueous-Electrolyte interface: Challenging macroscopic approaches for ion-specificity issues. *Physical Review Letters* **108,** 206102 (2012).
103. MATERLIK, G. Resonant anomalous X-ray scattering. *Theory and Applications* (1994).
104. Bomont, J.-M., Bretonnet, J.-L., Gonzalez, D. & Gonzalez, L. Computer simulation calculations of the free liquid surface of mercury. *Physical Review B* **79,** 144202 (2009).
105. Kiessig, H. Interferenz von Röntgenstrahlen an dünnen Schichten. *Annalen der Physik* **402,** 769–788 (1931).
106. Bard, A. J. & Faulkner, L. R. *Electrochemical Methods: Fundamentals and Applications* (John Wiley & Sons, 2001).
107. Schmickler, W. & Santos, E. *Interfacial electrochemistry* (Springer Science & Business Media, 2010).
108. Hamann, C., Hamnett, A. & Vielstich, W. *Electrochemistry* ISBN: 9783527310692. https://books.google.de/books?id=EXljvgAACAAJ (Wiley, 2007).
109. *LibreTexts libraries: Mass Transport Mechanisms* [accessed 2022-01-21]. https://chem.libretexts.org/@go/page/61293.
110. Perez, N. in *Electrochemistry and Corrosion Science* 151–197 (Springer, 2016).
111. Wang, J., Ocko, B., Davenport, A. J. & Isaacs, H. S. In situ x-ray-diffraction and-reflectivity studies of the Au (111)/electrolyte interface: Reconstruction and anion adsorption. *Physical Review B* **46,** 10321 (1992).
112. Grahame, D. C. The electrical double layer and the theory of electrocapillarity. *Chemical reviews* **41,** 441–501 (1947).
113. Grahame, D. Electrode processes and the electrical double layer. *Annual review of physical chemistry* **6,** 337–358 (1955).
114. Herman, H. B., McNeely, R., Surana, P., Elliott, C. & Murray, R. W. Surface solubility and reaction inhibition in lead bromide and iodide adsorbed on mercury electrodes. *Analytical Chemistry* **46,** 1258–1265 (1974).
115. Anson, F. C. Patterns of ionic and molecular adsorption at electrodes. *Accounts of Chemical Research* **8,** 400–407 (1975).
116. Callister, W. D. & Rethwisch, D. G. *Materials science and engineering: an introduction* (Wiley New York, 2018).
117. Gu, J. *et al.* Template-free preparation of crystalline Ge nanowire film electrodes via an electrochemical liquid–liquid–solid process in water at ambient pressure and temperature for energy storage. *Nano letters* **12,** 4617–4623 (2012).

118. Brown, J. *Cyclic Voltammetry (CV) Simulator* https://communities.acs.org/t5/Jay-Brown-s-Personal-Archive/Cyclic-Voltammetry-CV-Simulator-Written-in-Microsoft-Excel/ba-p/85509.
119. Elgrishi, N. *et al.* A practical beginner's guide to cyclic voltammetry. *Journal of chemical education* **95,** 197–206 (2018).
120. Savéant, J.-M. *Elements of molecular and biomolecular electrochemistry: an electrochemical approach to electron transfer chemistry* (John Wiley & Sons, 2006).
121. Gosser, D. K. *Cyclic Voltammetry; Simulation and Analysis of Reaction Mechanisms* (VCH, New York, 1993).
122. Scholz, F. *et al. Electroanalytical methods* (Springer, 2010).
123. Budevski, E. B., Staikov, G. T. & Lorenz, W. J. *Electrochemical phase formation and growth: an introduction to the initial stages of metal deposition* (John Wiley & Sons, 2008).
124. Tsakova, V. Theory of electrochemical nucleation and growth—revisited? *Journal of Solid State Electrochemistry* **24,** 2183–2185 (2020).
125. Raub, E. & Muller, K. Fundamentals of metal deposition. *1967, 268 P. ELSEVIER PUBLISHING CO., NEW YORK* (1967).
126. Pasa, A. A. & Munford, M. L. *Encyclopedia of chemical processing* chap. Electrodeposition (CRC Press, 2005).
127. Seeck, O. H. *et al.* The high-resolution diffraction beamline P08 at PETRA III. *Journal of synchrotron radiation* **19,** 30–38 (2011).
128. Runge, B. *X-Ray Scattering Investigations of the Temperature and Potential Dependent Structure of the Mercury-Electrolyte Interface* PhD thesis (Mathematisch-Naturwissenschaftliche Fakultät, Christian-Albrechts-Universität Kiel, 2015).
129. Murphy, B. *et al. A new Diffractometer for Studies of Liquid—Liquid Interfaces* in *AIP Conference Proceedings* **1234** (2010), 155–158.
130. Pershan, P. S. & Als-Nielsen, J. X-ray reflectivity from the surface of a liquid crystal: Surface structure and absolute value of critical fluctuations. *Physical review letters* **52,** 759 (1984).
131. Pershan, P. S., Braslau, A., Weiss, A. & Als-Nielsen, J. Smectic layering at the free surface of liquid crystals in the nematic phase: X-ray reflectivity. *Physical Review A* **35,** 4800 (1987).
132. Schlossman, M. L. *et al.* A synchrotron x-ray liquid surface spectrometer. *Review of scientific instruments* **68,** 4372–4384 (1997).
133. Lin, B. *et al.* The liquid surface/interface spectrometer at ChemMatCARS synchrotron facility at the Advanced Photon Source. *Physica B: Condensed Matter* **336,** 75–80 (2003).
134. Festersen, S. *et al.* X-ray reflectivity from curved liquid interfaces. *Journal of Synchrotron Radiation* **25,** 432–438 (2018).
135. Konovalov, O. V. *et al.* X-Ray reflectivity from curved surfacesas illustrated by a graphene layer on molten copper. *Journal of Synchrotron Radiation* **29.** accepted.

136. Elsen, A. *Grenzflächen zwischen zwei Flüssigkeiten mittels Röntgenstreumethoden* PhD thesis (Mathematisch-Naturwissenschaftliche Fakultät, Christian-Albrechts-Universität Kiel, 2012).
137. Hazelnis, J. P. *et al.* Detection of Ge-Containing Adlayers at the Liquid Hg/Water Interface by In Situ X-ray Reflectivity in Aqueous Borate Electrolytes Containing Dissolved GeO2. *The Journal of Physical Chemistry C* **126,** 8177–8189 (2022).
138. Fahrenkrug, E. & Maldonado, S. Electrochemical liquid–liquid–solid (ec-LLS) crystal growth: a low-temperature strategy for covalent semiconductor crystal growth. *Accounts of Chemical Research* **48,** 1881–1890 (2015).
139. DeMuth, J. *et al.* Eutectic-bismuth indium as a growth solvent for the electrochemical liquid-liquid-solid deposition of germanium microwires and coiled nanowires. *Crystal Growth & Design* **18,** 677–685 (2018).
140. Everest, D. & Salmon, J. Studies in the chemistry of quadrivalent germanium. Part II. The depolymerisation of the pentagermanate ion with change of pH, and ion-exchange studies of germanate solutions containing sulphate and orthophosphate. *Journal of the Chemical Society (Resumed),* 1444–1449 (1955).
141. Yan, J., Lu, Y., Chen, G., Yang, M. & Gu, Z. Advances in liquid metals for biomedical applications. *Chemical Society Reviews* **47,** 2518–2533 (2018).
142. Khondoker, M. & Sameoto, D. Fabrication methods and applications of microstructured gallium based liquid metal alloys. *Smart Materials and Structures* **25,** 093001 (2016).
143. Sarafraz, M., Arya, A., Hormozi, F. & Nikkhah, V. On the convective thermal performance of a CPU cooler working with liquid gallium and CuO/water nanofluid: A comparative study. *Applied Thermal Engineering* **112,** 1373–1381 (2017).

Scientific Contribution

Publications

- **Functionalized p-silicon photocathodes for solar fuels applications: Insights from electrochemical impedance spectroscopy**
  A. Sartori, M. Orlandi, S. Berardi, A. Mazzi, N. Bazzanella, S. Caramori, R. Boaretto, M. Natali, R. Fernandes, N. Patel, C. A. Bignozzi, A. Miotello,
  Electrochimica Acta, 271, 472-480, 2018

- **Evidence for Facilitated Surface Transport during Ge Crystal Growth by Indium in Liquid Hg–In Alloys at Room Temperature**
  D. Pattadar, Q. Cheek, *A. Sartori*, Y. Zhao, R. P. Giri, B. Murphy, O. Magnussen, and Stephen Maldonado
  Cryst. Growth Des. 21, 3, 1645–1656, 2021

- **Detection of Ge-Containing Adlayers at the Liquid Hg/Water Interface by In Situ X-Ray Reflectivity in Aqueous Borate Electrolytes Containing Dissolved GeO_2**
  J. P. Hazelnis[†], *A. Sartori*[†], Q. B. Cheek, R. P. Giri, M. M. MacInnes, B.t M. Murphy, O. M. Magnussen, S. Maldonado
  [†] J. P. Hazelnis and A. Sartori contributed equal to this work
  J. Phys. Chem. C, 126, 18, 8177-8189, 2022

- **Role of chemisorbing species in growth at liquid metal-electrolyte interfaces revealed by in situ X ray scattering**
  A. Sartori, R. P. Giri1, H. Fujii, S. C. Hövelmann, J. E. Warias, P. Jordt, C. Shen, B. M. Murphy, O. M. Magnussen
  Submitted Nature communications 2022

- **X-ray reflectivity from curved surfaces as illustrated by a graphene layer on molten copper**
  O. V. Konovalov, V. Belova, F. La Porta, M. Saedi, I. M. N. Groot, G. Renaud, I. Snigireva, A. Snigirev, M. Voevodina, C. Shen, *A. Sartori*, B. Murphy, M. Jankowski.
  J. Synchrotron Rad., 29, 711-720, 2022

Conference contributions

Posters:

In situ X-ray reflectivity studies of mercury electrolyte interfaces
A. Sartori, S. Festersen, J. Warias, F. Bertram, S. Maldonado, B. M. Murphy, O. M. Magnussen
DESY user meeting. 2018

In situ X-ray reflectivity studies of electrodeposition at mercury - electrolyte interfaces
A. Sartori, S. Festersen, J. Warias, F. Bertram, S. Maldonado,B. M. Murphy, O. M. Magnussen
The International Fischer Symposium (IFS). 2018

In situ X-ray reflectivity studies of electrodeposition at liquid metal electrolyte interfaces
A. Sartori, S. Festersen, H.Fujii, Q. Cheek, M. Maclnnes, S. Maldonado,B. M. Murphy, O. M. Magnussen
German conference for research with Synchrotron radiation Neutrons and Ion beams at large facilities (SNI). 2018

In situ investigation of electrochemical nucleation and growth at liquid-liquid interfaces through X-ray reflectivity
A. Sartori, S. Festersen, H.Fujii, Q. Cheek, M. Maclnnes, S. Maldonado,B. M. Murphy, O. M. Magnussen
Electrochemistry 2018, Electrochemical Surface Science: From Fundamentals to Applications

In situ X-ray reflectivity investigation of growth by electrodeposition at liquid-liquid interfaces
A. Sartori, S. Festersen, B. M. Murphy, O. M. Magnussen
DESY user meeting. 2019

In situ X-ray studies of electrodeposition of lead-halide compounds on the electrolyte-liquid mercury interfaces
A. Sartori, H. Fujii, R. P. Giri1, J. Warias, F. Bertram, O. M. Magnussen, B. M. Murphy
32^{nd} European Crystallographic Meeting (ECM). 2019

Electrodeposition on liquid metals: In-situ X-ray studies
A. Sartori, H. Fujii, R. P. Giri, J. Warias, F. Bertram, O. M. Magnussen, B. M. Murphy
DESY user meeting. 2020

X-ray reflectivity investigations at liquid metal/electrolyte interfaces
A. Sartori, H. Fujii, R. P. Giri, J. Warias, Q. Cheek, S. Maldonado, O. M. Magnussen, B. M. Murphy
Nanomaterial Formation at Fluid-Fluid Interfaces (Lorentz Center Workshop.) 2020

In situ X-ray studies of electrodeposition of lead-halide compounds on liquid mercury electrode
Electrodeposition on liquid metals: In-situ X-ray studies
A. Sartori, Q. Cheek, H. Fujii, R. P. Giri, J. Warias, S. Hövelmann, F. Bertram, S. Maldonado, O. M. Magnussen, B. M. Murphy
DESY user meeting. 2021
In situ X-ray investigation at liquid metal/electrolyte interfaces *A. Sartori*, H. Fujii, R. P. Giri, J. Warias, S. Hövelmann, F. Bertram, O. M. Magnussen, B. M. Murphy
DESY user meeting. 2022

Oral Presentation:

In situ X-ray studies at liquid-liquid interface
A. Sartori
Seminar talk, Chemistry department, University of Michigan. 2019

Acknowledgements

I would like to express my special thanks to Prof. Dr. Olaf Magnussen, who made it possible to write this thesis and supported me with his technical advice and expertise in electrochemical experiments and X-ray scattering.
Equally, many thanks to Prof. Dr. Bridget Murphy; I could count at all times on technical and moral support and to whom I owe an exciting and highly instructive time at the LISA diffractometer. My gratitude also goes to Prof. Dr. Stephen Maldonado, who significantly improved my chemistry, electrochemistry, and interface science knowledge.
The beam time on which the data used in this thesis were collected, would never have been possible without the help of the LISA team: Jonas Warias, Dr. Rajendra Giri, Svenja Hövelmann, Dr. Philipp Jordt, the former colleague Dr. Sven Festernsen, the visitor Dr. Hiromasa Fujii; and the members of the Maldonado group: Dr. Quintin Cheek, Joshua P. Hazelnis, Dr. Molly MacInnes, Dhruba K. Pattadar, Henry Wu, Dr. Nathanael Downes. Who spent numerous days and nights at the beamline for these experiments. In this context, I would also like to thank Dr. Florian Bertram, Dr. Chen Shen, Rene Kirchhof, Milena Lippmann, and other helpers at beamlines P08 at PETRA III for their support in technical and scientific matters. I would like to thank Matthias Greve and Karsten Tarhouni for their technical support in all hardware and software projects, in particular for the design of the electrochemical cell. Thanks to Claudia Läufer for her help in all organizational and bureaucratic matters. I thank my office colleagues Lasse Kattwinkel and Timo Fuchs for the lovely atmosphere, many conversations, and productive discussions. Likewise, I would like to thank the other group members: Dr.Victor DeManuel-Gonzalez, Dr. Jochim Stettner, Dr. Canrong Qiu, Reihaneh Amirbeigiarab, and Jing Tian as well the former colleagues Finn Reikowski, Nicolai Krekiehn and Martin Ruge. They have ensured a beautiful working environment. A special thank goes to Tim Wiegmann, Lukas Petersdorf, and Henning Vogt, who helped me in writing some of the *Python* codes necessary to analyze the data presented here.
I would also like to thank my friends for regularly supporting me during these years. Finally, I would like to thank Gwenael Thibault, whose love and support helped me through difficult times, especially this last period of my Ph.D. studies. Last but not least, my parents and sister always believed in me and whose support I could always rely on. GRAZIE.

Sworn Declaration

I, Andrea SARTORI, declare that this thesis titled, "*In-situ* X-ray scattering studies of growth at liquid metal-electrolyte interfaces" and the work presented in it are my own. Apart from the advice of my supervisors Prof. Dr. O. M. Magnussen and Prof. Dr. B. M. Murphy, and that I have received no other sources or assistance apart from those indicated. The work has been produced in accordance with the Rules of Good Scientific Practice of the German Research Foundation. No academic degree has been withdrawn from me. The submitted work has neither completely nor partially already been submitted to another body in the context of an examination procedure, but parts of the work have been published or submitted in scientific journals. An overview of the publications resulting from this thesis, can be found in the following:

- Chapter 4: **Andrea Sartori**, Rajendra Giri, Hiromasa Fujii, Svenja Hövelmann, Jonas, Warias, Philipp Jordt , Chen, Shen, Bridget M. Murphy, Olaf M. Magnussen . In situ X-ray studies of lead-halides adlayer and crystal growth at liquid mercury-electrolyte interface. Submitted (2022).
- Chapter 5: **Andrea Sartori**, Joshua P. Hazelnis, Quintin B. Cheek, Rajendra P. Giri, Molly I. MacInnes, Bridget Murphy, Olaf Magnussen and Stephen Maldonado. Detection of Ge-Containing Adlayers at the Liquid Hg/Water Interface by In Situ X-Ray Reflectivity in Aqueous Borate Electrolytes Containing Dissolved GeO_2. J. Phys. Chem. C 126, 18, 8177–8189 (2022).
- Chapter 6: Dhruba Pattadar, Quintin Cheek, **Andrea Sartori**, Yifan Zhao, Rajendra P. Giri, Bridget Murphy, Olaf Magnussen, and Stephen Maldonado Evidence for Facilitated Surface Transport during Ge Crystal Growth by Indium in Liquid Hg-In Alloys at Room Temperature, Crystal Growth & Design 21, 1645–1656 (2021).

Signed:

Date: